VILNIUS UNIVERSITY
CENTER FOR PHYSICAL SCIENCES AND TECHNOLOGY

Maksym
IVANOV

Singular Light Fields: Generation with an S-waveplate, Extension to THz Frequencies, Combination in OPA, and Applications in Optical Trapping

DOCTORAL DISSERTATION
Natural Sciences
Physics N 002

VILNIUS 2019

Research leading to this dissertation has been carried out between 2015 and 2019 at the Laser Research Center, Vilnius University. The research was supported by the Research Council of Lithuania. No white mouse was harmed in the course of this work.

Academic supervisor:
Doc. dr. Aidas Matijošius (Vilnius University, Natural Sciences, Physics N 002)

Dissertation Defence Panel:

Chairman – Prof. Habil. Dr. Audrius Dubietis (Vilnius University, Natural Sciences, Physics N 002)

Members:
Prof. Dr. Daniele Faccio (University of Glasgow, Natural Sciences, Physics N 002)
Assoc. Prof. Dr. Vygandas Jarutis (Vilnius University, Natural Sciences, Physics N 002)
Dr. Andrejus Michailovas (State research institute Center for Physical Sciences and Technology, Natural Sciences, Physics N 002)
Dr. Kęstutis Regelskis (State research institute Center for Physical Sciences and Technology, Natural Sciences, Physics N 002)

The dissertation shall be defended at a public meeting of the Dissertation Defence Panel at 14:00 on 24th September 2019 in Room 306 of the Laser Research Center, Vilnius University.
Address: Sauletekio al. 10, Lazerinių tyrimų centras, Room 306, Vilnius, Lithuania. Tel. +37064383075;

The text of this dissertation can be accessed at the Vilnius University Library, as well as on the website of Vilnius University: www.vu.lt/naujienos/ivykiu-kalendorius

VILNIAUS UNIVERSITETAS
FIZINIŲ IR TECHNOLOGIJOS MOKSLŲ CENTRAS

Maksym
IVANOV

Singuliariniai šviesos laukai: generacija S fazine plokštele, išplėtimas iki THz ruožo, derinimas parametrinio šviesos stiprinimo metu, ir taikymas šviesos gaudyklei

DAKTARO DISERTACIJA
Gamtos mokslai
Fizika N 002

VILNIUS 2019

Moksliniai tyrimai, pateikti disertacijoje, atlikti 2015–2019 m. Vilniaus universiteto Lazerinių tyrimų centre. Tyrimą palaikė Lietuvos mokslo taryba. Šio darbo metu nenukentėjo jokia balta pelė.

Mokslinis vadovas:
doc. dr. Aidas Matijošius (Vilniaus universitetas, Gamtos mokslai, fizika – N 002)

Dissertation Defence Panel:

Chairman – prof. habil. dr. Audrius Dubietis (Vilniaus universitetas, Gamtos mokslai, fizika – N 002)

Members:
prof. dr. Daniele Faccio (Glazgo universitetas, Gamtos mokslai, fizika – N 002)
doc. dr. Vygandas Jarutis (Vilniaus universitetas, Gamtos mokslai, fizika – N 002)
dr. Andrejus Michailovas (Valstybinis mokslinių tyrimų institutas Fizinių ir technologijos mokslų centras, Gamtos mokslai, fizika – N 002)
dr. Kęstutis Regelskis (Valstybinis mokslinių tyrimų institutas Fizinių ir technologijos mokslų centras, Gamtos mokslai, fizika – N 002)

Disertacija ginama viešame Gynimo tarybos posėdyje 2019 m. Rugsėjo mėn. 24 d. 14:00 val. fizikos fakulteto lazerinių tyrimų centro 306 auditorijoje.
Adresas: Saulėtekio al. 10, Lazerinių tyrimų centras, 306 aud., Vilnius, Lietuva. Tel. +37064383075;

Disertaciją galima peržiūrėti Vilniaus universiteto bibliotekoje ir VU interneto svetainėje adresu: www.vu.lt/naujienos/ivykiu-kalendorius

Acknowledgement

I am grateful for the opportunity and trust being first international full time PhD student at the Laser Research Center. I did my best to keep up with the high standards of the world-know Vilnius school of nonlinear optics.

Firstly, I would like to thank Valerijus Smilgevičius who introduced me to the world of nonlinear optics, accepted me for an internship at the Laser Research Center, and furthermore for offering me this opportunity to switch to PhD at Vilnius University. Aidas Matijošius for full support in any questions arising during the course of this work. Valdas Sirutkaitis and Virgilijus Vaičaitis for giving me a possibility to join the THz group at the Laser Research Center, which then turned into one of the chapters of this dissertation. Special thanks to Valdas and Aidas for upgrading my official status from student to employer, which allowed me to work on this dissertation while having my lovely wife by my side. Dag Hanstorp from the University of Gothenburg, Sweden, for accepting me for an internship during my first year of PhD study and during next two consecutive summers, which then resulted in one of the chapters of this dissertation.

Outside the work, I would like to thank football team of the Laser Research Center for all year around evening football matches, which were happening outside at any weather, sun or rain/snowfall, +25 or –20°C. These were giving a great amount of relief and amusement.

Finally, I would like to thank my wife and my parents for unconditional love and support.

Contents

List of abbreviations

AM	angular momentum	OPA	optical parametric amplification/amplifier
AT	azimuthal-type	OV	optical vortex
BBO	Beta Barium Borate	P	polarizer
BS	beam splitter	PBS	polarizing beam splitter
CCD	charge coupled device	PC	photonic crystals
CERS	cavity-enhanced Raman spectroscopy	PID	proportional-integral-derivative
CKE	collision kinetic energy	PSD	position sensitive detector
CW	continuous wave	QW	quarter wave
DPSS	diode pumped solid-state	QWP	quarter wave plate
EOM	electro-optical amplitude modulator	RMS	root mean square
FH	fundamental harmonic	RT	radial-type
fps	frames per second	SAM	spin angular momentum
FWHM	full width at half maximum	SE	surface energy
HW	half wave plate	SH	second harmonic
LC	liquid crystals	SHG	second harmonic generation
LG	Laguerre-Gaussian	STED	stimulated emission depletion
LED	light-emitting diode	SWP	S-waveplate
LIDT	laser-induced damage threshold	TC	topological charge
MO	micro-lens/objective	THz	terahertz
Nd:YAG	neodymium-doped yttrium aluminum garnet, Nd:$Y_3Al_5O_{12}$	TTL	transistor-transistor logic
nIR	near-infrared	UV	ultraviolet
OAM	orbital angular momentum	VIS	visible light spectrum

Introduction

> There is an urban legend about the infamous bank robber Willie Sutton (1901–1980) that claims that, when asked why he robbed banks, he answered, “because that’s where the money is.” It might similarly be said that the study of optics has traditionally, and quite reasonably, been about the regions where the intensity of light is nonzero, “because that’s where the light is.”
>
> *Gbur, G. (2017). Singular Optics. Boca Raton: CRC Press*

The essence of optical vortex beams can be explained based on the formalism of light interference. For example, in the interference experiment with three waves, light vanishes at some points due to destructive interference and enhances at others due to constructive summation of the waves. While most regions of non-zero intensity look locally as plane waves, the neighbourhoods of zeros of the field have unusual behaviour. Because the field intensity is zero, then the phase is indeterminate, or "singular". Such spots are called phase singularities. In general, all 2π phase values occur around the zero leading to circulation of flow of the optical energy. Zeros of field intensity typically manifest as lines in threedimensional space, around which the phase has a circulating or helical behavior, which led to the optical vortex (OV) term. One finds that, with limited exceptions, optical vortices are the typical singularities that occur in a general interference experiment with more than two waves. OVs have a well-defined mathematical structure [1] and, furthermore, this structure can strongly influence the overall behaviour of the wavefield and its interaction with matter. Now study of singularities of the light fields has grown to the developed subfield of optics known as *singular optics*. Since isolated zeros of light field can give as much information as the bright spots of light, singular optics provides an

alternative approach to study light. From the practical point of view, specially prepared vortex beams possess a variety of interesting structural properties which are useful across many fields of optics: optical trapping and manipulation, optical communication, microscopy, and astronomy, just to name a few.

First discoveries of the optical vortices have been made in natural (without special preparation) experiments on diffraction and interference. Naturally complex light field contains strongly connected pairs of vortices, topological dipoles [2], which can be tied in knots and links [3], be born and annihilate upon light propagation. This evolving light field is interesting for the fundamental research but has a little of practical importance. Therefore, since late 1980s, different research groups have been developing and proposing schemes for generation of stable, upon propagation, single OV at the axis of the monochromatic laser beam. Laser beam with a vortex at the axis is mathematically described by a Laguerre-Gaussian mode. Phase of OV beam varies azimuthally and its complex amplitude is proportional to $e^{il\phi}$, where ϕ is the azimuthal angle varying from 0 to 2π, l describes winding of the helical wavefront and known as the topological charge or strength of the phase singularity. The topological charge describes multiplicity of the helical wavefront and its sign denotes the handedness [2, 4]. Advent of ultra-short pulsed laser systems significantly complicated process of the generation of the vortex beams. This is because ultra-short laser pulses consist of a number of spectral components, i.e. they are broadband. Indeed, the wavefront of OV which give rise to the orbital angular momentum (OAM) of the beam has the tilt of $l\lambda/2\pi r$, where r is the radius [5]. Inherent dependence on wavelength λ makes generation of OV beams technically challenging using ultra-short pulses consisting of different spectral components. But strong motivation for broadband optical systems, e.g. in optical and quantum communication systems, and data transmission through photonic crystal fibers, pushes for generation of broadband OV beams.

Away from the optical domain, terahertz (THz) spectral region currently draws much of attention of physics community. THz radiation is of great current interest due to many applications such as nonlinear THz spectroscopy and imaging [6] or alternative for electron bunch compression [7]. Extending the reach of singular optics to new frequency domains, such as THz radiation, could open new horizons in the THz physics. Previous attempts on vortex generation at the THz frequencies [8–15] were exclusively based on manipulation of THz wave by external components which are inherently limited in terms of acceptable bandwidth. Therefore, alternative methods for ultra-broadband vortex generation at THz frequencies should be proposed and investigated. Very recently, vortex-shaped THz pulses have been generated without external shaping elements [16, 17] in ZnTe crystal, however, with relatively narrow bandwidth. Therefore, the question of generation of broadband THz vortices is still remains open.

Transformations of vortex beams have also been studied in nonlinear regimes. It was shown that for optical vortices the law of topological charge conservation holds in the form of $l_1 + l_2 = l_3$ during second order, $\chi^{(2)}$, nonlinear processes. Conservation of the topological charge was shown for the processes of second harmonic generation (SHG) [18], sum-(difference-) frequency generation [19, 20], nonlinear wave mixing [21] and parametric fluorescence [22]. Moreover, in [19,23] it was shown that arithmetic operations (and multiplication by -1) could be performed with optical vortices by addition and subtraction of topological charges in nonlinear processes. It should be mentioned that conservation of topological charge holds in collinear regime of second harmonic generation and at small angles in non-collinear regime, otherwise the topological charge is not conserved [24, 25]. Conservation of topological change upon optical parametric amplification (OPA), more precisely combination of vortices of different charges, leads to practically important implications. For example, it is possible to obtain radially polarized pulses, which can be applied in laser material processing [26–29], and acceleration of electrons by the longitudinal electric field component [30–32]. Conventionally generation of radial polarization relies on polarization conversion in dedicated optical component. However, damage threshold of the optical components dramatically limits energy of the laser pulse necessary for the high power applications. Therefore, generation of radially polarized pulse from OPA based on combination of OVs can be attractive alternative for the high power applications.

One of the applications of OV beams is in optical trapping and manipulation. The optically induced rotation of trapped particles is used, for example, in the noninvasive orientation of living cells, probing dynamics of particles, and investigations of tribological systems [33,34]. A particle can be set to a rotational motion by a rotating wavefront upon interference between two beams of slightly different frequencies [35], or using beams carrying angular momentum (AM). The AM of light consists of spin angular momentum (SAM) and orbital angular momentum (OAM) [36]. The SAM is associated with the circular polarization of the beam, whereas the OAM is associated with the vortex geometry of the beam, such that the trapped particle experiences an additional tangential force. Particles trapped on the axis of a beam can be set to rotate by either the SAM and OAM of the light, in the case of birefringent [37, 38] and absorbing particles [39, 40]. On the other hand, nonabsorbing (transparent) and isotropic particles, such as liquid droplets, cannot be rotated by SAM, such as a circularly polarized beam. Nevertheless, it is possible to optically rotate such particles using the OAM of light [34,41–43], as was first demonstrated by Volke-Sepulveda et al. using transparent silica beads in a liquid [41] and by McGloin et al. using water aerosol droplets in air [34]. However, in those cases, the beads and droplets exhibit only orbital motion, making circular trajectories around the center of a beam due to the doughnut shape of the laser beam. The spinning type of

motion for such particles—such as when a particle remains in place and spins around its axis—has not yet been demonstrated. Even though optical spinning of isotropic and nonabsorbing droplets can find applications outside optics, such as in fluid dynamics, where rotating droplets could be achieved in the study of collisional dynamics of liquid droplets in studies of raindrop formation [44].

Goal of the dissertation

Therefore, the goal of this dissertation is to develop methods of generation of (i) ultra-broadband optical vortices, (ii) terahertz vortices, (iii) radially polarized vortex-free beam, and to propose application of vortex beams in optical manipulation as part of development of the versatile modular system for optical manipulation experiments.

Tasks of the work

In order to reach this goal the following tasks were implemented:

1. To theoretically and experimentally study effect of perturbation of the phase delay of a geometric phase retarder on the phase, intensity, and polarization distribution of the generated optical vortex beam and radially/azimuthally polarized beam.

2. To numerically and experimentally demonstrate a method for generation of an optical vortex pulses in wide spectral region (more than octave spanning) from both temporarily coherent and incoherent light sources. Generated optical vortex should exhibit coaxiality (no spatial dispersion) of optical vortices generated at different wavelengths.

3. To experimentally investigate influence of laser-preformed plasma on the energy and spatial properties of terahertz beam generated in air by focused femtosecond bichromatic laser pulses.

4. To investigate generation of ultra-broadband (>30 terahertz) vortex pulses at terahertz frequencies from plasma filament formed in air by focused femtosecond bichromatic optical vortex laser pulses.

5. To develop optical parametric amplifier with radially polarized output without use of external polarization converters.

6. To develop part of the versatile modular system for optical manipulation experiments, particularly part for studies of collisional dynamics of micron-sized droplets under gravity with aid of two optical traps.

7. To develop a method for optically induced rotation (both spinning and orbiting) of nonbirefringent and nonabsorbing particles in optical vortex beam. To be used as an extension to the modular system from the sixth task.

Aim and tasks of this dissertation are schematically shown in Fig. 4.19.

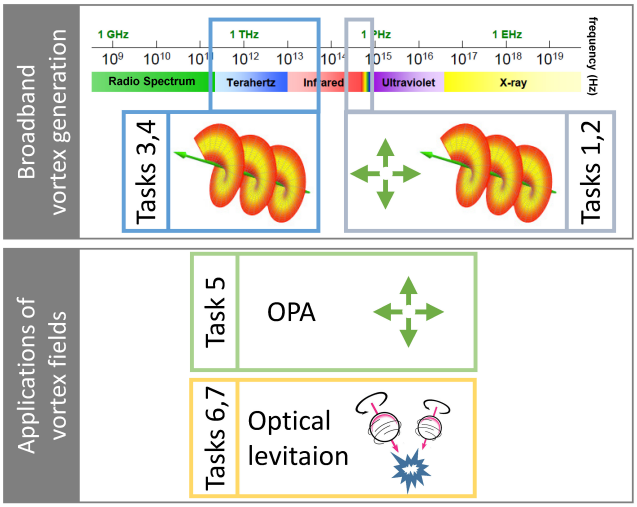

Figure 1: Schematic overview of the aim and tasks of this dissertation.

Novelty and importance of the work

Novel schemes for the generation of ultra-broadband optical vortex pulses, radially polarized pulses, and vortex pulses at THz frequencies were developed in the course of research described in this dissertation. Effect of inhomogeneous retardation on the properties of the beam generated with a geometric phase retarder was investigated for the first time. Novel schemes for the optically controlled switchable spinning and orbiting motion of a droplet, and for the optically initiated collisional dynamics of droplets were developed.

Broadband optical vortices has practical importance for quantum communication systems and broadband data transmission through photonic crystal fibers. High power radially polarized pulses has practical importance in laser material processing and acceleration of electrons by the longitudinal electric field component. Study of THz vortex pulses has a potential to open new routes towards an active control of ultra-broadband terahertz beam properties and opens new horizons in terahertz physics by extension of the field of singular optics to the terahertz frequencies. Developed optical methods for spinning of droplets and study their collisions has practical importance in fluid dynamics in studies of raindrop formation and to account for the effect of turbulence on it.

Key statements for defence

1. Even small perturbation of retardation of a geometric phase retarder leads to asymmetry in polarization, phase and intensity distribution of the generated beam. In the case of homogeneous retardation of the geometric phase retarder this asymmetry is strong. In the case of retardation oscillating around half wave plate retardation this asymmetry fades out during free space beam propagation, therefore, polarization, phase, and intensity becomes symmetrically distributed.

2. Vortex and non-vortex states of the pulse converted on a geometric phase retarder can be spatially separates with ensured coaxially of the vortices at any wavelength in the octave diapason around default wavelength.

3. Power of THz waves decreases in the presence of the prepulse-created plasma even when the crossing point of the two laser beams is well before or after the pump beam focus. At least two different mechanisms—namely, phase modification of the pump waves and screening of THz radiation by preformed plasma filaments—are responsible for this effect.

4. Terahertz radiation generated by electron currents in a plasma filament, induced by fundamental harmonic Gaussian and second harmonic optical vortex pump, becomes intensity modulated along the ring of light and contains two minima between two lobes of maximum intensity. Phase of the generated terahertz radiation does contain phase singularity.

5. Radial, azimuthal, or mixed polarization states can be obtained in the degenerate optical parametric amplifier (with Gaussian pump and vortex signal). Final polarization state can be actively controlled and switched between by control of relative phase between idler and signal, or idler and pump.

6. Developed optical trapping scheme allows controllable and repeatable experiments on collisional dynamics of micron-sized droplets under gravity as part of versatile modular system for optical manipulation experiments.

7. Optical levitation of a nonbirefringent (isotropic) and nonabsorbing (transparent) glycerol droplet in an optical vortex beam allows to switch between orbiting and spinning types of rotational motion. The type of motion depends on the size of the local waist of the trapping beam at the point of trapping, which is controlled by the power level of the trapping laser beam.

Layout of the dissertation

Generation, nonlinear conversion, and applications of vortex beams are discussed in this dissertation as schematically shown in Fig. 2.

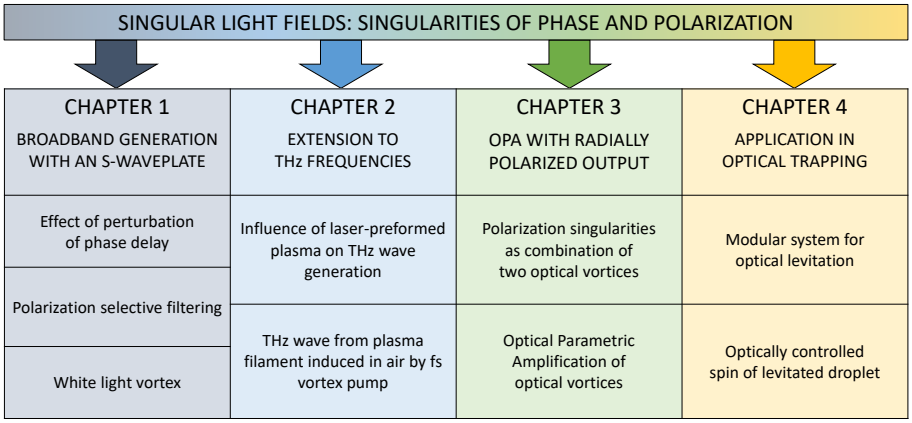

Figure 2: Layout of the dissertation.

Approbation of the research results

List of publications related to the dissertation

- *in peer-reviewed journals:*

[A1] M. Ivanov, I. Thiele, L. Bergé, S. Skupin, D. Buožius, and V. Vaičaitis, *Intensity modulated terahertz vortex wave generation in air plasma by two-color femtosecond laser pulses*, **Opt. Lett.** 44, 3889-3892 (2019)

doi: 10.1364/OL.44.003889

[A2] V. Vaicaitis, M. Ivanov, K. Adomavicius, Z. Svirskas, U. Morgner, and I. Babushkin, *Influence of laser-preformed plasma on THz wave generation in air by bichromatic laser pulses*, **Laser Phys.** 28 095402, (2018)

doi: 10.1088/1555-6611/aaca5f

[A3] M. Ivanov and D. Hanstorp, *Controlled spin of a nonbirefringent droplet trapped in an optical vortex beam*, **Opt. Commun.** 427 152–157 (2018)

doi: 10.1016/j.optcom.2018.06.021

[A4] M. Gecevicius, M. Ivanov, M. Beresna, A. Matijosius, V. Tamuliene, T. Gertus, A. Cerkauskaite, K. Redeckas, M. Vengris, V. Smilgevicius,

and P. G. Kazansky, *Towards the generation of broadband optical vortices: extending the spectral range of a geometric phase retarder by polarization-selective filtering*, **J. Opt. Soc. Am. B** 35, 190-196 (2018)

doi: 10.1364/JOSAB.35.000190

[A5] P. Stanislovaitis, M. Ivanov, A. Matijosius, V. Smilgevicius, and T. Gertus, *Generation of radially polarized beams and higher order polarization singularities by optical parametric amplification of optical vortices*, **Opt. Eng.** 56(9), 095101 (2017)

doi: 10.1117/1.OE.56.9.095101

[A6] M. Ivanov, K. Chang, I. Galinskiy, B. Mehlig, and D. Hanstorp, *Optical manipulation for studies of collisional dynamics of micron-sized droplets under gravity*, **Opt. Express** 25, 1391-1404 (2017)

doi: 10.1364/OE.25.001391

- *others:*

[B1] D. Hanstorp, M. Ivanov, A. F. Aleman Hernandez, J. Enger, A. M. Gallego, O. Isaksson, C-J Karlsson, R. Monroy Villa, A. Varghese, K. Chang, *A versatile system for optical manipulation experiments*, **Proc. SPIE** 10347, 103472C (2017)

doi: 10.1117/12.2272983

[B2] M. Ivanov, M. Viderstrom, K. Chang, C. Ramirez Contreras, B. Mehlig, D. Hanstorp, *Spectroscopy and optical imaging of coalescing droplets*, **Proc. SPIE** 9922, 99220I (2016)

doi: 10.1117/12.2236634

List of other publications not covered by the scope of this dissertation

- *in peer-reviewed journals:*

[C1] P. Stanislovaitis, A. Matijosius, M. Ivanov, and V. Smilgevicius, *Topological charge transformation of beams with embedded fractional phase step in the process of second harmonic generation* **J. Opt.** 19 105603 (2017)

doi: 10.1088/2040-8986/aa820d

[C2] N. Shostka, M. Ivanov, and V. Shostka, *Controllable Optical Trap Arrays*, **Tech. Phys. Lett.** 42: 944 (2016)

doi: 10.1134/S106378501609025X

[C3] M. Ivanov and N. Shostka, *Focusing of Gaussian beam passed under small angle to optical axis of uniaxial crystal* **J. Opt.** 18 075603 (2016)

doi: 10.1088/2040-8978/18/7/075603

[C4] T. Fadeyeva, C. Alexeyev, A. Rubass, M. Ivanov, A. Zinov'ev, V. Konovalenko, and A. Volyar, *Rotational spin Hall effect in a uniaxial crystal*, **Appl. Opt.** 51, C231-C240 (2012)

doi: 10.1364/AO.51.00C231

- *others:*

[D1] M. Ivanov and N. Shostka *Beam propagation in a uniaxial crystal under small angle to the optical axis and arrays of bottle beams*, **Proc. SPIE** 9194, 91941C (2014)

doi: 10.1117/12.2063661

[D2] T. Fadeyeva, M. Ivanov, Kh. Borysova, A. Borysov, A. Rubass, *Evolution of symmetric and asymmetric optical beam arrays passing along optical axis of uniaxial crystal*, **Proc. SPIE** 9066, 90660D (2013)

doi: 10.1117/12.2051788

[D3] M. Ivanov, A. Zinovyev, V. Konovalenko, A. Rubass, *Displacement of Bessel-Gaussian beams array passed through a uniaxial crystal*, **Scientific Notes of Taurida National V.I. Vernadsky University.** – Series: Physics and Mathematics Sciences. Vol. 24 (63), No.2. (2011)

[D4] M. Ivanov, B. Sokolenko, A. Rubass, *Algebra of interaction of polarized vortices and Bessel-Gaussian beam*, **IONS 8** (OSA), paper ILNO3 (2010)

doi: 10.1364/IONS_8.2010.ILNO3

List of conference contributions related to the dissertation

1. M. Ivanov, Illia Thiele, Luc Berge, Stefan Skupin, Danas Buozius, Virgilijus Vaicaitis, SPIE Optics+Photonics, 11 - 15 August 2019, San Diego, USA. Oral presentation

2. M. Ivanov, Illia Thiele, Luc Berge, Stefan Skupin, Danas Buozius, Virgilijus Vaicaitis, CLEO/EUROPE-EQEC 2019, 23 – 27 June 2019, Munich, Germany. Oral presentation

3. M. Ivanov, Illia Thiele, Stefan Skupin, Danas Buozius, Virgilijus Vaicaitis, Optics and Photonics Days "OPD2019". Espoo, Finland. 27-29 May 2019. Oral presentation

4. M. Ivanov, A. Matijosius, and V. Smilgevicius, 61st International Conference for Students of Physics and Natural Sciences "Open Readings 2018". Vilnius, Lithuania. 20-23 March 2018. Poster

5. M. Ivanov, P. Stanislovaitis, A. Matijosius, T. Gertus, and V. Smilgevicius. 42oji Lietuvos Nacionaline Fizikos Konferencija. Vilnius, Lithuania. 4-6 October 2017. Oral presentation

6. M. Ivanov, P. Stanislovaitis, A. Matijosius, T. Gertus, and V. Smilgevicius. 42oji Lietuvos Nacionaline Fizikos Konferencija. Vilnius, Lithuania. 4-6 October 2017. Poster

7. M. Ivanov, M. Viderstrom, K. Chang, C. R. Contreras, B. Mehlig, D. Hanstorp. "SPIE Optics + Photonics 2016". San Diego, California, USA. 28 August - 1 September 2016. Oral presentation

8. M. Ivanov, K. Chang, D. Hanstorp. "Cloud physics on the Zugspitze". Zugspitze, Munich, Germany. 17-20 April 2016. Oral presentation

9. M. Ivanov, M. Gecevicius, M. Beresna, T. Gertus, A. Matijosius, P. Kazansky and V. Smilgevicius. "41-oji Lietuvos Nacionalinė Fizikos Konferencija". Vilnius, Lithuania. 17-19 June 2015. Poster

10. M. Ivanov, M. Gecevicius, M. Beresna, T. Gertus, A. Matijosius, P. Kazansky, V. Smilgevicius. "Open Readings 2015". Vilnius, Lithuania. 24-27 March 2015. Poster

11. M. Gecevicius, M. Ivanov, T. Gertus, A. Matijosius, V. Smilgevicius, "Naujametė Fizikos Konferencija LTF 2015". Vilnius, Lithuania. 2-3 January 2015. Oral presentation

List of conference contributions not covered by the scope of this dissertation

1. M. Ivanov, N. Shostka, "SPIE Optics + Photonics 2014". San Diego, California, USA. 17-21 August 2014. Poster

2. T. Fadeyeva, M. Ivanov, Kh. Borysova, A. Borysov, A. Rubass, "Eleventh International Conference on Correlation Optics". Chernivtsi, Ukraine. 18-21 September 2013. Poster

3. T. Fadeyeva, M. Ivanov, Kh. Borysova, A. Borysov, A. Rubass, "International Workshop on NONLINEAR PHOTONICS NLP*2013". Sudak, Ukraine. 10-11 September 2013. Poster

4. M. Ivanov, T. Fadeyeva, A. Zinovyev, V. Konovalenko, A. Rubass. "5th International Conference "Singular Optics SO'2012"". Sevastopol, Ukraine. 16-21 September 2012. Poster

5. M. Ivanov, A. Zinovyev, V. Konovalenko, A. Rubass. "12th International Young Scientists Conference Optics and High Technology Material Science - SPO 2011". Kyiv, Ukraine. 27-30 October 2011. Poster

Contributions

- *contribution of the author:*

1. Publication [A1]. M. Ivanov has initiated this investigation by starting collaboration with I. Thiele from Chalmers University of Technology. M. Ivanov has conducted experiment, performed analysis of obtained data, and prepared manuscript for publication.

2. Publication [A2]. M. Ivanov has noticed described in the publication effect, performed experimental investigation, analysis of obtained data, and was involved in manuscript preparation for publication.

3. Publication [A3]. M. Ivanov has developed described in the paper novel method, performed experiment, analyzed acquired data, and prepared manuscript for publication.

4. Publication [A4]. M. Ivanov has conducted experiment, performed half of analysis of obtained data; performed modelling of the vortex generation from the incoherent source; performed more than a half of manuscript preparation.

5. Publication [A5]. M. Ivanov has conducted experiment, performed analysis of obtained data, and was heavily involved in preparation of manuscript for publication.

6. Publication [A6]. M. Ivanov has designed and built experimental setup, conducted experiment, performed major part of analysis of obtained data, and was heavily involved in preparation of manuscript for publication.

7. Publication [B1]. M. Ivanov has designed big part of experimental setup, conducted experiments on droplet rotation with vortex beam, and prepared part of the manuscript describing performed experiments.

8. Publication [B2]. M. Ivanov has developed and build experimental setup, collected and analyzed experimental data, and took important part in manuscript preparation.

- *contributions of other major co-authors:*

Prof. *Valerijus Smilgevičius* is responsible for me doing this dissertation, has provided hospitality and lab for the experiments on optical vortex generation

and parametric amplification from the publications [A4, and A5]; formulated tasks and participated in interpretation of the experiments from mentioned publications.

Dr. *Aidas Matijošius* has guided me thought the PhD and assisted with any questions; formulated tasks, helped to analyze and interpret the results from the publication [A4]; provided valuable discussions through out the study and research.

Prof. *Dag Hanstorp* has provided hospitality and laboratory for experiments on optical manipulation. Provided valuable discussions and interpretation of the experimental results from the publications [A3, A6, B1, B2], formulated tasks from the publications [A6, B1, B2].

Dr. *Virgilijus Vaičaitis* has provided lab for the experiments on THz, participated in formulation of the tasks, interpretations of results, and valuable discussions for the questions from the publications [A1, A2].

Dr. *Viktorija Tamulienė* has assisted with matlab modelling from the publication [A4].

Dr. *Paulius Stanislovaitis* has laid out theoretical background and idea from the publication [A5].

Dr. *Illia Thiele*, Dr. *Stefan Skupin*, and Dr. *Luc Bergé* have performed theoretical modelling of the THz vortex generation from the laser-induced plasma from the publication [A1].

1. Generation of broadband singular light fields with an S-waveplate

This chapter is partially based on the [A4] publication.

1.1. Literature review

Increasing number of photonic applications employ scalar vortex beams (OV) or vector beams with exotic polarization distribution, for example, with radial or azimuthal distribution of the electric field. Examples of such applications are in various areas [26–32, 43, 45–50]. Broadband OV beams are desired in most of those applications; however, their generation is technically challenging. Spectral bandwidths of different methods for efficient vortex generation are summarized in Table 1.1.

For generation of vortex beams and exotic polarization states this work employed a geometric-phase retarder, which by changing polarization of the incident beam changes its geometric (Pancharatnam-Berry) phase [51]. Retardation is induced by the nano-(sub-wavelength)-grating in a fused silica plate. Such retarders are also referred to as super-structured wave plates – S-waveplates. Since principle of work of all elements based on the geometric (Pancharatnam-Berry) retardation (see table 1.1) is based on the same physical principle, then the use of these terms will be interchangeable in this work. However, the term S-waveplate, in particular, is used for description of the experimental results.

A Gaussian beam propagating through an S-waveplate transforms to a beam with a doughnut intensity profile. Its phase and polarization distribution depends on the initial polarization state of the beam.

Circularly polarized input: the initial left (right) circularly polarized Gaussian beam (with, topological charge, $l = 0$, flat phase) transforms to right (left) circularly polarized optical vortex beam (with $|l| = 1$, helical phase). A decade ago, it was suggested that additional polarization sensitive [68] or

Method	**demonstrated bandwidth**	**ref.**
Forked grating	**250 nm**	[52]
Phase plates	**140 nm**	[53]
Axially-symmetric polarizer , quarter and half waveplates, and a glass cone	entire visible spectrum	[54–57]
Biaxial crystals + polarization filtering	**250 nm**	[58]
Uniaxial crystals + polarization filtering	**360 nm** (theoretical limit is transparency range of the crystal and polarizing optics)	[59–61]
geometric-phase retarder (q-plate, liquid crystals based)	variable monochromatic	[62, 63]
geometric-phase retarder (photonic crystals based)	**300 nm**	[64]
geometric-phase retarder (S-waveplate, nano-grating based)	monochromatic	[65–67]
S-waveplate + polarization filtering	***600 nm***	*this thesis, [A4]*

Table 1.1: Comparison of bandwidth over which vortex beam can be generated by different methods.

spatial filtering [69] can significantly broaden the spectral performance of Pancharatnam-Berry phase elements, such as S-waveplate, q-plate, etc. However, the experimental efforts were confined to far-infrared spectral range and did not demonstrate the polarization sensitive beam cleaning as spatial filtering was performed instead [69]. Similar polarization filtering was performed to reduce dispersion of topological charge of high order OVs [70]. Yet, enhancement of spectral performance was not demonstrated, and theoretical description of the process was not given.

Therefore, in the section 1.3.2 the polarization-sensitive filtering is theoretically described, and generation of an optical vortex beam over the entire visible and near infrared range, from temporarily coherent and incoherent light sources, is experimentally demonstrated. This technique allows converting any wavelength dependent (chromatic) Pancharatnam-Berry phase element to an achromatic one. For the experiments we have employed a high damage threshold S-waveplate [71] designed to work at the wavelength of 532 nm and demonstrated that it can be used to generate high contrast OV beams at any given wavelength in the range between 400 nm and 1040 nm.

Linearly polarized input: the initial linear polarization (with $l = 0$) becomes radial (with $l = 0$, vortex-free phase) if the S-waveplate is aligned parallel to the orientation of the incident linear polarization and azimuthal (with

$|l| = 0$, vortex-free phase) if aligned perpendicularly. Further linearly polarized input will be considered in a circularly polarized basis as a superposition of two orthogonal circularly polarized components. Therefore, radially and azimuthally polarized beams can be described as a superposition of two beams of opposite circular polarization, both carrying optical vortices at the center of the beam with opposite direction of vorticity (i.e. topological charges) [72, 73].

Since, the resulting beam is a superposition of two beams of equal intensities, which centers coincide, it is very sensitive to small perturbations of (i) retardance and (ii) orientation of varying optical axis (or grating pattern of the S-waveplate). (i) Proper (e.g. $\lambda/2$) retardance of a geometric-phase retarder ensures (a) equal intensities of LCP and RCP components of the beam, which results in "linear" (meaning zero ellipticity) polarization of the converted beam, and (b) coincidence of locations of vortices within the orthogonally polarized components of the beam. (ii) Gradual change of orientation of the optical axis of a geometric-phase retarder ensures gradual phase advance and rotation of direction of polarization vector of converted beam and its alignment in, e.g. radial or azimuthal pattern.

It is technically challenging to create a geometric-phase retarder plate with exactly half waveplate (π) retardation at every point of the plate (i.e. homogeneously distributed). Majority of techniques (including nano-grating and liquid crystals), especially at their early production years, have been producing plates with retardation which differs from π by up to 10% at different places on the plate (i.e. inhomogeneously distributed). Therefore, in the following sections, we investigate effect of perturbation of retardation (i) of a geometric-phase retarder (considering both homogeneous and inhomogeneous perturbations) on the polarization, phase, and intensity structure of the generated vector beam. Our theory suggests, and experiment confirms, that perturbation of retardation of a geometric-phase retarder leads to break in the symmetry of intensity, polarization, and phase distribution of the converted beam. These in turn results in mismatch of locations of optical vortices in orthogonally polarized components of the converted beam, and their motion along distinct trajectories, leading to appearance of the vortex phase in the generated radially/azimuthally polarized beam. Previously this problem was studied only partially. D'Errico et al. [74] considered features of a vector beam generated by a q-plate with retardation perturbed *only homogeneously*, which usually is not the case on the experiment. Additionally, effect of perturbation on spin-to-orbital coupling, which has significant practical implication, was not studied. Present investigation attempts to shade light on these missing areas. Perturbation of orientation of the optical axis (ii) will be studied elsewhere.

The rest of the chapter is organized as follows. Section 1.2 gives general description of the conversion process. Section 1.3 describes phase, polarization, and intensity structure of the beam converted by a plate with ideal and homogeneously perturbed retardation in the case of circularly (1.3.1) or linearly

(1.3.3) polarized input; section 1.3.2 describes a method to correct phase of the generated vortex beam in an ultra-broadband spectral region. Further, section 1.4 describes phase, polarization, and intensity structure of the beam converted by a plate with inhomogeneously perturbed retardation and how this might lead to recovery of the required (e.g. radial) polarization state. Finally, section 1.5 describes spin-to-orbital conversion of angular momentum of the beam.

1.2. Polarization-phase conversion of the beam

We will consider a geometric-phase retarder (q-plate, S-waveplate, etc) with topological charge of the plate q=1/2 (defining the rotation of the local optical axis around the singular point) [75]. The Jones matrix of the unperturbed retarder with exactly $\lambda/2$ or π retardation is given by:

$$M_q = \begin{bmatrix} \cos(\varphi) & \sin(\varphi) \\ \sin(\varphi) & -\cos(\varphi) \end{bmatrix}, \tag{1.1}$$

where φ is the azimuthal angle of a polar coordinate system. Now, we will discuss the action of the retarder on different input polarization states, so let us involve into consideration the Jones vectors of horizontally (X), vertically (Y) linearly, and left-handed (L) and right-handed (R) circularly polarized states that are given by:

$$E_X = \frac{1}{\sqrt{2}} \begin{bmatrix} 1 \\ 0 \end{bmatrix}; E_Y = \frac{1}{\sqrt{2}} \begin{bmatrix} 0 \\ 1 \end{bmatrix}; E_L = \frac{1}{\sqrt{2}} \begin{bmatrix} 1 \\ i \end{bmatrix}; E_R = \frac{1}{\sqrt{2}} \begin{bmatrix} 1 \\ -i \end{bmatrix}, \tag{1.2}$$

respectively. Fig. 1.1 schematically shows the process of conversion. A Gaussian beam with circular polarization converted by such a retarder transforms to a doughnut shaped beam (not shown). Left part labelled 'incident' shows incident polarization state and corresponding Jones vector. Projection of angular momenta of the beam on propagation axis z is also specified. The middle part of this figure schematically demonstrates orientation of the optical axis of the retarder, its retardation, and Jones matrix M_q. Right part labelled 'output' shows polarization state of the converted beam. Orientation of arrows show phase of the beam, as the phase map at the background. The conversion is accompanied by the following transformation of polarization and phase of the beam: (Fig. 1.1a) the initial left (right) circular polarization (with $|l| = 0$) transforms to right (left) circular polarization, the beam acquires vortex phase with topological charge $|l| = 1$, as evident from the $e^{i\varphi}$ component in the Jones matrix and by phase distribution in the corresponding subimage. With the notations of Eqs. (1.1), (1.2) we can write:

$$M_q E_L = E_R \exp(i\varphi);\ M_q E_R = E_L \exp(-i\varphi). \tag{1.3}$$

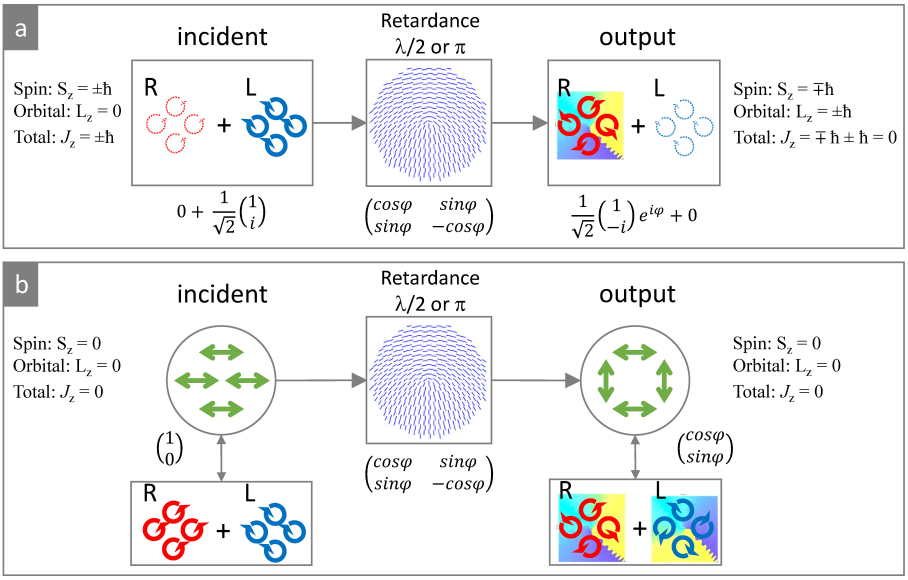

Figure 1.1: Schematic of polarization, phase, and angular momenta conversion for incident (a) circularly polarized and (b) linearly polarized beam. Arrows show polarization state, so as the Jones matrices by the arrows. Components shown by dotted lines do not exist. Retardance of the S-waveplate and orientation of its optical axis are shown in the middle together with its Jones matrix; φ is the azimuthal angle in polar coordinate system. S_z, L_z, and J_z are projections of spin, orbital, and total angular momenta of the beam on the propagation axis z.

Fig. 1.1b shows that the initial linear polarization becomes azimuthal if the retarder is oriented perpendicularly to the orientation of the incident linear polarization, and radial if this orientation is parallel (not shown). The output beam is a superposition of two vortices with opposite phases, so the total phase of the beam remains vortex-free, e.g.

$$M_q E_X = E_{RP};\ M_q E_Y = E_{AP}, \tag{1.4}$$

where

$$E_{RP} = \frac{1}{\sqrt{2}}\begin{bmatrix}\cos(\varphi)\\ \sin(\varphi)\end{bmatrix};\ E_{AP} = \frac{1}{\sqrt{2}}\begin{bmatrix}\sin(\varphi)\\ -\cos(\varphi)\end{bmatrix} \tag{1.5}$$

describe the radial and azimuthal polarizations, respectively.

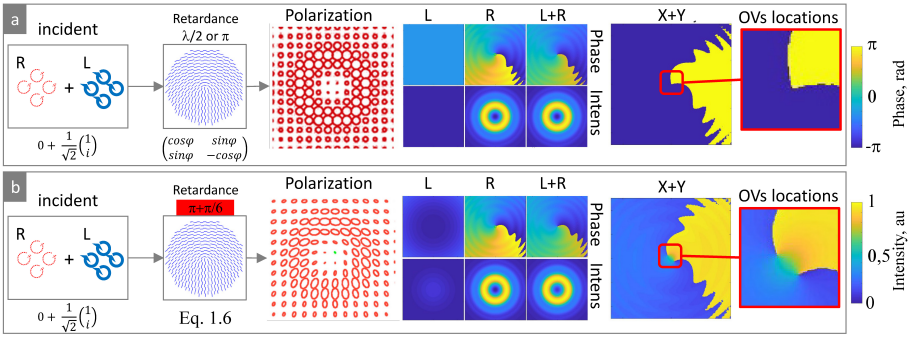

Figure 1.2: Modelling results of polarization, phase, and intensity distribution of the beam converted by the geometric phase retarder with (a) ideal π retardation and (b) perturbed retardation $\pi+\pi/6$. Circular polarization is incident. Arrows show polarization state, so as the Jones matrices by the arrows. Components show by dotted lines do not exist. Retardance of the S-waveplate and orientation of its optical axis are shown in the middle together with its Jones matrix. Columns labelled by L, R, $L+R$, and $X+Y$ show intensity and phase of left-hand, right-hand, combined left- and right-hand circularly polarized components, and combined horizontally and vertically polarized components of the beam, correspondingly. Locations of optical vortices in the combined beam are shown in the rightmost column.

1.3. Homogeneous retardation

1.3.1. Circularly polarized input for optical vortex generation

Unperturbed case

In this case, retardance of the plate is homogeneous and has π value.

Phase and Intensity. Fig. 1.2a in columns with corresponding labelling shows phase and intensity distribution in the left-hand circularly polarized ('L') and right-hand circularly polarized ('R') components of the converted beam. Incident L component has zero intensity after conversion. All the intensity is in the R component which has a vortex phase. Intensity distribution is symmetric.

Polarization. Upon conversion ellipticity of polarization conserves its value but changes its sign. Incident L polarization becomes R with homogeneously distributed ellipticity and orientation of polarization ellipses as shown in column 'Polarization' in Fig. 1.2a.

Location of vortices. Output beam was decomposed to X- and Y-polarized components, which phase is shown in column 'X+Y' in Fig. 1.2a. Vortices from orthogonally polarized components have the same locations within the beam, as seen in the rightmost 'OVs locations' column in Fig. 1.2a.

Perturbed case

The S-waveplate with the perturbed retardation is represented by the Jones matrix M_u:

$$M_u = \begin{bmatrix} \cos(q\varphi) & -\sin(q\varphi) \\ \sin(q\varphi) & \cos(q\varphi) \end{bmatrix} \begin{bmatrix} 1 & 0 \\ 0 & -\exp(iu) \end{bmatrix} \begin{bmatrix} \cos(q\varphi) & \sin(q\varphi) \\ -\sin(q\varphi) & \cos(q\varphi) \end{bmatrix}. \quad (1.6)$$

From Eq. (1.6) we obtain:

$$M_u = \frac{a}{2} M_q + \frac{b}{2} M_I, \quad (1.7)$$

where

$$a = [1 + \exp(iu)]\,,\ b = [1 - \exp(iu)] \quad (1.8)$$

and $M_I = \begin{bmatrix} 1 & 0 \\ 0 & 1 \end{bmatrix}$ is a unity matrix, M_q is the matrix of the unperturbed retarder (Eq. 1.1). u describes the perturbation of retardation. When $u = 0$, $b = 0$ and $M_u = M_q$. When $u \neq 0$, the effect of the plate on X, Y, L, R, and elliptic polarizations is described by:

$$M_u E_X = \frac{a}{2} E_{RP} + \frac{b}{2} E_X,\ M_u E_Y = \frac{a}{2} E_{AP} + \frac{b}{2} E_Y, \quad (1.9)$$

$$M_u E_L = \frac{a}{2} E_R \exp(i\varphi) + \frac{b}{2} E_L,\ M_u E_R = \frac{a}{2} E_L \exp(-i\varphi) + \frac{b}{2} E_R, \quad (1.10)$$

and

$$M_u E_e = \frac{1}{2} \left(acE_R \exp(i\varphi) + adE_L \exp(-i\varphi) + bcE_L + bdE_R \right), \quad (1.11)$$

respectively. As seen from Eqs. 1.9 and 1.10 the output beam now is a superposition of the desired polarization state (as from the unperturbed case) and some coherent background polarized as the incident beam. Fig. 1.2b shows results of modelling to demonstrate this as described below. Here we consider homogeneous retardation of the retarder, which differs from π by $u = \pi/6$ (Eqs. 1.7 and 1.8).

Phase and Intensity. In contrary to the unperturbed case, when retardation of the plate differs from π, the resulting beam has now both L and R components, as shown in the Fig. 1.2b in the columns with corresponding labelling. But only component orthogonal to the incident, which in our case is R, acquires vortex phase, while L component is just coherent background. Therefore, the beam with vortex phase can be spatially separated by filtering the resulting mixed beam by the polarization state. Intensity of the converted beam remains symmetric.

Polarization. Column 'Polarization' in Fig. 1.2b shows that even though

ellipticity of the incident polarization was homogeneous, ellipticity and orientation of polarization ellipses of the converted beam become inhomogeneous, i.e. spatially variable. Nonetheless, this elliptical polarization can be decomposed to L and R components to separate the homogeneously polarized vortex beam, as mentioned previously.

Location of vortices. Inhomogeneity of polarization of the converted beam, or in other words, coherent background in the generated vortex beam shifts vortex from the center of the beam. This is explicitly shown by the decomposing the resulting mixed beam into the X- and Y-polarized components (Fig. 1.2b columns 'X+Y' and 'OVs locations').

1.3.2. Optical vortices over octave-spanning spectral range

Polarization selective filtering

In this section we explicitly demonstrate mentioned above polarization selective filtering of the mixed beam for separation of the vortex phase. We again consider S-waveplate acting as a half-wave plate phase retarder. We rewrite the matrix for the S-waveplate as follows:

$$M_s = \begin{bmatrix} \cos(2\theta) & \sin(2\theta) \\ \sin(2\theta) & -\cos(2\theta) \end{bmatrix}; \tag{1.12}$$

where θ is an azimuthal angle of the optical axis of a half-wave plate. The resulting light field E_{out} can be presented as an action of a half-wave plate converter M_S on the initial field E_{in}: $E_{out} = M_s E_{in}$. If a right-handed circularly polarized light is transmitted through the S-waveplate, a left-handed circularly polarized OV (with the topological charge equal to 1) is generated:

$$E_{out} = \frac{1}{\sqrt{2}} M_s \begin{bmatrix} 1 \\ i \end{bmatrix} E_{in} = \frac{1}{\sqrt{2}} e^{i2\theta} \begin{bmatrix} 1 \\ -i \end{bmatrix} E_{in}, \tag{1.13}$$

where $E_{in} = e^{-r^2/w^2} e^{-i(2\pi/\lambda_0)r^2/(2R')}$ is Gaussian envelope, $R' = z(1+(z'/z)^2)$, $z' = \pi w_0^2/\lambda$, $r^2 = x^2+y^2$, x, y and z are Cartesian coordinates, w is waist of the beam and λ is the wavelength of light. So, left (right) handed circularly polarized light passed S-waveplate acquires vortex phase and orthogonal right(left) handed circular polarization. However, if the wavelength of incident light, λ, differs from the wavelength the S-waveplate was designed for, λ_0, the value of phase retardation would be different for different wavelengths: $\Delta = \pi\lambda_0/\lambda$. It means that only light at the wavelength λ_0 would remain circularly polarized. Arbitrary wavelength λ would acquire elliptical polarization and phase retardation Δ. By multiplying Jones vector for left circular polarization with Jones matrix for the retarder (S-waveplate) with phase retardation Δ and azimuth θ (orientation of

optical axis), we can calculate how circular polarization of the input light will be transformed:

$$\begin{gathered} E_{el} = \\ \frac{1}{\sqrt{2}} \begin{bmatrix} cos^2(\theta) + e^{i\Delta} sin^2(\theta) & (1 - e^{i\Delta}) sin(\theta) cos(\theta) \\ (1 - e^{i\Delta}) sin(\theta) cos(\theta) & sin^2(\theta) + e^{i\Delta} cos^2(\theta) \end{bmatrix} \begin{bmatrix} 1 \\ i \end{bmatrix} E_{in} = \\ \frac{1}{\sqrt{2}} \begin{bmatrix} cos^2(\theta) + e^{i\Delta} sin^2(\theta) + i(1 - e^{i\Delta}) sin(\theta) cos(\theta) \\ (1 - e^{i\Delta}) sin(\theta) cos(\theta) + i(sin^2(\theta) + e^{i\Delta} cos^2(\theta)) \end{bmatrix} E_{in} \end{gathered} \tag{1.14}$$

Eq. 1.14 does not give much information on phase or polarization dependence of the beam on phase retardation Δ or azimuthal angle θ. Now let us assume that the light with such polarization E_{el} (Eq. 1.14) passes the left L or right R circular polarizer (quarter wave plate and linear polarizer). Then, the electric fields (E_R and E_L) will be following:

$$\begin{aligned} E_R = RE_{el} = \tfrac{1}{2\sqrt{2}}(1 - e^{i\Delta}) e^{i2\theta} \begin{bmatrix} 1 \\ -i \end{bmatrix} E_{in}; \\ E_L = LE_{el} = \tfrac{1}{2\sqrt{2}}(1 + e^{i\Delta}) \begin{bmatrix} 1 \\ i \end{bmatrix} E_{in}, \end{aligned} \tag{1.15}$$

where R and L are the Jones matrices for right and left circular polarizers, respectively:

$$R = \frac{1}{2} \begin{bmatrix} 1 & i \\ -i & 1 \end{bmatrix}; L = \frac{1}{2} \begin{bmatrix} 1 & -i \\ i & 1 \end{bmatrix}; \tag{1.16}$$

After the left-handed circularly polarized light of $\lambda \neq \lambda_0$ passes through the S-waveplate and a right-handed circular polarizer, the electric field E_R (Eq. 1.15) becomes similar to what we would expect after passing through the S-waveplate when $\lambda = \lambda_0$ (Eq. 1.13). It contains the same factor $e^{i2\theta}$ which indicates the azimuthal phase variation of the field, i.e. presence of an OV. However, after the left-handed circular polarizer, the electric field E_L (Eq. 1.15) does not have this azimuthally dependent term. Therefore, after the S-waveplate, the circularly polarized light of wavelength $\lambda \neq \lambda_0$ can be separated into two parts according to the handedness of polarization. Only one of the polarizations will exhibit the azimuthally varying phase dependence, i.e. become an OV.

The ratio of the two resultant fields depends only on the phase retardation of the retarder:

$$I_R = E_{Rx} E_{Rx}^* + E_{Ry} E_{Ry}^* = \frac{1}{2}(1 - \cos \pi\lambda_0/\lambda) \tag{1.17}$$

$$I_L = E_{Lx} E_{Lx}^* + E_{Ly} E_{Ly}^* = \frac{1}{2}(1 + \cos \pi\lambda_0/\lambda) \tag{1.18}$$

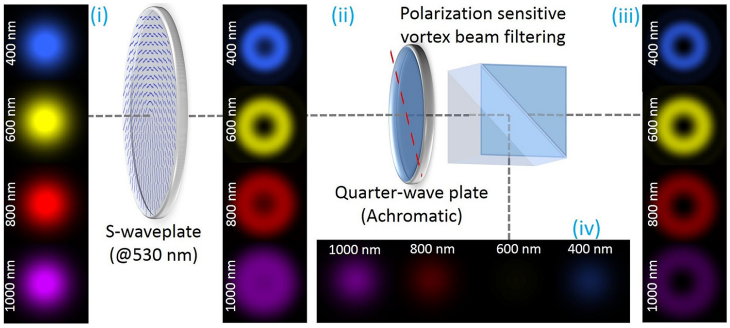

Figure 1.3: The simplified schematic and numerical model for OVs generation and polarization-sensitive beam cleaning. Gaussian beams (i) pass through the S-waveplate, resulting in OVs with different contrast, depending on the wavelength (ii). The quarter-wave plate and linear polarizer work as a polarization-sensitive vortex beam filter that separates the vortex beam (iii) and the background with no phase modulation (iv).

In summary, even if any S-waveplate or, in general, any other optical element based on the phase control of circularly polarized light by half-wave plates (e.g. [76]) is designed for a specific wavelength, a desired transformed part of the beam can be easily separated out using a circular polarizer.

As an illustration, using previous equations 1.15 and a Fourier propagation method, a situation was simulated, where a circularly polarized beam passes through the S-waveplate, quarter-wave plate and a linear polarizer (Fig. 1.3). The modelled S-waveplate is set for $\lambda_0 = 530$ nm wavelength, whereas the spectrum of the incident light ranges from 400 nm to 1000 nm. The results indicate that the contrast of the vortex beam generated with the S-waveplate strongly depends on the wavelength (Fig. 1.3(ii)). However, after passing the circular polarizer, at all wavelengths a high contrast OV is obtained (Fig. 1.3(iii)), with zero intensity at the center. Due to the wavelength mismatch all the "background", i.e. not phase modulated part of the beam is separated to the orthogonally polarized field (Fig. 1.3(iv)).

We used an S-waveplate designed for 530 nm (fabricated by Altechna R&D, developed at the University of Southampton [65, 66]). The S-waveplate was illuminated with femtosecond light pulses tuned in the range of $400 - 1040$ nm from an optical parametric amplifier "Topas" (Light Conversion Ltd.). The experimental setup was similar to the one illustrated in the Fig. 1.3. However, to achieve a perfect achromatic behaviour in a wide spectral range, achromatic quarter-wave plates (for circular polarization generation and for circular analyser) were replaced with two Fresnel rhombs and a calcite crystal was used to separate two orthogonal polarizations. The beam profiles were measured using a CCD camera (Chameleon CMLN-13S2M-CS).

The contrast (intensity in the center of the beam divided by the maximum

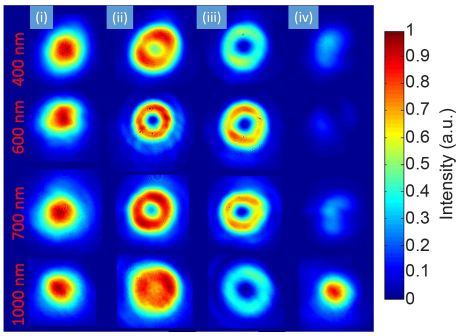

Figure 1.4: Experimental intensity distributions of: (i) Initial Gaussian beam before S-waveplate; (ii) – beam after S-waveplate; (iii) filtered vortex part of the beam (after a quarter-wave plate and a linear polarizer); (iv) Gaussian (background) part of the beam (after quarter-wave plate and linear polarizer).

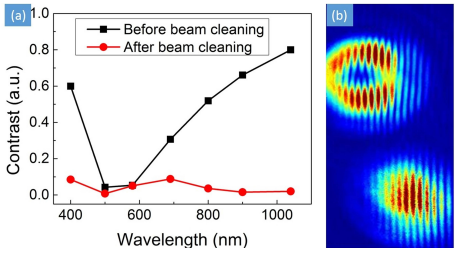

Figure 1.5: (a) The contrast of generated vortex beams at different wavelength before and after the polarization sensitive beam cleaning. (b) Interference of vortex- and Gaussian part (background) of the beam (at 1000 nm).

intensity of the beam: I_{min}/I_{max}) of the OVs generated by the S-waveplate strongly depended on the wavelength (Fig. 1.4(ii)). At wavelengths close to the design wavelength of 530 nm, the generated beams exhibited a well-defined doughnut shape, while at nearly twice longer wavelength (∼1000 nm) the generated beam had a flat top profile with no sign of singularity at the center. However, after the polarization-sensitive beam cleaning part of the setup (second Fresnel rhomb and calcite crystal), vortex and Gaussian parts of the beams were separated into two beams (Fig. 1.4(iii,iv)).

The further analysis of beams presented in Fig. 1.4(ii,iii) and (iii,iv) is shown in Fig. 1.5 and 1.6, respectively. The performance of the polarization-sensitive beam cleaning was evaluated by comparing the contrast of the generated OVs before and after beam cleaning (Fig. 1.5(a)). Before beam cleaning, the contrast exhibit a strong dependence on wavelength, whilst after the cleaning, contrast of OV is similar at all wavelengths. Small variations in the contrast after cleaning is caused by the variations in the quality of the input Gaussian beam (Fig. 1.4(i)) rather than the chromaticity of the setup.

In order to confirm the presence of phase helicity in the vortex part of the

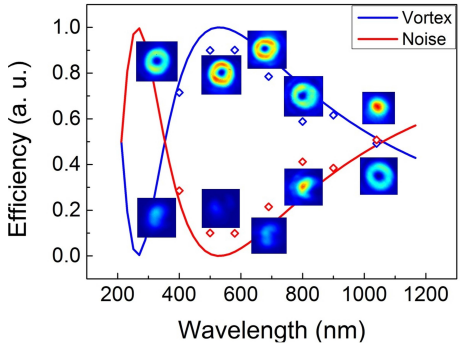

Figure 1.6: Polarization sensitive beam cleaning efficiency dependence on the wavelength. Experimental points are compared with the theoretical curve. Insets demonstrate measured beam profiles of generated OVs and beams profiles of filtered out background at different wavelengths.

beam and its absence in the orthogonally polarized part, both parts of the beams were injected into a Michelson interferometer and interference patterns were measured (Fig. 1.5(b)). As predicted, the interference pattern of the vortex beam exhibited a forked structure (which is a clear indication of the phase helicity) whereas the orthogonally polarized Gaussian (background) part of the beam produced regular fringes.

The reason for one polarization component to acquire vortex structure and for other not to is following. The beam is being transformed to OV by acquiring phase retardation $\lambda_0/2$ and changing its polarization state to orthogonally polarized. When the incident wavelength $\lambda \neq \lambda_0$, the phase delay and polarization state depend on λ; the beam become elliptically polarized. Dividing the beam into two orthogonally polarized parts and selecting the polarization orthogonal to initial, we automatically select the light which acquired $\lambda_0/2$ phase delay. Therefore, one polarization component carry an OV and other does not.

Fig. 1.4(iii,iv) shows that unlike the contrast, the power ratio between the cleaned vortex part of the beam and not phase modulated background (Gaussian "noise") part strongly depends on wavelength. The efficiency of the vortex/Gaussian conversion at different wavelengths (Fig. 1.6) can be evaluated using Eq. 1.18. Maximum efficiency is achieved at the design wavelength of the S-waveplate; the efficiency remains above 50% at the wavelength nearly two times larger than the design wavelength, demonstrating successful OV generation in the 600 nm wavelength range (in this range, the efficiency is more than 50%). Obviously the bandwidth scales with the central wavelength: an S-waveplate designed for the 1 μm wavelength would cover the bandwidth of 1.2 μm.

Besides OVs generation in a broad wavelength range, the presented scheme can also work as a polarization selective vortex converter. The handedness of

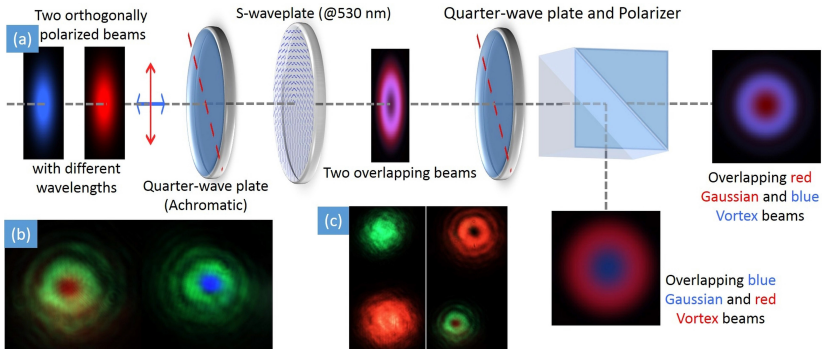

Figure 1.7: Polarization selective vortex beam generation: (a) experimental set-up and modeled results; (b) experimentally measured profiles of green (532 nm) vortex beam after polarization transformation superimposed with orthogonally polarized red (633 nm) and blue (400 nm) Gaussian beams in the middle; (c) experimental beam profiles (532 nm and 633 nm) before (on the left) and after (on the right) polarization sensitive transformation.

circular polarization determines whether the Gaussian beam passing through the setup stays Gaussian or is converted to an OV. Therefore, for example, if we have two beams with different wavelengths and orthogonal circular polarizations, only one of them will be converted to a vortex beam and the other would remain unaffected (Fig. 1.7(a)). This could be useful for stimulated emission depletion (STED) applications as both beams could travel in the same optical path and just before the objective, one of them would be converted to a vortex beam. The advantage of such geometry has already been demonstrated in [47,77], where an OV was generated using a highly chromatic optical component, which imposed a limit on how close the two wavelengths could be. Since our method is based on polarization selection, there is no such wavelength limitation for the two beams; only the "correctly" polarized beam will be converted to a vortex. In order to demonstrate how this works in practice, we performed an experiment using the setup illustrated in Fig. 1.7(a). We used three lasers with different wavelengths: red – HeNe laser (633 nm), green – second harmonics of Nd:YAG laser (532 nm), blue – OPA output at 400 nm wavelength. Orthogonally polarized beams of two of the lasers (red and green or blue and green) were launched collinearly through the polarization sensitive OV generator. As shown in Fig. 1.7(b), in each case, only one beam (green in the presented case) was transformed into a vortex whereas the other remained Gaussian. With currently available laser sources intensity efficiency of the methods does not impose limitation for the application. The proposed scheme with single optical path for both excitation and depletion beams could significantly facilitate extremely complicated process of alignment of STED systems.

Optical vortex generated from an incoherent white light source

Further, we expand our previous considerations to generate "white" light OV. Hereafter, white light means a broadband incoherent light emitted by an incandescent halogen lamp. Temporally incoherent incident light field $A(t)$ is given by the Gaussian-Gaussian noise model [78]:

$$A(t) = \frac{1}{\sqrt{N}} \sum_{j=1}^{N} e^{(it\Omega_j + i\xi_j)}, \tag{1.19}$$

where $\Omega_j = \omega_j - \omega_0$, ω_0 and ω_j are the central and normally distributed random frequencies, respectfully; dispersion σ^2 ($\sigma = (\omega_1 - \omega_2)/2\sqrt{2}$, $\omega_{1,2} = 2\pi c/\lambda_{1,2}$, c – speed of light). ξ_j are uniformly distributed random phases. N has to be significantly large in the simulation (here $N = 471$). The wavelengths $\lambda_1 = 360$ nm and $\lambda_2 = 830$ nm, $\lambda_0 = 530$ nm. Intensity distributions after each component in the experimental setup are obtained by the multiplication of the Fourier transformed complex amplitude $A(t)$ by the Jones matrix of the corresponding optical element. For example, the vortex E_V and not phase modulated E_G parts of the beam after the polarization filtering are given by:

$$E_{V(G)} = E_{right(left)} S(\omega), \tag{1.20}$$

where $S(\omega)$ is the Fourier transform of the $A(t)$, $E_{right(left)}$ is given by Eq. 1.15. Such field has Gaussian shaped spectrum and obeys Gaussian statistics [78]. Modeled intensity distributions are shown in the top row of the Fig. 1.8.

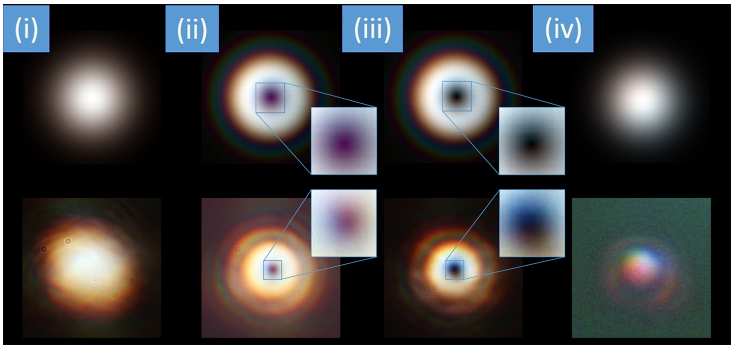

Figure 1.8: Intensity normalized numerical plots (top row) and experimental images (bottom row) of the beam from incoherent light source in the states (i), (ii), (iii), and (iv) as described in the Figs. 1.3 and 1.4.

For the white-light experiment the light source in the experimental setup described in the previous section was substituted by a 55 W tungsten halogen bulb and used as the source of an incoherent broadband white light. The light from the halogen bulb was collected (without focusing system) by a multimode

gradient optical fiber (86 cm long, cladding diameter 850 μm, core diameter 130 μm) placed close to the lamp. Only the light propagating through the core of the fiber was then selected by the first aperture (diameter 0.95 mm) placed 21 mm after the tip of the fiber. The spatial coherence of the light was controlled by the size of this aperture. It should be small enough to provide sufficient degree of spatial coherence for the generated optical vortex to be visible, i.e. to posses deep axial minimum of intensity ([60, 79] and references within). "White"-light beam with a high degree of spatial coherence was then collimated with the aid of a pair of lenses in the telescope configuration and spatially filtered by the second aperture (diameter 110 μm) placed in the common focus between these lenses. The role of the second aperture was to endow the beam with nearly Gaussian intensity profile and to control its waist size. The polarization tailoring of the beam were achieved by Fresnel rhombs and a Glan polarizer. An angle cut calcite crystal was used to separate two polarization states. Colored images of the beam were obtained by Canon 600d camera with the default settings for the white balance, saturation, contrast and color tone.

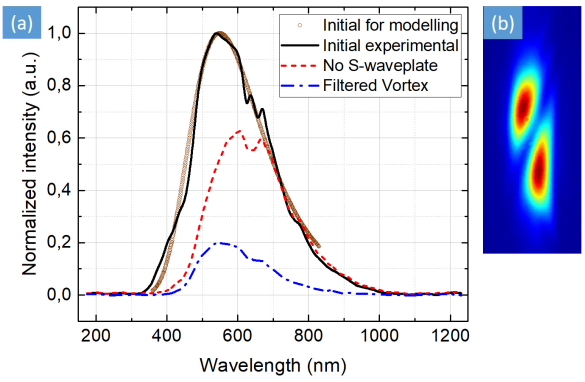

Figure 1.9: (a) Spectra of the "white" light beam in different states. *Experimental*: Black (solid): initial unpolarized white light; Red (dashed): spectrum of the polarized collimated beam after passing all the polarization optics but the S-waveplate; Blue (dashed-doted): vortex part of the beam after the polarization filtering (i.e. beam passed all the polarization optics and the S-waveplate). *Modelled*: Brown (hollow circles): initial spectrum used for modelling; cut at the limits of visible light. (b) Generated "white" light OV focused by a cylindrical lens. See text for details.

Bandwidth of the incident white light spans from 325 nm to 1030 nm and is shown in the Fig. 1.9a (solid black curve marked as "Initial experimental"). However, for modeled intensity distributions spectrum in the limits of human eye perception was used: from 360-830 nm (hollow brown circles in the Fig. 1.9(a)). The "white" light beam acquired its vortex structure upon propagation through the S-waveplate designed for conversion of light in the 20 nm bandwidth (as

stated by the manufacturer) around its central wavelength of 532 nm. Due to the far exceeding bandwidth of the incident "white" light, the visibility of the vortex core (zero intensity at the axis) is "masked" in the beam right after the S-waveplate (Fig. 1.8). As described in the previous sections, the maximum conversion efficiency is around design wavelength of the S-waveplate. Hence, the central part of the beam right after the S-waveplate is filled by the pink-violet shades, which are result of the substruction of green shades from the white color. After the polarization selective filtering vertically polarized part of the beam with "clean" vortex structure (zero axial intensity) is spatially separated from the horizontally polarized background part of the beam having no phase singularity. Intensity normalized experimental images are shown in the Fig. 1.8 bottom row and demonstrate good agreement with the model. Outer red shades and inner blue shades of the circle of light of OV could be explained by the scattering of white light on objects smaller then the wavelength of light, which are the nano "cracks" the grating of the S-waveplate is made of.

The spectrum of the filtered optical vortex is shown in the Fig. 1.9(a) marked as "Filtered vortex" (dashed-dotted blue curve). Red dashed curve in the Fig. 1.9(a) marked as "No S-waveplate" shows spectrum of the beam after it passed through all the polarizing optics in the setup (under condition that the S-waveplate is removed from the setup). Because some of the polarizing elements were made from calcite, the spectrum of the beam was cut at the blue side, so it differs from initial and spans from 400 to 1000 nm. The spectrum of the filtered vortex has its maximum at 545 nm and spans from 410 to 900 nm. Conversion efficiency at different wavelengths differs as described in the previous sections.

Different frequency components acquire different phase delay, resulting in a topological charge dispersion [80]. Based on this effect vortex with half integer topological charge $|l| = 1/2$ can be generated when the S-waveplate is illuminated by twice the wavelength it is designed for [67]. Above described polarization filtering compensate topological charge dispersion resulting in equal TC for all spectral components [70]. To demonstrate unit topological charge of the generated "white" light OV $|l| = 1$ the beam after the polarization filtering was focused by a cylindrical lens (focal distance $f = 125$ mm) as described in [81]. At the focal area the light possessed one dark stripe across the intensity distribution (Fig. 1.9(b)) indicating that the value of topological charge is $|l| = 1$. OV generation occurs through the phase and polarization modulation. Thus, optical vortices at different frequency components demonstrate coaxiality, hence, avoid anomalous spectral behavior near the vortex core [82].

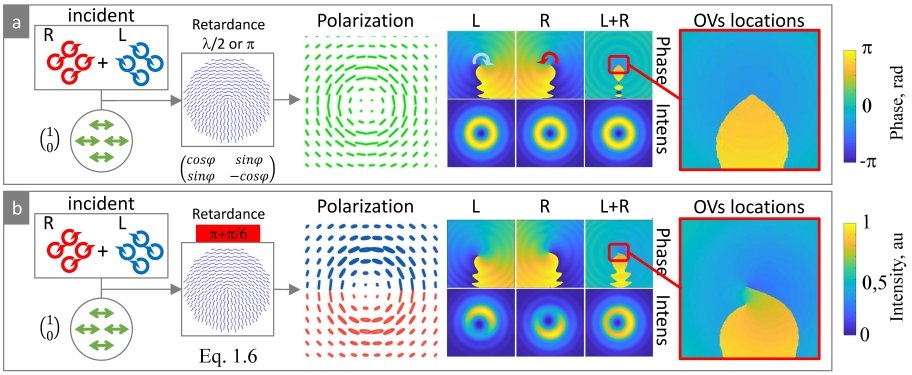

Figure 1.10: Modelling results of polarization, phase, and intensity distribution of the beam converted by the geometric retarder with (a) ideal π retardation and (b) perturbed retardation $\pi + \pi/6$. Linear polarization is incident. Arrows show polarization state, so as the Jones matrices by the arrows. Linear incidence is considered as superposition of two circular. Retardance of the S-waveplate and orientation of its optical axis are shown in the middle together with its Jones matrix; φ is the azimuthal angle in polar coordinate system. Columns labelled by L, R, $L + R$, and $X + Y$ show intensity and phase of left-hand, right-hand, combined left- and right-hand circularly polarized components, and combined horizontally and vertically polarized components of the beam, correspondingly. Locations of optical vortices in the combined beam are shown in the rightmost column.

1.3.3. Linearly polarized input for generation of radial polarization

Unperturbed case

In this case, retardance of the plate is homogeneous and has π value.

Phase and Intensity. Analysis of the beam we perform in the circularly polarized basis. Incident linear polarization is considered as superposition of L and R components, as schematically shown in the 'incident' column of Fig. 1.10a. Upon conversion both incident, L and R, components flip handedness and acquire vortex phase as shown in the columns 'L' and 'R'. Vortices in these components have orthogonal direction of vorticity (and both located at the same spot in the middle of the beam). Therefore, the generated azimuthally polarized beam is vortex-free, it has plane phase (column 'L+R'). L and R components have equal amplitudes and symmetric intensity distributions.

Polarization. Resultant polarization has homogeneously distributed zero ellipticity (i.e. it is linear at every point), and is is azimuthally oriented, as shown in column 'Polarization' in Fig. 1.10a.

Location of vortices. Since the resultant beam is superposition of two vortex components then there is no need to decompose it to the X- and Y-

polarized components. As shown in the rightmost 'OVs locations' column in Fig. 1.10a vortices from orthogonally polarized L and R components have the same locations within the beam. Then the vortex phase can be precisely cancelled such that the resultant phase of azimuthally polarized beam is vortex free.

Perturbed case

Here we consider homogeneous retardation of the retarder, which differs from π by $u = \pi/6$ (Eqs. 1.7 and 1.8). Fig. 1.10b shows results of modelling to demonstrate effect of such perturbation of the retardation.

Phase and Intensity. Upon conversion both incident, L and R, components flip handedness and acquire vortex phase as shown in the columns 'L' and 'R'. Vortices in these components have orthogonal direction of vorticity. L and R components have asymmetric intensity distributions, and so the combined resultant beam (Fig. 1.10b columns 'L', 'R', and 'L+R', correspondingly). Total phase of the generated azimuthally polarized beam is *not* vortex-free in this case.

Polarization. Column 'Polarization' in Fig. 1.10b shows that even though ellipticity of the incident polarization was homogeneous, ellipticity of polarization ellipses of the converted beam becomes inhomogeneous, i.e. spatially variable. It changes from the left-hand at the upper part of the beam to the right-hand elliptically polarized at the lower part. Orientation of ellipses remains azimuthal because it depends on the orientation of the optical axis of the geometric retarder and not on the retardance.

Location of vortices. Inhomogeneity of intensity and polarization of the converted beam in turn causes for optical vortices from orthogonally polarized components to have different locations within the beam, as explicitly shown in the rightmost 'OVs locations' column in Fig. 1.10b. This difference of locations of vortices does not allow for full cancellation of the vortex phase in the resultant beam.

Since for the generation of radially or azimuthally polarized beams both L and R components are required, then the described in the section 1.3.2 polarization selective filtering is not possible. However, there is another way to recover necessary polarization state of the beam as described in the following section 1.4.

1.4. Inhomogeneous retardation

1.4.1. Experimental observations

On practice it is hard to manufacture an element with spatially homogeneous retardation. For example, experimentally measured retardation of the nano-

structured geometric phase retarder (S-waveplate "RPC-532-04-216") manufactured for the central wavelength of $\lambda = 532$ nm is shown in Fig. 1.11 in the column with corresponding labelling. Its retardation oscillates around π value from $\pi - \pi/12$ to $\pi + \pi/5$ and has a sinusoidal-like profile. As a result, beam acquires spatially variable ellipticity. Which results in appearance of vortex phase in the beam, as seen from interference pattern shown the corresponding column in Fig. 1.11. Interference patterns demonstrate appearance of the vortex phase in the Y polarized component of the beam, which supposed to be vortex free. Position of the vortex is shifted far from the center of the beam. Therefore, the following question we aim to answer is: What effect the inhomogeneous retardation which "sinus-ides" around π value has on the beam conversion?

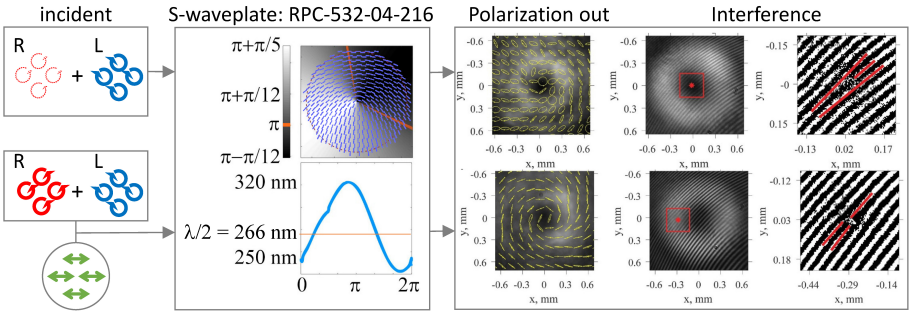

Figure 1.11: Experimentally retrieved polarization and locations of vortices in the beam converted on the S-waveplate (RPC-532-04-216) in the case of circularly and linearly polarized incidence. Vortex location is marked by red star. Rightmost column shows magnified area shown by the red square in the subimages with interference. Polarization of the reference beam for interference is vertical.

1.4.2. Effect of inhomogeneous (sinusoidal) retardation

Experimentally retrieved sinusoidal profile of retardation of the S-waveplate has led to consideration of sinusoidal profiles of retardation of the geometric phase retarder. Therefore, below we describe effect of retardation having $u = \sin(j\varphi)$ profiles (Eq. 1.8) as shown in 'Retardance' column in Fig. 1.13, where j is specified in the corresponding subimage, and φ is the azimuthal angle changing from 0 to 2π, on the phase, polarization, and intensity distribution of the beam converted on such a plate.

In this case, we make use of Jacobi-Anger expansion: $\exp(i\alpha \sin(j\varphi)) = \sum_{n=-\infty}^{\infty} J_n(\alpha) \exp(inj\varphi)$, where J_n is the Bessel function. Moreover, $J_{-n}(\alpha) = (-1)^n J_n(\alpha)$. We insert the expansion into coefficients a

and b of Eqs. (1.7) and (1.8):

$$a = 1 + \exp(iu) = 1 + J_0(\alpha) + J_1(\alpha)2i\sin(j\varphi) + J_2(\alpha)2\cos(2j\varphi) + \dots \quad (1.21)$$

and

$$b = 1 - \exp(iu) = 1 - J_0(\alpha) - J_1(\alpha)2i\sin(j\varphi) - J_2(\alpha)2\cos(2j\varphi) + \dots \quad (1.22)$$

When $\alpha < 1$, $J_0(\alpha) \approx 1$ and we note the difference in Eqs. (1.21) and (1.22): in Eq. (1.21) the main contribution is made of $(1 + J_0(\alpha))$ and the field is modulated by the following $\sin(j\varphi)$ and higher terms. In Eq. (1.22), the term $(1 - J_0(\alpha))$ vanishes, and the modulations are more prominent. Another important aspect is that during the free-space propagation the higher order oscillations diffract out faster than lower order oscillations (Fig. 1.12). This allows us to leave only J_0 and J_1 terms in expansions (1.21) and (1.22) and neglect oscillations of higher order. Fig. 1.12 demonstrates normalized intensity of the vortex and high-order background components (the latter are labelled by the corresponding j number). Size of the vortex component is 100 μm, size of the background component is 2.5 times bigger for $j = 8$. Therefore, upon beam propagation high-order component diffracts faster and leave the central part of the beam. This has important consequence for the generation of the beam with azimuthal/radial polarization, as discussed below.

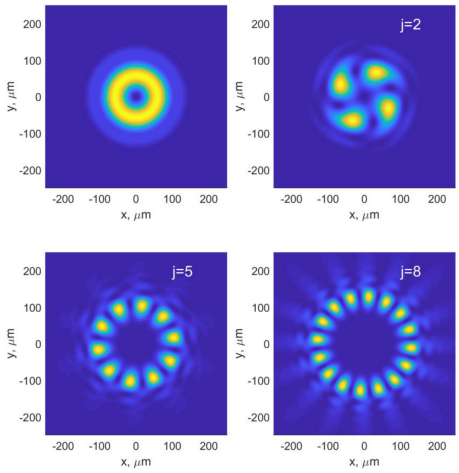

Figure 1.12: Size of the vortex component (top left) is 100 μm. Sizes of the background components for $j = 2, 5, 8$ (as specified in the labels) are 150, 200, 250 μm, correspondingly. Propagation distance $z = 1$ cm, size of the initial Gaussian beam is 100 μm, $\lambda = 532$ nm.

Fig. 1.13 shows results of modelling of the beam conversion on the geometric phase retarder with sinusoidally variable profile of retardance for circularly

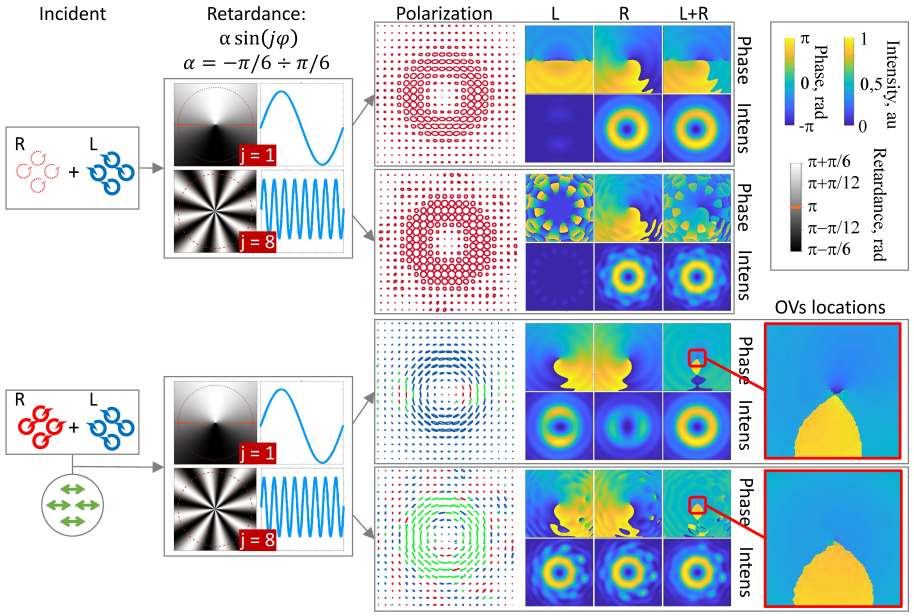

Figure 1.13: Modelling results of polarization, phase, and intensity distribution of the beam converted by the geometric phase retarder with sinusoidal profile of retardation, $u = \sin(j\varphi)$, for the case of circular input (upper part) and linear input (lower part). Retardance distribution and its profile are shown in the middle. Columns labelled by L, R, and $L + R$ show intensity and phase of left-hand, right-hand, combined left- and right-hand circularly polarized components, correspondingly. Locations of optical vortices in the combined beam are shown in the 'OVs locations' column.

(upper part) and linearly (lower part of the figure) polarized incidence. The retardance profile oscillates 1 or 8 times around π value with amplitude of $\pi/6$ as shown in the middle column 'Retardance'. Right part of the figure shows polarization, intensity and phase, and vortex locations in columns with corresponding labelling.

Circular incidence.

For the circular (L) incidence, the resulting beam has both L and R components with vortex phase not only in the vortex (R) component, but also in the background (L) component of the beam, as shown in the upper part of Fig. 1.13 in the columns with corresponding labelling. Described above in the Sec. 1.3.2 polarization selective filtering can be applied to separate vortex phase.

For $j = 1$, size of both polarization components is similar. Therefore, the main (brightest) ring of light is asymmetric. However, because intensity of the background component is comparatively low, this asymmetry is rather weak. The generated beam has spatially variable ellipticity and orientation of polarization ellipses (upper part of Fig. 1.13 'Polarization').

For $j = 8$, higher-order background component (L) diffracts faster as mentioned above. It is much bigger than the vortex component (R). Therefore, only periphery of the generated beam is affected, while the main (brightest) ring of light remains intact. The same is true for the polarization of the generated beam, which is homogeneous on the brightest ring of light.

Linear incidence.

For the linear incidence (which is considered as a superposition of two circularly polarized components), upon conversion, both L and R components acquire vortex phase as shown in the corresponding columns in lower part of Fig. 1.13.

For $j = 1$, size of both polarization components is similar and they have comparable intensity levels. Therefore, both components are strongly asymmetric. Polarization ellipses of the generated beam have spatially variable ellipticity (upper part of Fig. 1.13 'Polarization'). Polarization is right-hand elliptical at the upper and lower parts of the beam where the deviations of the retardation from π is maximal and it is linear at places of proper π retardation. Vortices from the orthogonally polarized components have different locations within the beam, as explicitly shown in the rightmost 'OVs locations' column in Fig. 1.13. This difference of locations of vortices does not allow for full cancellation of the vortex phase in the resultant beam.

For $j = 8$, similarly to the case of circular incidence, the sizes of vortex and background components are different. Thereby additional vortices appearing in the beam affect mostly periphery of the beam leading to smoothing of the most intense central part of the beam. Therefore, only periphery of the beam is affected while the main (brightest) ring of light remains almost intact. Then vortices of L and R components are located much closer to each other (Fig. 1.13 'OVs locations'), which leads to recovery of the linear polarization on the brightest ring of intensity of the beam (Fig. 1.13 'Polarization').

Therefore, even though the geometric phase retarder has strongly perturbed retardation, for $j > 5$, locations of vortices almost coincide, then the polarization of the generated beam acquires homogeneous ellipticity (e.g. linear), close to that in the case of ideal homogeneous retardation.

1.5. Spin-to-Orbital conversion of the angular momentum of the beam

Spin-to-Orbital conversion of the angular momentum of the beam is particularly important for applications, such as optical orientation of microparticles. Therefore, in this section we outline this process upon conversion on the geometric phase retarder for the above described cases of homogeneous and inhomogeneous retardation profiles. Mutual transformation of the spin and orbital parts of the

angular momentum of the beam is schematically shown in Fig. 1.14. Below we describe state of the converted beam for three cases of polarization of the incident beam: (i) linear; (ii) elliptical; (iii) circular. Incident ellipticity, χ_{in}, of polarization is changed by orientation of a quarter waveplate, Θ, which is shown as abscissa in Fig. 1.14.

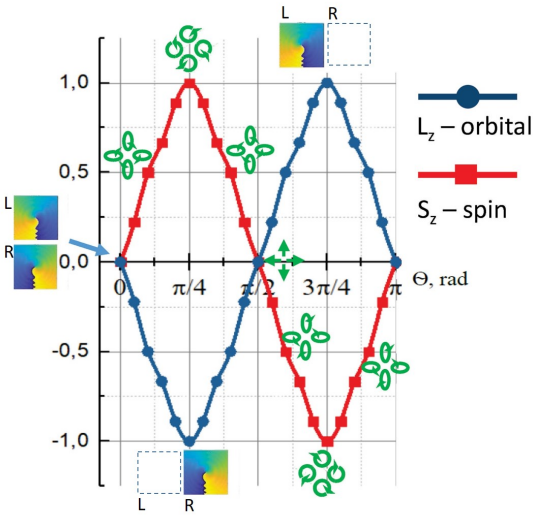

Figure 1.14: Spin-to-Orbital conversion of the angular momentum. Green arrows show polarization state. Insets show phase of the left- and right-hand circularly polarized components. Abscissa axis shows orientation of quarter wave plate, hence incident ellipticity. Ordinate axis shows normalized projection of spin S_z red (orbital L_z blue) angular momentum of the beam on the propagation axis z.

(i) $(\Theta_{in},\ \chi_{in}) = 0$: Consider linear polarization state (zero ellipticity) of the incident Gaussian beam falling onto the S-waveplate. At this point incident linear polarization state of the beam can be represented as a superposition of two beams of equal intensities both having circular polarization states but opposite handednesses. After conversion on the S-waveplate, both beams conserve their ellipticity but do change sign of its handedness. Superposition of these two beams of *equal* intensities both having circular polarization states but opposite handednesses results in a polarization state with zero ellipticity (linear polarization). As response to the flip of initial handedness of circular polarization states both beams acquire vortex phase. Handedness of vortex phase of the beam is opposite to that of the polarization state of the beam. Superposition of two beams of equal intensities both having vortex phase but opposite handedness l=1 and l=–1 results in a plane, vortex-free wave front of the converted beam. Thus, depending on the relative phases of two beams in a superposition resulting beam appears to be radially or azimuthally polarized

(zero ellipticity) with vortex free, plane phase front. Both orbital and spin angular momentum parts have zero value, Eqs.(1.4), (1.5).

(ii) $0^\circ < (\Theta_{in},\ \chi_{in}) < 45^\circ$: Incident Gaussian beam falling onto the S-waveplate is elliptically polarized. Its ellipticity, χ_{in}, is between 0 and 45°. Elliptically polarized beam can be represented as a superposition of two beams of *unequal* intensities ($c \neq d$) both having circular polarization states but opposite handednesses:

$$E_e = cE_L + dE_R, \tag{1.23}$$

where c and d are weights (intensities) of two polarized components. After conversion on the S-waveplate, both beams conserve their ellipticity but do change sign of its handedness. Superposition of these two beams of *unequal* intensities both having circular polarization states but opposite handednesses results in an elliptically polarized beam with incident value of ellipticity but opposite sign. As response to the flip of initial handedness of circular polarization states both beams acquire vortex phase. Handedness of vortex phase of the beam is opposite to that of polarization state of the beam. However, superposition of two beams of *unequal* intensities both having vortex phase but opposite handedness $l = 1$ and $l = -1$ in this case does not results in a plane, vortex-free wave front of the resulting beam, e.g.

$$M_q E_e = cE_R \exp(i\varphi) + dE_L \exp(-i\varphi), \tag{1.24}$$

Because of unequal intensities of two beams, vortex phase does not cancel exactly in the resulting beam. Some number of photons having vortex phase remain uncompensated and contribute to the orbital angular momentum of the beam. Thus, depending on the relative phases of two beams in a superposition resulting beam appears to be elliptically polarized with polarization vector oriented radially or azimuthally, and with complex phase front. Spin angular momentum of the beam is proportional to the ellipticity of the beam, orbital angular momentum has the same value but opposite sign of the spin part.

(iii) $(\Theta_{in}, \chi_{in}) = 45^\circ$: Incident Gaussian beam falling onto the S-waveplate is single circularly polarized beam. After conversion on the S-waveplate, the beam conserves its ellipticity value but does change sign of its handedness. As response to the flip of initial handedness of circular polarization states the beam acquires vortex phase. Handedness of vortex phase of the beam is opposite to that of polarization state of the beam. Spin and orbital parts of angular momentum of the beam have equal, maximal values but opposite signs. The Jones vectors transform as described in Eq. 1.3.

Therefore, change of ellipticity of the incident beam change relative intensities of two circularly polarized beams in superposition, which in turn result in total, partial, or no cancellation of vortex phase of the resulting beam, hence gradual control of orbital and spin angular momenta of the beam. Below, we investigate

the motion of vortices within the beam; how they appear in the circularly polarized vortex beam, move within singular elliptically polarized beam, and how disappear from the vortex-free azimuthally/radially polarized beam.

1.5.1. Ideal and homogeneously perturbed retardation

In the case of homogeneously distributed retardation locations of vortices in the orthogonally polarized components were shown in Figs. 1.2 and 1.10 'OVs locations' for the cases of incident $|S_z| = 1$ (circularly polarized input, $(\Theta_{in}, \chi_{in}) = 45°$) and $S_z = 0$ (linearly polarized input, $(\Theta_{in},\ \chi_{in}) = 0$), correspondingly. Figure 1.15 shows locations of the optical vortex within the beam for all possible incident values of S_z from +1 to –1. On the experiment this corresponds to rotation of the quarter wave plate by 180 deg. In the Fig. 1.15 orientation of the quarter wave plate is shown by Θ_{in} values changing from 0 to 180 deg. Correspondence between Θ_{in} and S_z can be done with the help of Fig. 1.14. Figure 1.15 is divided into 4 panels, labelled X, Y, L, and R, for each orthogonally polarized component of the converted beam. Each panel is divided further to 3 areas labelled "X-Y", "X-θ_{in}, χ_{in}", and "Y-θ_{in}, χ_{in}". "X-Y" panel shows intensity distribution of the beam in the background and locations of vortices in front, central part of the beam is additionally zoomed in and shown as a separate subimage in the red frame. Panel "X(Y)-θ_{in}, χ_{in}" shows projection of vortex locations on the $x(y)$ transverse axis, correspondingly, versus incident ellipticity of the polarization, χ_{in} and orientation of the quarter wave plate, θ_{in}.

Unperturbed (ideal) case

In the case of unperturbed half wave plate retardation of the geometric phase retarder, π (shown in blue in Fig. 1.15), optical vortex stays at the center of the beam at any incident ellipticity except one point, $\theta_{in} = 45°(135°)$ for L (R) circularly polarized component and 90°, 180° for X and Y linearly polarized components, where intensity of these components disappear completely, hence the vortex disappears too.

Homogeneously perturbed case

Homogeneous perturbation of retardation of the geometric phase retarder results in a drift of the vortex position from the center of the beam, as shown by green, red and pink shades in Fig. 1.15. Deviation of vortex location from the center increases with increase of perturbation, which is shown by different colors for 6 different values of retardation: $\pi \pm \pi/36$, $\pi \pm \pi/12$, and $\pi \pm \pi/6$. Trajectories of vortices in the R component of the beam are mirrored to that in L component (Fig. 1.15 panels L and R). In both L and R components OV crosses center of the beam once. This corresponds to the case of $\theta_{in} = 45°(135°)$ with generated

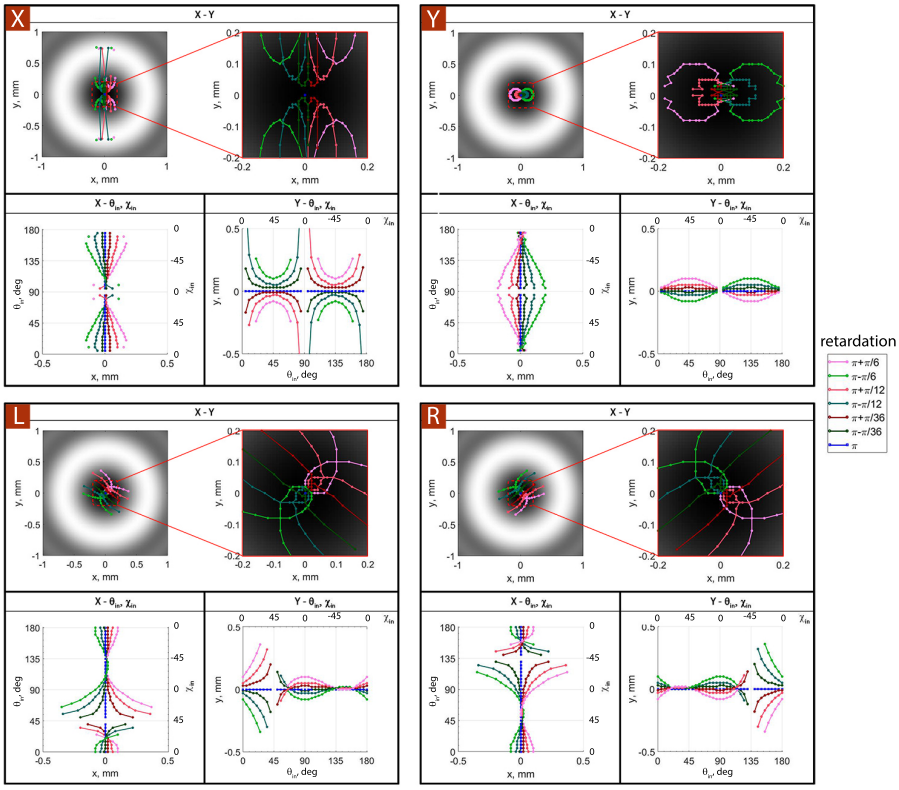

Figure 1.15: Locations of OVs in the X-, Y-, L-, and R- polarized components of the beam versus ellipticity, χ_{in}, of incident polarization (orientation of the quarter wave plate, θ_{in}). Retardation of the S-waveplate is indicated on the right. See text for further details.

left (right) circularly polarized OV beam with symmetrical intensity distribution. Unlike vortices in the L and R components, trajectories of vortices in the X- and Y- polarized components do not mirror each other and do not cross center of the beam at any incident θ_{in}. Larger perturbation of retardation shifts locations of vortices further away from center of the beam and causes more complex phase distribution, stronger asymmetry of intensity distribution, and more complex polarization in the center of the beam.

Therefore, perturbation of retardation affects spin-to-orbital coupling in the generated beam and deteriorates gradual control of orbital and spin angular momenta of the beam.

1.5.2. Inhomogeneously (sinusoidally) perturbed retardation profile

Experimental results for the S-waveplate

Experimentally measured retardation of the S-waveplate "RPC-532-04-216" was shown in Fig. 1.11 in the column with corresponding labelling. Its retardation oscillates around π value from $\pi - \pi/12$ to $\pi + \pi/5$ and has a sinusoidal-like profile of retardation. Experimentally retrieved locations of vortices in the X- and Y- polarized components after the beam conversion on the S-waveplate is shown in Fig. 1.16 by empty circles color coded in the hsv colormap.

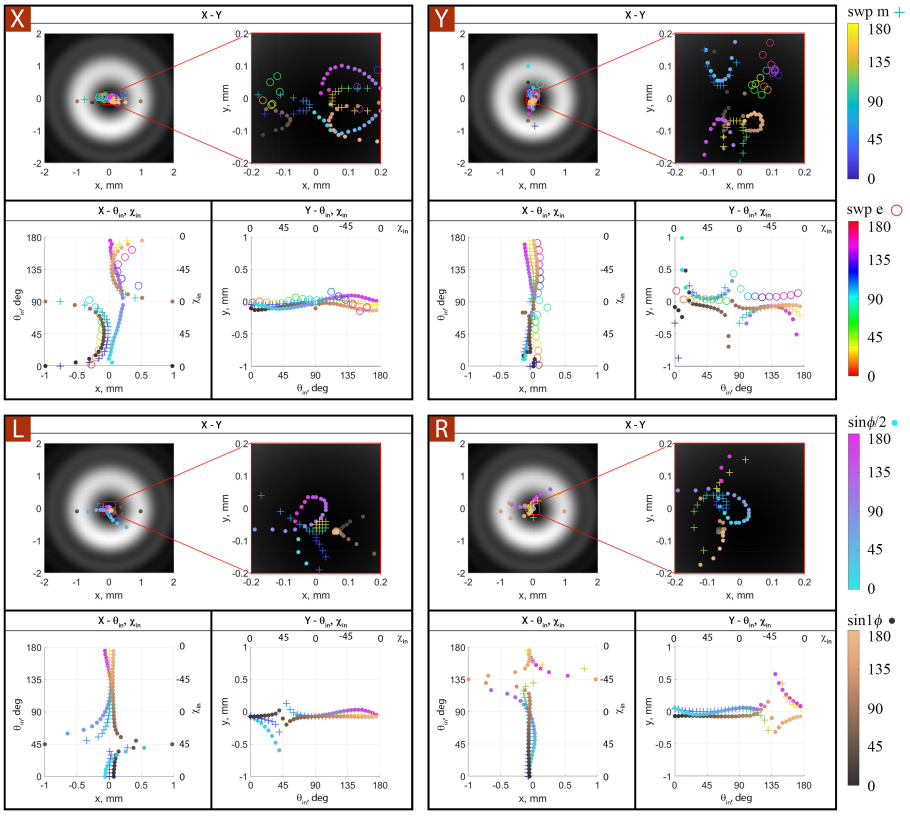

Figure 1.16: Locations of OVs in the X-, Y-, L-, and R- polarized components of the beam versus ellipticity of the incident polarization, χ_{in} (orientation of the quarter wave plate, θ_{in}). Empty circles (experiment) and crosses (modelling) are for the S-waveplate retardation profile from Fig. 1.11. Copper (solid circles) and cyan-to-magenta (solid circles) are for the $\sin(1\varphi)$, $\sin(\varphi/2)$ retardation profiles as described in Sec. 1.4.2 and schematically shown in Fig. 1.13. Colorbars on the right show orientation of the quarter wave plate (in degrees) used to change incident ellipticity. Intensity distribution at background is shown for $\sin(1\varphi)$.

Additionally, the retardation profile of the S-waveplate was modelled and motion of the vortex within the beam for 4 orthogonally polarized components is shown in Fig. 1.16 by the crosses color coded with the parula colormap. They show similar behaviour to that observed experimentally (hsv empty circles). Vortex in X- and Y-polarized component of the beam approaches center of the beam when incident polarization is circularly polarized and goes to the periphery of the beam when incident polarization is almost linear. Because of asymmetric intensity distribution in these components interaction of vortices does not "push" them to the infinity but they still remain in the beam. Vortex in the L (R) polarized component exhibit similar behaviour disappearing when incident polarization is purely right (left) hand circular.

Sinusoidal profile of retardation

Locations of OVs in the X-, Y-, L-, and R- polarized components of the beam versus incident polarization are shown in Fig. 1.16 for $j = 0.5$ and 1, and in Fig. 1.17 for $j = 2$ to 8 for sinusoidal profile of retardation $\sin(j\varphi)$ as described in Sec. 1.4.2 and schematically shown in Fig. 1.13.

In the cases of slow oscillations of the retardation profile, $j = 0.5$ and 1, deviation of the vortex from the center of the beam is the biggest (Fig. 1.16); trajectories of vortices in this case are highly asymmetric and different to that from the homogeneous retardation profile.

On contrary, in the cases of fast oscillations of the retardation profile, $j = 2\ to\ 8$, vortex stays close to the beam's center at any incident polarization state (Fig. 1.17) similarly to the case of ideal (unperturbed) retardation. Although the perturbation of retardation is inhomogeneous trajectories of vortices in this case ($j = 2\ to\ 8$) are symmetric and similar to that of homogeneous perturbation shown in Fig. 1.15.

Therefore, as mentioned in the section 1.4.2 lower order oscillations have larger impact on the beam, while oscillations of high order may keep the beam profile and spin-to-orbital coupling – unperturbed.

1.6. Conclusions to Chapter 1

In the section 1.2 we showed that perturbation of retardation of a geometric phase retarder results in the inhomogeneous polarization and intensity distribution of the generated beam because of the interplay between vortex and Gaussian beams. This leads to motion of vortices in the orthogonally polarized components of the generated beam. Deviation of the vortex location is bigger for bigger perturbation of the retardation value. Motion of vortices leads to the appearance of vortex phase in the generated radially/azimuthally polarized beam. These features should be accounted for in high precision experiments. On the other

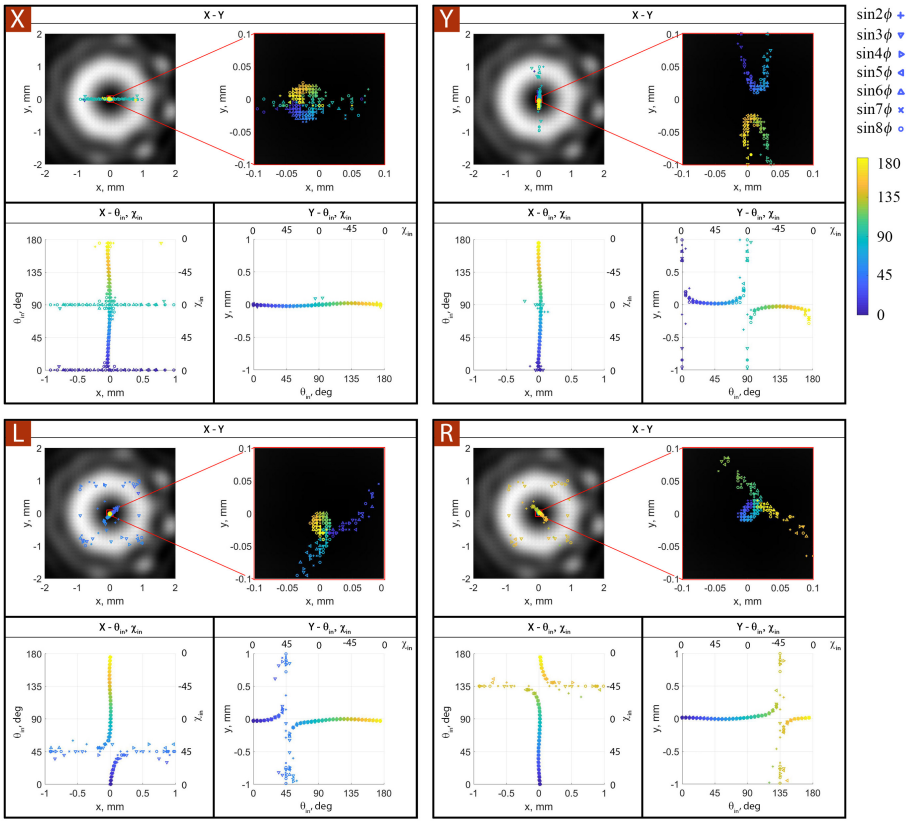

Figure 1.17: Locations of OVs in the X-, Y-, L-, and R- polarized components of the beam versus ellipticity of the incident polarization, χ_{in} (orientation of the quarter wave plate, θ_{in}). Retardation of a retarder follows $\sin(2\varphi)$, $\sin(3\varphi)$, $\sin(4\varphi)$, $\sin(5\varphi)$, $\sin(6\varphi)$, $\sin(7\varphi)$, and $\sin(8\varphi)$ profiles. Modelled data for different retardation profiles is shown by different pictograms as indicated on the right. Colorbars show orientation of quarter wave plate (in degrees) used to change incident ellipticity. Intensity distribution at background is shown for $\sin(8\varphi)$.

hand, intentional high frequency sinusoidal variation of retardation of the geometric phase retarder around π value, such as $\sin(8\varphi)$, leads to appearance of single- and multiple-vortex orthogonally polarized components. Multiple-vortex component diffracts much stronger, thus leaves the beam upon free space propagation. This implies that polarization and intensity of the generated beam "heals", i.e. becomes symmetric. Further investigation towards using this effect as a way towards achromatization of a geometric phase retarder, i.e. for the generation of ultra-broadband radially/azimuthally polarized beams, is necessary.

In the section 1.3.2 we have demonstrated generation of optical vortices over

the visible and nIR wavelength range by using a single three-component scheme based on the polarization-sensitive filtering, i.e. separation of the vortex and background components in the generated beam. The filtering scheme consists of widely available components, is simple to implement and can be extended to any optical element based on the phase control of circularly polarized light, e.g. q-plates, not only as optical vortex converter but also as, e.g., Airy beam converter [76]. The demonstrated wavelength range spans over 600 nm over the VIS and nIR range with the efficiency of filtering higher than 50%. Due to the polarization modulation the presented scheme ensures coaxiality, no spatial dispersion of optical vortices generated at different wavelengths, which could be useful for generation of ultrashort OV shaped pulses in quantum communication systems and data transmission through photonic fibers. We have also demonstrated the polarization-selective vortex generation, where only one of two orthogonally polarized beams with different wavelengths is transformed to optical vortex (doughnut mode) with no limit on how close the two wavelengths could be. Proposed scheme with single optical path for both excitation and depletion beams could significantly facilitate extremely complicated process of alignment of STED systems.

2. Extending vortex fields to terahertz frequencies

This chapter is based on the [A1] and [A2] publications.

2.1. Generation of THz radiation from laser induced plasma filament in air

One could distinguish four scenarios of generation of radiation at THz frequencies from the laser induced plasma filament (Fig. 2.1). (a) The THz emission mechanism is based on the radial acceleration of the ionized electrons due to the ponderomotive force generated by the radial intensity gradient of the optical beam [83], leading to a conical THz emission at an angle to the direction of propagation (Fig. 2.1a). (b) Applied an external DC bias to the plasma region to generates transverse polarization (the "DC-bias" method, Fig. 2.1b). (c) Another method to introduce the required transverse bias is by using a superposition of both fundamental harmonic (FH) and second harmonic (SH) pulse fields to generate the plasma ($\omega - 2\omega$ AC-bias method, Fig. 2.1c). Indeed, the use of two-color fields for generating asymmetric electron dynamics in the photo-induced plasma was already well established (e.g. [84]). As the frequency of the optical AC-bias is well above the plasma frequency, this method does not suffer from the strong screening effects as the DC-bias method does. (d) In the case of few-cycle pulses (i.e. with <10 fs duration), no additional SH field is required in order to observe the THz emission (Fig. 2.1d) [85], the amplitude of which now depends strongly on the carrier-envelope (CE) phase of the pulses.

In this Chapter we consider generation of THz only from plasma filament induced by two-color laser pulse, such as combination of FH and SH (Fig. 2.1c). In 2000 it was proposed that underlying mechanism for THz generation is a four-wave difference frequency (FWDF) mixing parametric process in ionized air plasmas produced by the laser fields themselves [86]. However, the third order nonlinearity originating from either/both bound electrons of ions ($\chi^{(3)}$ ions) or/and free electrons ($\chi^{(3)}$ free electrons) due to ponderomotive or thermal

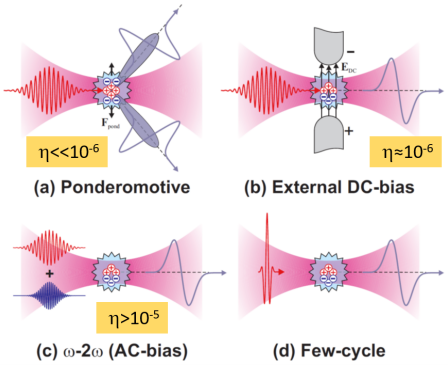

Figure 2.1: Overview of different plasma-based THz generation techniques. η denotes efficiency of conversion from optical to THz frequencies.

effects [87] is too small to explain the observed THz field strength [88]. In 2007 Kim et al. developed a transient photocurrent model [89] to explain coherent terahertz emission from air irradiated by a symmetry-broken laser field composed of the fundamental and its second harmonic laser pulses, which is generally accepted at this moment. Nonvanishing transverse plasma current $J_\perp = eN_e v_e$, where e is the electron charge, N_e is the electron density, and v_e is the electron velocity, can be produced when the bound electrons are stripped off by an asymmetric laser field, such as a mixed two-color field with the proper relative phase; $v_e = eE_1 \sin\varphi/(m_e\omega) + eE_2 \sin(2\varphi+\phi)/(2m_e\omega)$, where m_e is the electron mass. This photocurrent surge produces an electromagnetic pulse at THz frequencies. The relative phase between FH and SH of $\phi = \pi/2$ yields maximum THz generation efficiency, while in phase ($\phi = 0$) FH and SH produce almost no THz radiation. As demonstrated experimentally, with $\phi \approx 0$, the extrapolated THz yield approaches zero, which is consistent with the photocurrent model. However, this is in sharp contrast with polarization-based FWDF mixing which predicts the maximum THz yield at $\phi = 0$, because the rectified term from the third order polarization is proportional to $E_\omega^2(t)E_{2\omega}(t)\cos\phi$ [86]. Note that $\sin\phi$ dependence can also be obtained from FWDF mixing with an assumption of $E_\omega(t) = \sin(\omega)$ and $E_{2\omega}(t) = \sin(2\omega+\phi)$ [88]. In either case, THz radiation from polarization-based FWDF mixing becomes maximal when the peaks of ω and 2ω fields overlap in time. In contrast, the photocurrent model predicts that the maximal THz yield occurs with a $\phi = \pi/2$ phase slippage (or $\sin\phi$ dependence) between the ω and 2ω fields.

In order to understand the process of THz generation from the plasma filament and vote in favour of four-wave-mixing or local currents model we have performed experiment on influence of laser-preformed plasma on efficiency of THz wave generation. If $\chi^{(3)}$ nonlinearity in plasma is responsible for the

THz emission, then energy of the generated THz wave should increase in the presence of the pre-created plasma. Following section 2.2 clarifies this question. Further, once the THz generation mechanism is established, vortex fields are extended to the THz frequencies in the section 2.3.

2.2. Influence of laser-preformed plasma on terahertz wave generation in air by bichromatic laser pulses

2.2.1. Literature review

In this section, we perform an experimental investigation of both energy and spatial properties of THz radiation as a function of the preplasma position with respect to the pump beam axis and its focus. We demonstrate here the rather complicated dependence of the spectral and angular dependence of THz emission on the spatial position of the preplasma filament, showing the influence of the propagation effects both for the pump and THz radiation. In particular, we report a significant effect on THz emission even if the preplasma is created far away from the main plasma filament. Mechanisms responsible for the reduction of the THz yield at different positions are proposed and explained. The suppression of THz radiation generation by the precreated plasma has been studied previously in several experiments [90–92]. However, in these reports, the main emphasis has been placed on the investigation of plasma density dynamics, while geometric factors were not considered in detail.

2.2.2. Experimental observations

For the experiments, we have used a 1 kHz repetition rate femtosecond Ti:sapphire chirped pulse amplification laser system (Legend elite duo HE+, Coherent Inc.), delivering 35–40 fs (FWHM) light pulses centered at 790 nm with maximal pulse energy of 8 mJ. Laser pulses were split into two parts (main pulse and prepulse with energies of 5.2 and 1.65 mJ, respectively) as sown in Fig. 2.2. The main pump beam was focused into the ambient air by the lens of about 30 cm focal length through the nonlinear BBO crystal of 100 μm thickness (type I, cut angles: $\theta \approx 29^\circ$ and $\phi \approx 90^\circ$). Therefore, the main pump pulse consisted of the fundamental and second harmonic pulses and created a plasma filament (main plasma), where the generation of THz radiation took place. The azimuthal angle of the BBO crystal and its location were optimized to achieve a maximal THz radiation yield [93, 94]. The energy of generated THz pulses was measured using a calibrated pyroelectric detector, placed on the computer-controlled translation stage. For the measurements

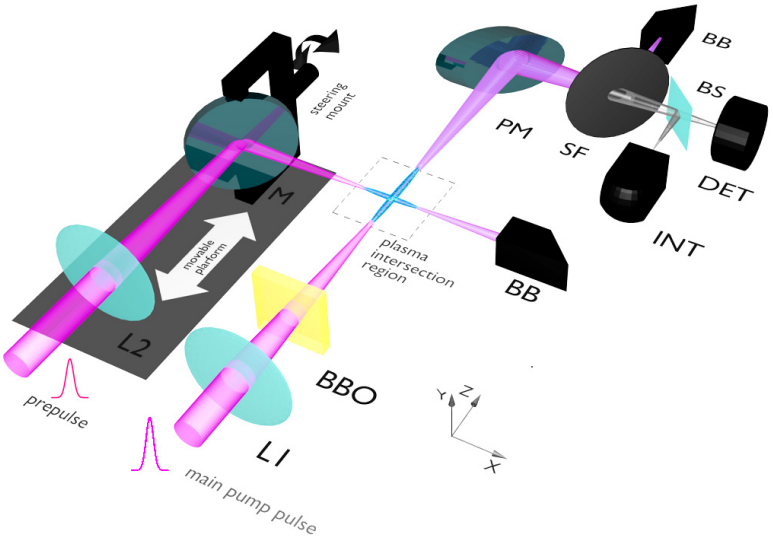

Figure 2.2: Experimental setup. Two pulses focused by the lenses L1 and L2 are superimposed to create two plasma filaments perpendicular to each other. One of the pulses (referred to as the main pulse) is sent before this superposition to a BBO crystal which makes it a two-colour one. The second pulse (referred to as the prepulse) is controlled by a delay stage and a moving mirror M which allows varying its temporal and spatial position relative to the main pulse. The detection setup consists of a parabolic mirror PM, filter SF, beam splitter BS, Michelson interferometer INT, and detector head DET.

of THz wave spectra, a home-made THz Michelson interferometer was used along with the pyroelectric detector. Before the entrance of the Michelson interferometer, a THz filter (0.5–1 mm thick Si wafer) was placed, to remove the high frequency part. During measurements of the spatial distributions of generated THz radiation, the pyroelectric detector was placed on a computer-controlled motorized translation stage located at about 50 cm from the plasma filament. By moving it across the pump beam (along the x and y directions), we were able to register the corresponding angular spectra of generated radiation. The prepulse was propagated and focused in the orthogonal direction with respect to the main beam, to generate a plasma filament that intercepted the main beam path (figure 2.2). The relative time delay and position of the two pulses (main pulse and prepulse) were respectively controlled by motorized and computer-controlled translation stages and by a steering mirror. A CCD camera was used to image the fluorescence of the plasma filaments. The length of fluorescence filament was about 2 cm for the pump pulse energy of 5 mJ.

The typical interference traces and corresponding amplitude spectra of generated THz radiation are presented in figure 2.3. The spectra were calculated

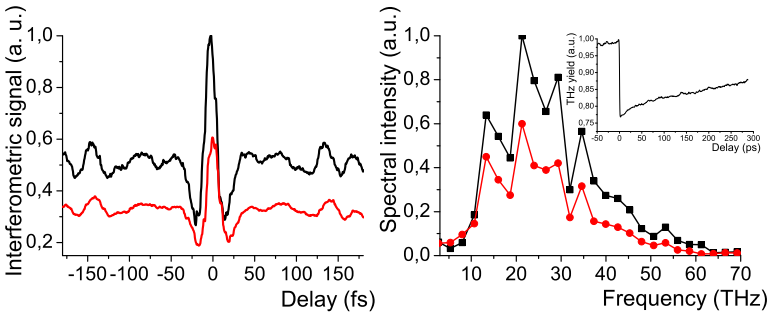

Figure 2.3: Interference traces (left) and corresponding THz spectra (right) of generated radiation with (red lines) and without preplasma (black lines). The preplasma filament was created by a 10 cm focal length lens and was located in the focal plane of the pump beam. Energies of the pump and preplasma pulses were 5.2 and 1.65 mJ, respectively. Modulation of the spectra is caused by the absorption of used THz filters and of the beam splitter of the interferometer (2 μm-thick nitrocellulose pellicle). The inset at the top right corner shows the typical dependence of the THz yield on the timing between the main pulse and prepulse.

by Fourier transformation of the interferograms, and in most cases a non-negligible signal could be observed up to 60 THz. One can see that the THz signal significantly decreases when the precreated plasma is present in the path of the pump beam. In most cases, the attenuation factor of the THz radiation was nearly the same for all frequencies. As has been reported elsewhere [90–92], the impact of the preplasma on the efficiency of THz generation was strongly dependent on the timing between the pump pulse and prepulse: the amplitude of THz signal did not change when the prepulse was sent after the main pulse, and rapidly decreased when the sign of the delay between these pulses was reversed (see inset of the figure 2.3). After the initial dropdown, the THz signal slowly recovered with a time constant of a few hundred picoseconds, which corresponds well with ballistic plasma expansion and free electron decay rates reported previously [90–92, 95]. However, in contrast to the previous reports where the effect of preplasma was observed only when the plasmas (main plasma and preplasma) were overlapping, in our experiment this effect was also registered when the main beam was intercepted by the preplasma in locations away from the main plasma. In addition, we have observed quite complex dependence of the THz attenuation on the mutual position of the two plasma filaments: depending on the position of interception point along the main beam (along the z coordinate axis) the THz yield as a function of preplasma position along the y coordinate mainly had either one or two minima (at the intersection points before and after the main plasma—see figure 2.4 and 2.5).

The dependence of THz yield on the mutual positions of the main plasma

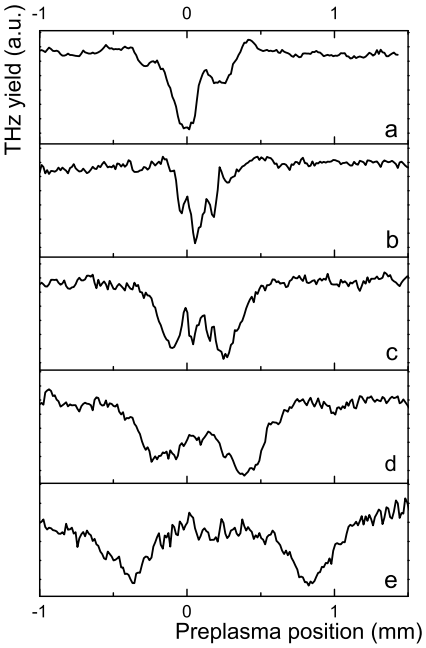

Figure 2.4: Dependence of the THz power on the position of the preplasma along the y axis (perpendicularly to both the main plasma and preplasma filaments—see figure 2.2) for various intersection points (corresponding to different z coordinates in figure 2.2): (a) before the onset of the main plasma, (b) at the onset of the main plasma, (c) at the middle of the main plasma, (d) at the tail of the main plasma, (e) after the main plasma.

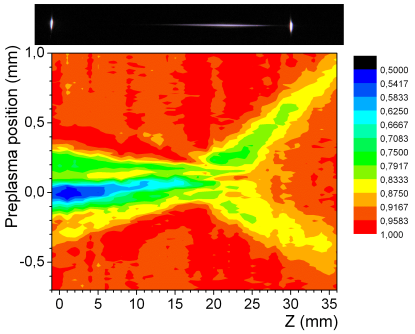

Figure 2.5: Dependence of the THz power on the position of the preplasma with respect to the main beam axis and relative distance along the z coordinate axis. For clarity, the main plasma filament (seen there as a long string) and preplasma (seen as light points at both ends) at the two exemplary positions of $z = -1$ mm and $z = 30$ mm are shown above.

and preplasma can be explained on taking into account at least two different phenomena. First, when the filaments intersect before the main plasma (figure 2.4(a)) and the preplasma position is scanned along the y direction (that is, perpendicularly to the propagation direction of both filaments), the pump beam refracts and diffracts on the preplasma filament, which directly and due to the interference of various parts of the beam modifies the light intensity distribution and phase relations of the bichromatic pump [96] in the focus of the beam, where THz generation is taking place. Naturally, the strongest interaction occurs when the preplasma is centered with respect to the main beam, and as a result the

dependence of THz yield has one main minimum (the local minimum seen in figure 2.4(a) may be attributed to the fact that during the experiment non-ideal Gaussian beams were used). At the onset and middle of the main plasma (figure 2.4(b) and (c) respectively), the dependence becomes more complicated, since at these points some THz radiation has already been generated and consequently is absorbed and reflected by the preplasma [97]. Therefore, in this case, the interplay of the interference, diffraction and plasma screening takes place. Finally, at the tail of the main plasma and after it (figure 2.4(d) and (e)) the preplasma does not influence the bichromatic pump beam, wherefore plasma screening becomes the main process reducing the efficiency of THz generation (absorption and reflection by the preplasma). Since the THz beam has a conical shape [98], the dependencies of the THz yield on the preplasma position have characteristic double minima. This is furthermore supported by a more detailed scan of the spatial distribution of the THz power versus the position of the preplasma shown in figure 2.5. There, one can also recognize regions with two minima and the one with a single one. In the former, the distance between the two minima increases when the intersection point moves along the z axis. The divergence angle of these two minima (about 4°) corresponds well to the apex angle of the conical THz beam itself. Thus, we see here the influence of the preplasma on the spatial structure of the THz beam.

2.2.3. Theoretical interpretation

The above interpretation is supported by the simple estimates of preplasma contribution to the THz and laser beams. Thus, assuming that the prepulse creates the plasma filament with electron density $n_e(r)$ as a function of the plasma filament radial coordinate r, the plasma frequency ω_p is defined as

$$\omega_p = \sqrt{\frac{n_e(r)e^2}{\epsilon_o m}}, \tag{2.1}$$

where e and m are the electron charge and mass, respectively. Then the plasma index variation $n(r)$ across the filament diameter is given by

$$n(r) = \sqrt{1 - \frac{\omega_p^2}{\omega_0^2}}, \tag{2.2}$$

where $\omega_0 = 2\pi c/\lambda$ is the light frequency and λ is the wavelength.

Phase change $\Delta\phi(x, y)$ of the light traversing the preplasma is given by:

$$\Delta\phi(x, y) = \frac{2\pi}{\lambda} \int_0^{L_p} n(r)dz, \tag{2.3}$$

where L_p represents the spatial extent of the preplasma filament along the x

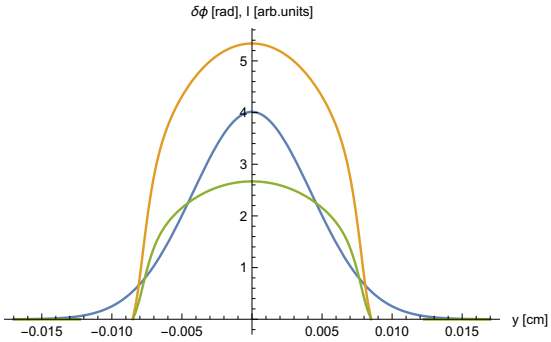

Figure 2.6: Dependence of the total preplasma-induced phase for 800 nm (orange line) and 400 nm waves (green line) as a function of the transverse spatial coordinate y according to equation (3). Blue line shows the intensity distribution of the preplasma filament.

axis (see Fig. 2.2).

Under our experimental conditions, the diameter of the preplasma filament can be about 100 μm, while the maximal plasma density inside it may reach 10^{19} cm^{-3} [90, 99]. The phase modification given by equation (3) is shown in figure 2.6 assuming plasma density in the multiphoton ionization regime of $|I|^{10}$ for 800 nm and $|I|^5$ for 400 nm and taking into account ionization potential 14.5 eV of nitrogen. The plasma frequency can be estimated as about 28 THz. Light of frequency lower than ω_p is fully reflected by the pre-created plasma, whereas for frequencies higher than ω_p, the plasma becomes transparent. However, even in that case, the light traversing the plasma filament may experience strong Fresnel losses if the ω_0 is of the same order as ω_p. We believe that this was the case in our experiment, since the maximal spectral intensity of the generated THz beam was near 28 THz. Thus, the lowest (0–28 THz) frequencies of the THz beam traversing the preplasma were reflected and absorbed, while the high-frequency part of the beam was attenuated by Fresnel reflections (according to equation (2.2), $n(r)$ is larger than 0.8 within the whole high-frequency range (28–60 THz) of generated THz beam).

Naturally, the impact of plasma on the optical pump waves is much weaker, but may still cause significant reduction of the THz yield. Thus, according to equation (2.3) a plasma filament of 100 μm in diameter may induce a maximal phase slippage of 5.4 radians and 2.7 radians for 800 nm and 400 nm waves, respectively. Note that a change of relative phase between the fundamental and second harmonic waves by $\pi/2$ may result in full suppression of THz generation [96, 100]. In addition, since laser-induced ionization of air is a highly nonlinear process, the transverse spatial electron distribution has a supergaussian shape even in the case that Gaussian intensity distribution of the laser beam is assumed (figure 2.6). Besides, the plasma-induced refraction

index almost directly follows the plasma density distribution—i.e. it is almost independent of the radial coordinate within the plasma filament. Therefore, although plasma-induced phase changes decrease with the radial coordinate, significant fractions of the bichromatic pump beam traversing the preplasma filament can still acquire significant phase-shifts. As shown in figure 2.6 (orange and green lines), the preplasma filament may induce more than 75% of maximal phase change within its 100 μm-wide spatial extent. Since the pump beam diameter at the focus is of the same order, a significant part of the pump beam area may be affected by the preplasma. Moreover, since the pump beam is converging as it crosses the preplasma filament, parts of the beam with different phases interfere at the focal point, decreasing the focal light intensity and thus further reducing THz yield. Note that similar strong modulation of the laser beam due to the abrupt index and accumulated phase changes across the plasma filament diameter for plasma densities even lower than 10^{18} cm^{-3} has recently been observed [101]. Thus, apart from the direct variation of the relative phase between the fundamental and second harmonic waves, the preplasma filament also modulates and decreases the pump beam intensity, which may also significantly reduce the total THz yield.

2.2.4. Conclusions to section 2.2

In conclusion, we have investigated the influence of a precreated plasma filament on the energy and spatial properties of terahertz radiation generated in air by focused femtosecond bichromatic laser pulses. It was found that plasma absorption and screening play an important role and significantly reduce the intensity of THz radiation when the intersection point of the bichromatic pump and prepulse beams is located after the pump beam focus. On the other hand, when the intersection point is before the pump beam focus, the main phenomenon responsible for the strong modification of generated THz radiation is the influence of the preplasma filament on the intensity and relative phase of the bichromatic pump beam.

2.3. Terahertz vortex wave generation in air plasma by two-color femtosecond laser pulses

2.3.1. Literature review

Terahertz radiation is of great current interest due to many applications such as nonlinear THz spectroscopy and imaging [6] or electron bunch compression [7]. As mentioned at the beginning of this Chapter, one of the compact and effective methods to obtain very high THz field strengths and extremely broadband spectral widths is THz wave generation from plasma filaments formed in air

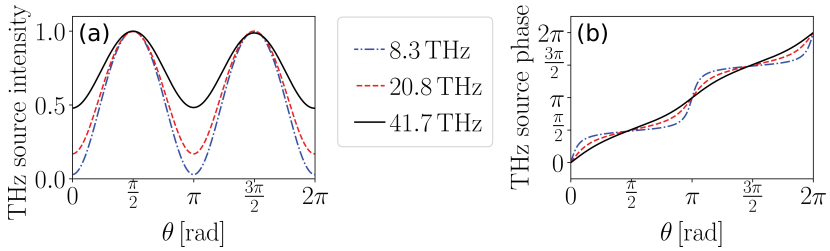

Figure 2.7: Azimuthal intensity (a) and phase (b) distribution of the Fourier-transformed THz source term $\partial_t J$ [see Eqs. (2.4), (2.5)] at four different frequencies as specified in the legend. The computation has been performed with parameters close to the experimental.

by focused bichromatic femtosecond laser pulses consisting of first and second harmonic waves [100, 102–104]. On the other hand, special light fields, such as optical vortex [105], radially polarized [73], Bessel [106,107] and Airy beams [108] are widely studied and employed in various fields [50, 109]. Previous attempts on vortex generation at THz frequencies [8–15, 110] were exclusively based on manipulation of THz waves by employing external components which are inherently limited in terms of acceptable bandwidth. Therefore, alternative methods for ultra-broadband vortex generation at THz frequencies should be proposed and investigated. Very recently, vortex-shaped THz pulses have been demonstrated without using external shaping elements [16, 17] from ZnTe crystals, which, however, supply relatively narrow bandwidths.

In this work we investigate vortex THz pulse generation in an air-plasma induced by the coupling between Gaussian FH and vortex SH pulses. In this novel scheme, the vorticity is created already at the THz generation stage. It appears that SH carrying an optical vortex charge affects not only the phase but also the intensity distribution of the generated THz pulse. We distinguish two stages of THz vortex generation: (i) At the beginning of the plasma filament, an intensity modulated THz vortex pulse is created. This intensity modulation is frequency dependent. (ii) Upon further propagation, the pump pulse may undergo spatio-temporal instabilities which induce secondary phase singularities in the THz field, but the total topological charge is conserved. Results of our investigation suggest an alternative method for the generation of structured THz waves spanning ultrabroadband frequency ranges, which is not limited by the spectral acceptance of the external shaping elements or down-converting crystals; can be used for active control of the THz pulse properties, giving great flexibility for applications of THz radiation.

2.3.2. Theoretical predictions

For two-color laser-induced gas plasmas, the ionization current mechanism [111] is the key player for THz emission, as confirmed in the previous section. This emission is caused by the macroscopic current of free electrons which are created by field ionization in the tunneling regime [112, 113] and driven by the laser electric field. The principal electric field component is transverse to the laser propagation direction, and we consider linear polarization. Neglecting electron collisions, the current equation reads

$$\partial_t J = \frac{q_\mathrm{e}^2}{m_\mathrm{e}} n_\mathrm{e} E \,, \tag{2.4}$$

with electron charge q_e, mass m_e, electron density n_e and electric field E. The electron density is a time-dependent parameter governed by the ionization rate and can be computed using ionization rate equations [114,115]. The electric field consists of both optical frequency components and generated THz components, which plays an important role in the THz spectral broadening [116]. However, certain effects can be already understood by considering only the impact of the bichromatic laser electric field. The down-conversion from laser to THz frequencies takes place because of the nonlinear product between the electron density and the laser electric field. It can be shown that at least two laser colors, here FH and SH with a relative phase angle of $\pi/2$, are required to obtain an efficient down-conversion towards THz frequencies [89, 117]. In order to understand this down-conversion process in the case of vortex pump pulses, we first evaluate Eq. (2.4) for the real-valued laser electric field

$$E_\mathrm{L}(t,\theta) = A(t)[E_{\omega_\mathrm{L}} \cos(\omega_\mathrm{L} t) + E_{2\omega_\mathrm{L}} \cos(2\omega_\mathrm{L} t + \phi + l_\mathrm{SH}\theta)], \tag{2.5}$$

with fundamental frequency ω_L, relative phase offset ϕ, pulse envelope $A(t)$; l_SH is the vortex charge of the SH beam. Here, we omit the radial and longitudinal coordinates, and write the electric field as a function of time t and azimuthal angle θ only. Equation (2.5) thus represents the rapid time- and θ-dependent distribution of the electric field along the vortex ring, assuming constant FH and SH amplitudes $E_{\omega_\mathrm{L},2\omega_\mathrm{L}}$. The resulting spectral intensity and phase of the source term $\partial_t J$ obtained by Fourier transform is presented in Fig. 2.7 for $\phi = 0$ and $l_\mathrm{SH} = 1$. The intensity is modulated along θ and is maximal when the relative phase angle $(\phi + l_\mathrm{SH}\theta)$ between the SH and FH takes the values $\pi/2$ and $3\pi/2$ and minimal for 0 and π (Fig. 2.7). The modulation depth is the largest at lower frequencies and decreases for larger frequencies, where also the phase approaches a linear ramp-up along θ as expected for a vortex. The results from this simple theoretical approach remain qualitatively the same when changing the laser and gas parameters within the parameter range allowing for efficient THz generation.

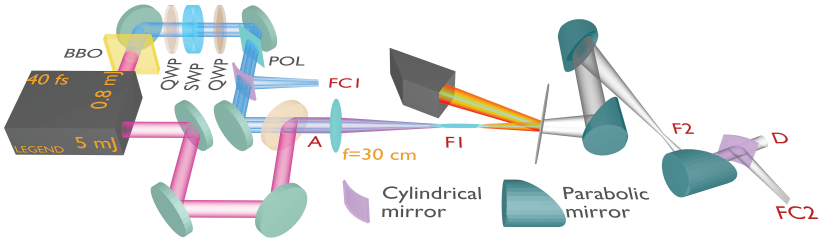

Figure 2.8: Sketch of experimental setup. QWP - quarter wave plate, SWP - S-waveplate (q-plate), POL - polarizer, BBO - nonlinear crystal for SH generation. SH is shown by blue, FH by red-pink, and THz radiation by gray color. Red letters label relevant positions (see text for details). THz fluency profiles taken in positions 'D' and 'FC2' are shown in Fig. 2.9 and 2.10.

2.3.3. Experimental observations

The experimental setup is sketched in Fig. 2.8. We used a 1 kHz repetition rate laser system (Legend elite duo HE+, Coherent Inc.). Right before the main focusing lens (silica, f=30 cm) labeled 'A' in the setup, the FH pulse had central wavelength of 790 nm, FWHM pulse duration 50 fs and energy of 6 mJ. The SH pulse had central wavelength of 395 nm, FWHM duration ∼50 fs and energy of 60 μJ in Gaussian state and 50 μJ in vortex state. Our Gaussian SH pulse was shaped into an optical vortex by the method described in [118], which ensures more than one-octave spectral bandwidth of vortex generation: First SH was circularly polarized by a quarter wave plate (QWP) and converted to an optical vortex (OV) beam by an S-waveplate (RPC-405-06-557, Workshop of Photonics) (SWP). Subsequent polarization filtering by a second quarter wave plate (QWP) and a polarizer (POL) ensured generation of a linearly polarized vortex in the SH beam profile over the whole spectral bandwidth of the SH pulse. A 0.5 mm thick Si wafer and various commercial THz filters were used to remove the high frequency part of the pump and transmit only THz radiation, which was then collimated and shrank by parabolic mirrors in a telescope configuration to match the detector aperture. Imaging of the generated THz beam was performed with a thermal camera detector (VarioCAM head HiRes 640, InfraTec GmbH), sensitive in the range 0.1 – 40 THz (3000 – 7.5 μm). Spectra of THz radiation were obtained from Fourier transformed interferometric measurements using pyroelectric detector (TPR-A-65 THz, Spectrum Detector Inc.), sensitive in the range 0.1 - 300 THz (3000 - 1 μm) with a flat response function from ∼3 to ∼100 THz. The laser-to-THz conversion efficiency for the regular Gaussian pulses was about 10^{-4}, but dropped to $\sim 10^{-5}$ in the case of the SH vortex pump, which we attribute to the differences in the spatial intensity distribution of the Gaussian FH and vortex SH beam.

During the experiment the FH beam was always kept Gaussian. Experimental images of the SH beam are shown in the left panel of Fig. 2.9. The first

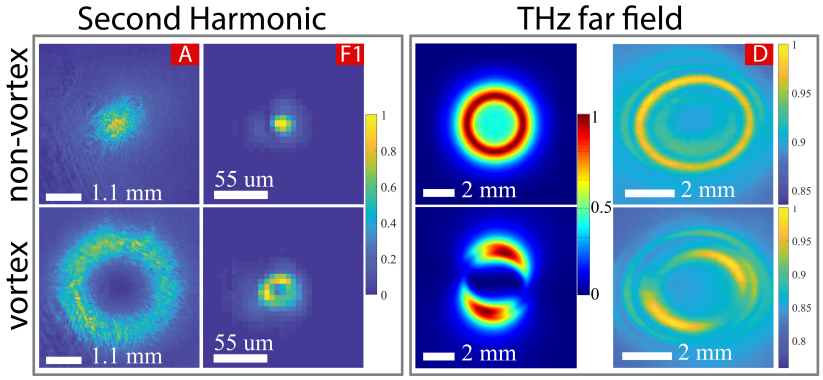

Figure 2.9: (Left panel) Images of second harmonic fluency (non-vortex and vortex, for Gaussian and vortex state, respectively). Column labeling correspond to locations where images were acquired as specified in Fig. 2.8. (Right panel) Corresponding simulated (first column) and experimentally observed (second column) far-field THz fluencies. See text for details.

and the second row present the SH Gaussian ('non-vortex') and vortex beam ('vortex'), respectively. The first column 'A' shows images of the harmonics prior to the main focusing lens at position A (see Fig. 2.8); the second column 'F1' refers to the focus position (F1 in Fig. 2.8). The FWHM beam widths are 33 and 38 μm for the FH and the vortex SH in the focal plane of the 30-cm focusing lens, respectively.

Experimental images of the THz far-field fluency obtained in position 'D' (Fig. 2.8) with the thermal camera (0.1-40 THz) are shown in the last column of Fig. 2.9). The THz fluency obtained with Gaussian SH (upper row) has a symmetric ring intensity distribution, as expected for conical THz emission [119, 120]. In contrast, the THz fluency obtained with vortex SH (lower row) has an intensity modulation manifesting as two maxima along the azimuthal angle, in agreement with our theoretical predictions (see Fig. 2.7). Simulation results shown for comparison in the first column of right-hand panel in Fig. 2.9) are in excellent agreement. The simulated fluency is obtained for the spectral range of 0.01 to 50 THz (see below for details on the simulations).

The presence of a phase singularity in the generated THz beam was confirmed by the well-controlled method of topological charge determination based on the astigmatic transformation of singular beams by a cylindrical mirror [81]. This method is valid even in the presence of intensity modulations affecting the generated THz beam profile. A beam without phase singularity focuses in a single line, whereas the appearance of a dark stripe in this line indicates a singular phase. The number of lines and their tilt correspond to the value and sign of the topological charge. As shown in the left panel of Fig. 2.10, the single dark stripe in the second row suggests that the topological charge of

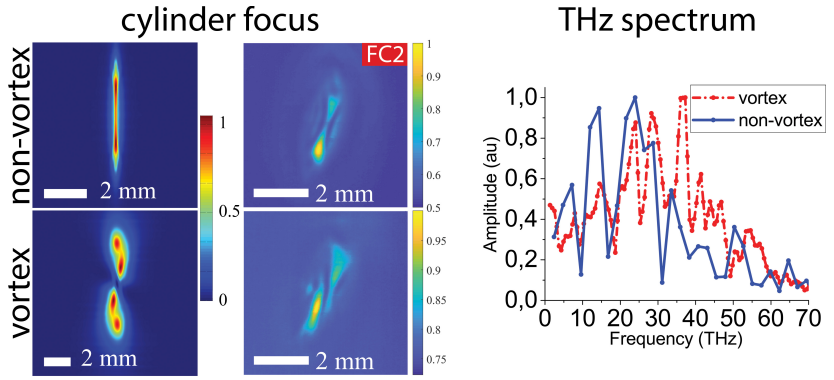

Figure 2.10: Left panel: Simulated (first column) and experimentally observed (second column) fluencies of the generated THz beams in the focus of a cylindrical mirror (f = 20 cm). Right panel: shows typical experimental amplitude spectra of the generated THz pulses in the case of vortex SH (red dash-dot "vortex") and Gaussian SH (blue solid line "non-vortex").

the generated THz vortex is $|l_{THz}| = 1$. Simulation results and experimental images show again excellent agreement.

As evidenced by the right-hand panel of Fig. 2.10, the experimental spectra of the generated THz pulses are broadband, spanning from 10 to 40 THz. We attribute the dips in these spectra to absorbance in optical elements such as Si filters with spectrally variable transmission (OCz-Si, Tydex) and pellicle beam splitters. In the case of the THz vortex the peak spectral intensity is located around 35 THz, while THz pulses without phase singularity have their maximum around 25 THz. This shift may occur because of the lower ionization rate at the periphery of the FH pump beam where the SH vortex has maximum intensity and due to transverse phase variations.

Although astigmatic transformation of generated vortex THz beam by cylindrical mirror was used as a primary detection method of phase singularity. Additionally, we can check it by looking at the intensity variation with the change of the relative phase between two harmonics. As noted in the theoretical section, the maximum THz yield is expected for a relative phase $(\phi + \theta) = \pi/2$ and $3\pi/2$ between FH and SH. Since the phase of the SH vortex beam changes by 2π over the full azimuthal angle, while the phase of the FH is constant along this angle, the intensity of the THz vortex beam has two minima and maxima. Changing the relative phase between FH and SH should result in position change (rotation) of these maxima and minima. To verify this property, the THz vortex intensity distribution was filmed by the thermal camera. The relative phase between FH and SH was not controlled but was fluctuating due to long beam pass distances (>5 meters for each harmonic), vibrations in the room/building, temperature variations, etc. Because of the random nature of the fluctuations, the THz vortex

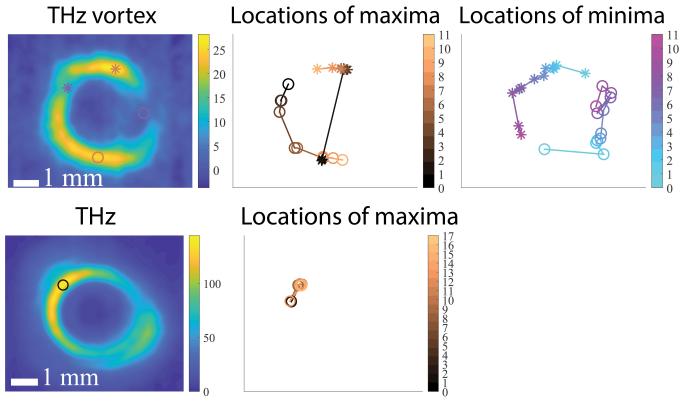

Figure 2.11: Left: Intensity distribution of vortex THz beam (top) and THz without phase singularity (bottom) versus fluctuations of relative phase ϕ between FH and vortex or Gaussian SH. Shown is one frame from a 12-frame long video-sequence. Positions of maxima are shown by brown circle and star; positions of minima are shown by magenta circle and star. Colorbar indicates intensity in a.u. Center: Locations of maxima obtained from the video sequence on the left are shown. Colorbar indicates frame number. Right-top: Locations of minima obtained from the video sequence on the left are shown. Colorbar indicates frame number. Animated: see links in the text

intensity distribution jitters and makes a full rotation once in a while. The typical time constant for these phase variations was of the order of 5 s, therefore we were able to register both the relatively stable THz patterns or the randomly rotating ones. The thermal camera takes 50 frames per second, corresponding to 20 milliseconds delay between subsequent frames. 12 consecutive frames (duration 240 ms) were chosen from a 1 sec long video to demonstrate the rotation of the intensity distribution due to fluctuations of the relative phase as shown in top of figure 2.11. Locations of the maxima and minima were found and plotted by a home written matlab script. The top-rightmost part of the Fig. 2.11 shows that minima of the beam change their locations in the beam by 180 degrees during the full video sequence. The colorbar on the right indicates the number of the frame; changing from cyan for the first frame to magenta for the twelfth frame. Locations of the maxima, color-coded to change from dark to light brown, demonstrate a similar behaviour. A video sequence of the intensity distribution rotation is available via the link: `https://drive.google.com/file/d/1ec_gVWqwTFPNjY3KAUK2SlpOcEEO2n4f/view?usp=sharing`. On the contrary, the intensity distribution of the THz beam without phase singularity doesn't change (figure 2.11 bottom). The fact that the THz beam has a distinct maximum is due to slight misalignment of transverse locations of the FH and SH beams. The maximum of the THz beam slightly oscillates

around the same position due to (flaws in) pointing stability of the laser. The video sequence available via the link: `https://drive.google.com/file/d/1esYNI5QfC0F0UE0ro6h30Kqwm_A6nf1J/view?usp=sharing` demonstrates a breathing (in-out) character of the intensity of the THz beam. While filming THz radiation with and without phase singularity alignment of the setup was not changed. Yet, the generated THz beam, in the cases of vortex and Gaussian SH pump, shows qualitatively different behaviour consistent with the theoretical predictions.

Please, note that the shown motion of locations of top maxima (stars) seems to be almost fixed, contrary to bottom maxima. This apparent discrepancy may be explained by the non-ideal intensity distributions of the FH and SH vortex beams and by the non-optimal alignment between these beams. Thus, as it is seen in Fig. 2.11 bottom. the THz intensity is larger on the left side of the ring, The same applies also to the case of the vortex pump (Fig. 2.11 top). Thus, the THz intensity maxima tends to be more pronounced at this position. The top maxima/top lobe of the beam does change at the same rate as the bottom maxima/lobe of the beam. The appearance of the slowly moving upper maximum is an artefact of the maxima position detection. Matlab detection scheme finds the biggest peak in the upper lobe maximum of the beam, this peak appears to be moving at a lower rate than the intensity distribution in this lobe around this peak, which vary at the same rate as bottom lobe/peak.

2.3.4. Simulations

For a complementary analysis we performed comprehensive numerical simulations of the full experiment by means of a unidirectional pulse propagation solver [117, 121]. Laser parameters and focusing conditions in the simulations are chosen such as in the experiments. Our simulation results reveal two distinct stages in the formation and subsequent evolution of the generated THz pulses. First, intensity and phase modulations of the THz source term due to the spatially variable relative phase difference between FH and vortex SH pump components emerge, as expected from our theoretical predictions (see Fig. 2.7). Second, the pump pulse develops spatio-temporal instabilities generic to the filamentation dynamics that directly affect the THz pulse distribution.

The right hand side of Fig. 2.12 shows collimated far field intensities and phases of the generated 10 and 25 THz spectral components at two stages of the propagation, namely at the beginning of the plasma filament ($z = -8$ mm), and after transverse pump instabilities have fully developed ($z = -4$ mm). All z positions are given relative to the focus position F1 ($z = 0$ mm) of the main pump focusing lens (see Fig. 2.8). To obtain the THz far field, the nonlinear interaction was stopped at the given z position and the THz field was further propagated over a few centimeters in vacuum (sufficiently to reach the far field)

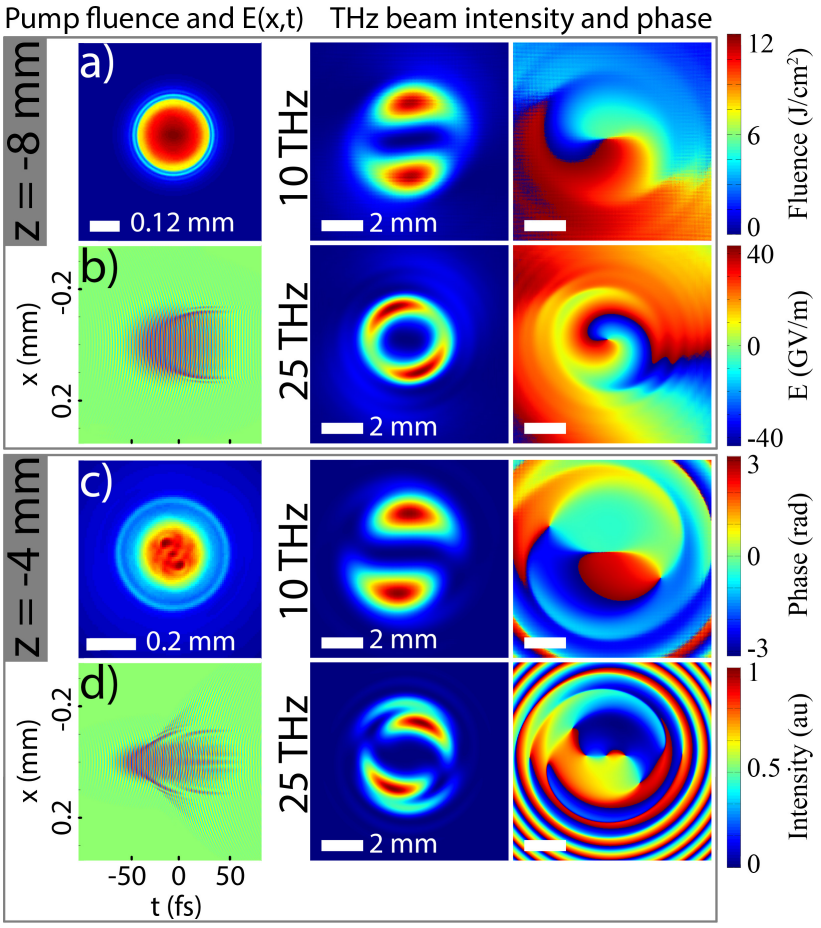

Figure 2.12: (a) and (c) show fluency, (b) and (d) show electric field $E(x,t)$ of the two-color pump at the beginning of the filament ($z = -8$ mm) and after transverse pump instabilities have fully developed ($z = -4$ mm). The two right-hand side columns show collimated far field intensity and phase of the 10 and 25 THz frequency components computed from the field at $z = -8$ mm and $z = -4$ mm, respectively (see text for details). Linear focus F1 is at $z = 0$ (see Fig. 2.8).

and collimated with a lens in thin element approximation.

At the beginning of the filament ($z = -8$ mm) the pump fluency is uniform, as evidenced by Fig. 2.12 (a). The corresponding spatio-temporal electric field profile in Fig. 2.12 (b) shows that plasma has only started to deplete the trailing part of the pump pulse, as one would expect from the usual filamentation dynamics [121, 122]. The generated THz vortex at this early stage of pump propagation has a single phase singularity in the center. The intensity is circular with azimuthal modulation, and the modulation depth is larger for lower frequencies, as predicted by Fig. 2.7. In contrast, at ($z = -4$ mm) the pump

pulse has undergone severe transverse distortion [see fluency in Fig. 2.12 (c)], and the spatio-temporal field profile in Fig. 2.12 (d) looks much more complex. These strong perturbations of the pump clearly affect the intensity distribution of the THz vortex and produce secondary singularities in the generated THz field. Nevertheless, additional singularities have alternating signs such that the total topological charge of the singular THz wave with $|l_{THz}| = 1$ is preserved during propagation at all relevant frequency components. Overall, our simulations results suggest that the produced THz vortices are surprisingly stable against pump distortions.

2.3.5. Conclusions to section 2.3

We have investigated the properties of THz radiation generated in air plasma by focused bichromatic femtosecond laser pulses, when one of the pump beams (second harmonic) is an optical vortex. The presence of a phase singularity in the generated THz beam was confirmed by astigmatic transformation of the singular THz beams in the focus of a cylindrical lens, as well as by fully space and time resolved numerical simulations. Furthermore, it was additionally confirmed by analyzing the change of the intensity distribution of the THz beam with respect to the relative phase between fundamental and second harmonic. We report that, in contrast to other nonlinear processes (second harmonic generation, parametric generation, etc.), the THz radiation generated by electron currents in a plasma filament cannot be characterized as a THz vortex beam in the 'classical' sense, such as a pure Laguerre-Gaussian beam. Instead, the intensity of the THz beam is modulated along the beam azimuthal angle and contains two minima between two lobes of maximum intensity. This is because the relative phase between two harmonics varies azimuthally when the SH pump pulse is a vortex. Moreover, our numerical simulations demonstrate that transverse instabilities in the filamentary pump propagation affect the THz vortex without destroying it. They may introduce secondary phase singularities, which renders the phase topology of produced structured THz fields particularly rich. One of the benefits of THz generation from plasma currents is the large (>40 THz) spectral range achievable, contrary to bandwidth limited external THz shaping techniques. We envisage that different combinations of the topological charges of the FH and SH pulses open a wide playground for the creation of structured singular THz sources.

3. Degenerate Optical Parametric Amplifier with radially polarized output

This chapter is based on the [A5] publication.

3.1. Literature review

In general radially polarized beams can be generated inside a laser resonator [123–128] as well as outside the resonator. Outside of a laser resonator, the radial polarization can be achieved by converting circularly polarized light by a radial analyzer (a polarizer which only transmits a radial polarization) [129,130], the radial polarization converter – S-waveplate ([66] and as discussed in the first Chapter of this dissertation), superimposing two orthogonally polarized Hermite-Gaussian modes [131], using a spatial light modulator [132–134], or propagating a circularly polarized optical vortex through a uniaxial birefringent crystal and splitting it by focusing into a radially and azimuthally polarized components [135].

Radially and azimuthally polarized beams are two examples of a wide family of beams with polarization singularities. Yang et. al. has demonstrated an experimental generation of such beams by superposition of Laguerre-Gaussian modes [72]. They used a spatial light modulator to generate two optical vortices of different topological charges and superimposed them.

In this chapter, we propose new alternative technique to generate beams with polarization singularities and demonstrate it experimentally. The proposed method is based on the optical parametric amplification and can be used to create powerful beams, limited only by the damage threshold of the nonlinear crystal. In the theoretical part we discuss the underlying physical principles of the technique and in the experimental part the concept of the technique is introduced. The experimental results and possible extensions of the method are presented and discussed in the last two sections of the experimental part.

3.2. Theoretical

To generate beams with polarization singularities, we use a superposition of two optical vortices obtained by optical parametric amplification. The signal and idler waves after the optical parametric amplification are combined using a quarter wave plate to create the output beam with the desired polarization.

Polarization singularities as a superposition of optical vortices. The polarization vector of a radially polarized beam can be written as follows:

$$\vec{v}_r = A(r) \begin{bmatrix} \cos\phi \\ \sin\phi \end{bmatrix} , \tag{3.1}$$

where r and ϕ are radial and azimuthal coordinates in the cylindrical coordinate system and $A(r)$ is the beam's envelope, which depends only on r. Using the well-known trigonometric identities, the polarization vector in Eq. (3.1) can be rewritten as a sum of two circularly polarized optical vortices with opposite topological charges:

$$\vec{v}_r = \frac{1}{2} A(r) \left(\exp(i\phi) \begin{bmatrix} 1 \\ -i \end{bmatrix} + \exp(-i\phi) \begin{bmatrix} 1 \\ i \end{bmatrix} \right) . \tag{3.2}$$

Note that in Eq. (3.2) the polarization handedness of the optical vortices are opposite as well as the sign of their topological charges.

A similar equation can be written for the azimuthal polarization vector:

$$\vec{v}_a = A(r) \begin{bmatrix} -\sin\phi \\ \cos\phi \end{bmatrix} = \tfrac{i}{2} A(r) \left(\exp(i\phi) \begin{bmatrix} 1 \\ -i \end{bmatrix} - \exp(-i\phi) \begin{bmatrix} 1 \\ i \end{bmatrix} \right) . \tag{3.3}$$

Also, higher order polarization singularities can be expressed as a superposition of optical vortices with higher topological charge:

$$\vec{v}_l^{(RT)} = A(r) \begin{bmatrix} \cos l\phi \\ \sin l\phi \end{bmatrix} = \tfrac{1}{2} A(r) \left(\exp(il\phi) \begin{bmatrix} 1 \\ -i \end{bmatrix} + \exp(-il\phi) \begin{bmatrix} 1 \\ i \end{bmatrix} \right) \tag{3.4}$$

or

$$\vec{v}_l^{(AT)} = A(r) \begin{bmatrix} -\sin l\phi \\ \cos l\phi \end{bmatrix} = \tfrac{i}{2} A(r) \left(\exp(il\phi) \begin{bmatrix} 1 \\ -i \end{bmatrix} - \exp(-il\phi) \begin{bmatrix} 1 \\ i \end{bmatrix} \right) \tag{3.5}$$

for two types of beams with polarization singularities. When $l = 1$, the Eq. (3.4) reduces to a simple radial polarization beam (as in Eq. (3.1)) and Eq. (3.5) reduces to an azimuthal polarization beam, just like in Eq. (3.3). Therefore, throughout this text, when we talk about the general class of beams

with phase singularity, we will call these beams radial-type (RT) and azimuth-type (AT) respectively. This is just a limited classification for the purposes of this work. For more extensive analysis of polarization singularities see the papers by Vyas et. al. [136] and Brown [137].

The phase relations in the optical parametric amplification. Optical parametric amplification is used in this work to obtain two optical vortices of opposite topological charges. Therefore, we analyze phase relations among the interacting waves. A certain phase difference between the optical vortices is important in order to obtain the desired output beam.

Assuming the full phase matching, a nearly lossless medium and the slowly-varying amplitude approximation the well-known coupled wave equations can be re-written in the following form [138] :

$$\frac{du_1}{d\zeta} = -u_3 u_2 \sin\Theta \ , \tag{3.6a}$$

$$\frac{du_2}{d\zeta} = -u_3 u_1 \sin\Theta \ , \tag{3.6b}$$

$$\frac{du_3}{d\zeta} = u_1 u_2 \sin\Theta \ , \tag{3.6c}$$

$$\frac{d\Theta}{d\zeta} = -K \cot\Theta \frac{d}{d\zeta} \ln\left(u_1 u_2 u_3\right) \ , \tag{3.6d}$$

where ζ is the normalized propagation distance, u_1, u_2 and u_3 are the absolute amplitudes of the signal, idler and pump waves, respectively, and Θ is the net phase, which can be expressed as

$$\Theta = \psi_3(\zeta) - \psi_2(\zeta) - \psi_1(\zeta) \ , \tag{3.7}$$

where $\psi_3(\zeta)$, $\psi_2(\zeta)$ and $\psi_1(\zeta)$ are the phases of the signal, idler and pump waves, respectively. The Eq. (3.6d) can be integrated [138] to show that:

$$u_1 u_2 u_3 \cos\Theta = \Gamma \tag{3.8}$$

where Γ is a constant. The relation in the Eq. (3.8) holds true during the parametric interaction for all values of ζ.

In the optical parametric amplification process, only the signal and pump waves are injected, while the idler wave is generated inside the crystal. Therefore, the initial condition for the idler wave is $u_2(0) = 0$. Inserting this into the Eq. (3.8), we can see that $\Gamma = 0$. Afterwards the amplification takes place and the idler wave appears, therefore $u_2(\zeta) > 0$ for values $\zeta > 0$. Then, for the Eq. (3.8) to hold true, it is required that $\cos\Theta = 0$. From this it follows, that

$$\Theta = \pm\frac{\pi}{2} \ . \tag{3.9}$$

The + or - sign in the Eq. (3.9) determines the energy transfer direction between the waves. In the optical parametric amplification, the energy transfer takes place from the pump to the signal and idler waves, therefore, the solution $\Theta = -\pi/2$ is appropriate for this case. From this solution and the Eq. (3.7), the phase of the idler wave can be expressed:

$$\psi_2(\zeta) = [\psi_3(\zeta) - \psi_1(\zeta)] + \frac{\pi}{2} \ . \tag{3.10}$$

The square brackets in the Eq. (3.10) emphasize that the idler's phase depends on the phase difference between the pump and the signal waves. Therefore, if a phase shift is introduced into either the signal or the pump wave, the idler's phase will change accordingly.

Let us discuss a particular case. The pump is a plane wave. Assuming a negligible pump depletion, we can consider that $\psi_3(\zeta) = \psi_{30} = const.$ The signal beam is an optical vortex with a topological charge l. If a constant phase shift $\Delta\psi_1$ is introduced to the signal wave, the phase of the signal wave will then be $\psi_1(z, \phi) = l\phi + \Delta\psi_1$. Inserting the pump's and signal's phases into the Eq. 3.10, the idler's phase can be obtained:

$$\psi_2(\zeta, \phi) = \psi_{30} - l\phi - \Delta\psi_1 + \frac{\pi}{2} \ . \tag{3.11}$$

The idler wave has the azimuthal phase modulation and its sign is opposite to that of the signal. In addition, as the signal's phase changes by a constant $\Delta\psi_1$, the idler's phase changes by $-\Delta\psi_1$. Therefore, the phase difference between the signal and idler waves can be controlled by changing the signal's phase. Alternatively, the phase shift could be introduced to the pump wave, while the signal's phase remained unchanged. As will be described in the experimental section, this phenomena will be used to obtain the desired phase difference between the signal and the idler waves at the output of the nonlinear crystal.

Transformation of the amplified beam by a quarter wave plate. After the optical parametric amplification we use a quarter wave plate to combine the amplified signal and idler optical vortices into the output beam with the desired polarization singularity.

First of all, the coordinate system has to be defined. We choose the left handed coordinate system and measure all the polarization and optical vortex wavefront handedness with respect to the source. In that case a polarization vector $\begin{bmatrix} 1 \\ i \end{bmatrix}$ will be left-handed and $\begin{bmatrix} 1 \\ -i \end{bmatrix}$ right-handed. Also, the wavefront of an optical vortex with topological charge $l > 0$ will be left-handed and with $l < 0$ will be right handed. Thus, we can see from Eqs. (3.2-3.5) that the wavefront of each optical vortex has a different handedness than its polarization vector.

With the coordinate system defined, we can now define the rotation transform.

The matrix of the counter-clockwise rotation transform by angle α around the z axis will be:

$$\widehat{T} = \begin{bmatrix} \cos\alpha & -\sin\alpha \\ \sin\alpha & \cos\alpha \end{bmatrix} . \tag{3.12}$$

This transform rotates a vector by angle α counter-clockwise. The inverse of this transform would naturally be the counter-clockwise rotation by $-\alpha$ (or, in other words, the clockwise rotation by α). Its matrix would be:

$$\widehat{T}^{-1} = \begin{bmatrix} \cos\alpha & \sin\alpha \\ -\sin\alpha & \cos\alpha \end{bmatrix} . \tag{3.13}$$

The Jones matrix of a simple quarter wave plate [139] would be:

$$\widehat{A} = \begin{bmatrix} 1 & 0 \\ 0 & i \end{bmatrix} . \tag{3.14}$$

If the quarter wave plate is rotated counter-clockwise by angle α, its matrix would be:

$$\widehat{Q} = \widehat{T}\widehat{A}\widehat{T}^{-1} = \begin{bmatrix} \cos^2\alpha + i\sin^2\alpha & \cos\alpha\sin\alpha(1-i) \\ \cos\alpha\sin\alpha(1-i) & i\sin^2\alpha + \cos^2\alpha \end{bmatrix} . \tag{3.15}$$

In the experiment a type-II nonlinear crystal is used for the optical parametric amplification. It produces two orthogonally polarized signal and idler optical vortices. The two optical vortices are then transformed by the quarter wave plate into the output beam with the desired polarization structure. We will now discuss two cases with different phase shifts between the signal and idler waves:

1) The phase shift between the signal and idler waves is $\pi/2$. In this case, assuming sufficiently large gain (so that the signal and idler waves will have approximately the same intensity), we can write the polarization vector of the outgoing beam:

$$\vec{v} = \begin{bmatrix} \exp(il\phi) \\ i\exp(-il\phi) \end{bmatrix} . \tag{3.16}$$

If a quarter wave plate, rotated by angle $\alpha = 45^o$ counter-clockwise is placed in the path of the beam, then $\cos\alpha = \sin\alpha = 1/\sqrt{2}$. Inserting this into the Eq. (3.15), the Jones matrix of such waveplate would be:

$$\widehat{A} = \begin{bmatrix} 1 & -i \\ -i & 1 \end{bmatrix} . \tag{3.17}$$

The normalization and phase factors have been dropped in Eq. (3.17). Multiplying the vector in Eq. 3.16 by the Jones matrix in Eq. (3.17) and

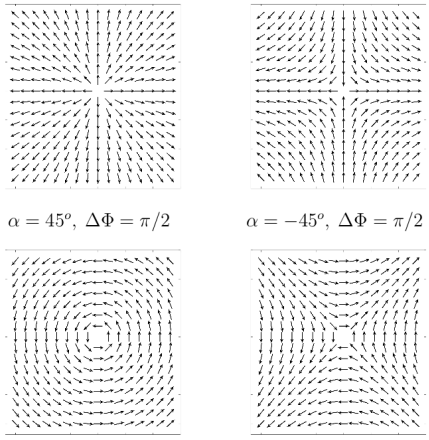

Figure 3.1: Possible polarizations of output beams width different orientations of the quarter wave plate (α) and phase shifts between the signal and the idler waves ($\Delta\Phi$) when $l = 1$. On the left the polarization of a radially (top-left) and azimuthally (bottom-left) polarized beam is shown. Polarization patterns shown on the right are obtained when the quarter wave plate is rotated to the opposite direction.

refactoring the expression, we can obtain the output polarization vector after the quarter wave plate:

$$\vec{w} = \begin{bmatrix} 1 & -i \\ -i & 1 \end{bmatrix} \begin{bmatrix} \exp(il\phi) \\ i\exp(-il\phi) \end{bmatrix} = 2 \begin{bmatrix} \cos(l\phi) \\ \sin(l\phi) \end{bmatrix} \ . \tag{3.18}$$

We can see that at the output of the quarter wave plate, a RT beam will be present. In the simplest case when $l = 1$ it will be a radially polarized beam.

Therefore, if there is a $\pi/2$ phase shift between the signal and idler waves, a quarter wave plate, rotated by 45^o counter-clockwise can transform the two orthogonally polarized optical vortices with opposite topological charges into a radially polarized beam (or any other RT beam, depending on the choice of the topological charge of the vortex). In the case when the signal is a unit-charged vortex ($l = 1$), the resulting beam is radially polarized as shown in the Fig. 3.1 (top-left).

2) Consider the same situation as in the case 1), except with the $-\pi/2$ phase shift between the signal and idler waves. Now the polarization vector of the combined signal-idler beam can be written:

$$\vec{v} = \begin{bmatrix} i\exp(il\phi) \\ \exp(-il\phi) \end{bmatrix} \ . \tag{3.19}$$

The quarter wave plate is also rotated by 45^o counter-clockwise. Following the same calculations, the result is obtained:

$$\vec{w} = \begin{bmatrix} 1 & -i \\ -i & 1 \end{bmatrix} \begin{bmatrix} i\exp(il\phi) \\ \exp(-il\phi) \end{bmatrix} = 2 \begin{bmatrix} -\sin(l\phi) \\ \cos(l\phi) \end{bmatrix} . \tag{3.20}$$

In this case, a beam of AT family is generated, which in the simplest case $l = 1$, reduces to an azimuthally polarized beam (Fig. 3.1, bottom-left).

If quarter wave plate is rotated clockwise instead of counter-clockwise, then $\alpha = -45^o$. In this case the result would be another type of polarization singularity which does not belong neither to RT nor to AT family (Fig. 3.1, top-right and bottom-right plots).

In an experiment, if a polarizer is put in the way of the output beam, a Hermite-Gaussian mode with two maxima will be observed. It will happen in both cases whether the quarter wave plate is rotated clockwise or counter-clockwise. The result of such an experiment might be ambiguous. To determine whether the quarter wave plate is oriented correctly, we have to rotate the polarizer. If the Hermite-Gaussian modes rotate in the same direction as the polarizer does, then a radially or azimuthally polarized beam is present at the output (Fig. 3.1 left images). If the Hermite-Gaussian mode rotates in the opposite direction, it indicates the presence of a phase singularity of another type (Fig. 3.1 right images).

3.3. Experimental

Experimental background. The basic idea of the proposed method is to obtain two optical vortices with opposite topological charges by means of the optical parametric amplification and to superimpose them by using a quarter wave plate. The pump beam carries no topological charge while the signal beam is an optical vortex. According to the law of the topological charge conservation [140], the idler wave will be formed with a topological charge opposite to that of the signal. Afterwards, with a properly oriented quarter wave plate, the combined signal-idler beam is converted to a radially or azimuthally polarized beam (in case of $l = 1$) or another beam of RT/AT type.

The conceptual design of the experiment is shown in the Fig. 3.2. The signal and pump waves are combined in a collinear fashion using the wavelength-selective mirror M. The signal wave is amplified in the nonlinear crystal (NLC in the Fig. 3.2). The optical parametric amplification has to take place in a type II nonlinear crystal so that the polarizations of the signal and idler beams are perpendicular. In addition, the wavelengths of the signal and idler beams have to coincide (the parametric interaction is degenerate with respect to the wavelength). The initial phase of the signal beam (or alternatively the pump

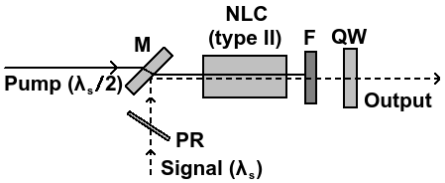

Figure 3.2: The conceptual experimental setup : M - a wavelength-selective mirror, PR - phase retarder (for example a thin glass plate which can be rotated to adjust the initial phase of the signal beam), NLC - nonlinear crystal (type II), F - filter, which filters out the pump beam and QW - the quarter wave plate. The pump beam is purely Gaussian and the signal beam is an optical vortex. The output is a beam with a polarization singularity.

beam) is controlled by a phase retarder PR which in a simplest case can be a glass plate which can be rotated to change the optical path of the passing beam or, alternatively, could be a mirror mounted on a piezoelectric translation stage. A $\pi/2$ phase difference between the signal and idler waves has to be achieved at the output of the crystal by controlling the angle of the phase retarder. After the crystal, the wavelength-selective filter F absorbs all the remaining pump beam. Then, a properly oriented quarter wave plate turns this composite signal-idler beam into a beam with a polarization singularity.

Key points in the experimental design.

- The phase difference between the signal and idler beams at the output of the crystal has to be $\pi/2$ for RT beams or $-\pi/2$ for AT beams.
- The beams have to be properly collimated. In the optical parametric amplification process, the phase conjugation takes place, therefore the wavefront has to be as flat as possible. Otherwise, if the signal beam's wavefront is concave, the idler's wavefront will be convex and vice versa. This can cause distortions of the output beam.
- The influence of the walk-off has to be diminished. For that purpose, a nonlinear crystal with critical phase matching can be chosen and the beam diameter has to be chosen sufficiently large.
- Gain should be sufficiently high. The energies of the output signal and idler beams will be different by the amount of the initial signal's energy. Therefore, if the gain is sufficiently high, this difference will be diminished.

Experimental setup. Fig. 3.3 shows the realization of the proposed experimental design. The input beam was generated by a Nd:YAG laser with the pulse duration of 50 ps at 1 kHz repetition rate. The input beam was collimated, linearly polarized and had a diameter of 2.175 mm at $1/e$ level. Then the beam

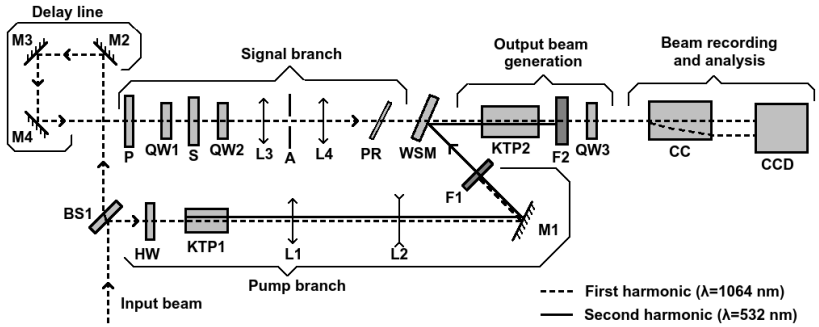

Figure 3.3: The experimental setup. BS1 - a beam splitter, P - a polarizer, M1-M4 - mirrors, HW - a half wave plate, QW1-QW3 - quarter wave plates, L1-L4 - lenses, S - a S-waveplate, PR - the phase retarder, KTP1, KTP2 - nonlinear crystals, A - an aperture, WSM - a wavelength-selective mirror, F1, F2 - filters, CC - a birefringent calcite crystal, CCD - a CCD camera.

was split into two branches by the beam splitter BS1: one to generate the pump beam (the pump branch) and one to generate the signal beam (signal branch).

In the pump branch, the $\lambda/2$ waveplate HW was used to correct the polarization direction and the second harmonic was generated in the nonlinear crystal KTP1. Lens L1 and L2 were then used to collimate the beam. The filter F1 filtered out the remains of the first harmonic beam. The second harmonic beam was used as the pump beam in the output beam generation stage.

The purpose of the signal branch is to convert the first harmonic beam to an optical vortex, which was used as the signal part in the output beam generation stage. Mirrors M2, M3, and M4 constitute a delay line to compensate the optical path differences between the signal and the pump beams. The polarizer P was used to correct any depolarization, resulting from reflections in the delay line. The system QW1-S-QW2, consisting of two $\lambda/4$ waveplates QW1 and QW2 and an S-waveplate, was used to convert the signal beam to a vortex of unit topological charge. The $\lambda/4$ waveplate QW1 was used to produce a circularly polarized beam while the S-waveplate converted it to an optical vortex [71]. Afterwards QW2 converted the optical vortex back into the linear polarization. The beam vortex was then collimated using the lens L3 and L4 and an aperture A was placed between them in order to filter out unwanted beam distortions. The phase retarder PR was then used to correct the phase of the signal beam.

Both pump and signal beams were combined by the wavelength-selective mirror WSM. The parametric amplification took place in the nonlinear crystal KTP2, producing the two oppositely-charged signal and idler vortex beams. The filter F2 then filtered off the remains of the pump beam and the signal and idler beams were converted to the output beam with a polarization singularity by the $\lambda/4$ waveplate QW3, as discussed in previous sections.

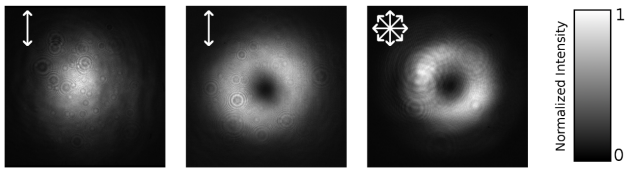

Figure 3.4: The intensity patterns of the initial pump beam (a), signal beam (b), the output beam (c), and color map of the normalized intensity (d). The polarization states of the beams are indicated by the arrows. The pump beam is a Gaussian beam, while the initial signal beam carries a topological charge of $l = 1$. The output beam is radially polarized. The powers of the pump, signal and the output beams are 0.9W, 0.55 mW and 290 mW respectively with the pulse duration of 50 ps.

The output beam's profile was recorded with the CCD camera. The polarization structure was analyzed using a birefringent calcite crystal (CC in the schematic), which separates the two orthogonal polarizations of the beam. The polarization structure of the beam was determined from the spatial distribution of the polarization components.

Experimental results. The recorded intensity profiles of the beams are shown in the Fig. 3.4. Their polarization states are given by the small arrows in the top-left corner of the images. Fig. 3.4(a) shows the intensity profile of the Gaussian pump beam. The signal beam, shown in the Fig. 3.4(b) is an optical vortex with a unit topological charge. It was formed using a S-waveplate from a circularly polarized Gaussian beam [71]. The resulting radially polarized beam is shown in the Fig. 3.4(c). The powers of the pump, signal and the radially polarized output beam were 0.9W, 0.55 mW and 290 mW respectively with the pulse duration of 50 ps.

Analysis of the output beam was carried out using the calcite crystal. The intensity profiles of the separated polarization components are depicted in the Fig. 3.5 with the small arrows indicating the polarization direction. Fig. 3.5(a) shows the observed polarization components of the radially polarized beam. The vertical polarization component (Fig. 3.5(a) upper image) has two maxima, situated vertically with respect to each other, while the horizontal polarization component (Fig. 3.5(a) lower image) has two horizontally situated maxima. The radial polarization was verified by rotating the calcite crystal (Fig. 3.6).

In addition, an azimuthally polarized beam was obtained by changing the phase between the signal and idler beams using the phase retarder PR. Its analyzed mode structure is depicted in the Fig.3.5(b). The vertical polarization component (Fig. 3.5(b) upper image) now has two horizontally situated maxima while the horizontal polarization component has (Fig. 3.5(b) lower image) has the vertically situated maxima.

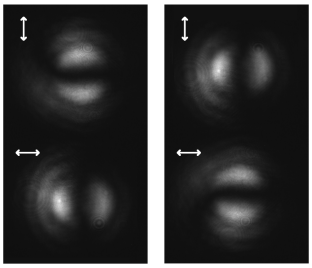

Figure 3.5: The vertical (top) and the horizontal (bottom) polarization components of a radially (a) and azimuthally (b) polarized beams after the calcite crystal. The polarization states are indicated by the arrows. The color map is the same as in the Fig. 3.4 (d).

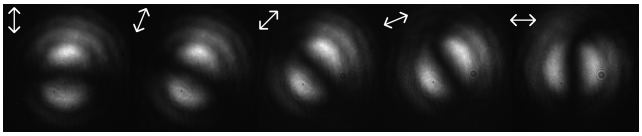

Figure 3.6: Observed patterns of one of the polarization components of the radially polarized beam as the calcite crystal was rotated. The polarization state is indicated by the white arrows. The color map is the same as in the Fig. 3.4 (d).

Another important point in this experiment is the amplification gain. The previously shown results were obtained at the gain of about 500 times. At the gain value of about 30, the periphery of the beam does not get correct polarization and side lobes were observed (Fig. 3.7).

Possible extensions of the method. So far we have shown that using this method, cylindrical vector beams which are a superposition of optical vortices with opposite topological charges can be produced. However, if the topological charge of the pump beam was chosen not equal to zero, then the idler wave would be formed in accordance to the topological charge conservation law [140] :

$$l_p = l_s + l_i \ , \tag{3.21}$$

where l_p, l_s, l_i are the topological charges of the pump, signal, and idler waves respectively.

Manipulation of topological charges of pump and signal waves allows the creation of other types of beams with polarization singularities, which are discussed elsewhere. Such beams have also been obtained using a spatial light modulator by Ching-Han Yang et. al. [72].

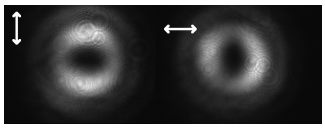

Figure 3.7: The vertical (left) and horizontal (right) polarization components of the output beam at low gain of about 30 times. The arrows indicate the polarization states of the beams. The proper Hermite-Gaussian modes were not obtained. The side lobes are visible at the periphery of the beam. The color map is the same as in the Fig. 3.4 (d).

The proposed method could be easily automated. For example, instead of a thin glass plate, a mirror mounted on piezoelectric translation stage can be used to control the phase of the signal or pump beam allowing easy switching between the radially and azimuthally polarized beam. In addition, a spatial light modulator could be used to modulate the initial signal beam and provide an easy way to obtain beams with polarization singularities of higher orders. While it is possible to obtain beams with polarization singularities by a spatial light modulator directly, the proposed method utilizes the optical parametric amplification, thus allowing creation of higher power beams than could be obtained using a spatial light modulator directly. In combination with automation possibilities this method could find applications in optical trapping of particles.

3.4. Conclusions to Chapter 3

We have shown a new technique to generate optical beams with polarization singularities by optical parametric amplification of an optical vortex and subsequent beam conversion by a quarter wave plate. Since this technique employs the optical parametric amplification, it does not require a powerful initial signal beam. It can produce a powerful output beam while using simple methods to obtain the initial signal beam such as a printed vortex hologram or a spatial light modulator, which would normally be limited by the optical damage threshold if used to obtain the desired output beams directly.

In addition to this, the proposed method can be easily automated. If a spatial light modulator is used to modulate the initial signal beam, it can provide an easy computer-controlled way of switching between the modes of the beam. In combination with increased power output, this method could find applications in optical trapping of particles and other applications such as nonlinear optics research and laser material processing.

However, in this Chapter we have demonstrated only the basic idea and discussed the underlying physical principles of the method. More research is

needed to determine the influence of dispersion and group velocity mismatch for ultrashort pulses and how it affects the quality of the resulting beam. In our case, we used 50 ps pulses in the KTP crystal. The dispersion length was of the order of several kilometers, therefore the second and higher order dispersion effects were negligible. In addition, some phenomena that are characteristic of ultrashort pulse amplification might be utilized in this method, such as the spatial capture (also called "trapping") of the amplified waves under the pump wave packet [141–143] or the giant subharmonic pulse generation [144].

4. A versatile modular system for optical manipulation experiments

This chapter is based on the [A3], [A6], [B1], and [B2] publications.

4.1. Introduction

Up to this end possibilities of generation of vortex and radially polarized beams were discussed. In this Chapter, application of a vortex beam in optical levitation (in the wider context of cloud physics), is demonstrated. Further, in the introduction, general description of optical levitation is given. Following section 4.2 outlines limitations of the performed research, sections 4.3 and 4.4 give general introduction to the problem and propose possible direction to solve this problem. Finally, section 4.5 demonstrates how optical vortex beams can facilitate the proposed solution.

In optical levitation, upward forces produced by radiation pressure of a laser beam counteracts the downward force of gravity to create a stable trap just above the focus of the laser beam. The technique was invented by Ashkin [145]. It predates the invention of the single beam gradient trap [146], a technique which has found wide applications in biology [147], soft matter physics [148] and atom optics [149]. Optical levitation, although less commonly used due to higher power demand on the input beam, has several advantages. First, the target could be trapped in gaseous environment, for example in air. Second, the target could be trapped at large distances from the trapping lens, typically at length scales of a few centimeters and larger. This allows an almost 4π access to the trapped particle which can be used to simultaneously implement different methods for analysis and manipulation. Third, the large trapping distance makes any wall effects on the trapped target negligible. The technique has, for instance, been used in in-vacuo high energy laser interaction experiments [150], the study of dynamics of many-body systems [151] and in the measurement of evaporation rate of supercooled water droplets [152].

The long term goal of this direction is to create a system where interactions of droplets with the surrounding media or with other droplets can be studied with full control of all physical parameters. In the following sections we review forces in optical trapping, introduce a versatile modular system which can be used to study a variety of physical phenomena. And demonstrate a few examples of such studies, with an emphasize of application of an optical vortex beam.

4.2. Forces in optical trapping

> Concerning radiation pressure forces: "A very short experience in attempting to measure these forces is sufficient to make one realize their extreme minuteness – a minuteness which appears to put them beyond consideration in terrestrial affairs . . . "
>
> *J. H. Poynting, 1905*

The study of radiation pressure in 1900th was considered exciting but not practical. With invention of lasers the situation has changed. High degree of spatial coherence allows tight (at the order of wavelength) focusing of a laser beam and dramatic increase of intensity. Consider following simple estimation. CW green laser light with $P = 1$ W is focused down to $d_0 \approx (1 \div 10)\lambda$. Mirror bead with the radius of $a \approx d_0$ is placed in the focus of the beam. Then, the force of light pressure is $F = 2P/c_0 \approx 10^{-8}$ N. Suppose density of the bead is $\rho = 1$ g/cm^3 and $d_0 \approx \lambda$, then its mass $m \approx 10^{-16}$ kg. Acceleration acquired by the bead due to the light pressure takes huge value $acc = F/m \approx 10^7 g$. Although light pressure is not the main trapping mechanisms, this estimation demonstrates that optical forces of focused laser light are significant and optical manipulation is possible in principle.

Depending on size and chemical composure of particles to be optically trapped and manipulated absolutely different mechanisms of optical trapping and rotation apply. Fig. 4.1 summarizes these mechanisms. Below their description is provided.

Depending on size of trapped particles two extreme regimes are considered in the theory of optical trapping, namely, Rayleigh and geometrical optics regimes. The Rayleigh regime is usually valid for beads for which the radius a is much smaller than the laser wavelength [153–155]. The geometrical optics regime is usually valid for beads for which the radius a is much larger than the laser wavelength λ. Mie–Debye spherical aberration theory of optical tweezers consistently covers all regimes from the Rayleigh limit up to the geometrical

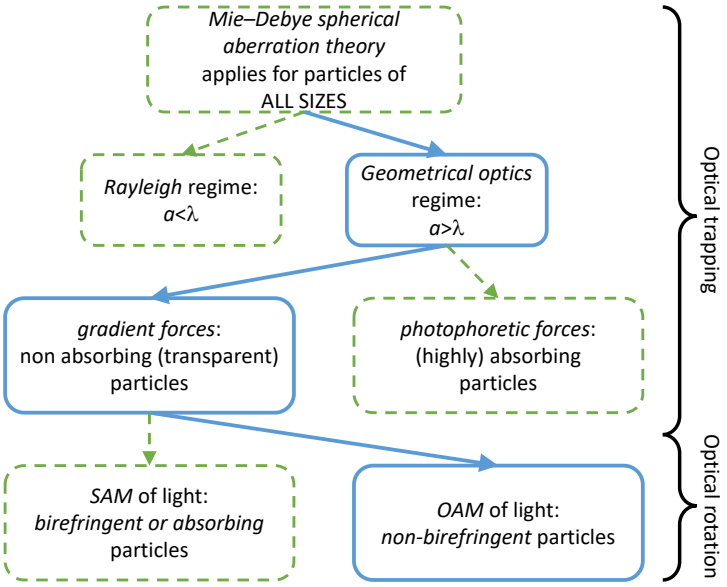

Figure 4.1: Summary of physical mechanisms responsible for optical trapping and rotation of microparticles. a is particle radius, λ is wavelength of trapping light. SAM and OAM stand for spin and orbital angular momentum of light, respectively. Regimes with solid (dashed) frames are (not) considered in this dissertation. See text for details.

optics limit [156, 157].

Optical trapping. In this dissertation, we work only in the geometrical optics regime. Based on physical mechanisms responsible for optical trapping, particles used in experiments can be divided into two main categories: non absorbing (transparent) and highly absorbing particles.

Non absorbing (transparent) particles. The force of radiation pressure estimated at the beginning of this section, results from reflection of the light from object's surface and cannot explain optical trapping. This is because its effect is to push the object in the direction of the incident beam. To understand how a laser beam traps an object, we must consider gradient forces. As conveniently described in [155], gradient forces are related to the beam's refraction at the object's surface. Figure 4.2(a) shows a bead slightly shifted from the center of the laser beam. The trapping beam has a Gaussian intensity profile before the focusing objective. Two rays from the beam refracting at the microsphere's surface are shown. Ray 1, with the wave vector $\boldsymbol{k}_1$, originates from the central part of the beam.This ray generates a force $\mathbf{F}_1$ on the microsphere upon refraction. Ray 2, with the wave vector $\boldsymbol{k}_2$, originates from the right side of the beam. It generates a force $\mathbf{F}_2$ on the microsphere. Note that $|\mathbf{F}_1| > |\mathbf{F}_2|$ because the intensity profile has a Gaussian shape. Therefore, the resulting force on the bead points toward the laser focus. In other words,

because the wave vector $\boldsymbol{k}$ of each ray changes during refraction, its momentum also changes. Therefore, an object in the beam also experiences a momentum change. However, in the opposite direction to that of the beam, because of momentum conservation of the combined system beam-object. This fact implies that a force acting on the object changes its momentum. Figure 4.2(b) shows another situation in which the bead is above the objective focus. Observe that the resulting force also points toward the focus in this situation. It is easy to see that the force acting on a bead in the laser beam always points toward the focus for any position of the microsphere relative to the focus. Described above situation explains optical trapping in geometrical optics regime if the refractive index of the object is bigger than the refractive index of surrounding medium, $n_{obj} > n_{med}$. If the refractive index of object is smaller than that of a surrounding medium, $n_{obj} < n_{med}$, the object will be pushed away from the area of maximum intensity, i.e focal area.

Absorbing particles. Absolutely different mechanism is responsible for optical trapping of absorbing particles [158, 159]. It is based on thermal forces. Although stochastic thermal forces does not allowed for stable trapping of absorbing particles in gases using conventional (Gaussian) beam profile. This is because absorbing particle is being pushed away from the area of maximum intensity. However, such particles can be stably trapped in minima of intensity of the beam, for example in the center of the optical vortex beam. In a gaseous medium optical trapping of absorbing particles complicates by the thermal interaction of the particle with the medium. The forces of thermal transpiration or thermal diffusion can be much stronger than the optical forces. It is possible to create the situation when the forces of thermal diffusion become the main mechanism of optical trapping. In this case, energy of the laser radiation is absorbed only by the object placed in optically transparent medium (e.g. gas). This leads to local increase of average kinetic energy of object's molecules. Hence, occurs rise of momentum, which is being transferred to the molecules of the surrounding gaseous medium. Gradient of pressure in the medium pushes particle to the region of minimum pressure. Such thermal forces are called photophoretic forces. If particle is surrounded by evenly distributed laser radiation, then the particle will be stably trapped by photophoretic forces based on heat transfer from absorbing particle to the surrounding gas, when the thermodynamic equilibrium is reached. Beams with optical vortices (e.g. optical bottle beam or two counter-propagating optical vortex beams) can create above described necessary conditions.

Optical rotation. Physical mechanisms responsible for optical rotation of microparticles are different for birefringent and non-birefringent particles. In general, any particle can be optically rotated by a rotating wavefront of a beam, e.g. upon interference [160]. Other mechanisms of optical rotation exploit angular momentum (AM) of light, which consists of spin angular momentum

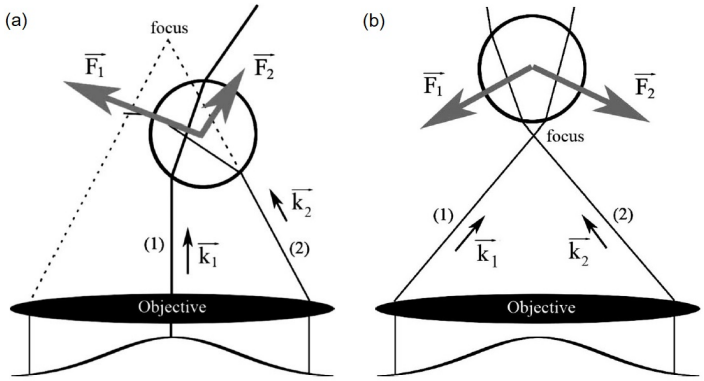

Figure 4.2: (a) Two rays (wave vectors $\boldsymbol{k}_1$ and $\boldsymbol{k}_2$) from the beam are represented. The rays exert forces $\mathbf{F}_1$ and $\mathbf{F}_2$ when refracted on the bead surface. The resulting gradient force points to the laser focus. (a) A bead localized below the focus; (b) a bead localized above the focus.

(SAM) and orbital angular momentum (OAM) parts [161].

Non-birefringent microparticles. It is possible to optically rotate non-absorbing, transparent and isotropic particles using OAM of light [162–165], as first shown by Volke-Sepulveda et al using transparent silica beads in liquid [162] and by McGloin et al using water aerosol droplets in air [163]. Intensity profile of a beam caring OAM is ring or doughnut shaped in the transverse plane and can be described by e.g. non-zero order Laguerre-Gaussian and Bessel-Gaussian vortex beam. Transparent, non-birefringent microparticle can be trapped in the ring of maximum beam intensity. The phase front of optical vortex beam is helically varying around beam's axis upon propagation. Due to this helical variation its Poynting vector is tilted with respect to the beam's axis with local angle given by $\theta_{screw} = l/kr$, where k - is the wavenumber and l is topological charge of OV [166]. This tilt give rise to the OAM of a beam, which imparts a tangential force on trapped droplet (which is not restricted azimuthally due to the cylindrical symmetry of the intensity distribution) making droplet to orbit around beam's axis. The torque is proportional to $l\hbar$ per photon. The direction of rotation is determined by the handedness of the helical phase front, i.e. by the sign of topological charge $\pm l$. Due to the describes geometry of a trapping beam it is possible to optically rotate particles of any composition, including non-birefringent and non-absorbing droplets. However, the particle exhibit only orbital motion drawing circular trajectory around the center of a beam.

Birefringent microparticles. In the case of non-absorbing birefringent particles [167, 168], particles trapped on the beam axis can be set to rotate by transferring SAM by a mechanism first observed by Beth in 1936 [169], when he reported a tiny torque developed in a quartz 'wave-plate' owing to the change in polarization of transmitted light. Depending on the polarization of the incident

beam, the particles either become aligned with the plane of polarization (and thus can be rotated through specified angles) or spin with constant rotation frequency. The torque is proportional to $\sigma\hbar$ per photon, where $\sigma = \pm 1$ for left (right) circularly polarized light, respectively.

Absorbing (non-transparent) microparticles. For absorbing particles [168, 170, 171], both spin and orbital angular momenta are transferred with the same efficiency so that the applied torque is proportional to the total angular momentum, that is $(l - \sigma)\hbar$ per photon.

It is possible to gradually control AM experienced by a microparticle. In the beams with coupled spin-angular momentum, total angular momentum per photon is given by AM $= (l - \sigma)\hbar$, where its orbital part is represented by OAM $= l\hbar$ and its spin part by SAM $= \sigma\hbar$, where $\sigma = \pm 1$, for left/right circularly polarized beam, respectively (note, that the conventional way of writing AM is $(l + \sigma)\hbar$, with $\sigma = \mp 1$) [161]. For example, total torque experienced by a particle trapped by an OV beam with $l = +1$ is proportional to total AM $= 0\hbar$ per photon for the case of left circular polarization (i.e. particle is stopped) and to AM $= 2\hbar$ per photon (i.e. maximum rotation rate) for the case of right circular polarization. Elliptical polarization would give intermediate rotation rates.

4.3. A modular system for optical levitation experiments

In this section, an overview of the modular system used for optical levitation of droplets in air is given. Glycerol droplets are levitated using a laser beam focused at a point inside a rectangular aluminium chamber that isolates the droplets from external laboratory air. Figure 4.3 shows the setup schematically. On each side of the chamber windows, lenses and various optical components can be mounted. A droplet-on-demand dispenser produces droplets that descend in still air into the trap. The dispenser nozzle can be equipped with an electrode in order to vary the amount of charges of the droplets. A borosilicate convex lens is positioned below the chamber at a position such that the droplets are trapped in the center of the chamber. Two different lasers have been used for the experiments described in this section: (i) A diode pumped solid-state (DPSS) continuous-wave (cw) laser with a wavelength of 532 nm. It has an RMS stability of 5% and a divergence of 2.5 mRad. (ii) A 660 nm DPSS cw laser with an RMS stability of less than 1.0% and a divergence of less than 1.5 mRad. The power of both lasers can be controlled with a PID feedback system in order to stabilize the vertical position of a trapped droplet.

The trapped droplet can be observed through any of the four access ports on the chamber walls. The position of the droplet can be measured with high

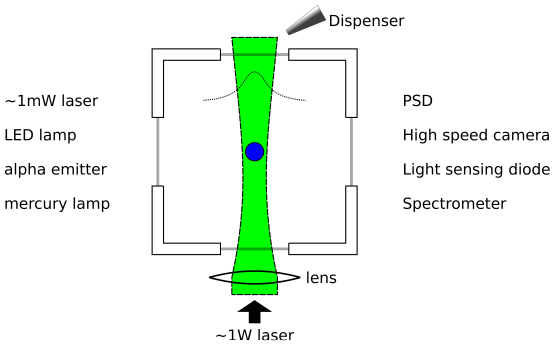

Figure 4.3: A schematic of the modular experimental system. Droplets are injected by a dispenser into a cage where they are trapped in a position slightly above the focus point of the laser beam. The dotted line shows the radial intensity distribution of the laser that has mostly been used (Gaussian) but for trapping in optical vortices a Laguerre-Gaussian beam profile was utilized. A large number of analysis and manipulation devices can be attached to the setup. Some examples of such devices are listed in the figure.

precision by focusing the light scattered by the droplet onto a Position Sensitive Detector (PSD). The scattered light can also be directed into a spectrometer. The size of the droplet can be measured directly with a camera equipped with a telescope or by directing a low power laser at the droplet and imaging the diffraction pattern created on a remote screen. The charge of the droplet can be determined by recording the motion of the droplet in free fall between two large capacitor plates. Alternatively, the displacement of a trapped droplet when a electric field is applied in the vertical direction. High speed cameras are used to image the motion of the droplets and the process when two droplets coalesce. The charge of the trapped droplet can be varied by directing α-radiation or UV-light towards the droplet. The system is modular. Instruments can therefore be conveniently attached to the system to study different properties of the droplets. In one version, the chamber is made such that it can be hermetically sealed, and hence evacuated. This could be used for studies of droplet properties at low air pressures or by using other gases.

Examples of possible experimental investigations include but not limited to:

i **Charged droplets** constitute an interesting physical system frequently occurring in nature. Clouds, for instance, usually carry a net charge [172] and properties like surface tension can be changed by charging [173, 174]. The question is whether the charge of the droplets affects physical processes such as droplet growth rate in clouds. In order to study the effect of charge on droplet collisions and coalescence, the possibility to control the charge of the droplets by applying an electric field over the nozzle used to produce the droplets was investigated [B1].

ii **(Time-resolved) spectroscopy**. Another example is the Raman spectroscopy of an optically levitated droplet with aim to determine the structural correlation function, i.e. to observe a character of accumulation of disorder in non-crystalline solids. Or time resolved spectroscopy of coalescing droplets containing fluorescent dyes to precisely determine time when two droplets begin molecules exchange [B1, B2].

iii **Time-resolved** observation of **elastic scattering** of trapping light to determine time of coalescence of droplets [B2].

iv **Collisional dynamics of micron-sized droplets under gravity**. The collision efficiency, defined as the ratio of the collision cross-section to the geometric cross-section, is a dimensionless measure of the probability of collision. In addition to determining the droplet growth rates (see e.g. [175]), the collision efficiency is a key ingredient in the collision theory of cloud droplets widely used in many weather and climate models [176, 177]. The collision efficiency is the most uncertain aspect of collision rate theories [177]. Experimental determination of the collision efficiency remains elusive [175, 178–182], although recent studies have yielded some empirical conclusions [183].

v **Rotating and spinning droplets**. Rotating droplets could be achieved for the previously mentioned study of collisional dynamics of liquid droplets (iv) in studies of raindrop formation [44]. Progress in study of rotational dynamics of spinning droplets will advance our understanding of the strong interactions between turbulence and the microphysical processes in clouds [184].

In the following sections we give details of (iv) and (v) examples. For further details and other possibilities the reader is referred to publications [A3, A6, B1, and B2].

4.4. Optical manipulation for studies of collisional dynamics of micron-sized droplets under gravity

As mentioned above, the collision efficiency is a key ingredient in the study of cloud droplets growth. How the droplet in clouds grow from the sizes ($<5\ \mu m$), when condensation of water vapour is effective, to the sizes ($>100\ \mu m$) for collision cascade to be effective growth mechanism? Theoretically predicted time scale of droplets growth (of sizes in the transitional region: 10 - 90 μm) is not relevant to that observed empirically. This discreancy of the theory and experimental observations is called "bottleneck problem" [185, 186].

For example, Hopkins *et al.* [187] used optical tweezers to observe the coagulation of aerosol droplets, and they determined the droplet growth rates

using cavity-enhanced Raman spectroscopy (CERS) with nanometer precision. Power *et al.* [188] used a single-beam gradient-force optical trap to coalesce droplets of 2 μm to 12 μm in diameter and observed the elastically scattered light from the trapped particles to investigate the time-resolved dynamics of mixing. Horstmann *et al.* [189] constructed a single-aerosol particle trap and coupled it to a conventional optical tweezers to guide and coalesce droplets of 500 nm to 19 μm in diameter. In all of the above studies, optical tweezers provide a fully controllable and convenient way to investigate droplet collisions. However, the light field interacts with the trapped droplets and modifies their dynamics. The work presented in this dissertation demonstrates a new method of optical manipulation technique that circumvents this problem. The method allows us to precisely image droplet collisions in free fall.

4.4.1. Experimental background

We trap two glycerol droplets of different sizes in air by means of two pairs of focused counter-propagating beams (Fig. 4.4). Two microscope objectives MO1 and MO2 focus light from two counter-propagating beams to a common focal point, forming the lower trap for the small glycerol droplet. Similarly, the microscope objectives MO3 and MO4 focus light from two laser beams to a second point, forming the upper trap for the large glycerol droplet. The two traps are vertically separated. By switching off the laser beams with the appropriate timing, the droplets fall under the influence of gravity and may collide at a predictable distance below the lower trap. The droplet motion is captured by two high-speed digital video cameras arranged in a horizontal plane. Their lines of sight intersect at an angle of 90°.

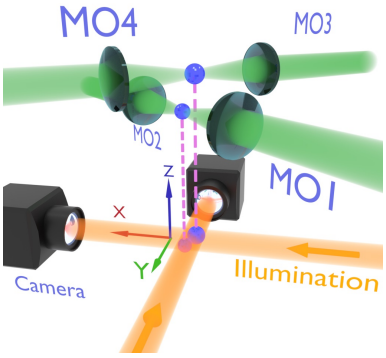

Figure 4.4: The principle scheme for studies of droplet interactions. MO1, MO2 and MO3, MO4 are microscope objectives that focus the laser light and form the "lower" and "upper" optical trap, respectively. The droplets are illuminated with LEDs, and their motion recorded by a pair of cameras with their lines of sight arranged at a 90° angle.

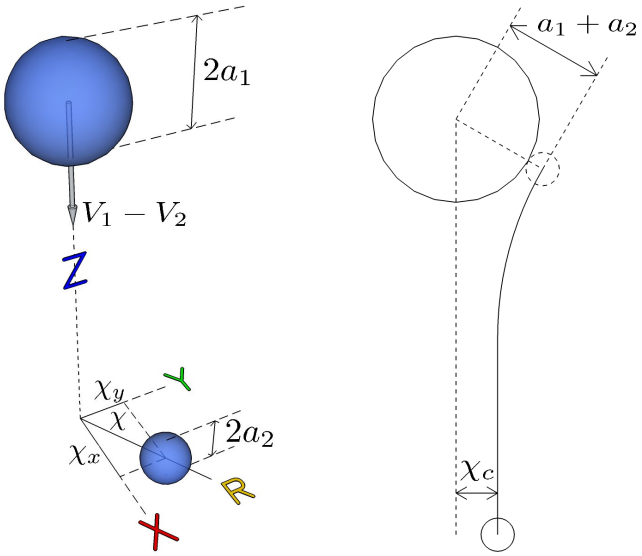

Figure 4.5: Panel (a) shows the geometry for the determination of the impact parameter, χ, of the collision process from its two orthogonal projections on x and y-axes. Two droplets with radii a_1 (top) and a_2 (bottom) fall in gravitational field, along the z-axis. The parameters χ_x and χ_y are the projections of the impact parameter χ onto the x and y-axes, respectively. Panel (b) shows the trajectory of the interacting droplets under gravity, as observed from the reference frame of the larger droplet. χ_c is the critical impact parameter for a grazing trajectory of the smaller droplet.

The geometry of the collision process is described in Fig. 4.5. A droplet with radius a_1 is positioned above a second droplet with radius a_2, where $a_1 > a_2$. The impact parameter, χ, is the projection of the distance between the centers of the two droplets perpendicular to their initial relative velocity, $V_1 - V_2$. The projections of the impact parameter onto the x-z and y-z planes yield χ_x and χ_y, respectively, and they are related by the equation

$$\chi = \sqrt{\chi_x^2 + \chi_y^2}\,. \tag{4.1}$$

In the experiment, we control the droplet impact parameter χ by adjusting the relative horizontal position between the two traps. At a critical impact parameter, χ_c, a grazing trajectory results, as depicted in Fig. 4.5(b). The collision efficiency is defined as $E = \chi_c^2/(a_1+a_2)^2$. The geometrical arrangement of the droplets is described by the dimensionless impact number, defined as [190]

$$\mathrm{B} = \frac{\chi}{a_2\,(1+\Gamma)}\,, \tag{4.2}$$

where χ is the impact parameter defined in equation (4.1), a_2 is the radius of

the small droplet and $\Gamma = a_1/a_2$ is the size ratio. Thus, values of 0 or 1 for the impact number designate head-on or grazing collisions, respectively.

The droplet physical and kinematic parameters investigated in this work are summarized in table 4.1. For calculation of these parameters the reader is referred to the publication [A4].

Table 4.1: The droplet physical characteristics and the collision parameters in the experiments.

Experimental section	4.4.3.1		4.4.3.2		4.4.3.3	
Diameter, $2a$ (μm)	31.9	40.0	29.9	37.9	29.9	33.9
Terminal velocity, V (cm s^{-1})	3.55	5.58	3.12	5.01	3.12	4.01
Reynolds number, Re	0.04	0.07	0.03	0.06	0.03	0.04
Stokes number, St	8.0	15.9	6.6	13.5	6.6	9.7
Diameter ratio, Γ	1.25		1.27		1.13	
Impact number, B	0.51		0.50		0.14	
Weber number, We	2.6×10^{-4}		2.1×10^{-4}		4.7×10^{-5}	

4.4.2. The experiment

Optics and imaging system. A sketch of the experimental setup is shown in Fig. 4.6. A laser beam generated by a solid state laser (Laser quantum "gem532", 532 nm, 2 W maximum power) passes through a beam splitter (BS) to form two optical traps at different heights, which we named the "upper" and "lower" trap. The transmitted beam that is collinear to the incident beam is used to form the "lower" trap. This beam is split a second time by a polarizing beam splitter PBS1. A micro-lens (MO) with focal length 5 mm focuses each beam such that the foci of the two counter-propagating beams overlap. The combined trapping power from the two beams is approximately 350 mW. In a similar manner, the reflected beam from BS is used to create the "upper" trap, which is positioned approximately 2 mm above the lower trap. Two half wave plates (HW1 and HW2) and the polarizing beam splitters ensure that the counter propagating beams have orthogonal polarization states, thus eliminating undesirable interference at the focal points. Two electro-optical amplitude modulators (EOM1 and EOM2) and two polarizers (P1 and P2) allow us to control the timing of the release of the droplets. The region where

the droplets interact is illuminated by two collimated cold white light LED (Thorlabs MCWHL5) operated at 10% of the maximum power. Shadow images are observed by two perpendicularly mounted high speed cameras (Phantom Miro LAB310). In order to minimize heating by the LED the illumination is pulsed synchronously with the droplet collisions. The cameras are equipped with Infinity Model K2 DistaMax Long-Distance Microscope System set to 5×-30× magnification with a mean working distance of 13 cm. Laser light from the trapped droplets is blocked by a notch filter (Thorlabs NF533-17), so that the cameras see only shadow images of the droplets with a bright Poisson (Arago) spot in the center.

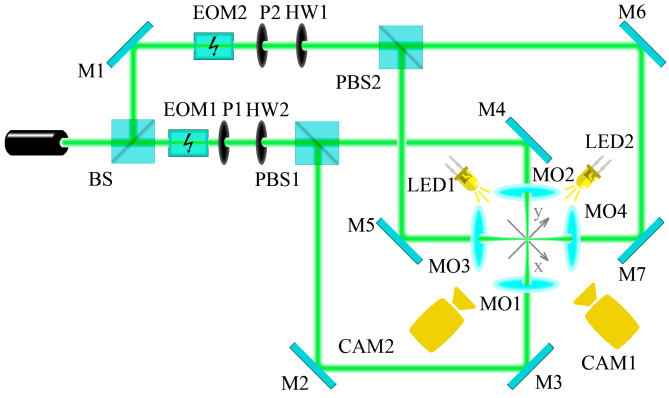

Figure 4.6: Sketch of the experimental setup. BS - beam splitter, EOM - electro-optical modulators, M - mirrors, P - polarizers, HW - half-wave plates, PBS - polarizing beam splitters, MO - micro-lenses, LED - illumination, CAM - high speed digital movie camera. The x-y coordinate system represents the laboratory frame. The z-axis points out of the page, whereas gravity points into the page.

Droplet generation and size control. We generate droplets in the size range from 4 to 60 μm in diameter using a commercial printer cartridge (Hewlett-Packard C6614). The cartridge works as a drop-on-demand system, where a droplet is ejected each time a TTL pulse is sent to the cartridge from a pulse generator (see [191] and [192] and references within for the droplet generation technique). The cartridge, washed and filled with a solution mixed with 90% (by volume) of distilled water and 10% of glycerol (produced by Fisher Scientific with a purity of 99.6%), produces droplets with a uniform diameter of approximately 22 μm. The water evaporates rapidly as the droplet descends down towards the trap. Hence, the size of the trapped droplet can be controlled by changing the mixing ratio of glycerol solution. As an example, a solution containing 5% of glycerol in water yields droplets of approximately 11 μm in diameter after the water has completely evaporated away. Alternatively, the

droplet can be made larger by allowing two drops to coalesce in the trap. The size of the largest droplet that can be levitated is determined by the laser beam waist and the available laser power. For the results presented in this work, the droplet size distribution is in the range from 29.9 to 40.0 μm in diameter.

The droplet chamber. An important part of the setup is the chamber for delivery, trapping and interaction of droplets. Air current within the chamber easily affects the droplet motion. In order to shield the droplets from air turbulence, the cartridge and micro-lenses are mounted in an enclosed chamber. The chamber is made out of metal and cover glass plates connected by flexible construction sealant (Sikaflex 291i). The flexible connection allows the movement of the micro-lenses to be decoupled from the metal plates of the chamber. Hence, the position of the optical traps can be independently adjusted without breaking the seal. Droplets descend from the cartridge through a flexible polymer tubing and enter the chamber through a glass cylindrical tube (2.5 cm in diameter) placed above the chamber. Droplets ejected from the cartridge travel a few centimeters before reaching their terminal velocity and descend vertically down the tube to the trapping points. The chamber has four windows on the sides for illumination and optical access and one on top for visual control and physical access. The volume of the chamber is approximately 0.24 liters.

The initial control. In order to produce a collision, the two droplets are released from the same horizontal position but at different vertical positions. As a coarse adjustment the separation of the traps is adjusted by moving the lenses for the optical traps (MO1/MO2 or MO3/MO4) in pair. Fine adjustment in the separation of the traps is accomplished by distributing the input power in one of the counter-propagating beams for the optical trap asymmetrically. This is done with a slight rotation of the half wave plate HW1 or HW2 that is placed before the beam enters the polarizing beam splitters PBS1 or PBS2 (Fig. 4.6). The vertical separation of the two optical traps is 1.7 mm, which is sufficiently large for the upper droplet to reach its terminal velocity before approaching the lower droplet.

The release mechanism. The droplets are released from the optical traps by switching off the laser beams using electro-optical amplitude modulators (EOM1 and EOM2) (Thorlabs EO-AM-NR-C4) in combination with linear polarizers (P1 and P2) (Fig. 4.6). The polarizers P1 and P2 are aligned along the initial polarization vector of the laser beam. By applying the half wave voltage V_π to the EOMs (in our case $V_\pi = 186$ V), the EOMs rotate the polarization by 90°, so it is being blocked by the polarizers P1 and P2. Hence, the optical traps are turned off and the droplets are released.

The acquisition system and timing mechanism. The imaging system consists of two high-speed digital movie cameras (Phantom Miro LAB310 from Vision Research) arranged in a horizontal plane with an angular separation of approximately 90°. Shadow images of the droplets are obtained by projecting

incoherent collimated light from two LEDs (Thorlabs MCWHL5) onto the sensors of the cameras (see e.g. [193]). This arrangement not only offers a simple approach in the alignment of the two droplets, but also allows a precise determination of the droplet positions and impact parameters. Movies of the droplet motion are recorded synchronously by the cameras at a resolution of 64×768 pixels (width $\times$ height). The field of view is sufficiently large to observe both the trapped droplets and the interaction region. In order to resolve the droplet motion at high spatial resolution, each camera is equipped with a K2 DistaMax long-distance microscope from Infinity Photo-Optical Company. Each camera pixel observes an area of 3.98 μm $\times$ 3.98 μm in space, so that the total field of view is 0.26 mm by 3.06 mm (width $\times$ height). The maximum frame rate at this resolution is 63000 Hz. After loading the droplets into both traps, the LED illumination projects shadows of the droplets onto the camera sensors for the fine positioning. Both cameras and voltage supply for the EOMs are synchronised and controlled by an external pulse generator (BNC model 565). At time t_0, the pulse generator delivers a trigger signal to the voltage supply of the EOM2 to release the upper droplet, and to initiate the recording of the movies on both cameras. At time $t_{2/3}$ when the upper droplet has traveled 2/3-rd of its way to the lower droplet, a second signal synchronized with the first one triggers the voltage supply to the EOM1 to release the lower droplet. The cameras continue imaging the motion of both droplets until they are out of view. For the initial separation of 1.7 mm, 2/3-rd of it is 1.134 mm and $t_{2/3}$ is approximately 100 ± 50 ms, depending on the droplet size. For a glycerol droplet of 31.9 μm in diameter, $t_{2/3}$ is 100.012 ms.

Spatial resolution. To map out the laboratory coordinates in real space, a Thorlabs calibration mask (model R2L2S3P1) containing uniform dots of 62.5 μm in diameter arranged in a square lattice with a separation of ℓ =125 μm between adjacent dots is placed in the mutual focal plane of the cameras. An automated particle center finding routine, written in the Matlab programming language, was used to extract the two-dimensional coordinates of the center of the dots, from which the mean separation between adjacent dots L (in pixels) was derived. The spatial resolution of each pixel, R, was obtained from $R = \ell/L$. In our experiments, the spatial resolution was approximately 4.0$\pm$0.4 μm per pixel. Because the light sources were collimated, the error in determining the diameters of the droplets is expected to be fairly small, which is shown as follows. The areas of the dot shadows were measured to size the dots. The areas were equal to the number of pixels below a certain threshold. By this method, the shadow diameters of the dots were consistently about 1.06 times larger than the actual diameter of the dots. After correction for the bias, the uncertainty in determining the mean diameters was about 2 μm, which is representative of the error in the sizing of the droplets.

4.4.3. Results

We have recorded 127 movies of collisions of droplets with different impact parameters and sizes. In the following sections, we present three main cases: the coalescence of a gravitationally settling droplet with an optically trapped droplet, the collision between two gravitationally settling droplets in the absence of trapping laser light resulting in non-coalescence, and coalescence. In all three cases we show the trajectories of droplets as they fall, collide and possibly coalesce.

4.4.3.1 ***Coalescence of droplets in an optical trap.*** Figure 4.7 shows the coalescence process between a gravitationally settling droplet and an optically trapped droplet, imaged at a frame rate of 32 kHz, similar to the experiments in [187–189, 194]. The settling droplet is 31.9±2.0 μm in diameter, whereas the optically trapped droplet is 40.0±2.0 μm in diameter, and the resultant droplet is 43.8± 2.0 μm in diameter. The high value of impact number B = 0.51, calculated from the projections of droplet separations χ_x and χ_y, indicates no coalescence in the case of absence of laser field. In this experiment, the laser light in the lower trap holds the larger droplet stationary in space and guides the settling droplet towards the trap, as can be seen in the trajectories in Fig. 4.7. As the two droplets reach a critical separation, they merge to form a larger drop. The resulting droplet stays in the trap and executes a damped oscillatory motion

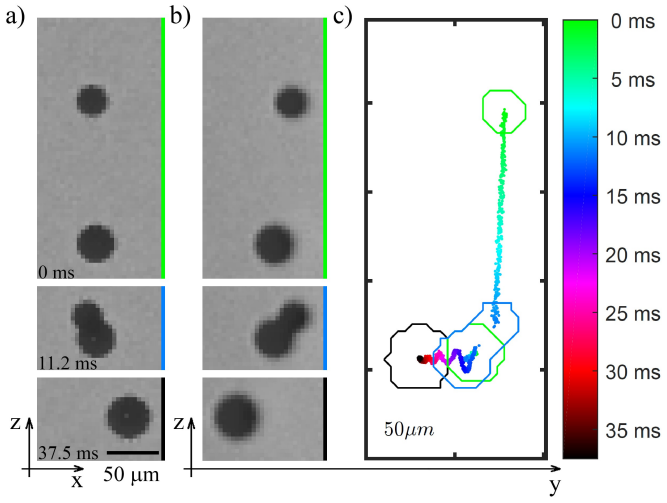

Figure 4.7: Coalescence of two droplets while the bottom droplet is trapped by laser light as viewed in (a) the x-z plane and (b) the y-z plane. Panel (c) shows the droplet trajectories as well as their surfaces extracted from the movie recorded in panel (b). Adjacent tick marks on both axes indicate spatial separation of 50 μm. The color bar indicates the progression in time in milliseconds.

(see video visualization 1: `https://www.osapublishing.org/oe/viewmedia.cfm?uri=oe-25-2-1391&seq=v001`). For clarity, this video has been slowed down by a factor of 320 to 100 fps.

Figure 4.8 shows the coalescence process that is shown in Fig. 4.7 in a more detailed frame-by-frame sequence of images at a temporal resolution of 31.25 μs per frame. In both sequences, the coalescence process is completed within a time scale of approximately 180 μs. In comparison with earlier works [187–189], in which the droplets were guided by the trapping laser light, in our case droplet coalescence is still the favored outcome.

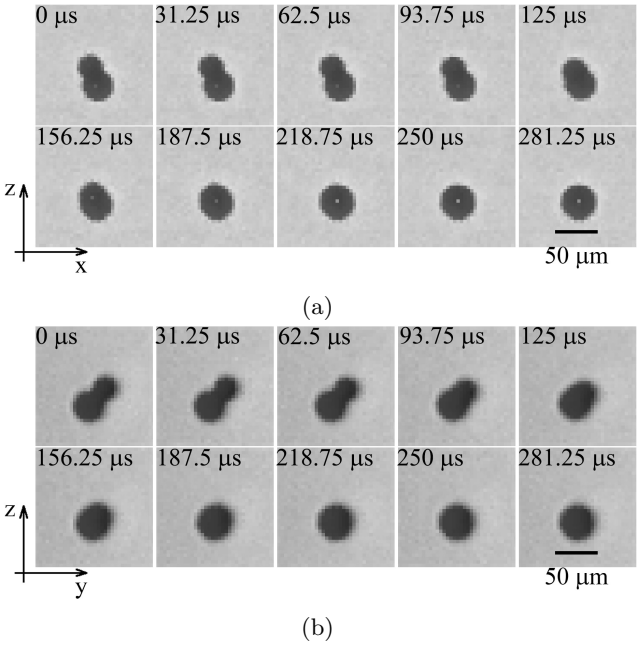

Figure 4.8: Projection on x and y directions of time resolved coalescence of two droplets when the bottom droplet is trapped by laser light.

4.4.3.2 ***Gravitational settling with kiss-and-tumbling motion.*** Figure 4.9 shows the motion of two droplets of different sizes settling under gravity, imaged at a frame rate of 63 kHz. The diameter of the larger droplet is 37.9±2.0 μm and the diameter of the smaller droplet is 29.9±2.0 μm. The impact number, calculated from the projection of droplet separations χ_x and χ_y, is B = 0.5. Before the larger droplet affects the smaller one (0 ms in Fig. 4.9) the separation between them is $\chi_x = 14\pm2$ μm along the x-axis. Consideration based on the initial geometry of the droplet trajectories predicts that they will collide. However, as the large droplet approaches the small one, it deflects the small droplet to the side without touching, so much so that when the large droplet finally catches up with the small one the separation χ_x reaches a maximum of 35±2.0 μm (at $t = 16.5$ ms on Fig. 4.9). As the large droplet

continues to fall, the small droplet moves around the large one and gradually recovers its initial vertical motion ($t = 25.3$ ms in Fig. 4.9) due to Stokesian microscopic reversibility. This microscopic kiss-and-tumbling motion, whereby the small droplet bends its trajectory around the big droplet without touching, has been theoretically described by Zhang and Davis [195] and observed in experiment for sub-millimeter-size droplets [196]. The total interaction time, which is approximately the duration of time the centers of the droplets stay within a separation of a_1+a_2 from each other, is approximately 4.2±0.1 ms. The movie describing this process is available as supplementary material (see video visualization 2: `https://www.osapublishing.org/oe/viewmedia.cfm?uri=oe-25-2-1391&seq=v002`). The temporal resolution in this movie is 15.86 μs. For clarity, this movie has been slowed down to 100 fps.

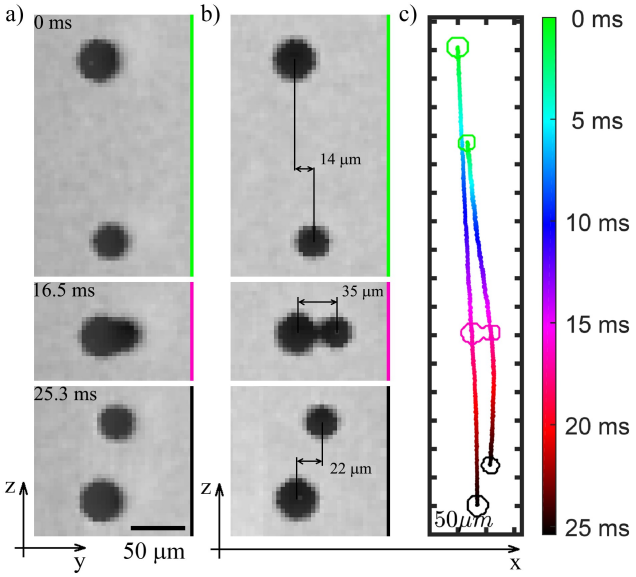

Figure 4.9: The motion of two droplets settling in quiescent air under gravity as viewed on (a) the y-z plane and (b) the x-z plane that results in kiss-and-tumbling motion. Panel (c) shows the trajectories of the two droplets as seen in panel (b). Adjacent tick marks on both axes indicate spatial separation of 50 μm. Color bar indicates temporal progression in milliseconds.

4.4.3.3 ***Gravitational settling with permanent coalescence.*** In Fig. 4.10 and 4.11, the sequences of images show the coalescence process of droplets settling under gravity and interacting without the geometrical confinement of the laser light (see video visualization 3: `https://www.osapublishing.org/oe/viewmedia.cfm?uri=oe-25-2-1391&seq=v003`), imaged at 63 kHz. The diameters of droplets before interaction are 29.9±2.0 and 33.9±2.0 μm, and the diameter of the resultant droplet is 37.9±2.0 μm. The impact parameter, calculated from the projection of droplet separations χ_x and χ_y, is B = 0.14,

indicating a near head-on collision. The separation between the centers of the droplets along the x axis is $\chi_x = 5.98\ \mu m$ (0 ms in Fig. 4.10). During the next 11.7 ms, as both droplets approach each other, the larger droplet displaces the smaller droplet, thereby increasing χ_x to as much as 12 μm prior to coalescence. The droplets spent as much as 5.8 ± 0.2 ms together during which time their center-to-center separation stays less than or equal to the sum of their radii $a_1 + a_2$. During coalescence the droplets are being pulled towards each other by capillary forces. The center of mass of the newly formed droplet is in between those of the individual droplets. The duration of the coalescence process is approximately 150 μs. In the accompanying movie (see video visualization 3: `https://www.osapublishing.org/oe/viewmedia.cfm?uri=oe-25-2-1391&seq=v003`), the temporal resolution of the image acquisition system is 15.86 μs from frame to frame, but for clarity the movie has been slowed down to 100 fps.

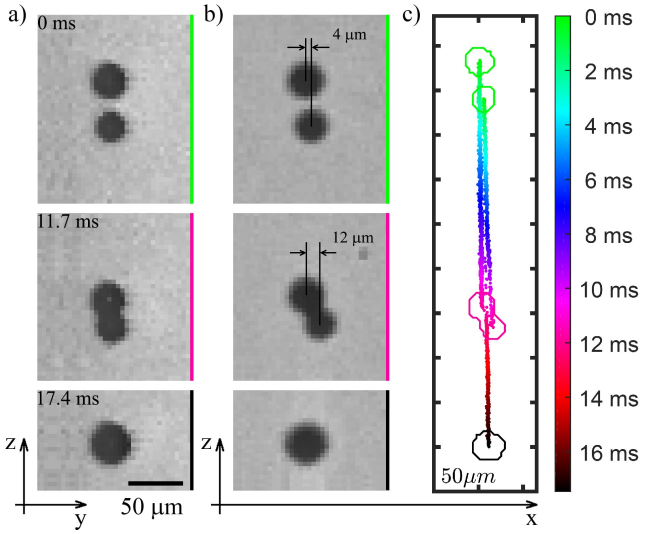

Figure 4.10: Snapshots of two droplets that interact without the influence of laser light resulting in coalescence as seen on (a) the y-z plane and (b) the x-z plane. Panel (c) shows the trajectories of the droplets rendered from the images featured in panel (b). Adjacent tick marks on both axes indicate spatial separation of 50 μm. Color bar indicates temporal progression in milliseconds.

Similar to previous section, the horizontal separation between droplets increases as the droplets approach each other (Fig. 4.10). But on the contrary, the droplet interaction here results in coalescence. The main difference, between this and the previous section, is the value of the impact parameter: $B = 0.14$ in the case of coalescence and $B = 0.5$ in the case of non-coalescence. A smaller impact parameter allows the droplets to come into physical contact. Our estimation of the collision kinetic energy (CKE) and the surface energy (SE)

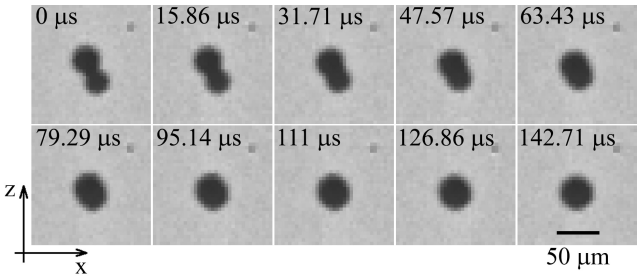

(a)

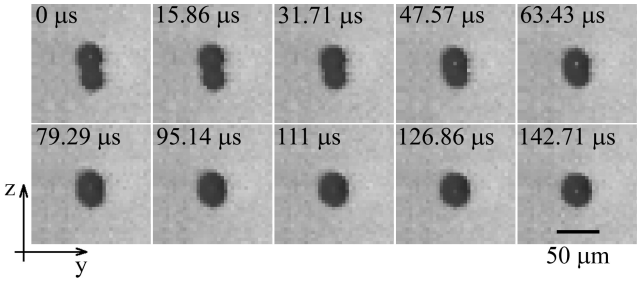

(b)

Figure 4.11: Frame-by-frame sequence of images showing the coalescence of two droplets sedimenting in quiescent air as seen on the (a) x-z plane and (b) the y-z plane.

of colliding droplets (as discussed in [178] and [181]) showed that the CKE is insufficient to overcome the SE of the droplets (the CKE is 4 orders of magnitude less than the SE). This implies that the role of the CKE is to bring the two droplets close to each other, so that other intermolecular forces could activate the coalescence process.

4.4.4. Conclusions to section 4.4

We have developed a new technique to image the trajectories of a pair of micron-sized droplets settling and colliding under gravity. Unlike previous studies with optical tweezers, in our experiment the droplets interact without the confinement of the optical trap. We have full control over the initial conditions of the collision process, namely the impact parameter, the size ratio, and the chemical compositions of the droplets.

For large impact parameter (B = 0.5), we have observed that the approaching droplets repel each other from their settling trajectories. For small impact parameter (B = 0.14), the collision results in permanent coalescence. To the best of our knowledge this is the first attempt to probe interactions of micron-sized droplets under gravity with fully controllable initial conditions. The experiment described here indicates the potential of the technique for studying

the important problem of droplet growth by gravitational collision of cloud droplets. In more sophisticated experiments, the technique could be used to obtain fluorescence spectra of colliding droplets [197], and to probe collision between electrically charged droplets, post-collision dissipative phenomena and rotational dynamics of spinning droplets. Progress in these areas of study will advance our understanding of the strong interactions between turbulence and the microphysical processes in clouds [184].

4.5. Controlled spin of a nonbirefringent droplet trapped in an optical vortex beam

In this section we are going to introduce a novel method for optical spin of a droplet trapped in the laser beam, which can be used in the bigger study of cloud formation by investigating collisional dynamics of spinning droplets in the modular system demonstrated in the previous section.

In this section, we demonstrate a method to optically spin a nonbirefringent and nonabsorbing (transparent) microparticle—a glycerol droplet—around its axis when it is optically trapped in air by an optical vortex beam. In this experiment, a droplet is initially trapped in the ring of a Laguerre–Gaussian light beam. The droplet is unconstrained azimuthally and demonstrates an orbital motion around the axis of the beam caused by the angular momentum of the light. By reducing the laser power, the droplet moves towards the waist of the laser beam. At some point, the size of the droplet becomes of the order of the size of the laser beam. The trapped droplet is then azimuthally constrained. The angular momentum of the light then causes the particle to spin around its own axis. The rate at which a trapped droplet rotates is continuously controlled from zero to maximum using spin–orbit angular momentum coupling performed by rotating a quarter-wave plate, as described in [40, 43]. The motion of the trapped droplet is observed using a high-speed camera, and the frequency of rotation is measured using a photodiode.

4.5.1. Beam preparation

A single optical vortex beam was used to optically levitate and rotate liquid droplets in air. The complex amplitude of an optical vortex beam can be written in the form

$$u(r, \phi, z) = A(r, z)e^{il\phi}, \tag{4.3}$$

where r, ϕ and z are the cylindrical coordinates, A is the amplitude of the beam (e.g., a nonzero-order Laguerre–Gaussian or Bessel–Gaussian beam), and $e^{il\phi}$ describes the azimuthally varying phase of a beam, with l being the strength or the topological charge of the optical vortex. The intensity profile of such a

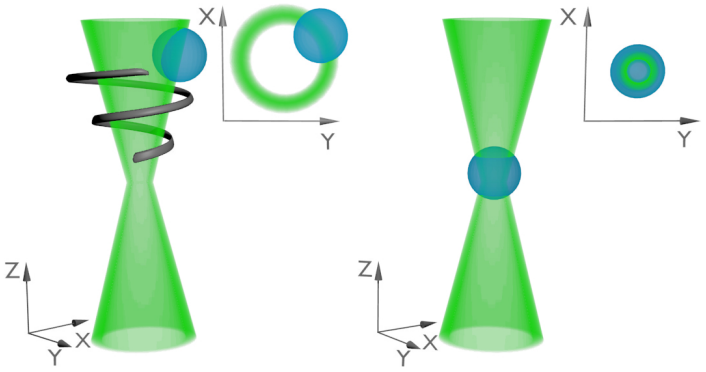

Figure 4.12: Schematic of a droplet in an optical vortex trapping beam. Left: The droplet is trapped above the waist of the beam. Inset: The droplet is orbiting around the axis of the beam. As the power of the beam is reduced, the droplet moves to the axial position, as indicated by the black spiraling trajectory. Right: The droplet is trapped at the waist of the beam. Inset: The droplet positioned at the axis of the laser beam is spinning.

beam is ring-shaped or doughnut-shaped in the transverse plane. The droplet is trapped in the ring of maximum beam intensity, as schematically shown in the left part of figure 4.12. The phase front of the optical vortex beam varies helically around the axis of the beam upon propagation. Due to this helical variation, its Poynting vector is tilted with respect to the axis of the beam with a local angle given by $\theta_{screw} = l/kr$, where k is the wavenumber [5]. This tilt gives rise to the OAM of the beam, which imparts a tangential force on the trapped droplet. This is not restricted azimuthally due to the cylindrical symmetry of the intensity distribution, making the droplet orbit around the axis of the beam. The direction of rotation is determined by the handedness of the helical phase front—i.e., by the sign of the topological charge $\pm l$. The geometry of the trapping beam makes it possible to optically rotate particles of any composition, including nonbirefringent and nonabsorbing droplets.

The optical vortex beam can be generated by various methods. This experiment employed an S-waveplate, which is a nanograting-based q-plate, in order to make use of the spin–orbit coupling of angular momentum in the beam to control the spinning frequency of a trapped droplet. A Gaussian beam propagating through an S-waveplate transforms to an optical vortex beam with a Laguerre-Gaussian beam profile ($l \neq 0$) (Fig. 4.13), as described in detail in the first Chapter of this dissertation. The conversion is accomplished using the following transformation of the polarization state: the initial left (right) circular polarization (with $l = 0$) transforms to right (left) circular polarization (with $|l| = 1$), (Figs. 4.13b and 4.14b); the initial linear polarization (with $|l| = 0$)

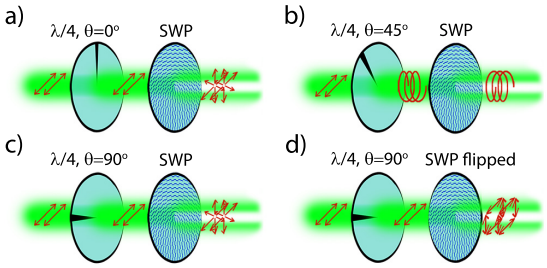

Figure 4.13: Schematic showing the preparation of the trapping beam. θ indicates the orientation of the quarter-wave plate, $\lambda/4$, with respect to the direction of the incident polarization. SWP denotes an S-waveplate. SWP flipped denotes an S-waveplate that is physically flipped around the Z-axis. The red arrows schematically indicate the polarization state. The resulting polarizations are a) radial, b) circular, c) radial, d) azimuthal.

becomes radial (with $|l| = 1$) if the S-waveplate is aligned parallel to the orientation of the incident linear polarization (Figs. 4.13a,c and 4.14a,c) and azimuthal (with $|l| = 1$) if aligned perpendicularly (Figs. 4.13d and 4.14d). In general, the generated radially and azimuthally polarized beams should be vortex free. However, in the region(s) where the retardation of the S-waveplate slightly deviates from the half-wave value, these beams become elliptically polarized with vortex phase $|l| = 1$ (Fig. 4.14). The stiffness of the optical trapping due to the different polarization patterns does not vary significantly [199] and does not affect the presented results. Detailed information on the beam conversion with aid of the S-waveplate/q-plate can be found in [43, 67, 74] and references within. The transmittance, T, of the S-waveplate depends on the incident wavelength, which for 532 nm is $T \geq 50\%$ [200]. The damage threshold of the S-waveplate LIDT$\approx$ 5 J/cm^2 for λ=532 nm and LIDT$>$ 20 J/cm^2 for λ=1064 nm [200].

The experimentally obtained polarization maps shown in figure 4.14 confirm the polarization states of the generated beams. The interferograms in the same figure confirm the presence of azimuthally varying phase. The interferograms show the positions of points of bifurcation of the interference lines (the "characteristic fork"), which indicate the point around which the phase circulates. For a circularly polarized beam, the point of bifurcation coincides with the center of the beam (Fig. 4.14b). The location of the bifurcation point is (x; y) = (0.02; 0) mm, with (0; 0) being the center of the beam. The radius of the ring of maximum intensity is 0.42 mm. However, for radially/azimuthally polarized beams, the center of the phase circulation shifts from the center of the beam to (-0.21; -0.01), (-0.27; -0.03) and (-0.29; 0.03) mm, respectively (Fig. 4.14a,c,d). The fact that the position of the phase circulation does not coincide with the center of a beam results in an asymmetric distribution of OAM over the beam. The effect of this asymmetry on the motion of droplets will be discussed later.

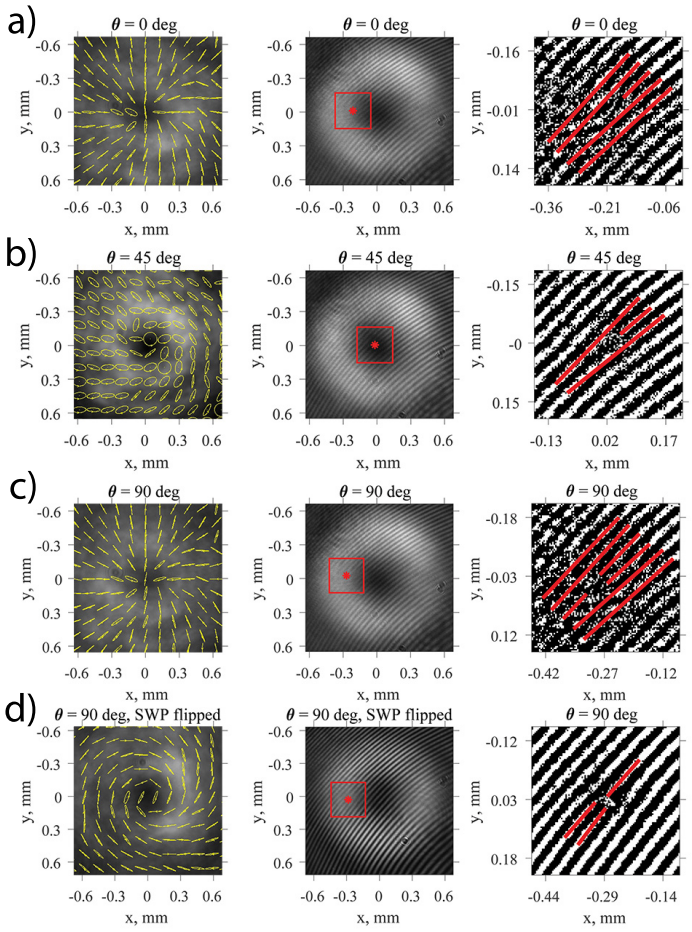

Figure 4.14: Experimentally obtained polarization maps and interferograms of a beam prepared as shown in figure 4.13. θ denotes the orientation of a quarter-wave plate with respect to the direction of the incident polarization. First column: the polarization distribution is superimposed on the intensity distribution. Second column: the position of the characteristic "fork" is marked by a red star. Polarization of reference beam used to generate interference is vertical. Third column: magnified area marked by the red square in the second column. The position and direction of the bifurcation lines are highlighted by red lines. Topological charges are as follows: a) l = -1, b) l = -1, c) l = -1, d) l = +1.

Rotational frequency control. The total angular momentum per photon is given by AM = $(l-\sigma)\hbar$, with the orbital part represented by OAM = $l\hbar$ and the spin part by $SAM = -\sigma\hbar$, and $\sigma = \pm 1$, for left/right circularly polarized beam, respectively. Note that here AM = $(l-\sigma)\hbar$ and $\sigma = \pm 1$ has been used instead of the conventional way of writing AM = $(l+\sigma)\hbar$ with $\sigma = \mp 1$ [36]. With the

beam prepared as described above, the total AM experienced by the droplet per photon is given by AM $= (l - \sigma)\hbar = (-1 - 0)\hbar = -1\hbar$ for the radially polarized beam (the trapped droplet demonstrates right-hand rotation), AM $= (l - \sigma)\hbar = (+1 - 0)\hbar = +1\hbar$ for the azimuthally polarized beam (the trapped droplet demonstrates left-hand rotation) and AM $= (l - \sigma)\hbar = (-1 + 1)\hbar = 0$ for the right-hand circularly polarized beam (no rotation). The maximum frequency of rotation can thus be obtained with a linearly (radially/azimuthally) polarized beam and with zero rotational frequency using a circularly polarized beam. The transient polarization states give intermediate values of the AM. By changing the orientation of the quarter-wave plate (Fig. 4.13) to alter in turn the polarization state of the trapping beam, the rotational frequency of the droplet can thus be controlled. This effect of the spin–orbit coupling of the angular momentum in the beam is used to gradually control the frequency of the rotation of the droplet, as demonstrated by [40] for absorbing particles and by [43] for nonabsorbing and nonbirefringent solid particles. In this work, the maximum OAM value is restricted to $|l| = 1$. In general, however, it is not limited to this value. The maximum value is determined by the charge, q, of the plate, which is controlled in the production of the plate.

Transition from orbiting to spinning. The switch from orbiting to spinning character of motion is governed by the geometry of the beam; this can be illustrated with an analogy with the motion of an object being pulled down a water vortex in a sink or bath: such an object experiences a reduction in the radius of its orbit and a corresponding increase in the angular velocity. The vertical position of a droplet depends on the power of the trapping beam. By lowering the power, the droplet gradually falls down from its stable trapping position above the focal region to the second stable position in the focal region (Fig. 4.12). The radius of the circle described by the orbiting droplet is approximately equal to the waist of the beam at the vertical position of the droplet. When the droplet is within (or close to) the focal area, the beam waist is smaller than the droplet diameter (right part of Fig. 4.12). The droplet still experiences AM and the orbiting motion is hence transferred to the spinning motion when the droplet is locally confined. The transition from orbiting to spinning motion is accompanied by an increase in rotational frequency.

4.5.2. Results and Discussion

A diode pumped solid-state (DPSS) continuous-wave (cw) laser (Laser quantum "gem532", 532 nm, 2 W maximum power) was used for this experiment. An S-waveplate (Altechna R&D) and a quarter-wave plate were used to modulate the phase, spatial distribution, and polarization of the trapping beam (Figs. 4.13 and 4.14). The motion of a trapped glycerol droplet (n=1.47), shown in Fig. 4.15, was captured with a Phantom Miro eX4 high-speed camera equipped with a

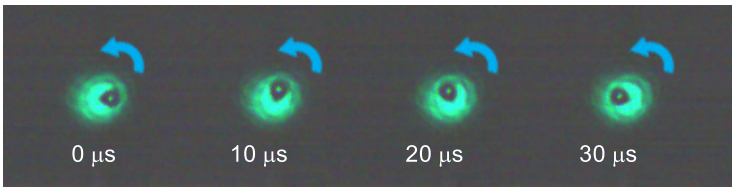

Figure 4.15: Snapshots of a rotating transparent glycerol droplet (n=1.47) levitated in air with a radially polarized optical vortex beam of strength l= -1. The bright spot in the center of the dark droplet is the Fresnel spot. Trapping power is 196 mW. Focal length of the trapping lens is f = 8 mm. Droplet diameter is 24.2 μm.

Canon MP-E 65 mm lens and a Canon EF 2X III Extender lens. To quantify the rotational frequency, the light scattered from the trapped droplet was collected using a photodiode. The time series obtained with the photodiode was Fourier-transformed to obtain the rotational frequency of the droplet.

Rotational frequency control. Figure 4.16 shows the Fourier-transformed photodiode signal obtained from a 19.5 μm droplet orbiting in a ring of light, as shown in figure 4.15. The maximum rotational frequency, marked by f_0 and f_{90}, is achieved with a linear polarization state incident on the S-waveplate, which corresponds to the orientation of the quarter-wave plate at 0° and 90° with respect to the orientation of the polarization of the incident beam. Deviation from these orientations dramatically decreases the orbiting frequency: 10° deviation (i.e., the orientation of the quarter-wave plate at 10° or 80°) results in the frequency being approximately halved (shown as the curves f_{10} and f_{80} in figure 4.16); 45° orientation, which corresponds to circular polarization, completely eliminates the AM experienced by the droplet and the droplet stops rotating (curve f_{45} in figure 4.16). The direction of rotation remains the same, independent of the orientation of the quarter-wave plate. Reversal of the rotational motion is achieved by physically flipping the S-waveplate around the Z (gravity) axis (that is, by aiming the light through the front face of the plate instead of the back face), which reverses the handedness of the helicity of the generated optical vortex. The "fork" in figure 4.14d then points in the opposite direction to that observed in figure 4.14a–c.

The shift of the "characteristic fork" from the center of a beam (as shown in figure 4.14) leads to an aperiodic motion of the trapped droplet and hence a widening of the peaks in the frequency spectrum recorded with the photodiode. The difference between the rotational frequencies f_0 and f_{90} is caused either by disturbances due to the open trapping chamber or a slight misalignment of the optical components. The appearance of strong higher harmonics has two origins, being due either to the photodiode being positioned at neither 0° or 90° with respect to the droplet position and beam axis, or due to the aperiodic

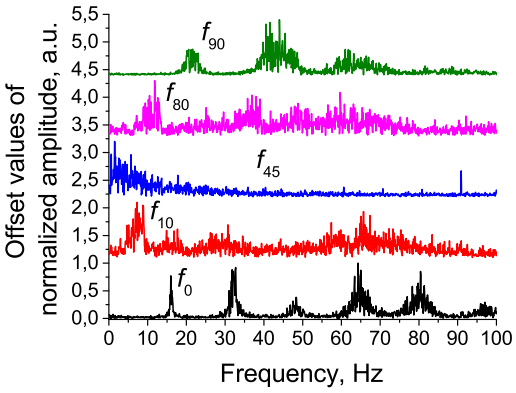

Figure 4.16: Angular frequencies f_θ obtained from the Fourier-transformed photodiode signals acquired at different angles θ of the quarter-wave plate orientation (see text for details). The greatest rotation rates, seen as the fundamental Fourier component $f_0 = 16$ Hz and $f_{90} = 20$ Hz, correspond to the quarter-wave plate orientations at $\theta = 0°$ and 90°, respectively. An orientation of the quarter-wave plate at 45° leads to no rotation—that is, $f_{45} = 0$ Hz; 10° and 80° orientations lead to intermediate values of rotational frequency of f_{10} = 9 Hz and $f_{80} = 11.5$ Hz, respectively. Trapping power is 230 mW, droplet diameter 19.5 μm, beam diameter measured as the diameter of the ring of maximum intensity 39.2 μm.

motion mentioned above.

Transition from orbiting to spinning. By reducing the laser power of the trapping beam, the droplet approaches both the focal plane of the laser beam and the beam axis. As a result, due to a decrease in the radius of the orbit, the droplet rotates faster. Figure 4.17 shows the droplet rotational frequency as a function of the beam power for different trapping lens focal lengths and different droplet sizes. The behavior is similar for all focal lengths investigated. Larger beam divergence causes more rapid transformation of the droplet from orbiting to spinning.

In the limit where the droplet diameter is equal to or greater than the beam diameter, the nature of the rotation changes from orbiting to spinning. The insets on the right side of figure 4.17 show an orbiting droplet trapped at 197 mW and a spinning droplet trapped at 98 mW. From the high-speed camera recording, it can be observed that the droplet conserves its axial position. However, the axial constraint makes it difficult to spot the spin in the video recording (see image insets in figure 4.18). The spinning of the particles is instead verified by the time series of the signal from the photodiode, which indeed shows a spinning particle. To verify this, two cases were compared. In the first case, the quarter-wave plate was oriented at 45°, such that the

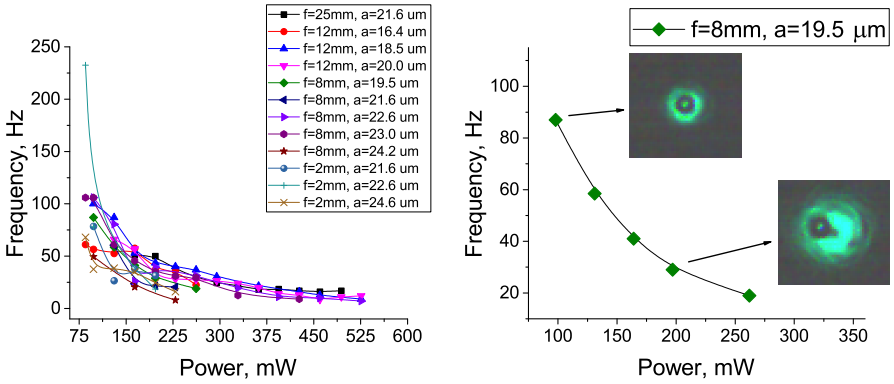

Figure 4.17: Angular frequency of the droplet rotation as a function of the trapping power. The left side shows the dependency under various specified experimental conditions, while the right side is an example of a particular case. f is the focal distance of the trapping lens in mm, and a is the droplet diameter in μm. Image insets on the right side: glycerol droplet trapped on the axis (top) and within the ring of light (bottom) of Laguerre–Gaussian beam. Trapping power is 98 mW and 197 mW, respectively. Droplet diameter is 19.5 μm.

polarization before the S-waveplate is circular and the total AM experienced by the droplet is this zero. In the second case, the quarter-wave plate was oriented at 90°, such that the polarization before the S-waveplate is linear and AM = -1$\hbar$ (see figure 4.16 and section 4.5.1). As shown in figure 4.18, there is a clear difference between the two signals, despite the similar image sequences observed with the high-speed camera. The analysis indicates that the droplet spins with a frequency of $f_{90} = 65.6$ Hz when AM is maximum, and stops spinning when AM is minimum, giving a frequency of $f_{45} = 0$ Hz.

In the case of axial localization of the isotropic spinning droplet, there are two reasons a nonzero photodiode signal is seen. Over a short time scale, an inhomogeneity or impurity in droplet composition could give rise to a periodic signal. However, since the droplet is in the liquid phase, it should smear out over a long time scale, unless the impurity inside the droplet is trapped by the beam and constituted the main contribution to the signal. Over a long time scale, variability in the position of the droplet gives rise to the observed frequency. An asymmetric distribution of OAM or a slight inclination of the plane of rotation of the droplet with respect to the normal to the direction of gravity would result in nanometer-scale variations in the position, which is the main cause of the observed periodic signal.

4.5.3. Conclusions to section 4.5

We have demonstrated a single-beam technique for optical levitation and rotation of nonabsorbing (transparent) and nonbirefringent liquid droplets in air. The

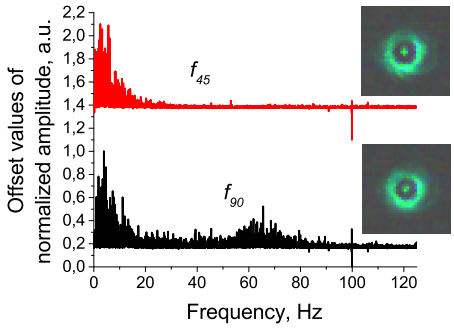

Figure 4.18: Comparison of two Fourier-transformed photodiode signals obtained at two different orientations of the quarter-wave plate. The quarter-wave plate oriented at 45° (circular polarization, AM is minimum) leads to zero spin, $f_{45} = 0$ Hz, while the 90° orientation (linear polarization, AM is maximum) leads to spin at a frequency of $f_{90} = 65.6$ Hz. Insets: snapshots from the high-speed camera recordings showing a glycerol droplet trapped on the axis of the Laguerre–Gaussian beam; the bright spot in the center of each droplets is the Fresnel spot. Trapping power is 98 mW, and droplet diameter 19 μm.

trapped droplet can be made to either orbit or spin around the axis of the trapping beam. The type of rotational motion depends on the size of the local waist of the trapping beam at the point of trapping. The vertical trapping position is controlled by the power level of the trapping laser beam. The frequency of the rotation of the droplet depends on the polarization of the beam (even though the droplet is not birefringent) due to the spin–orbit coupling of the angular momentum in the beam. The polarization is continuously controlled by the orientation of the quarter-wave plate. This single-beam method may be preferential to multiple-beam technique on account of interference between two beams of slightly different frequencies, and for extending the abilities of conventional optical tweezers and complex setups in the analysis and probing of microparticles, as discussed in [198]. Although the experiment was performed in air with liquid droplets the described method can be successfully used in conventional optical tweezers with samples in any phase (gas/liquid/solid) as long as the standard condition $n_p > n_s$ for refractive indices of surrounding, n_s, and particle/sample, n_p, is met. Additionally, this method can find applications outside optics, such as in fluid dynamics, where rotating droplets could be achieved in the study of collisional dynamics of liquid droplets in studies of raindrop formation [44] which was introduced in the previous section.

4.6. Conclusions to Chapter 4

A versatile modular apparatus for optical levitation has been presented in this chapter. The apparatus allows simultaneous control of the droplet size, charge, spin and rotation, allowing the dynamics and chemical structure of glycerol droplets to be studied using optical imaging technique and Raman spectrometry. The modular design allows further experimental methods to be developed for studies of the physics of droplets. The long term goal of this work is to create a system where interactions of droplets with the surrounding media or with other droplets can be studied with full control of all physical parameters. The experiments presented in this chapter constitute important steps towards this goal.

Conclusions

1. Perturbation of retardation of the S-waveplate (and a geometric phase retarder in general), whether by mismatch of the incident wavelength or defects in the manufacturing, leads to complex converted beam consisting of the vortex and non- or multiple-vortex components. This is turn leads to shift in position of the vortex within the beam and to asymmetry in intensity distribution and appearance of a vortex phase in the generated radial/azimuthal polarization. Bigger the perturbation of the retardation, bigger the vortex shift. When perturbation of the retardation is homogeneous, e.g. due to mismatch of the incident wavelength, the spatial size of the non-vortex component is the same as of the vortex component, which strongly distorts vortex position, intensity, phase, and polarization distribution of the generated beam. However, when the perturbation of the retardation is inhomogeneous, e.g. due to manufacturing error, and oscillates around π value, then both components in the complex beam carry vortices. However, size of the multiple-vortex (background) component is bigger than that of the (main) vortex component, and diffracts much faster upon propagation. Higher oscillations lead to bigger size of the multiple-vortex (background) component. Therefore, proper polarization and phase state of the generated beam recovers after some free space propagation.

2. White light and broadband (more than octave spanning) vortex beam generation from a single S-waveplate has been demonstrated. S-waveplate (and a geometric phase retarder in general) should induce exactly half wave phase delay for correct conversion of the polarization and phase of the incident beam. When incident wavelength vary, the phase delay, which the beam experience also vary. Therefore, resultant complex beam consist of the vortex and non-vortex components, which can be spatially separates by polarization. Selecting circularly polarized (with direction opposite to that of the incident beam) component of the converted beam, we select only those components of the beam, which have experienced proper half wave phase delay, hence we select only vortex component. S-waveplate used in the experiment had half wave retardation for $\lambda_0 = 532$ nm. Vortex

generation was demonstrated at incident wavelength varying from 400 nm to 1000 nm, at expense of lower efficiency of generation at the wavelengths further from the λ_0, but still higher than 50% at all demonstrated bandwidth.

3. When THz generating plasma filament intersects with another pre-created plasma filament then plasma absorption and screening play an important role and significantly reduce the intensity of THz radiation when the intersection point of the bichromatic pump and prepulse beams is located after the pump beam focus. On the other hand, when the intersection point is before the pump beam focus, the main phenomenon responsible for the strong modification of generated THz radiation is the influence of the preplasma filament on the intensity and relative phase of the bichromatic pump beam.

4. For the first time to the best of our knowledge, we have demonstrated generation of the vortex THz pulse from plasma filament in air induced by the Gaussian fundamental harmonic and optical vortex second harmonic pulses. The presence of a phase singularity in the generated THz beam was confirmed by astigmatic transformation of the singular THz beams in the focus of a cylindrical lens, as well as by fully space and time resolved numerical simulations. Furthermore, it was additionally confirmed by analyzing the change of the intensity distribution of the THz beam with respect to the relative phase between fundamental and second harmonic. The intensity of the vortex THz beam is modulated along the beam azimuthal angle and contains two minima between two lobes of maximum intensity. This is because the relative phase between two harmonics varies azimuthally when the SH pump pulse is a vortex. Moreover, our numerical simulations demonstrate that transverse instabilities in the filamentary pump propagation affect the THz vortex without destroying it. They may introduce secondary phase singularities, which renders the phase topology of produced structured THz fields particularly rich. One of the benefits of THz generation from plasma currents is the large (>40 THz) spectral range achievable, contrary to bandwidth limited external THz shaping techniques.

5. Generated, from vortex signal pulse and Gaussian pump pulse, idler pulse has vortex phase with direction of vorticity opposite to that of the signal. In type II nonlinear crystal, linear polarizations of the signal and idler are also orthogonal. Therefore, in the case of degenerate parametric amplification, signal and idler vortices (of the same wavelength) of opposite topological charges and orthogonal linear polarizations combine to the vortex-free exotic polarization state by a simple quarter waveplate converting orthogonal linear polarization states of vortices to orthogonal

circular states. Exotic polarization state, e.g. radial, azimuthal or mixed, is controlled by changing phase delay between signal and idler. $\pi/2$ phase delay results in radial polarization, while π phase delay changes polarization state to azimuthal. Possibility of active polarization control and polarization shaping without external optical components (hence, high damage threshold and possibility of extremely high energy levels) make this method very attractive for applications.

6. We have undertook significant steps towards creation of a versatile system for optical manipulation experiments, where interactions of droplets with the surrounding media or with other droplets can be studied with full control of all physical parameters. We have designed and demonstrated system for precise and repeatable collision of micronsized liquid droplets under gravity. We controlled diameter (hence, terminal velocity), impact number, chemical composure, and electric charge of droplets.

7. Further, we have developed a novel method to rotate nonbirefringen and nonabsorbing liquid droplets in an optical vortex beam. The trapped droplet can be made to either orbit or spin around the axis of the trapping beam. The type of rotational motion depends on the size of the local waist of the trapping beam at the point of trapping. The vertical trapping position is controlled by the power level of the trapping laser beam. The frequency of the rotation of the droplet depends on the polarization of the beam (even though the droplet is not birefringent) due to the spin–orbit coupling of the angular momentum in the beam. The polarization is continuously controlled by the orientation of the quarter wave plate. Rotation of droplets is another possible parameter to control in the collision experiment. Investigation of collisional dynamics of droplets with precise control of the mentioned parameter is core in the studies of cloud formation in the field of fluid dynamics.

Santrauka

Įvadas

Optinių sūkurių pluoštų esmę galima paaiškinti remiantis šviesos interferencijos formalizmu. Pavyzdžiui, interferencijos eksperimente su trimis bangomis šviesa kai kuriuose taškuose išnyksta, o kituose sustiprėja atitinkamai dėl destruktyvaus ir konstruktyvaus bangų sumavimo. Nors dauguma nenulinio intensyvumo diapazonų lokaliai atrodo kaip plokščios bangos, šalimai esantys nulinio lauko taškai pasižymi neįprastomis savybėmis. Kadangi lauko intensyvumas yra nulis, jo fazė yra neapibrėžta arba "singuliari". Tokios vietos vadinamos fazės singuliarumais. Apskritai, aplink šį tašką galimos visos 2π fazės vertės, o tai leidžia optinės energijos srauto sukimąsi. Lauko intensyvumo nuliai trimatėje erdvėje paprastai pasireiškia kaip linijos, aplink kurias fazė sukasi arba pasižymi spiraline forma, dėl ko ir atsirado terminas "optinis sūkurys" (OS). Nustatyta, kad, su tam tikromis ribotomis išimtimis, optiniai sūkuriai yra tipiški singuliarumai, atsirandantys daugelio interferencijos eksperimentų su daugiau nei dviejomis bangomis, metu. OS turi gerai matematiškai apibrėžtą struktūrą [1], be to, ši struktūra gali stipriai įtakoti per bendras šviesos lauko savybes, įskaitant ir jo sąveiką su medžiaga. Šiuo metu šviesos laukų singuliarumų tyrimai išsiplėtė iki pilnai išsivysčiusios optikos srities, žinomos kaip *singuliarinė optika*. Kadangi izoliuoti lauko nuliai gali suteikti tiek pat informacijos, kiek ir šviesios sritys, singuliarinė optika įgalina alternatyvius šviesos tyrimo metodus. Praktiniu požiūriu, specialiai paruošti sūkuriniai pluoštai turi daugybę įdomių struktūrinių savybių, kurios yra naudingos daugelyje optikos sričių: nuo optinio lokalizavimo ir manipuliavimo iki optinių komunikacijų, mikroskopijos bei astronomijos, paminint tik keletą savarbiausių.

Lazerio pluoštas su sūkuriu ašyje matematiškai aprašomas kaip "Lagero-Gauso" moda. OS pluošto fazė kinta priklausomai nuo pluošto azimuto, o jo kompleksinė amplitudė yra proporcinga $e^{il\phi}$, kur ϕ yra azimutinis kampas, kintantis nuo 0 iki 2π, o l apibūdina spiralinės bangos frontą ir žinomas kaip topologinis krūvis arba fazinio singuliarumo stipris. Topologinis krūvis apibūdina spiralinės bangos fronto kreivumą, o jo ženklas reiškia sukimosi kryptį [2, 4]. Labai trumpų impulsinių lazerinių sistemų atsiradimas stipriai

komplikavo sūkurinių pluoštų generavimo procesą. Taip yra todėl, kad itin trumpi lazeriniai impulsai susideda iš daugybės spektrinių komponentų, t.y., jie yra plačiajuosčiai. Iš tiesų, OS bangos frontas, kuris sąlygoja orbitinį šviesos pluošto sukimo momentą (OSM), yra pakreiptas kampu $l\lambda/2\pi r$, kur r yra pluošto spindulys [5]. Charakteringa priklausomybė nuo bangos ilgio λ OS pluoštų generaciją, naudojant itin trumpus impulsus, susidedančius iš skirtingų spektrinių komponentų, padaro techniškai sudėtinga. Tačiau didelis plačiajuosčių optinių sistemų poreikis, pvz., optinėse ir kvantinių ryšių sistemose bei duomenų perdavimas fotoninių kristalų skaidulomis skatina plačiajuosčių OS pluoštų kūrimą.

Toliau nuo optinės srities, terahercų (THz) dažnio spektrinis diapazonas šiuo metu tarp fizikos bendruomenės pritraukia daug dėmesio. THz spinduliuotė yra labai aktuali dėl daugelio taikomųjų tyrimų, tokių kaip netiesinė THz spektroskopija ir vaizdinimas [6] arba kaip alternatyva elektronų pluoštelio suspaudimui [7]. Singuliarinės optikos išplėtimas į naujus dažnio diapazonus, pvz., į THz dažnių sritį, galėtų atverti naujus horizontus THz fizikoje. Ankstesnės sūkurinių THz dažnio pluoštų kūrimo pastangos [8–15] buvo paremtos tik THz dažnio spinduliuotės manipuliavimu išoriniais komponentais, kas iš esmės riboja taip gaunamos priimtinos pralaidumo juostos plotį. Todėl, vystant šią sritį, itin svarbu siūlyti ir tirti alternatyvius plačiajuosčių sūkurinių THz dažnio pluoštų generavimo metodus. Taip, visai neseniai, sūkurio formos THz dažnio impulsai buvo sukurti be išorinių formavimo elementų [16, 17] ZnTe kristaluose, tačiau buvo gauta palyginti siaura pralaidumo juosta. Todėl plačiajuosčių THz dažnio sūkurinių pluoštų kūrimo problema vis dar lieka atvira ir reikalauja išsamių tyrimų.

Banginių frontų dislokacijų transformacijos taip pat buvo tiriamos ir netiesiniuose režimuose. Buvo parodyta, kad optinių sūkurių atveju topologinio krūvio išsaugojimo dėsnis antrosios eilės, $\chi(2)$ netiesinės sąveikos metu yra $l_1 + l_2 = l_3$. Topologinių krūvių išsaugojimas optinio parametrinio stiprinimo (OPS) metu, tiksliau skirtingų krūvių sūkurių kombinacija sukelia svarbius praktinius padarinius. Pavyzdžiui, galima gauti radialiai poliarizuotus impulsus, kurie gali būti naudojami lazeriniams medžiagų apdorojimui [26–29] ir elektronų pagreitinimui/suspaudimui išilginiu elektrinio lauko komponentu [30–32]. Paprastai radialinės poliarizacijos pluoštų generavimas priklauso nuo poliarizacijos keitimo specialiame optiniame komponente. Tačiau optinių komponentų optinės pažeidos slenkstis labai apriboja lazerio impulso energiją, reikalingą didelės galios taikymams. Todėl radialiai poliarizuotų impulsų generavimas OPS metu, pagrįstas OS pluoštų deriniu gali būti patraukli alternatyva didelės galios taikymams.

Vienas iš OS pluoštų taikymų yra optinis dalelių lokalizavimas ir manipuliavimas. Optiškai indukuotas pagautų dalelių sukimas naudojamas, pavyzdžiui, neinvazinei gyvų ląstelių orientacijai, dalelių dinamikos tyrimuose ir tribologinių

sistemų tyrimuose [33, 34]. Dalelę galima sukti, naudojant šviesos pluoštus, turinčius kampinį sukimosi momentą (SM). Šviesos SM sudaro kampinis sukimo momentas (KSM) ir orbitinis šviesos pluošto sukimo momentas (OSM) [36]. OSM yra susietas su apskritimine pluošto poliarizacija, o KSM yra susietas su geometrine sūkurinio pluošto struktūra taip, kad lokalizuota dalelė yra veikiama papildoma tangentine jėga. Sukamojo judesio tipas izotropinėms ir neabsorbuojančioms dalelėms, pvz., kai dalelė lieka vietoje ir sukasi aplink savo ašį, dar nėra pademonstruotas. Nepaisant to, izotropinių ir nesugeriančių lašelių optinis sukimasis gali būti pritaikytas ne tik optikoje, bet ir, pvz., skysčių dinamikoje, kur, tiriant skystų lašelių susidūrimo procesus, gali susidaryti besisukantys lašeliai [44].

Disertacijos tikslas

Todėl šios disertacijos tikslas – sukurti ir išvystyti (i) ultraplačiajuosčių optinių sūkurių generavimo metodus, (ii) terahercų dažnio sūkurius, (iii) radialinės poliarizacijos besūkurinius pluoštus, ir pasiūlyti sūkurinių pluoštų taikymą dalelių optinio manipuliavimo srityje, kaip universalios modulinės sistemos, skirtos optinio manipuliavimo eksperimentams, dalį.

Darbo užduotys

Siekiant mokslo darbo tikslo, buvo įgyvendintos šios užduotys:

1. Teoriškai ir eksperimentiškai ištirti geometrinio fazės lėtintuvo fazės vėlinimo netolygumų poveikį generuojamo optinio sūkurio pluošto ir radiališkai/azimutiškai poliarizuotų pluoštų fazei, intensyvumui ir poliarizacijai.

2. Skaitmeniškai ir eksperimentiškai plataus spektro diapazone (daugiau nei oktavos pločio) pademonstruoti optinių sūkurinių impulsų gamybos būdą, naudojant laikiškai koherentinius ir nekoherentinius šviesos šaltinius. Sukurtas optinis sūkurys turėtų pasižymėti generuojamų skirtingų bangų ilgių optinių sūkurių koaksialumu (be erdvinės dispersijos).

3. Ištirti ultraplataus spektro ryšio (>30 terahercų) sūkurinių impulsų generavimą terahercų dažnių srityje ore susidarančiose plazmos gijose, tam naudojant fokusuotus bichromatinius femtosekundinius ir sūkurinius lazerio impulsus.

4. Eksperimentiškai ištirti lazeriu sukurtos plazmos įtaką terahercų dažnio spinduliuotės, generuojamos ore fokusuotais femtosekundiniais bichromatiniais lazerio impulsais, energijai ir erdvinėms savybėms.

5. Sukurti optinį parametrinį stiprintuvą, pasižymintį radialinės poliarizacijos išėjimo pluoštu, tam nenaudojant išorinių poliarizacijos keitiklių.

6. Sukurti universalios modulinės sistemos, skirtos optinio manipuliavimo eksperimentams, dalį, visų pirma tinkamą mikronų dydžio lašelių susidūrimo dėl gravitacijos dinamikos tyrimams, tam naudojant dvi optinių gaudyklių sistemas.

7. Sukurti optiškai indukuoto dvejopalaužiškumu nepasižyminčių bei nesugeriančių dalelių sukimo ir sukiojimo metodą optiniame sūkuriniame pluošte. Būtų galima naudoti kaip modulinės sistemos aprašytos šeštojoje užduotyje plėtinį.

Disertacijos tikslas, uždaviniai ir išdėstymas schematiškai parodyti Pav. 4.19.

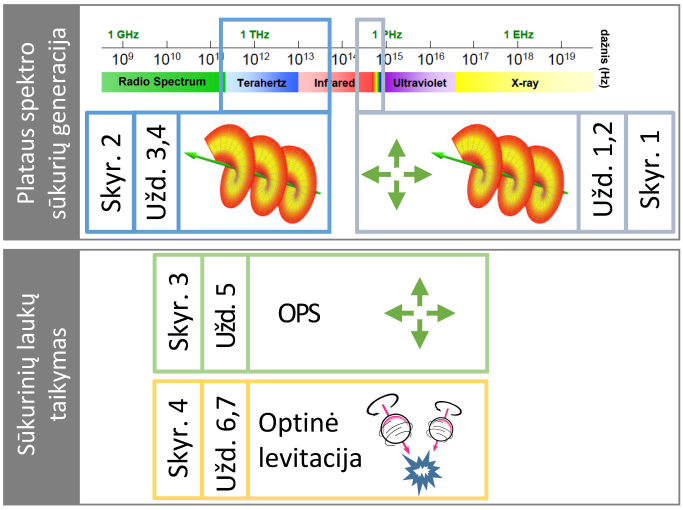

Figure 4.19: Disertacijos tikslo, užduočių ir išdėstymo schema.

Darbo naujumas ir svarba

Šiame disertacijoje aprašytų tyrimų metu buvo sukurtos naujoviškos ultraplataus spektro optinių sūkurinių impulsų, radialinės poliarizacijos impulsų ir THz dažnio sūkurinių impulsų generavimo schemos. Pirmą kartą buvo ištirtas nehomogeninio vėlinimo poveikis pluoštų, generuojamų geometriniame fazės lėtintuve, savybėms. Buvo sukurtos naujos schemos, skirtos lašelių optiniu būdu valdomo sukamojo sukimosi ir orbitinio judėjimo kontrolei, taip pat buvo išvystyta schema, skirta optiškai inicijuotų lašelių susidūrimų dinamikai tirti.

Plačiajuosčiai šviesos sūkuriai turi praktinę reikšmę kvantinių ryšių sistemoms ir duomenų transformavimui per fotoninius pluoštus. Didelio galingumo radialinės poliarizacijos impulsai yra svarbūs ir lazeriniame medžiagų apdorojime bei elektronų greitinimui išilginiu šviesos elektrinio lauko komponentu. THz dažnio sūkurinių impulse tyrimas potencialiai gali atverti naujus kelius aktyviai plačiajuosčių terahercų dažnio pluoštų savybių kontrolei bei atveria naujas terahercų dažnio fizikos galimybes, singuliarinės optikos sritį išplečiant iki terahercų dažnio. Sukurti optiniai lašelių sukimo metodai ir jų susidūrimų tyrimas turi praktinę reikšmę skysčių dinamikoje, tyrinėjant lietaus lašų susidarymą ir turbulencijos įtaką šiam procesui.

Pagrindiniai ginamieji teiginiai

1. Net nedideli fazes vėlinimo netikslumai geometriniame fazės vėlinime sukelia generuojamo pluošto poliarizacijos, fazės ir intensyvumo pasiskirstymų asimetriją. Homogeniškų fazės vėlinimų geometriniame fazės lėtintuve atveju, ši asimetrija yra stipri. Kai vėlinimas osciliuoja apie pusės bangos plokštelės vėlinimą, ši asimetrija išnyksta laisvo pluošto sklidimo metu, todėl pluošto poliarizacijos, fazės ir intensyvumo pasiskirstymai tampa simetriški.

2. Geometriniu fazės lėtintuvu konvertuojamos impulso sūkurinės ir nesūkurinės būsenos gali būti erdviškai atskirtos užtikrinant bet kurios bangos ilgio (oktavos diapazone aplink numatytąjį bangos ilgį) sūkurių koaksialumą.

3. THz dažnio bangų galia mažėja, joms sklindant per iš anksto lazerio impulsais sukurtą plazmą net tada, kai dviejų lazerio pluoštų susikirtimo taškai yra daug arčiau arba už žadinančio lazerio pluošto sąsmaukos. Už šį efektą atsakingi ne mažiau kaip du skirtingi mechanizmai, t.y., žadinančių bangų fazių modifikavimas ir ekranavimas lazerio impulsais iš anksto sukurtoje plazmoje.

4. Terahercų dažnio spinduliuotės, generuojamos elektronų srove, indukuota pirmosios harmonikos Gauso ir antrosios harmonikos optinio sūkurio žadinimo, intensyvumas tampa moduliuotas THz pluošto azimutinio kampo atžvilgiu ir turi du minimumus tarp dviejų maksimalaus intensyvumo taškų. Šitaip generuojamos terahercinės spinduliuotės fazė yra singuliari.

5. Radialinę, azimutinę arba mišrią poliarizacijos būseną galima generuoti išsigimusiame optiniame parametriniame stiprintuve (su Gauso žadinimu ir sūkuriniu signalu). Galutinę poliarizacijos būseną galima aktyviai valdyti ir perjunginėti, valdant santykinę fazę tarp skirtuminės ir signalinės bangų, arba tarp skirtuminės bangos ir žadinimo.

6. Sukurta optinė dalelių lokalizavimo schema, kaip dalis universalios modulinės sistemos skirtos optinio dalelių manipuliavimo eksperimentams, leidžia kontroliuojamus ir atsikartojančius mikronų dydžio lašelių susidūrimo dinamikos gravitaciniame lauke eksperimentus.

7. Dvejopalaužiškumu nepasižyminčių (izotropinių) ir nesugeriančių (skaidrių) glicerolio lašelių optinė levitacija sūkuriniame šviesos pluošte leidžia perjunginėti sukimosi ir sukiojimosi judesius. Judesio tipas priklauso nuo gaudančiojo pluošto sąsmaukos matmenų, kurie yra kontroliuojami gaudančiojo lazerio pluošto galios lygiu.

Plačiajuosčių singuliarinių šviesos laukų generavimas S bangine plokštele

Šis skyrius iš dalies pagrįstas [A4] publikacija.

Pirmoje šio skyriaus dalyje aptariama homogeninių ir nehomogeninių vėlinimo nuokrypių (perturbacijų) geometriniame fazės lėtintuve įtaka generuojamo pluošto poliarizacijai ir fazinei struktūrai (radiališkai/ azimutiškai poliarizuoti pluoštai, apskritimiškai poliarizuotas optinis sūkurinis pluoštas) kuris buvo ištirtas teoriškai ir eksperimentiškai. Buvo tirtas asimetrijos ir nehomogeniškumo atsiradimas intensyvumo/poliarizacijos pasiskirstymuose, kaip ir optinio sūkurio padėties poslinkis. Rezultatai aptariami remiantis sukinio konvertavimo į orbitinį momentą formalizmu. Azimutiškai nehomogeninių (sinusinio svyravimo) perturbacijų tyrimai parodė galimybę išvengti generuojamos šviesos iškraipymų. Mūsų teorija rodo, ir eksperimentas tai patvirtina, kad vėlinimo nuokrypiai geometriniame fazės lėtintuve lemia intensyvumo, poliarizacijos ir konvertuoto pluošto fazės pasiskirstymo simetrijos susilpnėjimą. Tai savo ruožtu lemia ortogonaliai poliarizuotų konvertuojamų pluoštų optinių sūkurių lokalizacijų neatitikimą, bei jų judėjimą pagal skirtingas trajektorijas, kas sukelia sūkurio fazės atsiradimą generuojamuose radiališkai/azimutiškai poliarizuotuose pluoštuose (4.20a pav.). Kai lėtinimo nuokrypis yra nehomogeniškas ir svyruoja aplink π vertę, tuomet abiejuose priešingai apskritimiškai poliarizuotuose kompleksiniuose pluošto komponentuose atsiranda optiniai sūkuriai. Tačiau "blogo" komponento matmenys yra didesni, nei "naudingo" sūkurio komponento ir sklisdami difraguoja daug greičiau. Todėl norima azimutriškai simetriška fazė, intensyvumas ir poliarizacija automatiškai atsistato.

Antrajame skyriuje aprašomas optinių sūkurinių pluoštų generavimas matomojo ir artimojo infraraudonojo spektro srityje plačiame bangų ilgių diapazone, tam naudojant poliarizacijos konverterį su viena S bangine plokštele ir taikant selektyvų poliarizacijos filtravimą. Naudojant siūlomą poliarizacijai jautrų filtravimą, mes demonstruojame optinio sūkurinio pluošto generavimą iš kvazikoherentinių ir nekoherentinių šviesos šaltinių visame matomame ir

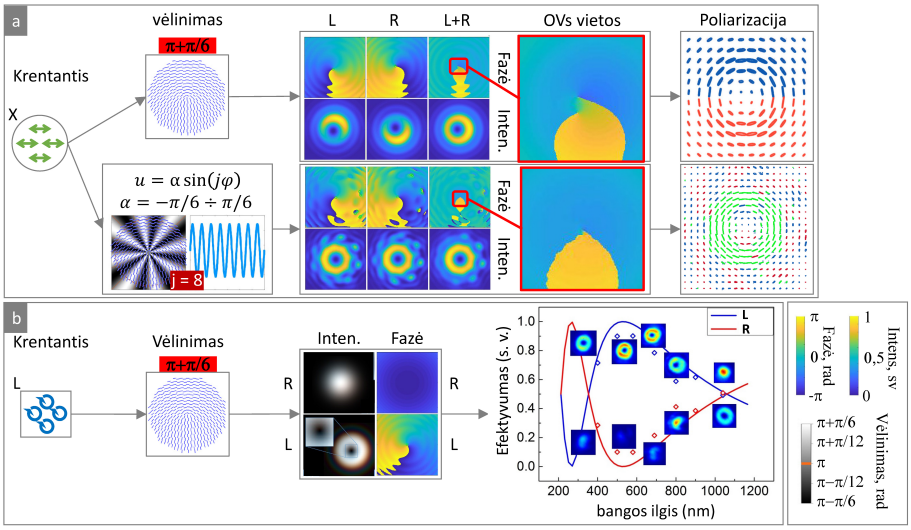

Figure 4.20: **(a)** šviesos pluošto, transformuoto geometriniame fazės lėtintuve su sinusiniu vėlinimo profiliu $u = \sin(j\varphi)$ poliarizacijos, fazės ir intensyvumo pasiskirstymų modeliavimo rezultatai. Vėlinimo pasiskirstymas ir gautas pluošto profilis parodyti stulpelyje "Retardance". Žymėjimai L, R, ir $L + R$ atitinkamai parodo kairinių, dešininių bei kombinuotų kairinių ir dešininių apskritiminės poliarizacijos pluošto komponentų intensyvumą ir fazę. Kombinuotų kairinių ir dešininių apskritiminės poliarizacijos pluošto komponentų optinių sūkurių vietos parodytos stulpelyje "OVs locations". **(b)** Poliarizacijai jautraus šviesos pluoštų valymo efektyvumo priklausomybė nuo bangos ilgio. Eksperimentiniai taškai lyginami su teorine kreive. Intarpai demonstruoja eksperimentiškai išmatuotus generuojamų OS pluoštų profilius ir išfiltruotos foninės spinduliuotės profilius skirtingiems bangos ilgiams. 532 nm bangos ilgiui vėlinimas lygus π.

artimajame infraraudonajame spektro diapazone. Šis metodas leidžia bet kurį nuo bangos ilgio priklausomą (chromatinį) Pancharatnam-Berry fazinį elementą konvertuoti į achromatinį. Mes naudojome aukšto optinės pažeidos slenksčio S banginę plokštelę [71] 532 nm bangos ilgiui ir parodėme, kad didelio kontrasto OS pluoštų generavimui ji gali būti naudojama bet kuriame bangos ilgių intervale nuo 400 nm iki 1040 nm (4.20b pav.). Filtravimo efektyvumas, t.y., galios santykis tarp išvalytos sūkurinės pluošto dalies ir nemoduliuotos fazės fono ('R' 4.20b paveikslėlyje) labai priklauso nuo bangos ilgio. Didžiausias efektyvumas pasiekiamas projektiniam S banginės plokštelės bangos ilgiui; filtravimo efektyvumas išlieka didesnis, nei 50% bangos ilgiui, kuris yra beveik du kartus didesnis už projektinį bangos ilgį, o tai rodo sėkmingas OS generavimas 600 nm bangos ilgio diapazone (šiame diapazone efektyvumas yra didesnis nei 50%).

Sūkurinių laukų išplėtimas į terahercų dažnių diapazoną

Šis skyrius pagrįstas [A1] ir [A2] publikacijomis.

Pirmajame skyriuje buvo pademonstruotas plačiajuosčių sūkurų generavimas matomoje ir artimojo infraraudonojo spektro srityje. Šiame skyriuje parodytas sūkurinių laukų generacijos metodų išplėtimas į tolimąją infraraudonąją spektro sritį ir THz dažnius.

Norint suprasti THz dažnių spinduliuotės generavimo iš plazmos gijų procesą, kaip aprašyta šio skyriaus pirmojoje dalyje mes atlikome eksperimentą, kurio metu tyrėme lazeriu sukurtos plazmos įtaką THz spinduliuotės generavimo efektyvumui. Be to, išsiaiškinus THz dažnio spinduliuotės generavimo mechanizmą, antrojoje šio skyriaus dalyje sūkurinių laukų generavimo metodai buvo išplėsti iki THz dažnių.

Pirmojoje šio skyriaus dalyje aprašytas eksperimentas, kuriame buvo tiriamos energinių ir erdvinių generuojamos THz dažnio spinduliuotės saybių priklausomybės nuo pirminės iš anksto sukurtos plazmos padėties, žadinimo pluošto ašies ir jo sąsmaukos atžvilgiu. Buvo nustatyta, jog, priklausomai nuo dviejų plazmos gijų santykinės padėties už generuojamos THz bangos galios sumažėjimą yra atsakingi skirtingi mechanizmai (4.21a pav.). **(1)** prieš pagrindinę plazmą (z = 0 ÷ 17 mm): (a) faziniai poslinkiai, sukelti žadinimo pluošto lūžio (refrakcijos) iš anksto sukurtos plazmos gijoje; (b) žadinimo intensyvumo moduliacija, kurią sukelia difrakcija ir interferencija iš anksto sukurtoje plazmoje. **(3)** už pagrindinės plazmos (z = 25 ÷ 35 mm): (c) plazmos sugertis ir atspindys: 0–28 THz dažnių atspindys ir refrakcija 28–60 THz dažnių atveju; d) Fresnelio atspindys (zona tarp dviejų terpių). **(2)** plazmos viduryje (z = 17 ÷ 25 mm): visi aukščiau minėti: (a), (b), (c), (d).

Antroje šio skyriaus dalyje buvo ištirtos ultraplačiajuosčių THz dažnio (mažiausiai tarp 10 ir 40 THz) impulsų, turinčių fazinį singuliarumą, generavimo dviejų spalvų femtosekundinių impulsų lazeriu sukurtoje dujų plazmoje ypatumai. Kai antrosios harmonikos pluoštas turi sūkurinį krūvį, THz pluoštas taip pat įgauna įvairialypę sūkurinę struktūrą. Be to, paaiškėjo, kad THz intensyvumas taip pat yra moduliuotas azimutinio pluošto kampo atžvilgiu (4.21b pav.). Intensyvumo moduliavimas susijęs su skirtingais erdviniais santykinių fazių skirtumais tarp dviejų žadinimo harmonikų. Teoriškai numatytas intensyvumo moduliavimas buvo eksperimentiškai pademonstruotas, naudojant šiluminę kamerą. Fazinio singuliarumo buvimas susidariusiame THz pluošte buvo patvirtintas, naudojant gerai išvystytą topologinio krūvio nustatymo metodą, pagrįstą astigmatine singuliarinių pluoštų transformacija cilindriškai fokusuojančiu veidrodžiu [81]. Papildomai fazinio singuliarumo buvimas buvo patvirtintas stebint THz dažnio sūkurio pokyčius, keičiant santykinę

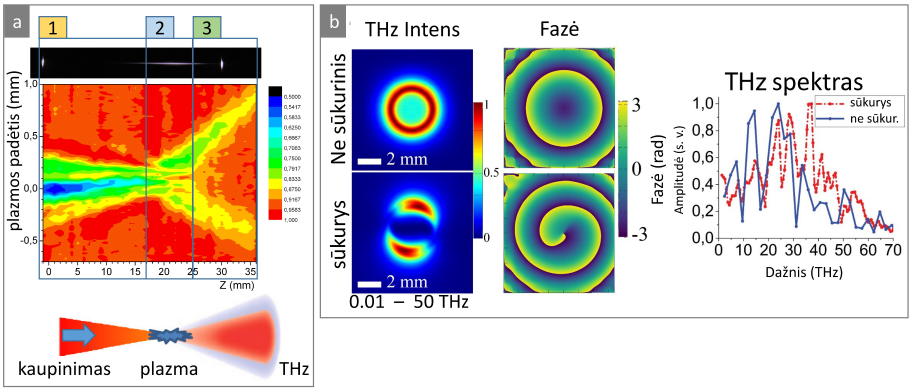

Figure 4.21: **(a)** THz intensyvumo sumažėjimas (schematiškai parodyta apačioje), kaip santykinės padėties tarp dviejų plazmos gijų (kurių nuotraukos yra) viršuje funkcija. **(b)** THz intensyvumas, fazė ir spektrai sūkuriniuose ir nesūkuriniuose pluoštuose.

fazę tarp pirmosios ir antrosios žadinimo harmonikų. Moduliuoto intensyvumo pasiskirstymas sukosi pasikeitus santykinei fazei tarp žadinimo bangų. Tolesnė teorinė analizė atskleidė du singuliarinių THz pluoštų formavimo mechanizmus. Pirma, tai yra THz spinduliuotės šaltinio nario intensyvumo ir fazės moduliavimas dėl kintamo erdvinio santykinės fazes dydžio tarp FH ir sūkurinės SH bangų. Antra, tai yra skersiniai žadinimo impulso nestabilumai. Plazmos gijos pradžioje žadinimo intensyvumas yra pasiskirstęs tolygiai ir čia atsirandantis THz sūkurys centre turi tik vieną singuliarų tašką. Jo intensyvumo pasiskirstymas yra azimutiškai moduliuotas žiedas. Priešingai, žadinimo gijos viduryje ir toliau iki jos galo žadinimo impulsas veikiamas plazmos defokusavimo, kas ir sukelia pluošto iškraipymus. Žadinimas sustiprina stipriausius iškraipymus ir šie stiprūs nestabilumai daro įtaką THz sūkurio intensyvumo pasiskirstymui bei generuojamame THz dažnio pluošte sukuria antrinius singuliarumo taškus. Papildomi singuliarūs taškai turi besikeičiančius krūvio ženklus taip, kad sklidimo metu bendras topologinis pluošto krūvis būtų išsaugomas ir lygus vienetui $l_{THz} = 1$ visiems dažnio komponentams. Vienas iš THz dažnio sūkurių generavimo plazmos srovėmis privalumų yra ultraplačiajuosčių sūkurių generavimas, kas buvo parodyta didesniam nei 40 THz spektro pločiui, skirtingai nuo spektriškai riboto THz sūkurių formavimo išoriniais optiniais elementais.

Optinis parametrinis stiprintuvas generuojantis radiališkai poliarizuotą pluoštą

Šis skyrius pagrįstas [A5] publikacija.

Yang et. al. [72] eksperimentiškai parodė, kad “Laguerre-Gauso” modų

(optinių sūkurių) superpozicija yra radiališkai ir azimutiškai poliarizuotas pluoštas (4.22a pav.). Jie naudojo erdvinį šviesos moduliatorių, kad sukurtų du optinius skirtingų topologinių krūvių sūkurius ir juos sutapatintų. Šiame darbe buvo pasiūlytas naujas radiališkai ir azimutiškai poliarizuotų pluoštų formavimo būdas, taip pat buvo pasiūlyta kurti aukštesnio laipsnio poliarizacijos singuliarumus, sudedant optinius sūkurius su priešingais topologiniais krūviais, kurie gaunami naudojant optinį parametrinį stiprinimą (OPS). Pasiūlytas metodas gali būti naudojamas kurti galingus pluoštas, kuriuos riboja tik netiesinių kristalų pažeidimo slenkstis. Apibendrinami pagrindiniai šio metodo fizikiniai principai ir galimi jo išplėtimai. Pateikiami eksperimentiniai rezultatai.

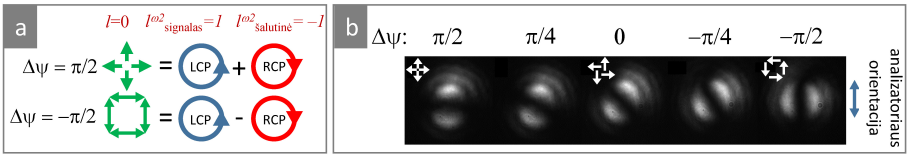

Figure 4.22: **(a)** Sūkurinių pluoštų kombinacijos schema, skirta radialinei arba azimutinei pluošto poliarizacijai suformuoti. **(b)** Eksperimentiškai derinama OPS išėjimo pluošto poliarizacija.

Be to, siūlomas metodas gali būti lengvai automatizuojamas. Jei pradinio signalo pluošto moduliavimui naudojamas erdvinis šviesos moduliatorius, jis gali suteikti galimybę lengvai kompiuteriu valdyti ir perjunginėti pluošto modas (4.22b pav.). Atsižvelgiant į padidėjusią išėjimo galią, šis metodas gali rasti taikymus lazerinių medžiagų apdorojimo ir elektronų greitinimo/suspaudimo išilginiu fokusuoto radiališkai poliarizuoto pluošto elektrinio lauko komponento elektriniame lauke ir fundamentiniuose tyrimuose.

Universali modulinė sistema, skirta optinio dalelių manipuliavimo eksperimentams

Šis skyrius pagrįstas [A3], [A6], [B1] ir [B2] publikacijomis.

Optinė levitacija, nors ir rečiau naudojama dėl didesnės pluošto galios poreikio, palyginti su optiniais pincetais, turi keletą privalumų. Pirma, taikinį galima pagauti dujinėje aplinkoje, pavyzdžiui, ore. Antra, taikinys gali būti sulaikytas dideliais atstumais nuo pagaunančio lęšio, paprastai kelių centimetrų ar net didesniu atstumu. Tai leidžia beveik 4π prieigą prie pagautos dalelės, kuri gali būti naudojama vienu metu įgyvendinant skirtingus analizės ir manipuliavimo metodus. Trečia, dėl didelio gaudymo atstumo, bet kokie sienų efektai sulaikytai dalelelei yra nereikšmingi. Ilgalaikis šios krypties tikslas yra sukurti sistemą, kurioje galimabūtų tirti lašelių sąveiką su aplinkinėmis terpėmis ar kitais lašeliais, visiškai kontroliuojant visus fizinius parametrus. Šio darbo metu

siekiant šio tikslo buvo įdėta daug pastangų. Konkrečiai, buvo sukurtos šios modulinės sistemos dalys, skirtos optinės levitacijos eksperimentams.

Pirma, tai yra dalis mikrono dydžio lašelių susidūrimo dinamikos tyrimų gravitacijos sąlygomis. Susidūrimo efektyvumas, apibrėžiamas kaip susidūrimo skerspjūvio ir geometrinio skerspjūvio santykis, yra bedimensinis susidūrimų tikimybės matas. Be lašelių augimo greičio nustatymo, susidūrimų efektyvumas yra pagrindinis debesų lašelių, plačiai naudojamų daugelyje oro ir klimato modelių, teorijos elementas. Susidūrimų efektyvumas yra labiausiai neapibrėžtas susidūrimų greičio teorijų aspektas. Eksperimentinis susidūrimo efektyvumo nustatymas tebėra sudėtingas. Todėl šiame darbe pateikiama naujas eksperimentinis metodas, leidžiantis sukurti ir vaizdinti mikronų dydžio lašelių susidūrimą gravitacijos sąlygomis. Dviejų optinių gaudyklių pagalba ore sulaikoma pora glicerolio lašelių (4.23a pav.). Santykiniai lašelių greičiai nustatomi pagal lašelių dydžius. Susidūrimo parametras yra tiksliai reguliuojamas, lašelius pozicionuojant dviejomis optinėmis gaudyklėmis. Lašeliai paleidžiami išjungiant gaudymo spinduliuotę, tam naudojant elektrooptinius moduliatorius. Tuomet nusėdančių lašelių judėjimą fiksuoja dvi sinchronizuotos didelės spartos kameros, kurių kadravimo dažnis yra iki 63 kHz. Skirtingai nuo ankstesnių tyrimų su optiniais pincetais, šis metodas leidžia tiesiogiai vaizdinti lašelių susidūrimą, nepaveikiant optinės izoliacijos, sukurtos, sulaikančiomis jėgomis. Mes visiškai kontroliuojame pradines susidūrimų proceso sąlygas, būtent susidūrimo parametrą, dydžių santykį ir lašelių cheminę sudėtį. Dideliems susidūrimo parametrams ($B = 0.5$) matėme, kad artėjantys lašeliai vienas kitą atstumia nuo savo nusistovėjusių trajektorijų (4.23 pav.). Mažo susidūrimų parametro ($B = 0.14$) atveju susidūrimas sukelia nuolatinį susiliejimą (neparodytas). Mūsų žiniomis, tai yra pirmasis bandymas ištirti mikrono dydžio lašelių sąveiką veikiant gravitacijai ir esant visiškai kontroliuojamoms pradinėms sąlygoms. Pažanga šiose tyrimų srityse paspartins mūsų supratimą apie debesyse vykstančią stiprią turbulencijos ir mikroskopinių procesų sąveiką.

Antra, kaip nurodyta šio skyriaus pirmoje dalyje, tai yra dalis lašelių optinio sukimosi tyrimo sistemos, leidžiančios atsižvelgti į turbulencijos poveikį debesyse. Šviesos kampinio momento sukimosi dalis dvejopai šviesą laužiančią dalelę gali sukti aplink jos ašį, tačiau neturi jokio poveikio šia savybe nepasižyminčioms dalelėms. Orbitinė šviesos kampinio momento dalis, kita vertus, gali priversti abi (dvejopai šviesą laužiančią ir šia savybe nepasižyminčią) daleles suktis apie šviesos pluošto ašį. Šiame darbe buvo pademonstruota, kad šviesos dvejopalaužiškumu nepasižyminčios dalelės taip pat gali suktis apie savo ašį, jei yra pagautos optiniame sūkuriniame pluošte. Šiame eksperimente lašelis iš pradžių yra įstrigęs optinio sūkurinio pluošto žiede (4.23b pav.). Lašelis yra nesuvaržytas azimutiškai ir rodo orbitinį judėjimą aplink pluošto ašį, kurį sukelia šviesos kampinis momentas. Sumažinus lazerio galią, lašelis juda link lazerio pluošto sąsmaukos. Tam tikru momentu lašelių dydis tampa palyginamas su lazerio

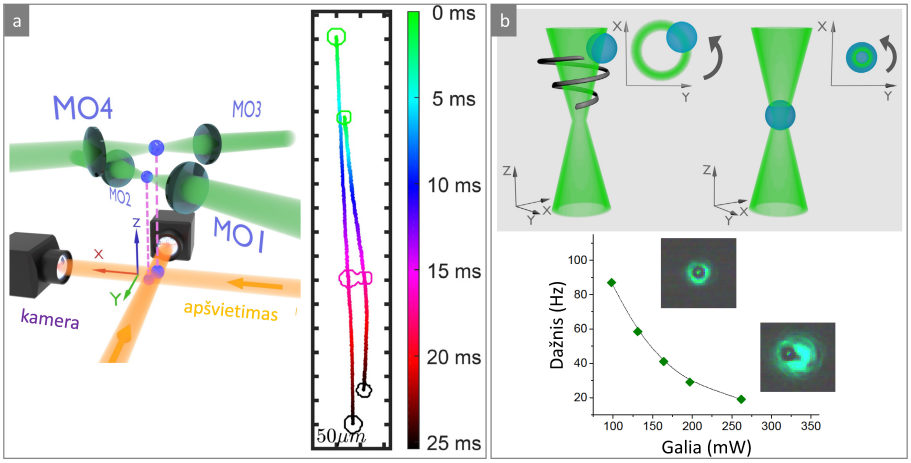

Figure 4.23: **(a)** Eksperimentinės grandinės schema (kairėje pusėje) ir eksperimentinis laisvai krintančių lašelių dinamikos rezultatų pavyzdys (dešinėje pusėje). **(b)** Idėjos iliustracija (viršutinė dalis) ir eksperimentiniai rezultatai, rodantys lašelių judesio perjungimą iš orbitinio sukimosi į sukiojimąsi aplink savo ašį (apatinė dalis).

pluošto sąsmaukos matmenimis. Tada įstrigęs lašelis yra azimutiškai lokalizuojamas ir šviesos kampinis momentas sukelia dalelės sukimąsi aplink savo ašį. Besisukančių lašelių sukimosi greitis yra nuolat kontroliuojamas nuo nulio iki maksimalaus, tam naudojant sukiojimosi ir orbitinio sukimosi momentų sąveiką, kuri pasiekiama, sukant ketvirčio bangos ilgio fazinę plokštelę. Įstrigusio lašelio judėjimas stebimas naudojant didelės spartos kamerą, o sukimosi dažnis matuojamas fotodiodu. Nors eksperimentas buvo atliktas ore su skysčių lašeliais, aprašytas metodas gali būti sėkmingai naudojamas įprastiniuose optiniuose pincetuose. Todėl šis metodas gali rasti taikymų ne tik optikoje, bet ir kitose srityse, pvz., skysčių dinamikos tyrimuose, kai tyrinėjant lietaus lašų formavimąsi, besisukantys lašeliai gali būti gaunami tiriant skystų lašelių susidūrimo dinamiką [44], kas jau buvo minėta šio skyriaus pirmojoje dalyje.

Išvados

1. Nedideli fazes vėlinimo netikslumai S banginėje plokštelėje (ir geometriniame fazės lėtintuve apskritai), nepaisant to, ar jie sukelti pradinio bangos ilgio netikslumų, ar gamybos defektų, pasireiškia sudėtinga konvertuojamo pluošto struktūra, susidedančia iš sūkurinių ir nesūkurinių komponentų. Savo ruožtu tai sukelia sūkurių padėties poslinkius pluošte, asimetrinę šviesos intensyvumo pasiskirstymo asimetriją ir sūkurinės fazės atsiradimą, generuojant radialinę/azimutinę poliarizaciją. Kuo didesni lėtinimo netikslumai, tuo didesnis sūkurio poslinkis. Kai lėtėjimo netikslumas yra

homogeniškas, pvz., dėl pradinio bangos ilgio nesutapimo, nesūkurinio komponento erdvinis dydis yra toks pat, kaip ir sūkurinio, kas stipriai iškraipo generuojamo pluošto sūkurio padėtį, intensyvumą, fazę ir poliarizacijos pasiskirstymą. Tačiau, kai lėtėjimo netikslumas yra nevienalytis, pvz., dėl gamybos klaidų, ir svyruoja apie π vertę, tuomet abu sudėtinio pluošto komponentai turi sūkurius. Tačiau "blogo" komponento matmenys yra didesni už "naudingo" sūkurio komponento dydį ir sklindant difraguoja daug greičiau. Aukštesni svyravimai lemia didesnį "blogo" komponento dydį. Todėl po tam tikro laisvos erdvės sklidimo norima generuojamo pluošto poliarizacija ir fazinė būsena automatiškai atsistato.

2. Pademonstruota baltos šviesos ir plačiajuosčio (apimančio daugiau, nei oktavą) sūkurinio pluošto generacija, naudojant vieną S banginę plokštelę (geometrinį fazes lėtintuvą). S banginė plokštelė (ir geometrinis fazės lėtintuvas apskritai) turi indukuoti tikslų pusės bangos ilgio fazės vėlavimą tam, kad būtų teisingai konvertuojamos pradinio pluošto poliarizacija ir fazė. Kai pradinis bangos ilgis keičiasi, fazės vėlavimas, kurį šviesos pluoštai patiria, taip pat kinta. Todėl susidaręs kompleksinis šviesos pluoštas susideda iš sūkurinių ir nesūkurinių sudedamųjų dalių, kurios gali būti atskiriamos pagal poliarizacijas. Pasirenkant apskritimiškai poliarizuotą (nukreiptą priešinga pradinės spinduliuotės kryptimi) komponentą, mes pasirenkame tik tuos pluošto komponentus, kurie patyrė tinkamą pusės bangos ilgio fazės vėlavimą, taigi, mes pasirenkame tik sūkurinį komponentą. Eksperimento metu naudota S banginė plokštelė indukuodavo pusės bangos ilgio fazes vėlinimą $\lambda_0 = 532$ nm bangos ilgio šviesai. Sūkurių generacija buvo pademonstruota, kai bangos ilgis kito nuo 400 nm iki 1000 nm, atitinkamai mažėjant generacijos efektyvumui labiau nutolusiems nuo numatytojo bangos ilgio λ_0 šviesos pluoštams bet visiems demonstruotiems spektro pločiams vis dar būnant didesniam nei 50%.

3. Kai THz dažnio spinduliuotę genegeneruojanti plazmos gija susikerta su kita iš anksto sukurta plazmos gija, o bichromatinio žadinimo ir papildomą plazmą kuriančio pluoštų susikirtimo taškas yra už žadinančio pluošto sąsmaukos, plazmos sugertis ir ekranavimas vaidina svarbų vaidmenį ir žymiai sumažina THz spinduliuotės intensyvumą. Kita vertus, kai susikirtimo taškas yra prieš žadinimo pluošto sąsmauką, pagrindinis reiškinys atsakingas už žymų THz spinduliuotės modifikavimą yra išanksto sukurtos plazmos gijos įtaka bichromatinio žadinimo pluošto intensyvumui ir santykinei fazei.

4. Pirmą kartą, mūsų žiniomis, mes pademonstravome sūkurinių THz dažnio impulsų generavimą plazmos gijose, indukuotose gausiniais pirmosios lazerio harmonikos impulsais kartu su sūkurine antrosios harmonikos spinduliuote. Fazinio singuliarumo buvimas susidariusiame THz pluošte buvo

patvirtintas, naudojant astigmatinę singuliarinių THz pluoštų transformacija cilindriškai fokusuojančio veidrodžio sąsmaukoje bei pilnai erdvę ir laiką aprašančiu skaitmeniniu modeliavimu. Be to, tai papildomai buvo patvirtinta analizuojant THz pluošto intensyvumo pasiskirstymo pokyčius, atsirandančius, keičiant santykinę faze tarp pirmosios ir antrosios lazerio harmonikų, kuriančių plazmos giją. Sūkurinio THz pluošto intensyvumas yra moduliuotas jo azimutinioį kampo atžvilgiu ir susideda iš dviejų minimumų ir tarp jų esančių dviejų didžiausio intensyvumo sričių. Taip yra todėl, kad santykinė fazė tarp dviejų harmonikų kinta priklasomai nuo pluošto azimuto, kai antrosios harmonikos žadinimo impulsas yra sūkurinis. Be to, mūsų skaitmeniniai modeliai rodo, kad skersinis nestabilumas žadinimo pluošto gijoje sklidimo metu gali įtakoti THz sūkurį, jo nesunaikindamas. Tai gali indukuoti antrinius fazinius singuliarumus, dėl kurių generuojamų struktūrizuotų THz laukų fazinė topologija tampa ypač turtinga. Vienas iš THz spinduliuotės generavimo iš plazmos srovių privalumų yra didelis (>40 THz) spektro diapazonas, nepasiekiamas alternatyviais metodais, tokiais kaip spektriškai ribotų THz dažnio sūkurių formavimas išoriniais optiniais elementais.

5. Skirtuminės bangos impulsas, generuojamas gausiniu žadinimo impulsu ir sūkurine signaline banga pasižymi sūkurine faze, kurios sūkurio kryptis yra priešinga signalinės bangos sūkurio krypčiai. II tipo netiesiniuose kristaluose signalinės ir skirtuminės bangų poliarizacijos taip pat yra ortogonalios. Todėl išsigimusio parametrinio stiprinimo atveju signalinės ir skirtuminės bangų sūkuriai (vienodo bangos ilgio), turėdami priešingą topologinį krūvį ir ortogonalias tiesines poliarizacijas gali suformuoti besūkurinę egzotinę poliarizacijos būseną, tam naudojant paprastą ketvirčio bangos ilgio plokštelę, konvertuojančią ortogonalias tiesines sūkurių poliarizacijos būsenas į ortogonalias nesūkurines apskritiminės poliarizacijos būsenas. Egzotinių poliarizacijos būsenų, pvz., radialinių, azimutinių arba jų kombinaciją, kontroliuojamos, keičiant fazės vėlavimą tarp signalinės ir skirtuminės bangų. $\pi/2$ fazės vėlinimas indukuoja radialinę poliarizaciją, o π fazės vėlinimas keičia poliarizacijos būseną į azimutinę. Aktyvaus poliarizacijos valdymo ir poliarizacijos formavimo galimybė be išorinių optinių komponentų (taigi, didelio optinio pažeidimo slenksčio ir labai aukštų energijos lygių) šį metodą daro labai patraukliu įvairiems taikymams.

6. Buvo įdėta daug pastangų, kuriant universalią sistemą, skirtą dalelių optinio manipuliavimo eksperimentams, kurių metu galima tirti lašelių sąveiką su aplinkinėmis terpėmis ar kitais lašeliais, visiškai kontroliuojant visus fizikinius parametrus. Mes sukūrėme ir pademonstravome sistemą, skirtą modeliuoti tiksliems ir atsikartojantiems susidūrimams tarp smulkių mikrono eilės dydžio skysčių lašelių. Naudojant šią sistemą galima valdyti

dalelių skersmenį (taigi, ir galutinį greitį), smūgių skaičių, cheminę sudėtį ir elektrinį lašelių krūvį.

7. Be to, mes sukūrėme naują metodą, optiniame sūkuryje leidžiantį sukti dvejopalaužiškumu nepasižyminčius ir nesugeriančius skysčio lašelius. Pagauti lašeliai gali suktis apie gaudančio pluošto ašį arba suktis apie savo ašį. Sukimosi judesio tipas priklauso nuo gaudančio pluošto sąsmaukos matmenų ties pagauta dalele. Vertikali pagavimo padėtis valdoma, keičiant gaudančio lazerio pluošto galios lygį. Lašelio sukimosi dažnis priklauso nuo pluošto poliarizacijos (nors lašelis nepasižymi dvejopalaužiškumu) dėl pluošto kampinio ir orbitinio momentų sąveikos. Poliarizaciją galima tolygiai kontroliuoti keičiant ketvirčio bangos ilgio plokštelės orientaciją. Dar vienas galimas parametras, leidžiantis kontroliuoti susidūrimų eksperimentą, yra lašelių sukimasis. Lašelių susidūrimo dinamikos tyrimai, tiksliai kontroliuojant minėtą parametrą yra esminiai, srityje skysčių dinamikos sprendžiant debesų susidarymo problemas.

Bibliography

[1] J. F. Nye, M. V. Berry, F. C. Frank, Dislocations in wave trains, Proceedings of the Royal Society of London. A. Mathematical and Physical Sciences **336**(1605), 165–190 (1974).

[2] M. S. Soskin, V. N. Gorshkov, M. V. Vasnetsov, J. T. Malos, N. R. Heckenberg, Topological charge and angular momentum of light beams carrying optical vortices, Phys. Rev. A **56**, 4064–4075 (1997).

[3] J. Leach, M. R. Dennis, J. Courtial, M. J. Padgett, Knotted threads of darkness, Nature **432** (2004).

[4] I. V. Basistiy, M. S. Soskin, M. V. Vasnetsov, Optical wavefront dislocations and their properties, Opt. Commun. **119**(5–6), 604 – 612 (1995).

[5] J. Leach, S. Keen, M. J. Padgett, C. Saunter, G. D. Love, Direct measurement of the skew angle of the poynting vector in a helically phased beam, Opt. Express **14**(25), 11919–11924 (2006).

[6] P. U. Jepsen, D. G. Cooke, M. Koch, Terahertz spectroscopy and imaging – modern techniques and applications, Laser Photonics Rev **5 (1)**, 124–166 (2011).

[7] C. Kealhofer, W. Schneider, D. Ehberger, A. Ryabov, F. Krausz, P. Baum, All-optical control and metrology of electron pulses, Science **352**, 429–433 (2016).

[8] J. He, X. Wang, D. Hu, J. Ye, S. Feng, Q. Kan, Y. Zhang, Generation and evolution of the terahertz vortex beam, Opt. Express **21**(17), 20230–20239 (2013).

[9] R. Imai, N. Kanda, T. Higuchi, K. Konishi, M. Kuwata-Gonokami, Generation of broadband terahertz vortex beams, Opt. Lett. **39**(13), 3714–3717 (2014).

[10] K. Miyamoto, B. J. Kang, W. T. Kim, Y. Sasaki, H. Niinomi, K. Suizu, F. Rotermund, T. Omatsu, Highly intense monocycle terahertz vortex generation by utilizing a tsurupica spiral phase plate, Scientific Reports **6**, 38880 (2016).

[11] S. Ge, P. Chen, Z. Shen, W. Sun, X. Wang, W. Hu, Y. Zhang, Y. Lu, Terahertz vortex beam generator based on a photopatterned large birefringence liquid crystal, Opt. Express **25**(11), 12349–12356 (2017).

[12] S.-J. Ge, Z.-X. Shen, P. Chen, X. Liang, X.-K. Wang, W. Hu, Y. Zhang, Y.-Q. Lu, Generating, separating and polarizing terahertz vortex beams via liquid crystals with gradient-rotation directors, Crystals **10**(7), 314 (2017).

[13] A. Minasyan, C. Trovato, J. Degert, E. Freysz, E. Brasselet, E. Abraham, Geometric phase shaping of terahertz vortex beams, Opt. Lett. **42**(1), 41–44 (2017).

[14] C. Liu, J. Liu, L. Niu, X. Wei, K. Wang, Z. Yang, Terahertz circular airy vortex beams, Scientific Reports **7**, 3891 (2017).

[15] Z. Wu, X. Wang, W. Sun, S. Feng, P. Han, J. Ye, Y. Yu, Y. Zhang, Vectorial diffraction properties of thz vortex bessel beams, Opt. Express **26**(2), 1506–1520 (2018).

[16] Q. Lin, S. Zheng, Q. Song, X. Zeng, Y. Cai, Y. Li, Z. Chen, L. Zha, X. Pan, S. Xu, Generation of terahertz vortex pulses without any need of manipulation in the terahertz region, Opt. Lett. **44**(4), 887–890 (2019).

[17] A. A. Dhaybi, J. Degert, E. Brasselet, E. Abraham, E. Freysz, Generation of terahertz vortex pulses without any need of manipulation in the terahertz region, J. Opt. Soc. Am. B **36**(1), 12–18 (2019).

[18] K. Dholakia, N. B. Simpson, M. J. Padgett, L. Allen, Second-harmonic generation and the orbital angular momentum of light, Phys. Rev. A **54**, R3742 – R3745 (1996).

[19] A. Berzanskis, A. Matijosius, A. Piskarskas, V. Smilgevicius, A. Stabinis, Conversion of topological charge of optical vortices in a parametric frequency converter, Opt. Commun. **140**(4–6), 273 – 276 (1997).

[20] A. Berzanskis, A. Matijosius, A. Piskarskas, V. Smilgevicius, A. Stabinis, Sum-frequency mixing of optical vortices in nonlinear crystals, Opt. Commun. **150**(1–6), 372 – 380 (1998).

[21] A. Bahabad, A. Arie, Generation of optical vortex beams by nonlinearwave mixing, Opt. Express **15**(26), 17619 17624 (2007).

[22] J. Arlt, K. Dholakia, L. Allen, M. J. Padgett, Parametric down-conversion for light beams possessing orbital angular momentum, Phys. Rev. A **59**, 3950 – 3952 (1999).

[23] W. T. Buono, L. F. C. Moraes, J. A. O. Huguenin, C. E. R. Souza, A. Z. Khoury, Arbitrary orbital angular momentum addition in second harmonic generation, New J. Phys. **16**, 093041 (2014).

[24] T. Roger, J. J. F. Heitz, E. M. Wright, D. Faccio, Non-collinear interaction of photons with orbital angular momentum, Sci. Rep. **3**, 3491 (2013).

[25] F. A. Bovino, M. Braccini, M. Giardina, C. Sibilia, Orbital angular momentum in noncollinear second-harmonic generation by off-axis vortex beams, J. Opt. Soc. Am. B **28**(11), 2806 – 2811 (2011).

[26] V. G. Niziev, A. V. Nesterov, Influence of beam polarization on laser cutting efficiency, Journal of Physics D: Applied Physics **32**(13), 1455 (1999).

[27] M. Kraus, M. A. Ahmed, A. Michalowski, A. Voss, R. Weber, T. Graf, Microdrilling in steel using ultrashort pulsed laser beams with radial and azimuthal polarization, Opt. Express **18**(21), 22305–22313 (2010).

[28] R. Weber, A. Michalowski, M. Abdou-Ahmed, V. Onuseit, V. Rominger, M. Kraus, T. Graf, Effects of radial and tangential polarization in laser material processing, Physics Procedia **12**, 21 – 30 (2011).

[29] O. J. Allegre, W. Perrie, S. P. Edwardson, G. Dearden, K. G. Watkins, Laser microprocessing of steel with radially and azimuthally polarized femtosecond vortex pulses, Journal of Optics **14**(8), 085601 (2012).

[30] D. N. Gupta, N. Kant, D. E. Kim, H. Suk, Electron acceleration to gev energy by a radially polarized laser, Physics Letters A **368**(5), 402 – 407 (2007).

[31] V. Marceau, A. April, M. Piché, Electron acceleration driven by ultrashort and nonparaxial radially polarized laser pulses, Opt. Lett. **37**(13), 2442–2444 (2012).

[32] S. Payeur, S. Fourmaux, B. E. Schmidt, J. P. MacLean, C. Tchervenkov, F. Légaré, M. Piché, J. C. Kieffer, Generation of a beam of fast electrons by tightly focusing a radially polarized ultrashort laser pulse, Applied Physics Letters **101**(4), 041105 (2012).

[33] D. G. Grier, A revolution in optical manipulation, Nature **424**(6950), 810–816 (2003).

[34] D. McGloin, D. R. Burnham, M. D. Summers, D. Rudd, N. Dewara, S. Anandc, Optical manipulation of airborne particles: techniques and applications, Faraday Discuss. **137**, 335–350 (2008).

[35] M. P. MacDonald, L. Paterson, K. Volke-Sepulveda, J. Arlt, W. Sibbett, K. Dholakia, Creation and manipulation of three-dimensional optically trapped structures, Science **296**(5570), 1101–1103 (2002).

[36] S. M. Barnett, L. Allen, R. P. Cameron, C. R. Gilson, M. J. Padgett, F. C. Speirits, A. M. Yao, On the natures of the spin and orbital parts of optical angular momentum, J. Opt. **18**, 064004 (2016).

[37] M. E. J. Friese, T. A. Nieminen, N. R. Heckenberg, H. Rubinsztein-Dunlop, Optical alignment and spinning of laser-trapped microscopic particles, Nature **394**, 348–350 (1998).

[38] A. T. O'Neil, I. MacVicar, L. Allen, M. J. Padgett, Intrinsic and extrinsic nature of the orbital angular momentum of a light beam, Phys. Rev. Lett. **88**(5), 053601 (2016).

[39] H. He, M. E. J. Friese, N. R. Heckenberg, H. Rubinsztein-Dunlop, Direct observation of transfer of angular momentum to absorptive particles from a laser beam with a phase singularity, Phys. Rev. Lett. **75**(5), 826 – 829 (1995).

[40] N. B. Simpson, K. Dholakia, L. Allen, M. J. Padgett, Mechanical equivalence of spin and orbital angular momentum of light: an optical spanner, Opt. Lett. **22**(1), 52–54 (1997).

[41] K. Volke-Sepulveda, V. Garces-Chavez, S. Chavez-Cerda, J. Arlt, K. Dholakia, Orbital angular momentum of a high-order bessel light beam, J. Opt. B: Quantum Semiclass. Opt. **4**, S82 (2002).

[42] O. Brzobohaty, M. Siler, J. Jezek, P. Jakl, P. Zemanek, Optical manipulation of aerosol droplets using a holographic dual and single beam trap, Opt. Lett. **38**(22), 4601–4604 (2013).

[43] M. Geceviius, R. Drevinskas, M. Beresna, P. G. Kazansky, Single beam optical vortex tweezers with tunable orbital angular momentum, Appl. Phys. Lett. **104**(23), 231110 (2014).

[44] M. Ivanov, K. Chang, I. Galinskiy, B. Mehlig, D. Hanstorp, Optical manipulation for studies of collisional dynamics of micron-sized droplets under gravity, Opt. Express **25**(2), 1391–1404 (2017).

[45] H. Huang, G. Xie, Y. Yan, N. Ahmed, Y. Ren, Y. Yue, D. Rogawski, M. J. Willner, B. I. Erkmen, K. M. Birnbaum, S. J. Dolinar, M. P. J. Lavery, M. J. Padgett, M. Tur, A. E. Willner, 100 tbit/s free-space data link enabled by three-dimensional multiplexing of orbital angular momentum, polarization, and wavelength, Opt. Lett. **39**(2), 197–200 (2014).

[46] M. P. J. Lavery, F. C. Speirits, S. M. Barnett, M. J. Padgett, Detection of a spinning object using light's orbital angular momentum, Science **341**(537), 537–540 (2013).

[47] L. Yan, P. Gregg, E. Karimi, A. Rubano, L. Marrucci, R. Boyd, S. Ramachandran, Q-plate enabled spectrally diverse orbital-angular-momentum conversion for stimulated emission depletion microscopy, Optica **2**(10), 900–903 (2015).

[48] J. Fischer, M. Wegener, Three-dimensional optical laser lithography beyond the diffraction limit, Laser Photonics Rev. **7**(1), 22–44 (2012).

[49] G. Foo, D. M. Palacios, , J. G. A. Swartzlander, Optical vortex coronagraph, Opt. Lett. **30**(24), 3308—-3310 (2005).

[50] M. Ivanov, D. Hanstorp, Controlled spin of a nonbirefringent droplet trapped in an optical vortex beam, Optics Communications **427**, 152 – 157 (2018).

[51] L. Marrucci, C. Manzo, D. Paparo, Optical spin-to-orbital angular momentum conversion in inhomogeneous anisotropic media, Phys. Rev. Lett. **96**, 163905 (2006).

[52] J. Atencia, M.-V. Collados, M. Quintanilla, J. Marin-Saez, I. J. Sola, Holographic optical element to generate achromatic vortices, Opt. Express **21**(18), 21056–21061 (2013).

[53] J. Grover A. Swartzlander, Achromatic optical vortex lens, Opt. Lett. **31**(13), 2042–2044 (2006).

[54] Y. Tokizane, K. Oka, R. Morita, Supercontinuum optical vortex pulse generation without spatial or topological-charge dispersion, Opt. Express **17**(17), 14519–14525 (2009).

[55] T. Wakayama, K. Komaki, Y. Otani, T. Yoshizawa, Achromatic axially symmetric wave plate, Opt. Express **20**(28), 29260–29265 (2012).

[56] F. Bouchard, H. Mand, M. Mirhosseini, Achromatic orbital angular momentum generator, New J. Phys. **16**, 123006 (2014).

[57] N. Radwell, R. D. Hawley, J. B. Gotte, S. Franke-Arnold, Achromatic vector vortex beams from a glass cone, Nat. Commun. **7**, 10564 (2016).

[58] C. Fallet, G. Sirat, Achromatization of conical diffraction: application to the generation of a polychromatic optical vortex, Opt. Lett. **41**(4), 769–772 (2016).

[59] Y. A. Egorov, T. A. Fadeyeva, A. V. Volyar, The fine structure of singular beams in crystals: colours and polarization, J. Opt. A: Pure Appl. Opt. **6**(5), S217 – S228 (2004).

[60] V. Shvedov, W. Krolikowski, A. Volyar, D. N. Neshev, A. S. Desyatnikov, Y. S. Kivshar, Focusing and correlation properties of white-light optical vortices, Opt. Express **13**(19), 7393 – 7398 (2005).

[61] E. Brasselet, Y. Izdebskaya, V. Shvedov, A. S. Desyatnikov, W. Krolikowski, Y. S. Kivshar, Dynamics of optical spin-orbit coupling in uniaxial crystals, Opt. Lett. **34**(7), 1021 – 1023 (2009).

[62] S. Slussarenko, A. Murauski, T. Du, V. Chigrinov, L. Marrucci, E. Santamato, Tunable liquid crystal q-plates with arbitrary topological charge, Opt. Express **19**(5), 4085–4090 (2011).

[63] Y. S. Rumala, G. Milione, T. A. Nguyen, S. Pratavieira, Z. Hossain, D. Nolan, S. Slussarenko, E. Karimi, L. Marrucci, , R. R. Alfano, Tunable supercontinuum light vector vortex beam generator using a q-plate, Opt. Lett. **38**(23), 5083–5086 (2013).

[64] K. Yamane, Y. Toda, R. Morita, Ultrashort optical-vortex pulse generation in few-cycle regime, Opt. Express **20**(17), 18986–18993 (2012).

[65] M. Beresna, M. Gecevičius, P. G. Kazansky, Polarization sensitive elements fabricated by femtosecond laser nanostructuring of glass [invited], Opt. Mater. Express **1**(4), 783–795 (2011).

[66] M. Beresna, M. Gecevicius, P. G. Kazansky, T. Gertus, Radially polarized optical vortex converter created by femtosecond laser nanostructuring of glass, Appl. Phys. Lett. **98**(20), 201101 (2011).

[67] A. Matijosius, P. Stanislovaitis, T. Gertus, V. Smilgevicius, Formation of optical vortices with topological charge $|l| = 1$ and $|l| = 1/2$ by use of the s-waveplate, Opt. Commun. **324**(15), 1–9 (2014).

[68] L. R. Watkins, M. Derbois, White-light ellipsometer with geometric phase shifter, Appl. Opt. **51**(21), 5060–5065 (2012).

[69] A. Niv, G. Biener, V. Kleiner, E. Hasman, Polychromatic vectorial vortex formed by geometric phase elements, Opt. Lett. **32**(7), 847–849 (2007).

[70] M. Sakamoto, R. Fukumoto, N. Murakami, R. Morita, K. Oka, Dispersion reduction in generation of high-order optical vortex using axially symmetric half-wave plates, Opt. Rev. **22**(1), 174–178 (2015).

[71] Altechna R&D, Operation manual of the S-waveplate, `https://www.altechna.com/wp-content/uploads/2018/10/operation-manual--130701.pdf`.

[72] C.-H. Yang, Y.-D. Chen, S.-T. Wu, A. Y.-G. Fuh, Independent manipulation of topological charges and polarization patterns of optical vortices, Scientific reports **6**(31546) (2016).

[73] P. Stanislovaitis, M. Ivanov, A. Matijosius, V. Smilgevicius, T. Gertus, Generation of radially polarized beams and higher order polarization singularities by optical parametric amplification of optical vortices, Optical Engineering **56**(9), 095101 (2017).

[74] A. D'Errico, M. Maffei, B. Piccirillo, C. de Lisio, F. Cardano, L. Marrucci, Topological features of vector vortex beams perturbed with uniformly polarized light, Scientific Reports **7**(40195) (2017).

[75] L. Marrucci, C. Manzo, D. Paparo, Optical spin-to-orbital angular momentum conversion in inhomogeneous anisotropic media, Phys. Rev. Lett. **96**, 163905 (2006).

[76] M. Gecevicius, M. Beresna, R. Drevinskas, P. G. Kazansky, Airy beams generated by ultrafast laser-imprinted space-variant nanostructures in glass, Opt. Lett. **39**(24), 6791–6794 (2014).

[77] M. Reuss, J. Engelhardt, S. W. Hell, Birefringent device converts a standard scanning microscope into a sted microscope that also maps molecular orientation, Opt. Express **18**(2), 1049–1058 (2010).

[78] R. Loudon, *The Quantum Theory of Light* (Oxford Science Publications, 2000), 3 edition.

[79] D. M. Palacios, I. D. Maleev, A. S. Marathay, J. G. A. Swartzlander, Spatial correlation singularity of a vortex field, Phys. Rev. Lett. **92**(14), 143905 (2004).

[80] G. A. Swartzlander, J. Schmit, Temporal correlation vortices and topological dispersion, Phys. Rev. Lett. **93**, 093901 (2004).

[81] V. Denisenko, V. Shvedov, A. S. Desyatnikov, D. N. Neshev, W. Krolikowski, A. Volyar, M. Soskin, Y. S. Kivshar, Determination of topological charges of polychromatic optical vortices, Opt. Express **17**, 23374–23379 (2009).

[82] M. V. Berry, Coloured phase singularities, New J. Phys. **4**, 66.1 – 66.14 (2002).

[83] H. Hamster, A. Sullivan, S. Gordon, R. W. Falcone, Short-pulse terahertz radiation from high-intensity-laser-produced plasmas, Phys. Rev. E **49**, 671–677 (1994).

[84] D. W. Schumacher, P. H. Bucksbaum, Phase dependence of intense-field ionization, Phys. Rev. A **54**, 4271–4278 (1996).

[85] M. Kreß, T. Loffler, M. D. Thomson, R. Dorner, H. Gimpel, K. Zrost, T. Ergler, R. Moshammer, U. Morgner, J. Ullrich, H. G. Roskos, Determination of the carrier-envelope phase of few-cycle laser pulses with terahertz-emission spectroscopy, Nature Physicsvolume **2** (2006).

[86] D. J. Cook, R. M. Hochstrasser, Intense terahertz pulses by four-wave rectification in air, Opt. Lett. **25**(16), 1210–1212 (2000).

[87] J. F. Federici, Review of four-wave mixing and phase conjugation in plasmas, IEEE Transactions on Plasma Science **19**(4), 549–564 (1991).

[88] M. Kress, T. Löffler, S. Eden, M. Thomson, H. G. Roskos, Terahertz-pulse generation by photoionization of air with laser pulses composed of both fundamental and second-harmonic waves, Opt. Lett. **29**(10), 1120–1122 (2004).

[89] K. Y. Kim, J. H. Glownia, A. J. Taylor, G. Rodriguez, Terahertz emission from ultrafast ionizing air in symmetry-broken laser fields, Opt. Express **15**(8), 4577–4584 (2007).

[90] H. Wen, D. Daranciang, A. M. Lindenberg, High-speed all-optical terahertz polarization switching by a transient plasma phase modulator, Applied Physics Letters **96**(16), 161103 (2010).

[91] Y. Minami, M. Nakajima, T. Suemoto, Effect of preformed plasma on terahertz-wave emission from the plasma generated by two-color laser pulses, Phys. Rev. A **83**, 023828 (2011).

[92] J. Das, M. Yamaguchi, Terahertz wave excitation from preexisting air plasma, J. Opt. Soc. Am. B **30**(6), 1595–1600 (2013).

[93] H. Roskos, M. Thomson, M. Kress, T. Loffler, Broadband thz emission from gas plasmas induced by femtosecond optical pulses: From fundamentals to applications, Laser & Photonics Reviews **1**(4), 349–368 (2007).

[94] V. Vaicaitis, V. Smilgevicius, V. Jarutis, Phase relations between focused bichromatic laser pulses in terahertz wave generation from gas plasma, Opt. Commun. **284**(8), 2206–2209 (2011).

[95] I. Babushkin, S. Skupin, A. Husakou, C. Köhler, E. Cabrera-Granado, L. Bergé, J. Herrmann, Tailoring terahertz radiation by controlling tunnel photoionization events in gases, New Journal of Physics **13**(12), 123029 (2011).

[96] V. Pyragaitė, V. Smilgevičius, K. Steponkevičius, B. Makauskas, V. Vaičaitis, Phase shifts in terahertz wave generation by tightly focused bichromatic laser pulses, J. Opt. Soc. Am. B **31**(7), 1430–1435 (2014).

[97] J. Zhao, L. Zhang, T. Wu, C. Zhang, Y. Zhao, Terahertz wave absorption via preformed air plasma, Optics Communications **380**, 87 – 90 (2016).

[98] H. Zhong, N. Karpowicz, X.-C. Zhang, Terahertz emission profile from laser-induced air plasma, Applied Physics Letters **88**(26), 261103 (2006).

[99] F. Théberge, W. Liu, P. T. Simard, A. Becker, S. L. Chin, Plasma density inside a femtosecond laser filament in air: Strong dependence on external focusing, Phys. Rev. E **74**, 036406 (2006).

[100] D. J. Cook, R. M. Hochstrasser, Intense terahertz pulses by four-wave rectification in air, Opt. Lett. **25(16)**, 1210–1212 (2000).

[101] G. Rodriguez, A. R. Valenzuela, B. Yellampalle, M. J. Schmitt, K.-Y. Kim, In-line holographic imaging and electron density extraction of ultrafast ionized air filaments, J. Opt. Soc. Am. B **25**(12), 1988–1997 (2008).

[102] B. Clough, J. Dai, X.-C. Zhang, Laser air photonics: beyond the terahertz gap, Mater. Today **15(1-2)**, 50–58 (2012).

[103] M. Clerici, M. Peccianti, B. E. Schmidt, L. Caspani, M. Shalaby, M. Giguere, A. Lotti, A. Couairon, F. Legare, T. Ozaki, D. Faccio, R. Morandotti, Wavelength scaling of terahertz generation by gas ionization, Phys. Rev. Lett. **110**, 253901 (2013).

[104] P. G. de Alaiza Martinez, I. Babushkin, L. Berge, S. Skupin, E. Cabrera-Granado, C. Kohler, U. Morgner, A. Husakou, J. Herrmann, Boosting terahertz generation in laser-field ionized gases using a sawtooth wave shape, Phys. Rev. Lett. **114(18)**, 183901 (2015).

[105] W. Ji, C.-H. Lee, P. Chen, W. Hu, Y. Ming, L. Zhang, T.-H. Lin, V. Chigrinov, Y.-Q. Lu, Meta-q-plate for complex beam shaping, Scientific Reports **6**(25528) (2016).

[106] J. Durnin, Exact solutions for nondiffracting beams. i. the scalar theory, J. Opt. Soc. Am. A **4(4)**, 651–654 (1987).

[107] V. Vaicaitis, S. Paulikas, Formation of bessel beams with continuously variable cone angle, Optical and Quantum Electronics **35(11)**, 1065–1071 (2003).

[108] G. Siviloglou, D. Christodoulides, Accelerating finite energy airy beams, Opt. Lett. **32(8)**, 979–981 (2007).

[109] S. W. Hell, J. Wichmann, Breaking the diffraction resolution limit by stimulated emission: stimulated-emission-depletion fluorescence microscopy, Opt. Lett. **19**(11), 780–782 (1994).

[110] V. A. Semenova, M. S. Kulya, N. V. Petrov, Y. V. Grachev, A. N. Tsypkin, S. E. Putilin, V. G. Bespalov, Amplitude-phase imaging of pulsed broadband terahertz vortex beams generated by spiral phase plate, in *2016 41st International Conference on Infrared, Millimeter, and Terahertz waves (IRMMW-THz)* (2016), 1–2.

[111] K. Y. Kim, A. J. Taylor, S. L. Chin, G. Rodriguez, Coherent control of terahertz supercontinuum generation in ultrafast laser-gas interactions, Nat. Photon. **2**, 605 (2008).

[112] M. Ammosov, N. Delone, V. Krainov, Tunnel ionization of complex atoms and of atomic ions in an alternating electric field, Sov. Phys. JETP **64**, 1191 (1986).

[113] G. L. Yudin, M. Y. Ivanov, Nonadiabatic tunnel ionization: Looking inside a laser cycle, Phys. Rev. A **64**, 013409 (2001).

[114] M. D. Thomson, M. Kress, T. Löffler, H. G. Roskos, Broadband THz emission from gas plasmas induced by femtosecond optical pulses: From fundamentals to applications, Laser & Photonics Review **1**, 349 (2007).

[115] I. Thiele, B. Zhou, A. Nguyen, E. Smetanina, R. Nuter, K. J. Kaltenecker, P. G. de Alaiza Martínez, J. Déchard, L. Bergé, P. U. Jepsen, S. Skupin, Terahertz emission from laser-driven gas plasmas: a plasmonic point of view, Optica **5**(12), 1617–1622 (2018).

[116] E. Cabrera-Granado, Y. Chen, I. Babushkin, L. Bergé, S. Skupin, Spectral self-action of thz emission from ionizing two-color laser pulses in gases, New Journal of Physics **17**(2), 023060 (2015).

[117] I. Babushkin, W. Kuehn, C. Köhler, S. Skupin, L. Berge, K. Reimann, M. Woerner, J. Herrmann, , T. Elsaesser, Ultrafast spatiotemporal dynamics of terahertz generation by ionizing two-color femtosecond pulses in gases, Phys. Rev. Lett. **105**, 053903 (2010).

[118] M. Gecevicius, M. Ivanov, M. Beresna, A. Matijosius, V. Tamuliene, T. Gertus, A. Cerkauskaite, K. Redeckas, M. Vengris, V. Smilgevicius, P. G. Kazansky, Toward the generation of broadband optical vortices: extending the spectral range of a q-plate by polarization-selective filtering, J. Opt. Soc. Am. B **35**, 190–196 (2018).

[119] P. Klarskov, A. C. Strikwerda, K. Iwaszczuk, P. U. Jepsen, Experimental three-dimensional beam profiling and modeling of a terahertz beam generated from a two-color air plasma, New Journal of Physics **15**(7), 075012 (2013).

[120] V. Vaicaitis, M. Ivanov, K. Adomavicius, Z. Svirskas, U. Morgner, I. Babushkin, Influence of laser-preformed plasma on thz wave generation in air by bichromatic laser pulses, Laser Physics **28**(9), 095402 (2018).

[121] M. Kolesik, J. V. Moloney, Nonlinear optical pulse propagation simulation: From Maxwell's to unidirectional equations, Physical Review E **70**, 036604 (2004).

[122] A. Vinçotte, L. Bergé, Femtosecond optical vortices in air, Phys. Rev. Lett. **95**, 193901 (2005).

[123] D. Pohl, Operation of a ruby laser in the purely transverse electric mode te01, Applied Physics Letters **20**(7), 266–267 (1972).

[124] K. Yonezawa, Y. Kozawa, S. Sato, Generation of a radially polarized laser beam by use of the birefringence of a c-cut nd:yvo4 crystal, Opt. Lett. **31**(14), 2151–2153 (2006).

[125] M.-D. Wei, Y.-S. Lai, K.-C. Chang, Generation of a radially polarized laser beam in a single microchip nd:yvo4 laser, Opt. Lett. **38**(14), 2443–2445 (2013).

[126] J. lang Li, K. ichi Ueda, M. Musha, A. Shirakawa, Z. ming Zhang, Converging-axicon-based radially polarized ytterbium fiber laser and evidence on the mode profile inside the gain fiber, Opt. Lett. **32**(11), 1360–1362 (2007).

[127] J.-F. Bisson, J. Li, K. Ueda, Y. Senatsky, Radially polarized ring and arc beams of a neodymium laser with an intra-cavity axicon, Opt. Express **14**(8), 3304–3311 (2006).

[128] M. A. Ahmed, A. Voss, M. M. Vogel, T. Graf, Multilayer polarizing grating mirror used for the generation of radial polarization in yb:yag thin-disk lasers, Opt. Lett. **32**(22), 3272–3274 (2007).

[129] Q. Zhan, J. R. Leger, Microellipsometer with radial symmetry, Appl. Opt. **41**(22), 4630–4637 (2002).

[130] Q. Zhan, J. R. Leger, Interferometric measurement of the geometric phase in space-variant polarization manipulations, Optics Communications **213**(4–6), 241 – 245 (2002).

[131] N. Passilly, F. Treussart, R. Hierle, R. de Saint Denis, K. Aït-Ameur, J.-F. Roch, Simple interferometric technique for generation of a radially polarized light beam, J. Opt. Soc. Am. A **22**(5), 984–991 (2005).

[132] M. Bashkansky, D. Park, F. K. Fatemi, Azimuthally and radially polarized light with a nematic slm, Opt. Express **18**(1), 212–217 (2010).

[133] S. Zhou, S. Wang, J. Chen, G. Rui, Q. Zhan, Creation of radially polarized optical fields with multiple controllable parameters using a vectorial optical field generator, Photon. Res. **4**(5), B35–B39 (2016).

[134] X. Dong, X. Weng, H. Guo, S. Zhuang, Generation of radially polarized beams using spatial light modulator, Optik - International Journal for Light and Electron Optics **123**(5), 391 – 394 (2012).

[135] T. Fadeyeva, V. Shvedov, N. Shostka, C. Alexeyev, A. Volyar, Natural shaping of the cylindrically polarized beams, Opt. Lett. **35**(22), 3787–3789 (2010).

[136] S. Vyas, Y. Kozawa, S. Sato, Polarization singularities in superposition of vector beams, Opt. Express **21**(7), 8972–8986 (2013).

[137] T. G. Brown, Unconventional polarization states, Progress in Optics **56**, 81 – 129 (2011).

[138] Y. R. Shen, *The principles of nonlinear optics* (John Wiley & Sons, New York, 1984).

[139] B. E. A. Saleh, M. C. Teich, *Fundamentals of Photonics* (John Wiley & Sons, 1991).

[140] M. S. Soskin, M. V. Vasnetsov, Nonlinear singular optics, Pure and Applied Optics: Journal of the European Optical Society Part A **7**(2), 301 (1998).

[141] M. M. Sushckik, V. M. Fortus, , G. I. Freidman, Parametric amplification and generation of light, Radiophys. Quantum Electron. **13**(5), 489–521 (1970).

[142] M. M. Sushckik, V. M. Fortus, , G. I. Freidman, Trapping of parametrically coupled waves by pulses and beams of pump radiation, Radiophys. Quantum Electron. **12**(2), 235–538 (1969).

[143] M. M. Sushckik, V. M. Fortus, , G. I. Freidman, Excitation of parametrically amplified waves during spatial capture by pumping-radiation wave packets, Radiophys. Quantum Electron. **13**(2), 192–196 (1970).

[144] S. A. Akhmanov, V. A. Vysloukh, A. S. Chirkin, *Optics of Femtosecond Laser Pulses* (American Intitute of Physics, 1992).

[145] A. Ashkin, J. M. Dziedzic, Optical levitation by radiation pressure, Applied Physics Letters **19**(8), 283–285 (1971).

[146] A. Ashkin, J. M. Dziedzic, J. E. Bjorkholm, S. Chu, Observation of a single-beam gradient force optical trap for dielectric particles., Optics letters **11**(5), 288 (1986).

[147] K. Svoboda, S. M. Block, Biological applications of optical forces, Annu. Rev. Biomol. Struct. **23**, 247–285 (1994).

[148] D. G. Grier, A revolution in optical manipulation, Nature **424**(6950), 810–816 (2003).

[149] A. Ashkin, Optical trapping and manipulation of neutral particles using lasers, Proceedings of the National Academy of Sciences **94**(10), 4853–4860 (1997).

[150] C. J. Price, T. D. Donnelly, S. Giltrap, N. H. Stuart, S. Parker, S. Patankar, H. F. Lowe, D. Drew, E. T. Gumbrell, R. A. Smith, An in-vacuo optical levitation trap for high-intensity laser interaction experiments with isolated microtargets, Review of Scientific Instruments **86**(3), 1–11 (2015).

[151] J. Moore, L. L. Martin, S. Maayani, K. H. Kim, H. Chandrahalim, M. Eichenfield, I. R. Martin, T. Carmon, Regular oscillations and random motion of glass microspheres levitated by a single optical beam in air, Optics Express **24**(3), 2850–2857 (2016).

[152] S. Ruberto, J. Reutsch, N. Roth, B. Weigand, A systematic experimental study on the evaporation rate of supercooled water droplets at subzero temperatures and varying relative humidity, Experiments in Fluids **58**(55) (2017).

[153] A. Rohrbach, E. H. K. Stelzer, Trapping forces, force constants, and potential depths for dielectric spheres in the presence of spherical aberrations, Appl. Opt. **41**(13), 2494–2507 (2002).

[154] A. Rohrbach, Stiffness of optical traps: Quantitative agreement between experiment and electromagnetic theory, Phys. Rev. Lett. **95**, 168102 (2005).

[155] M. S. Rocha, Optical tweezers for undergraduates: Theoretical analysis and experiments, American Journal of Physics **77**(8), 704–712 (2009).

[156] P. A. M. Neto, H. M. Nussenzveig, Theory of optical tweezers, Europhys. Lett. **50**(5), 702 (2000).

[157] A. Mazolli, P. A. M. Neto, h. M. Nussenzveig, Theory of trapping forces in optical tweezers, Proceedings of the Royal Society of London A: Mathematical, Physical and Engineering Sciences **459**(2040), 3021–3041 (2003).

[158] A. S. Desyatnikov, V. G. Shvedov, A. V. Rode, W. Krolikowski, Y. S. Kivshar, Photophoretic manipulation of absorbing aerosol particles with vortex beams: theory versus experiment, Opt. Express **17**(10), 8201–8211 (2009).

[159] V. Shvedov, Interaction of cw and pulsed singular optical beams with micro- and nanoparticles, dissertacia na soiskanie uchenoy stepeni doktora fiziko-matematicheskih nauk (2011).

[160] M. P. MacDonald, L. Paterson, K. Volke-Sepulveda, J. Arlt, W. Sibbett, K. Dholakia, Creation and manipulation of three-dimensional optically trapped structures, Science **296**(5570), 1101–1103 (2002).

[161] S. M. Barnett, L. Allen, R. P. Cameron, C. R. Gilson, M. J. Padgett, F. C. Speirits, A. M. Yao, On the natures of the spin and orbital parts of optical angular momentum, J. Opt. **18**, 064004 (2016).

[162] K. Volke-Sepulveda, V. Garces-Chavez, S. Chavez-Cerda, J. Arlt, K. Dholakia, Orbital angular momentum of a high-order bessel light beam, J. Opt. B: Quantum Semiclass. Opt. **4**, S82 (2002).

[163] D. McGloin, D. R. Burnham, M. D. Summers, D. Rudd, N. Dewara, S. Anandc, Optical manipulation of airborne particles: techniques and applications, Faraday Discuss. **137**, 335–350 (2008).

[164] O. Brzobohaty, M. Siler, J. Jezek, P. Jakl, P. Zemanek, Optical manipulation of aerosol droplets using a holographic dual and single beam trap, Opt. Lett. **38**(22), 4601–4604 (2013).

[165] M. Gecevicius, R. Drevinskas, M. Beresna, P. G. Kazansky, Single beam optical vortex tweezers with tunable orbital angular momentum, Appl. Phys. Lett. **104**, 231110 (2014).

[166] J. Leach, S. Keen, M. J. Padgett, C. Saunter, G. D. Love", Direct measurement of the skew angle of the poynting vector in a helically phased beam, Opt. Express **14**(25), 11919–11924 (2006).

[167] M. E. J. Friese, T. A. Nieminen, N. R. Heckenberg, H. Rubinsztein-Dunlop, Optical alignment and spinning of laser-trapped microscopic particles, Nature **394**, 348–350 (1998).

[168] A. T. O'Neil, I. MacVicar, L. Allen, M. J. Padgett, Intrinsic and extrinsic nature of the orbital angular momentum of a light beam, Phys. Rev. Lett. **88**(5), 053601 (2016).

[169] R. A. Beth, Mechanical detection and measurement of the angular momentum of light, Phys. Rev. **50**, 115–125 (1936).

[170] H. He, M. E. J. Friese, N. R. Heckenberg, H. Rubinsztein-Dunlop, Direct observation of transfer of angular momentum to absorptive particles from a laser beam with a phase singularity, Phys. Rev. Lett. **75**(5), 826 – 829 (1995).

[171] N. B. Simpson, K. Dholakia, L. Allen, M. J. Padgett, Mechanical equivalence of spin and orbital angular momentum of light: an optical spanner, Opt. Lett. **22**(1), 52–54 (1997).

[172] T. Takahashi, Measurement of electric charge of cloud droplets, drizzle and raindrops, Reviews of Geophysics and Space Physics **11**(4), 903–924 (1973).

[173] M. Sato, N. Kudo, N. Saito, Surface tension reduction of liquid by applied electric field using vibrating jet method, IEEE Transactions on Industry Applications **34**(2), 294–300 (1998).

[174] B. M. Weon, J. H. Je, Ionization-induced surface tension reduction of water droplets, Applied Physics Letters **93**(24), 244105 (2008).

[175] H. R. Pruppacher, J. D. Klett, *Microphysics of clouds and precipitation* (Springer, 2010).

[176] R. A. Shaw, Particle-turbulence interactions in atmospheric clouds, Annual Review of Fluid Mechanics **35**(1), 183–227 (2003).

[177] W. W. Grabowski, L.-P. Wang, Growth of cloud droplets in a turbulent environment, Annual Review of Fluid Mechanics **45**(1), 293–324 (2013).

[178] T. B. Low, R. List, Collision, coalescence and breakup of raindrops. part i: Experimentally established coalescence efficiencies and fragment size distributions in breakup, Journal of the Atmospheric Sciences **39**(7), 1591–1606 (1982).

[179] K. V. Beard, H. T. Ochs, Collisions between small precipitation drops. part ii: Formulas for coalescence, temporary coalescence, and satellites, Journal of the Atmospheric Sciences **52**(22), 3977–3996 (1995).

[180] R. Bordás, C. Roloff, D. Thévenin, R. A. Shaw, Experimental determination of droplet collision rates in turbulence, New Journal of Physics **15**(4), 045010 (2013).

[181] M. Szakall, S. Kessler, K. Diehl, S. K. Mitra, S. Borrmann, A wind tunnel study of the effects of collision processes on the shape and oscillation for moderate-size raindrops, Atmospheric Research **142**, 67 – 78, the 16th International Conference on Clouds and Precipitation (2014).

[182] B. Nagare, C. Marcolli, O. Stetzer, U. Lohmann, Comparison of measured and calculated collision efficiencies at low temperatures, Atmos. Chem. Phys. **15**(23), 13759–13776 (2015).

[183] B. J. Devenish, P. Bartello, J.-L. Brenguier, L. R. Collins, W. W. Grabowski, R. H. A. IJzermans, S. P. Malinowski, M. W. Reeks, J. C. Vassilicos, L.-P. Wang, Z. Warhaft, Droplet growth in warm turbulent clouds, Quarterly Journal of the Royal Meteorological Society **138**(667), 1401–1429 (2015).

[184] E. Bodenschatz, S. P. Malinowski, R. A. Shaw, F. Stratmann, Can we understand clouds without turbulence?, Science **327**(5968), 970–971 (2010).

[185] Bottlenecks in turbulent aerosols, `http://particlesinturbulence.org/`.

[186] B. Mehlig, Bottlenecks for particle growth in turbulent aerosols, `http://norlx51.nordita.org/~brandenb/TurboPart/KAW2015/prop_orig.pdf`.

[187] R. J. Hopkins, L. Mitchem, A. D. Ward, J. P. Reid, Control and characterisation of a single aerosol droplet in a single-beam gradient-force optical trap, Phys. Chem. Chem. Phys. **6**, 4924–4927 (2004).

[188] R. Power, J. P. Reid, S. Anand, D. McGloin, A. Almohamedi, N. S. Mistry, A. J. Hudson, Observation of the binary coalescence and equilibration of micrometer-sized droplets of aqueous aerosol in a single-beam gradient-force optical trap, The Journal of Physical Chemistry A **116**(35), 8873–8884 (2012).

[189] M. Horstmann, K. Probst, C. Fallnich, Towards an integrated optical single aerosol particle lab, Lab Chip **12**, 295–301 (2012).

[190] Y. J. Jiang, A. Umemura, C. K. Law, An experimental investigation on the collision behaviour of hydrocarbon droplets, Journal of Fluid Mechanics **234**, 171–190 (1992).

[191] A. V. Sergeyev, R. A. Shaw, An inexpensive uniform-size aerosol generator, Measurement Science and Technology **17**(10), N41–N44 (2006).

[192] I. Galinskiy, O. Isaksson, I. R. Salgado, M. Hautefeuille, B. Mehlig, D. Hanstorp, Measurement of particle motion in optical tweezers embedded in a sagnac interferometer, Opt. Express **23**(21), 27071–27084 (2015).

[193] K. Nishino, H. Kato, K. Torii, Stereo imaging for simultaneous measurement of size and velocity of particles in dispersed two-phase flow, Measurement Science and Technology **11**(6), 633–645 (2000).

[194] A. Ashkin, J. M. Dziedzic, Optical levitation of liquid drops by radiation pressure, Science **187**(4181), 1073–1075 (1975).

[195] X. Zhang, R. H. Davis, The rate of collisions due to brownian or gravitational motion of small drops, Journal of Fluid Mechanics **230**, 479–504 (1991).

[196] X. Zhang, R. H. Davis, M. F. Ruth, Experimental study of two interacting drops in an immiscible fluid, Journal of Fluid Mechanics **249**, 227–239 (1993).

[197] M. Ivanov, M. Viderstrom, K. Chang, C. R. Contreras, B. Mehlig, D. Hanstorp, Spectroscopy and optical imaging of coalescing droplets, Proc. SPIE **9922** (2016).

[198] D. Hanstorp, M. Ivanov, A. F. A. Hernandez, J. Enger, A. M. Gallego, O. Isaksson, C.-J. Karlsson, R. M. Villa, A. Varghese, K. Chang, A versatile system for optical manipulation experiments, Proc. SPIE **10347** (2017).

[199] T. A. Nieminen, N. R. Heckenberg, H. Rubinsztein-Dunlop, Forces in optical tweezers with radially and azimuthally polarized trapping beams, Opt. Lett. **33**(2), 122–124 (2008).

[200] Workshop of Photonics, `https://www.wophotonics.com/product/radial-polarization-converter-s-waveplate/`.

COPIES OF PUBLICATIONS

A1

INTENSITY MODULATED TERAHERTZ VORTEX WAVE GENERATION IN AIR PLASMA BY TWO-COLOR FEMTOSECOND LASER PULSES

M. Ivanov, I. Thiele, L. Bergé, S. Skupin, D. Buožius, and V. Vaičaitis

Opt. Lett. **44**, 3889 (2019)

Intensity modulated terahertz vortex wave generation in air plasma by two-color femtosecond laser pulses

MAKSYM IVANOV[1,*], ILLIA THIELE[2], LUC BERGÉ[3], STEFAN SKUPIN[4], DANAS BUOŽIUS[1], AND VIRGILIJUS VAIČAITIS[1]

[1] Laser Research Center, Vilnius University, 10 Sauletekio avenue, Vilnius, Lithuania, LT-10223
[2] Department of Physics, Chalmers University of Technology, Göteborg, Sweden, SE-412 96
[3] CEA, DAM, Arpajon, France, DIF - 91297
[4] Institut Lumiere Matiere, UMR 5306 Université Lyon 1 - CNRS, Université de Lyon, Villeurbanne, France, F-69622
[*] Corresponding author: maks.ivannov@gmail.com

Compiled July 19, 2019

We investigate the generation of broadband terahertz (THz) pulses with phase singularity from air plasmas created by fundamental and second harmonic laser pulses. We show that when the second harmonic beam carries a vortex charge, the THz beam acquires a vortex structure as well. A generic feature of such THz vortex is that the intensity is modulated along the azimuthal angle, which can be attributed to the spatially varying relative phase difference between the two pump harmonics. Fully space and time resolved numerical simulations reveal that transverse instabilities of the pump further affect the emitted THz field along nonlinear propagation, which produces additional singularities resulting in a rich vortex structure. The predicted intensity modulation is experimentally demonstrated with a thermal camera, in excellent agreement with simulation results. The presence of phase singularities in the experiment is revealed by astigmatic transformation of the beam using a cylindrical mirror.

http://dx.doi.org/10.1364/ao.XX.XXXXXX

1. INTRODUCTION

Terahertz (THz) radiation is of great current interest due to many applications such as nonlinear THz spectroscopy and imaging [1] or electron bunch compression [2]. A compact and effective method to obtain very high THz field strengths and extremely broadband spectral widths is THz wave generation from plasma filaments formed in air by focused bichromatic femtosecond laser pulses consisting of first harmonic (FH) and second harmonic (SH) waves [3–6]. On the other hand, special light fields, such as optical vortex [7], radially polarized [8], and Bessel beams [9] are widely studied and employed in various fields [10, 11]. Previous attempts on vortex generation at THz frequencies [12–19] were exclusively based on manipulation of THz waves by employing external components which are inherently limited in terms of acceptable bandwidth. Therefore, alternative methods for ultra-broadband vortex generation at THz frequencies should be proposed and investigated. Very recently, vortex-shaped THz pulses have been demonstrated without using external shaping elements [20, 21] from ZnTe crystals. These, however, supply relatively narrow bandwidths, while air plasmas were only theoretically considered in [22, 23].

In this work we investigate vortex THz pulse generation in an air-plasma induced by the coupling between Gaussian FH and vortex SH pulses. In this novel scheme, the vorticity is created already at the THz generation stage. It appears that SH carrying an optical vortex charge affects not only the phase but also the intensity distribution of the generated THz pulse. We distinguish two stages of THz vortex generation: (i) At the beginning of the plasma filament, an intensity modulated THz vortex pulse is created. This intensity modulation is frequency dependent. (ii) Upon further propagation, the pump pulse may undergo spatio-temporal instabilities which induce secondary phase singularities in the THz field, but the total topological charge is conserved. Results of our investigation suggest an alternative method for the generation of structured THz waves spanning ultrabroadband frequency ranges.

2. THEORY

For two color-laser-induced gas plasmas, the ionization current mechanism [24] is the key player for THz emission. This emission is caused by the macroscopic current of free electrons which are created by field ionization in the tunneling regime [25, 26] and driven by the laser electric field. The principal electric field component is transverse to the laser propagation direction, and we consider linear polarization. Neglecting electron collisions, the current equation reads

$$\partial_t J = \frac{q_e^2}{m_e} n_e E\,, \tag{1}$$

with electron charge q_e, mass m_e, electron density n_e and electric field E. The electron density is a time-dependent parameter governed by the ionization rate and can be computed using ionization rate equations [5, 27]. The electric field consists of both optical frequency components and generated THz components,

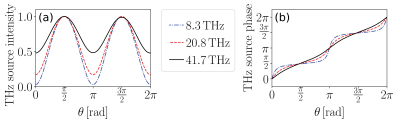

Fig. 1. Azimuthal intensity (a) and phase (b) distribution of the Fourier-transformed THz source term $\partial_t J$ [see Eqs. (1), (2)].

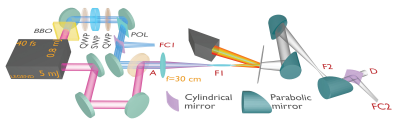

Fig. 2. Sketch of experimental setup. QWP - quarter wave plate, SWP - S-waveplate (q-plate), POL - polarizer, BBO - nonlinear crystal for SH generation. SH is shown by blue, FH by red-pink, and THz radiation by gray color. Red letters label relevant positions (see text for details). THz fluency profiles taken in positions 'D' and 'FC2' are shown in Fig. 3 and 4.

which plays an important role in the THz spectral broadening [28]. However, certain effects can be already understood by considering only the impact of the bichromatic laser electric field. The down-conversion from laser to THz frequencies takes place because of the nonlinear product between the electron density and the laser electric field. It can be shown that at least two laser colors, here FH and SH with a relative phase angle of $\pi/2$, are required to obtain an efficient down-conversion towards THz frequencies [6, 29]. In order to understand this down-conversion process in the case of vortex pump pulses, we first evaluate Eq. (1) for the real-valued laser electric field

$$E_{\mathrm{L}}(t,\theta) = A(t)[E_{\omega_{\mathrm{L}}}\cos(\omega_{\mathrm{L}}t) + E_{2\omega_{\mathrm{L}}}\cos(2\omega_{\mathrm{L}}t + \phi + l_{\mathrm{SH}}\theta)], \quad (2)$$

with fundamental frequency ω_{L}, relative phase offset ϕ, pulse envelope $A(t)$; l_{SH} is the vortex charge of the SH beam. Here, we omit the radial and longitudinal coordinates, and write the electric field as a function of time t and azimuthal angle θ only. Equation (2) thus represents the rapid time- and θ-dependent distribution of the electric field along the vortex ring, assuming constant FH and SH amplitudes $E_{\omega_{\mathrm{L}},2\omega_{\mathrm{L}}}$. The resulting spectral intensity and phase of the source term $\partial_t J$ obtained by Fourier transform is presented in Fig. 1 for $\phi = 0$ and $l_{\mathrm{SH}} = 1$. The intensity is modulated along θ and is maximal when the relative phase angle $(\phi + l_{\mathrm{SH}}\theta)$ between the SH and FH takes the values $\pi/2$ and $3\pi/2$ and minimal for 0 and π (Fig. 1). The modulation depth is the largest at lower frequencies and decreases for larger frequencies, where also the phase approaches a linear ramp-up along θ as expected for a vortex. The results from this simple theoretical approach remain qualitatively the same when changing the laser and gas parameters within the parameter range allowing for efficient THz generation.

3. EXPERIMENTS

The experimental setup is sketched in Fig. 2. We used a 1 kHz repetition rate laser system (Legend elite duo HE+, Coherent Inc.). Right before the main focusing lens (silica, f=30 cm) labeled 'A' in the setup, the FH pulse had central wavelength of

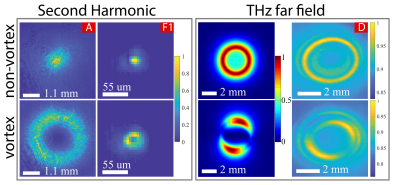

Fig. 3. (Left panel) Images of second harmonic fluency (non-vortex and vortex, for Gaussian and vortex state, respectively). Column labeling correspond to locations where images were acquired as specified in Fig. 2. (Right panel) Corresponding simulated (first column) and experimentally observed (second column) farfield THz fluencies. See text for details.

790 nm, FWHM pulse duration 50 fs and energy of 6 mJ. The SH pulse had central wavelength of 395 nm, FWHM duration ∼50 fs and energy of 60 μJ in Gaussian state and 50 μJ in vortex state. Our Gaussian SH pulse was shaped into an optical vortex by the method described in [30], which ensures more than one-octave spectral bandwidth of vortex generation: First SH was circularly polarized by a quarter wave plate (QWP) and converted to an optical vortex (OV) beam by an S-waveplate (RPC-405-06-557, Workshop of Photonics) (SWP). Subsequent polarization filtering by a second quarter wave plate (QWP) and a polarizer (POL) ensured generation of a linearly polarized vortex in the SH beam profile over the whole spectral bandwidth of the SH pulse. A 0.5 mm thick Si wafer and various commercial THz filters were used to remove the high frequency part of the pump and transmit only THz radiation, which was then collimated and shrank by parabolic mirrors in a telescope configuration to match the detector aperture. Imaging of the generated THz beam was performed with a thermal camera detector (VarioCAM head HiRes 640, InfraTec GmbH), sensitive in the range 0.1 – 40 THz (3000 – 7.5 μm). Spectra of THz radiation were obtained from Fourier transformed interferometric measurements using pyroelectric detector (TPR-A-65 THz, Spectrum Detector Inc.), sensitive in the range 0.1 - 300 THz (3000 - 1 μm) with a flat response function from ∼3 to ∼100 THz. The laser-to-THz conversion efficiency for the regular Gaussian pulses was about 10^{-4}, but dropped to $\sim 10^{-5}$ in the case of the SH vortex pump, which we attribute to the differences in the spatial intensity distribution of the Gaussian FH and vortex SH beam.

During the experiment the FH beam was always kept Gaussian. Experimental images of the SH beam are shown in the left panel of Fig. 3. The first and the second row present the SH Gaussian ('non-vortex') and vortex beam ('vortex'), respectively. The first column 'A' shows images of the harmonics prior to the main focusing lens at position A (see Fig. 2); the second column 'F1' refers to the focus position (F1 in Fig. 2). The FWHM beam widths are 33 and 38 μm for the FH and the vortex SH in the focal plane of the 30-cm focusing lens, respectively.

Experimental images of the THz farfield fluency obtained in position 'D' (Fig. 2) with the thermal camera (0.1-40 THz) are shown in the last column of Fig. 3). The THz fluency obtained with Gaussian SH (upper row) has a symmetric ring intensity distribution, as expected for conical THz emission [31, 32]. In contrast, the THz fluency obtained with vortex SH (lower row) has an intensity modulation manifesting as two maxima along the azimuthal angle, in agreement with our theoretical predic-

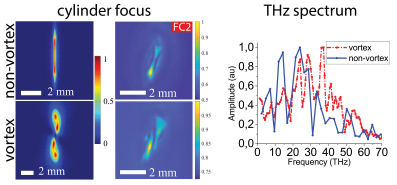

Fig. 4. Left panel: Simulated (first column) and experimentally observed (second column) fluencies of the generated THz beams in the focus of a cylindrical mirror (f = 20 cm). Right panel: shows typical experimental amplitude spectra of the generated THz pulses in the case of vortex SH (red dash-dot "vortex") and Gaussian SH (blue solid line "non-vortex").

tions (see Fig. 1). Simulation results shown for comparison in the first column of right-hand panel in Fig. 3) are in excellent agreement. The simulated fluency is obtained for the spectral range of 0.01 to 50 THz (see below for details on the simulations).

The presence of a phase singularity in the generated THz beam was confirmed by the well-controlled method of topological charge determination based on the astigmatic transformation of singular beams by a cylindrical mirror [33]. This method is valid even in the presence of intensity modulations affecting the generated THz beam profile. A beam without phase singularity focuses in a single line, whereas the appearance of a dark stripe in this line indicates a singular phase. The number of lines and their tilt correspond to the value and sign of the topological charge. As shown in the left panel of Fig. 4, the single dark stripe in the second row suggests that the topological charge of the generated THz vortex is $|l_{THz}| = 1$. Simulation results and experimental images show again excellent agreement.

As evidenced by the right-hand panel of Fig. 4, the experimental spectra of the generated THz pulses are broadband, spanning from 10 to 40 THz. We attribute the dips in these spectra to absorbance in optical elements such as Si filters with spectrally variable transmission (OCz-Si, Tydex) and pellicle beam splitters. In the case of the THz vortex the peak spectral intensity is located around 35 THz, while THz pulses without phase singularity have their maximum around 25 THz. This shift may occur because of the lower ionization rate at the periphery of the FH pump beam where the SH vortex has maximum intensity and due to transverse phase variations.

An astigmatic transformation of the generated vortex THz beam by a cylindrical mirror was used as the primary experimental detection method of the phase singularity, yielding patterns in excellent agreement with our simulation results. However, we also looked at alternative methods to confirm that our understanding of intensity modulated THz vortex production is indeed correct. According to our theory, the azimuthal intensity modulation comes from the fact that the phase of the SH vortex beam changes by 2π over the full azimuthal angle, while the phase of the FH is constant along this angle. Thus, changing the relative phase between FH Gaussian and SH vortex should result in a rotation of the THz vortex intensity modulation. To verify this property, the THz vortex intensity distribution was recorded by the thermal camera over several minutes. The relative phase between FH and SH was not under control and fluctuated due to long beam pass distances (> 5 meters for each harmonic), vibrations in the room/building, temperature variations, etc. Because

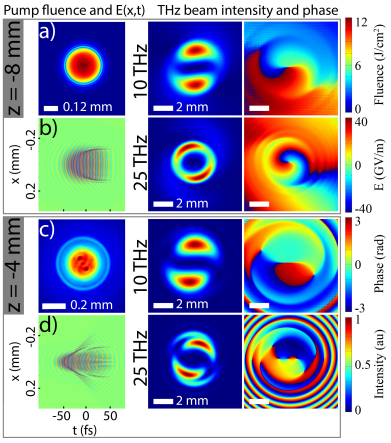

Fig. 5. (a) and (c) show fluency, (b) and (d) show electric field $E(x,t)$ of the two-color pump at the beginning of the filament ($z = -8$ mm) and after transverse pump instabilities have fully developed ($z = -4$ mm). The two right-hand side columns show collimated far field intensity and phase of the 10 and 25 THz frequency components computed from the field at $z = -8$ mm and $z = -4$ mm, respectively (see text for details). Linear focus F1 is at $z = 0$ (see Fig. 2).

of the random nature of the fluctuations, the THz vortex intensity distribution clearly jittered and made even a full rotation once in a while (link Visualization1). In contrast, when we used FH and SH Gaussian beam profiles, the intensity distribution of the THz beam (without phase singularity) did not change. The maximum of the THz beam just slightly oscillated around the same position due to pointing instabilities of the laser.

4. SIMULATIONS

For a complementary analysis we performed comprehensive numerical simulations of the full experiment by means of a unidirectional pulse propagation solver [6, 34]. Laser parameters and focusing conditions in the simulations are chosen such as in the experiments. Our simulation results reveal two distinct stages in the formation and subsequent evolution of the generated THz pulses. First, intensity and phase modulations of the THz source term due to the spatially variable relative phase difference between FH and vortex SH pump components emerge, as expected from our theoretical predictions (see Fig. 1). Second, the pump pulse develops spatio-temporal instabilities generic to the filamentation dynamics that directly affect the THz pulse distribution.

The right hand side of Fig. 5 shows collimated far field intensities and phases of the generated 10 and 25 THz spectral components at two stages of the propagation, namely at the beginning of the plasma filament ($z = -8$ mm), and after transverse pump instabilities have fully developed ($z = -4$ mm). All z positions are given relative to the focus position F1 ($z = 0$ mm)

of the main pump focusing lens (see Fig. 2). To obtain the THz far field, the nonlinear interaction was stopped at the given z position and the THz field was further propagated over a few centimeters in vacuum (sufficiently to reach the far field) and collimated with a lens in thin element approximation.

At the beginning of the filament ($z = -8$ mm) the pump fluency is uniform, as evidenced by Fig. 5 (a). The corresponding spatio-temporal electric field profile in Fig. 5 (b) shows that plasma has only started to deplete the trailing part of the pump pulse, as one would expect from the usual filamentation dynamics [34, 35]. The generated THz vortex at this early stage of pump propagation has a single phase singularity in the center. The intensity is circular with azimuthal modulation, and the modulation depth is larger for lower frequencies, as predicted by Fig. 1. In contrast, at ($z = -4$ mm) the pump pulse has undergone severe transverse distortion [see fluency in Fig. 5 (c)], and the spatio-temporal field profile in Fig. 5 (d) looks much more complex. These strong perturbations of the pump clearly affect the intensity distribution of the THz vortex and produce secondary singularities in the generated THz field. Nevertheless, additional singularities have alternating signs such that the total topological charge of the singular THz $|l_{THz}| = 1$ is preserved during propagation at all relevant frequency components. Overall, our simulations results suggest that the produced THz vortices are surprisingly stable against pump distortions.

5. CONCLUSIONS

We have investigated the properties of THz radiation generated in air plasma by focused bichromatic femtosecond laser pulses, when one of the pump beams (second harmonic) is an optical vortex. The presence of a phase singularity in the generated THz beam was confirmed by astigmatic transformation of the singular THz beams in the focus of a cylindrical lens, as well as by fully space and time resolved numerical simulations. We report that, in contrast to other nonlinear processes (second harmonic generation, parametric generation, etc.), the THz radiation generated in a plasma filament cannot be characterized as a THz vortex beam in the 'classical' sense as it is mediated by photocurrents. Instead, the intensity of the THz beam is modulated along the beam azimuthal angle and contains two minima between two lobes of maximum intensity. This is because the relative phase between two harmonics varies azimuthally when the SH pump pulse is a vortex. Moreover, our numerical simulations demonstrate that transverse instabilities in the filamentary pump propagation affect the THz vortex without destroying it. They may introduce secondary phase singularities, which renders the phase topology of produced structured THz fields particularly rich. One of the benefits of THz generation from plasma currents is the large (> 40 THz) spectral range achievable, contrary to bandwidth limited external THz shaping techniques. We envisage that different combinations of the topological charges of the FH and SH pulses open a wide playground for the creation of structured singular THz sources.

Funding. Laserlab-Europe EU-H2020 654148. This research was funded by a grant (No. S-MIP-19-46) from the Research Council of Lithuania. Simulations were performed using HPC resources from Grand Équipement National De Calcul Intensif (Grant No. A0060507594).

Acknowledgments. MI, DB, and VV are grateful to Titas Gertus from Workshop of Photonics, Lithuania, for the S-waveplate used in this experiment as an optical vortex generator.

REFERENCES

1. P. U. Jepsen, D. G. Cooke, and M. Koch, Laser Photonics Rev **5 (1)**, 124 (2011).
2. C. Kealhofer, W. Schneider, D. Ehberger, A. Ryabov, F. Krausz, and P. Baum, Science **352**, 429 (2016).
3. D. J. Cook and R. M. Hochstrasser, Opt. Lett. **25(16)**, 1210 (2000).
4. B. Clough, J. Dai, and X.-C. Zhang, Mater. Today **15**, 50 (2012).
5. M. D. Thomson, M. Kress, T. Löffler, and H. G. Roskos, Laser & Photonics Rev. **1**, 349 (2007).
6. I. Babushkin, W. Kuehn, C. Köhler, S. Skupin, L. Berge, K. Reimann, M. Woerner, J. Herrmann, , and T. Elsaesser, Phys. Rev. Lett. **105**, 053903 (2010).
7. W. Ji, C.-H. Lee, P. Chen, W. Hu, Y. Ming, L. Zhang, T.-H. Lin, V. Chigrinov, and Y.-Q. Lu, Sci. Reports **6** (2016).
8. P. Stanislovaitis, M. Ivanov, A. Matijosius, V. Smilgevicius, and T. Gertus, Opt. Eng. **56**, 095101 (2017).
9. V. Vaicaitis and S. Paulikas, Opt. Quantum Electron. **35(11)**, 1065 (2003).
10. S. W. Hell and J. Wichmann, Opt. Lett. **19**, 780 (1994).
11. M. Ivanov and D. Hanstorp, Opt. Commun. **427**, 152 (2018).
12. J. He, X. Wang, D. Hu, J. Ye, S. Feng, Q. Kan, and Y. Zhang, Opt. Express **21**, 20230 (2013).
13. R. Imai, N. Kanda, T. Higuchi, K. Konishi, and M. Kuwata-Gonokami, Opt. Lett. **39**, 3714 (2014).
14. K. Miyamoto, B. J. Kang, W. T. Kim, Y. Sasaki, H. Niinomi, K. Suizu, F. Rotermund, and T. Omatsu, Sci. Reports **6**, 38880 (2016).
15. S. Ge, P. Chen, Z. Shen, W. Sun, X. Wang, W. Hu, Y. Zhang, and Y. Lu, Opt. Express **25**, 12349 (2017).
16. S.-J. Ge, Z.-X. Shen, P. Chen, X. Liang, X.-K. Wang, W. Hu, Y. Zhang, and Y.-Q. Lu, Crystals **10**, 314 (2017).
17. A. Minasyan, C. Trovato, J. Degert, E. Freysz, E. Brasselet, and E. Abraham, Opt. Lett. **42**, 41 (2017).
18. C. Liu, J. Liu, L. Niu, X. Wei, K. Wang, and Z. Yang, Sci. Reports **7**, 3891 (2017).
19. Z. Wu, X. Wang, W. Sun, S. Feng, P. Han, J. Ye, Y. Yu, and Y. Zhang, Opt. Express **26**, 1506 (2018).
20. Q. Lin, S. Zheng, Q. Song, X. Zeng, Y. Cai, Y. Li, Z. Chen, L. Zha, X. Pan, and S. Xu, Opt. Lett. **44**, 887 (2019).
21. A. A. Dhaybi, J. Degert, E. Brasselet, E. Abraham, and E. Freysz, J. Opt. Soc. Am. B **36**, 12 (2019).
22. H. Wang, Y. Bai, E. Wu, Z. Wang, P. Liu, and C. Liu, Phys. Rev. A **98**, 013857 (2018).
23. H. Wang, Q. Song, S. Zheng, Q. Lin, E. Wu, Y. Ai, C. Liu, and S. Xu, J. Opt. (2019).
24. K. Y. Kim, A. J. Taylor, S. L. Chin, and G. Rodriguez, Nat. Photon. **2**, 605 (2008).
25. M. Ammosov, N. Delone, and V. Krainov, Sov. Phys. JETP **64**, 1191 (1986).
26. G. L. Yudin and M. Y. Ivanov, Phys. Rev. A **64**, 013409 (2001).
27. I. Thiele, B. Zhou, A. Nguyen, E. Smetanina, R. Nuter, K. J. Kaltenecker, P. G. de Alaiza Martínez, J. Déchard, L. Bergé, P. U. Jepsen, and S. Skupin, Optica **5**, 1617 (2018).
28. E. Cabrera-Granado, Y. Chen, I. Babushkin, L. Bergé, and S. Skupin, New J. Phys. **17**, 023060 (2015).
29. K.-Y. Kim, J. H. Glownia, A. J. Taylor, and G. Rodriguez, Opt. Express **15**, 4577 (2007).
30. M. Gecevicius, M. Ivanov, M. Beresna, A. Matijosius, V. Tamuliene, T. Gertus, A. Cerkauskaite, K. Redeckas, M. Vengris, V. Smilgevicius, and P. G. Kazansky, J. Opt. Soc. Am. B **35**, 190 (2018).
31. P. Klarskov, A. C. Strikwerda, K. Iwaszczuk, and P. U. Jepsen, New J. Phys. **15**, 075012 (2013).
32. V. Vaicaitis, M. Ivanov, K. Adomavicius, Z. Svirskas, U. Morgner, and I. Babushkin, Laser Phys. **28**, 095402 (2018).
33. V. Denisenko, V. Shvedov, A. S. Desyatnikov, D. N. Neshev, W. Krolikowski, A. Volyar, M. Soskin, and Y. S. Kivshar, Opt. Express **17**, 23374 (2009).
34. M. Kolesik and J. V. Moloney, Phys. Rev. E **70**, 036604 (2004).
35. A. Vinçotte and L. Bergé, Phys. Rev. Lett. **95**, 193901 (2005).

A2

INFLUENCE OF LASER-PREFORMED PLASMA ON THZ WAVE GENERATION IN AIR BY BICHROMATIC LASER PULSES

V. Vaicaitis, **M. Ivanov**, K. Adomavicius, Z. Svirskas, U. Morgner, and I. Babushkin

Laser Phys. **28**, 095402 (2018)

https://doi.org/10.1088/1555-6611/aaca5f
https://iopscience.iop.org/article/10.1088/1555-6611/aaca5f

IOP Publishing | Astro Ltd Laser Physics
Laser Phys. **28** (2018) 095402 (6pp) https://doi.org/10.1088/1555-6611/aaca5f

Influence of laser-preformed plasma on THz wave generation in air by bichromatic laser pulses

V Vaičaitis[1], M Ivanov[1], K Adomavičius[1], Ž Svirskas[1], U Morgner[2] and I Babushkin[2]

[1] Laser Research Center, Vilnius University, Saulėtekio 10, Vilnius LT-10223, Lithuania
[2] Institute of Quantum Optics, Leibniz University of Hannover D30167, Germany

E-mail: Virgilijus.Vaicaitis@ff.vu.lt

Received 5 April 2018
Accepted for publication 4 June 2018
Published 10 July 2018

Abstract

Influence of laser-preformed plasma on the energy and spatial properties of terahertz (THz) emission generated in air by focused femtosecond bichromatic laser pulses has been investigated. It was found that the power of THz waves decreases in the presence of the prepulse-created plasma even when the crossing point of the two laser beams is well before or after the pump beam focus. Analysis of the experimentally obtained data revealed that at least two different mechanisms—namely, phase modification of the pump waves and screening of THz radiation by preformed plasma filaments—are responsible for this effect.

Keywords: terahertz generation, air plasma screening, diffraction, bichromatic laser pulses

(Some figures may appear in colour only in the online journal)

1. Introduction

Terahertz (THz) radiation generation in gaseous media by focused bichromatic femtosecond laser pulses is a simple, efficient, and well-established technique [1–3], making it possible to obtain very high THz field strengths and extremely broadband spectral widths [4–7]. Since the ionization of gas molecules is involved in the generation process (see, for example, [2, 6, 8] and references therein), it is reasonable to expect that gas preionization before the generation of THz radiation would influence the yield of THz emission. Thus, in the case of a single-colour pump [9] or when two two-colour plasma filaments are concatenated to a single one [10], the emitted THz radiation increases. In contrast, in the case of a 'cross geometry', when the prepulse creates a plasma filament perpendicular to the direction of the main bichromatic pump beam, THz radiation yield can decrease by nearly 40% [11]. Investigation of this effect might be useful to reveal specific features of this laser–matter interaction and THz radiation generation; therefore, the suppression of THz radiation generation by the precreated plasma has been studied in several experiments [11–13]. However, in these reports, the main emphasis has been placed on the investigation of plasma density dynamics, while geometric factors were not considered in detail. In this paper, we perform an experimental investigation into both the energy and spatial properties of THz radiation as a function of the preplasma position with respect to the pump beam axis and its focus. We demonstrate here the rather complicated dependence of the spectral and angular dependence of THz emission on the spatial position of the preplasma filament, showing the influence of the propagation effects both for the pump and THz radiation. In particular, we report a significant effect on THz emission even if the preplasma is created far away from the main plasma filament.

2. Experimental setup

For the experiments, we have used a 1 kHz repetition rate femtosecond Ti:sapphire chirped pulse amplification laser system (Legend elite duo HE+, Coherent Inc.), delivering 35–40 fs (FWHM) light pulses centered at 790 nm with maximal pulse energy of 8 mJ. Laser pulses were split into two parts (main pulse and prepulse with energies of 5.2 and 1.65

mJ, respectively). The main pump beam was focused into the ambient air by the lens of about 30 cm focal length through the nonlinear BBO crystal of 100 μm thickness (type I, cut angles: $\theta \approx 29°$ and $\phi \approx 90°$). Therefore, the main pump pulse consisted of the fundamental and second harmonic pulses and created a plasma filament (main plasma), where the generation of THz radiation took place. The azimuthal angle of the BBO crystal and its location were optimized to achieve a maximal THz radiation yield [2, 14]. The energy of generated THz pulses was measured using a calibrated pyroelectric detector, placed on the computer-controlled translation stage. For the measurements of THz wave spectra, a home-made THz Michelson interferometer was used along with the pyroelectric detector. Before the entrance of the Michelson interferometer, a THz filter (0.5–1 mm thick Si wafer) was placed, to remove the high frequency part. During measurements of the spatial distributions of generated THz radiation, the pyroelectric detector was placed on a computer-controlled motorized translation stage located at about 50 cm from the plasma filament. By moving it across the pump beam (along the x and y directions), we were able to register the corresponding angular spectra of generated radiation. The prepulse was propagated and focused in the orthogonal direction with respect to the main beam, to generate a plasma filament that intercepted the main beam path (figure 1). The relative time delay and position of the two pulses (main pulse and prepulse) were respectively controlled by motorized and computer-controlled translation stages and by a steering mirror. A CCD camera was used to image the fluorescence of the plasma filaments. The length of fluorescence filament was about 2 cm for the pump pulse energy of 5 mJ.

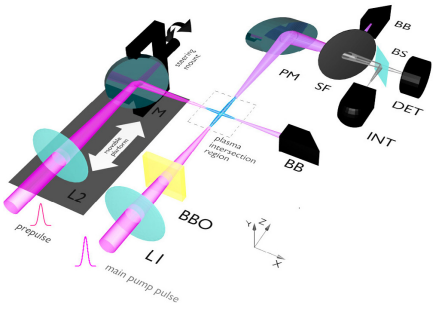

Figure 1. Experimental setup. Two pulses focused by the lenses L1 and L2 are superimposed to create two plasma filaments perpendicular to each other. One of the pulses (referred to as the main pulse) is sent before this superposition to a BBO crystal which makes it a two-colour one. The second pulse (referred to as the prepulse) is controlled by a delay stage and a moving mirror M which allows varying its temporal and spatial position relative to the main pulse. The detection setup consists of a parabolic mirror PM, filter SF, beam splitter BS, Michelson interferometer INT, and detector head DET.

3. Results and discussion

The typical interference traces and corresponding amplitude spectra of generated THz radiation are presented in figure 2. The spectra were calculated by Fourier transformation of the interferograms, and in most cases a non-negligible signal could be observed up to 60 THz. One can see that the THz signal significantly decreases when the precreated plasma is present in the path of the pump beam. In most cases, the attenuation factor of the THz radiation was nearly the same for all frequencies. As has been reported elsewhere [11–13], the impact of the preplasma on the efficiency of THz generation was strongly dependent on the timing between the pump pulse and prepulse: the amplitude of THz signal did not change when the prepulse was sent after the main pulse, and rapidly decreased when the sign of the delay between these pulses was reversed (see inset of the figure 2). After the initial dropdown, the THz signal slowly recovered with a time constant of a few hundred picoseconds, which corresponds well with ballistic plasma expansion and free electron decay rates reported previously [6, 11–13]. However, in contrast to the previous reports where the effect of preplasma was observed only when the plasmas (main plasma and preplasma) were overlapping, in our experiment this effect was also registered when the main beam was intercepted by the preplasma in locations away from the main plasma. In addition, we have observed quite complex dependence of the THz attenuation on the mutual position of the two plasma filaments: depending on the position of interception point along the main beam (along the z coordinate axis) the THz yield as a function of preplasma position along the y coordinate mainly had either one or two minima (at the intersection points before and after the main plasma—see figures 3 and 4).

The dependence of THz yield on the mutual positions of the main plasma and preplasma can be explained on taking into account at least two different phenomena. First, when the filaments intersect before the main plasma (figure 3(a)) and the preplasma position is scanned along the y direction (that is, perpendicularly to the propagation direction of both filaments), the pump beam refracts and diffracts on the preplasma filament, which directly and due to the interference of various parts of the beam modifies the light intensity distribution and phase relations of the bichromatic pump [15] in the focus of the beam, where THz generation is taking place. Naturally, the strongest interaction occurs when the preplasma is centered with respect to the main beam, and as a result the dependence of THz yield has one main minimum (the local minimum seen in figure 3(a) may be attributed to the fact that during the experiment non-ideal Gaussian beams were used). At the onset and middle of the main plasma (figures 3(b) and (c) respectively), the dependence becomes more complicated, since at these points some THz radiation has already been generated and consequently is absorbed and reflected by the preplasma [16]. Therefore, in this case, the interplay of the interference, diffraction and plasma screening takes place. Finally, at the tail of the main plasma and after it (figures 3(d) and (e)) the preplasma does not influence the bichromatic pump beam, wherefore plasma screening becomes the main process reducing the efficiency of THz generation (absorption

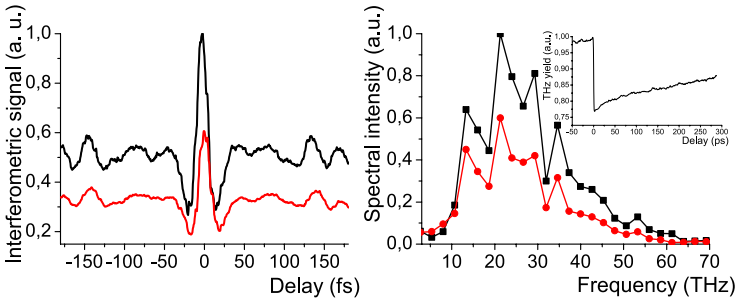

Figure 2. Interference traces (left) and corresponding THz spectra (right) of generated radiation with (red lines) and without preplasma (black lines). The preplasma filament was created by a 10 cm focal length lens and was located in the focal plane of the pump beam. Energies of the pump and preplasma pulses were 5.2 and 1.65 mJ, respectively. Modulation of the spectra is caused by the absorption of used THz filters and of the beam splitter of the interferometer (2 μm-thick nitrocellulose pellicle). The inset at the top right corner shows the typical dependence of the THz yield on the timing between the main pulse and prepulse.

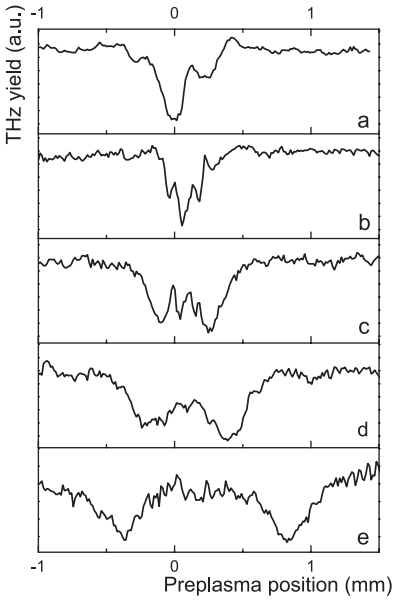

Figure 3. Dependence of the THz power on the position of the preplasma along the y axis (perpendicularly to both the main plasma and preplasma filaments—see figure 1) for various intersection points (corresponding to different z coordinates in figure 1): (a) before the onset of the main plasma, (b) at the onset of the main plasma, (c) at the middle of the main plasma, (d) at the tail of the main plasma, (e) after the main plasma.

and reflection by the preplasma). Since the THz beam has a conical shape [17], the dependencies of the THz yield on the preplasma position have characteristic double minima. This

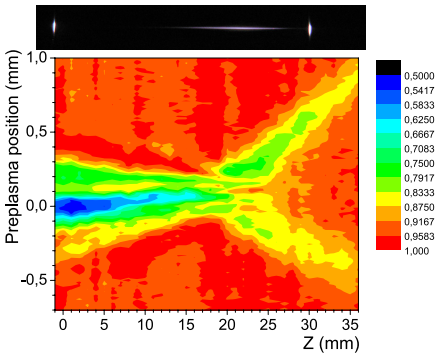

Figure 4. Dependence of the THz power on the position of the preplasma with respect to the main beam axis and relative distance along the z coordinate axis. For clarity, the main plasma filament (seen there as a long string) and preplasma (seen as light points at both ends) at the two exemplary positions of $z = -1$ mm and $z = 30$ mm are shown above.

is furthermore supported by a more detailed scan of the spatial distribution of the THz power versus the position of the preplasma shown in figure 4. There, one can also recognize regions with two minima and the one with a single one. In the former, the distance between the two minima increases when the intersection point moves along the z axis. The divergence angle of these two minima (about 4°) corresponds well to the apex angle of the conical THz beam itself. Thus, we see here the influence of the preplasma on the spatial structure of the THz beam.

The above interpretation is supported by the simple estimates of preplasma contribution to the THz and laser beams. Thus, assuming that the prepulse creates the plasma filament with electron density $n_e(r)$ as a function of the plasma filament radial coordinate r, the plasma frequency ω_p is defined as

$$\omega_p = \sqrt{\frac{n_e(r)e^2}{\varepsilon_0 m}}, \quad (1)$$

where e and m are the electron charge and mass, respectively. Then the plasma index variation $n(r)$ across the filament diameter is given by

$$n(r) = (1 - \frac{\omega_p^2}{\omega_0^2})^{1/2}, \quad (2)$$

where $\omega_0 = \frac{2\pi c}{\lambda}$ is the light frequency and λ is the wavelength.

Phase change $\Delta\varphi(x, y)$ of the light traversing the preplasma is given by:

$$\Delta\varphi(x, y) = \frac{2\pi}{\lambda}\int_0^{L_p} n\,(r)\,dz, \quad (3)$$

where L_p represents the spatial extent of the preplasma filament along the x axis (see figure 1).

Under our experimental conditions, the diameter of the preplasma filament can be about 100 μm, while the maximal plasma density inside it may reach 10^{19} cm^{-3} [11, 18]. The phase modification given by equation (3) is shown in figure 5 assuming plasma density in the multiphoton ionization regime of ~I^{10} for 800 nm and ~I^5 for 400 nm and taking into account ionization potential 14.5 eV of nitrogen. The plasma frequency can be estimated as about 28 THz. Light of frequency lower than ω_p is fully reflected by the pre-created plasma, whereas for frequencies higher than ω_p, the plasma becomes transparent. However, even in that case, the light traversing the plasma filament may experience strong Fresnel losses if the ω_0 is of the same order as ω_p. We believe that this was the case in our experiment, since the maximal spectral intensity of the generated THz beam was near 28 THz. Thus, the lowest (0–28 THz) frequencies of the THz beam traversing the preplasma were reflected and absorbed, while the high-frequency part of the beam was attenuated by Fresnel reflections (according to equation (2), $n(r)$ is larger than 0.8 within the whole high-frequency range (28–60 THz) of generated THz beam).

Naturally, the impact of plasma on the optical pump waves is much weaker, but may still cause significant reduction of the THz yield. Thus, according to equation (3) a plasma filament of 100 μm in diameter may induce a maximal phase slippage of 5.4 radians and 2.7 radians for 800 nm and 400 nm waves, respectively. Note that a change of relative phase between the fundamental and second harmonic waves by $\pi/2$ may result in full suppression of THz generation [1, 15]. In addition, since laser-induced ionization of air is a highly nonlinear process, the transverse spatial electron distribution has a supergaussian shape even in the case that Gaussian intensity distribution of the laser beam is assumed (figure 5). Besides, the plasma-induced refraction index almost directly follows the plasma density distribution—i.e. it is almost independent of the radial coordinate within the plasma filament. Therefore, although plasma-induced phase changes decrease with the radial coordinate, significant fractions of the bichromatic pump beam traversing the preplasma filament can still acquire significant

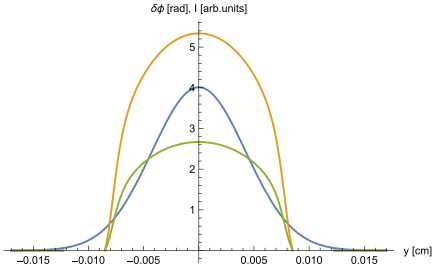

Figure 5. Dependence of the total preplasma-induced phase for 800 nm (orange line) and 400 nm waves (green line) as a function of the transverse spatial coordinate y according to equation (3). Blue line shows the intensity distribution of the preplasma filament.

phase-shifts. As shown in figure 5 (orange and green lines), the preplasma filament may induce more than 75% of maximal phase change within its 100 μm-wide spatial extent. Since the pump beam diameter at the focus is of the same order, a significant part of the pump beam area may be affected by the preplasma. Moreover, since the pump beam is converging as it crosses the preplasma filament, parts of the beam with different phases interfere at the focal point, decreasing the focal light intensity and thus further reducing THz yield. Note that similar strong modulation of the laser beam due to the abrupt index and accumulated phase changes across the plasma filament diameter for plasma densities even lower than 10^{18} cm^{-3} has recently been observed [19]. Thus, apart from the direct variation of the relative phase between the fundamental and second harmonic waves, the preplasma filament also modulates and decreases the pump beam intensity, which may also significantly reduce the total THz yield.

To further analyze the spatial structure of the THz radiation, we first registered the intensity distribution of THz beam as a function of angle, when no preplasma was present (see figure 6, red lines). The same measurements were then performed under the conditions of preplasma-modified THz generation (in most cases, the preplasma position was set at THz power minimum—see figure 6). Since the preplasma-modified beam can no longer be considered as axially symmetric, the measurements have been performed in both orthogonal (x and y) directions, whereas preplasma was always scanned along the y direction. As seen in figure 6, we indeed observe a notable asymmetry of the preplasma-modified THz beams. Thus, at the intersection point before the plasma onset the angular dependence of preplasma-modified THz beam intensity, scanned along the x axis, consists of four maxima (figure 6(a), black line). Compared to the two-maxima spectrum of the unmodified conical THz beam, it is clearly seen that apart from the overall decrease of generation efficiency, the preplasma impact results in strong modification of the THz angular spectrum. Similarly, apart from the overall decrease of THz yield, some decrease of the apex angle of preplasma-modified THz emission along the y axis has been registered (figure 6(b), black line).

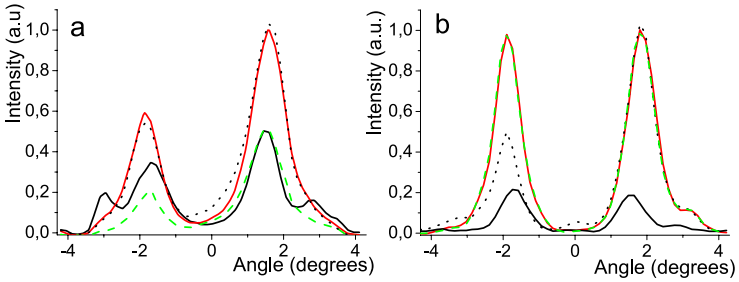

Figure 6. Angular spectra of THz beam scanned (a) along the x and (b) along the y coordinate directions. Red lines show the angular profile of the unperturbed THz beam, black solid and green dashed curves correspond to the beam profile registered when the main and preplasma beams are centered before and after the main plasma (at $z = 4$ mm and $z = 28$ mm respectively—see figure 4). Black dotted curves show the angular spectra, when the preplasma position in y-direction is set exactly at the one of two THz power minimums after the main plasma (at $z = 28$ mm).

The strongest asymmetry of the preplasma-modified THz beam angular spectrum was observed when the intersection point was located after the plasma tail. In particular, when the preplasma position was set to one of the THz energy minima and the beam was scanned along the x axis, the resulting angular spectrum remained very similar to the one without the preplasma, while the spectrum along the y direction showed a strong symmetric decrease of the THz yield (compare black dotted lines in figures 6(a) and (b)). In addition, when the preplasma position was centered with respect to the pump beam axis, the overall angular intensity of the beam significantly decreased along the x axis, but remained almost intact along the y direction (green dashed lines in figures 6(a) and (b)). Note that in contrast to the case in which the intersection point was set before the plasma onset, there was no modification of the angular THz spectrum (only decrease of angular intensity was observed) when the interaction took place after the plasma tail. This fact additionally confirms the assumption that depending on the interaction position with respect to the z axis, different phenomena are taking place: after the plasma tail, the preplasma filament simply absorbs and screens the THz radiation, while before the plasma onset, the modification of spatial properties and phase relations of the bichromatic pump beam occurs due to propagation in the preplasma, making a strong impact on the yield and angular spectrum of the generated THz radiation.

4. Conclusions

In conclusion, we have investigated the influence of a precreated plasma filament on the energy and spatial properties of terahertz radiation generated in air by focused femtosecond bichromatic laser pulses. It was found that plasma absorption and screening play an important role and significantly reduce the intensity of THz radiation when the intersection point of the bichromatic pump and prepulse beams is located after the pump beam focus. On the other hand, when the intersection point is before the pump beam focus, the main phenomenon responsible for the strong modification of generated THz radiation is the influence of the preplasma filament on the intensity and relative phase of the bichromatic pump beam.

Funding

This project has received funding from the European Union's Horizon 2020 research and innovation programme under grant agreement no 654148 Laserlab-Europe. IB and UM are thankful to financial support of DFG (MO 850-19/1, MO 850-20/1, BA 4156/4-1).

References

[1] Cook D J and Hochstrasser R M 2000 *Opt. Lett.* **25** 1210–12
[2] Thomson M D, Kress M, Loffler T and Roskos H 2007 *Laser Photonics Rev.* **1** 349–68
[3] Clough B, Dai J and Zhang X-C 2012 *Mater. Today* **15** 50–8
[4] Kim K Y, Taylor A J, Glownia J H and Rodriguez G 2008 *Nat. Photon.* **2** 605–9
[5] Minami Y, Kurihara T, Yamaguchi K, Nakajima M and Suemoto T 2013 *Appl. Phys. Lett.* **102** 041105
[6] Babushkin I, Skupin S, Husakou A, Koehler C, Cabrera-Granado E, Berge L and Herrmann J 2011 *New J. Phys.* **13** 123029
[7] de Alaiza Martínez P G, Babushkin I, Bergé L, Skupin S, Cabrera-Granado E, Köhler C, Morgner U, Husakou A and Herrmann J 2015 *Phys. Rev. Lett.* **114** 183901
[8] Oh T I, You Y S, Jhajj N, Rosenthal E W, Milchberg H M and Kim K Y 2013 *New J. Phys.* **15** 075002
[9] Xie X, Xu J, Dai J and Zhang X-C 2007 *Appl. Phys. Lett.* **90** 141104
[10] Manceau J-M, Massaouti M and Tzortzakis S 2010 *Opt. Lett.* **35** 2424–6
[11] Wen H, Daranciang D and Lindenberg A M 2010 *Appl. Phys. Lett.* **96** 161103

[12] Minami Y, Nakajima M and Suemoto T 2011 *Phys. Rev.* A **83** 023828
[13] Das J and Yamaguchi M 2013 *J. Opt. Soc. Am.* B **30** 1595–600
[14] Vaicaitis V, Smilgevicius V and Jarutis V 2011 *Opt. Commun.* **284** 2206–9
[15] Pyragaite V, Smilgevicius V, Steponkevicius K, Makauskas B and Vaicaitis V 2014 *J. Opt. Soc. Am.* B **31** 1430–5
[16] Zhao J, Zhang L, Wu T, Zhang C and Zhao Y 2016 *Opt. Commun.* **380** 87–90
[17] Zhong H, Karpowicz N and Zhang X-C 2006 *Appl. Phys. Lett.* **88** 261103
[18] Théberge F, Liu W, Simard P Tr, Becker A and Chin S L 2006 *Phys. Rev.* E **74** 036406
[19] Rodriguez G, Valenzuela A R, Yellampalle B, Schmitt M J and Kim K-Y 2008 *J. Opt. Soc. Am.* B **25** 1988–97

A3

CONTROLLED SPIN OF A NONBIREFRINGENT DROPLET TRAPPED IN AN OPTICAL VORTEX BEAM

M. Ivanov and D. Hanstorp

Opt. Commun. **427**, 152–157 (2018)

Optics Communications 427 (2018) 152–157

Contents lists available at ScienceDirect

Optics Communications

journal homepage: www.elsevier.com/locate/optcom

Controlled spin of a nonbirefringent droplet trapped in an optical vortex beam

Maksym Ivanov [a,*], Dag Hanstorp [b]

[a] Laser Research Center, Vilnius University, LT-10223, Vilnius, Lithuania
[b] Department of Physics, University of Gothenburg, SE-41296 Gothenburg, Sweden

ARTICLE INFO

Keywords:
Optical vortices and phase singularities
Optical trapping and manipulation
Angular momentum of light
Polarization singularities
Radial polarization
q-plate

ABSTRACT

The spin part of the angular momentum of light can cause a birefringent particle to spin around its axis, while having no effect on a nonbirefringent particle. The orbital part of light's angular momentum, on the other hand, can cause both birefringent and nonbirefringent particles to orbit around the axis of a light beam. In this paper, we demonstrate that nonbirefringent particles can also be made to spin around their axis when trapped in an optical vortex beam. The rotation of the particle depends on the ratio of the size of the particle and the diameter of the laser beam in which the particle is trapped. It can therefore be controlled by varying the position of the particle with respect to the focal point of the laser beam. The rotational frequency can also be controlled by changing the polarization state of the beam, since spin–orbit coupling affects the total angular momentum experienced by the trapped particle. The motion of the trapped particle is detected by a photodiode and a high-speed camera. Most microparticles found in nature are nonbirefringent, and the method presented in this paper will therefore open up new applications for optically induced rotations.

1. Introduction

The optical rotation of trapped particles is used, for example, in the noninvasive orientation of living cells, probing dynamics of particles, and investigations of tribological systems [1,2]. A particle can be set to a rotational motion by a rotating wavefront upon interference between two beams of slightly different frequencies [3], or using beams carrying angular momentum (AM). The AM of light consists of spin angular momentum (SAM) and orbital angular momentum (OAM) [4]. The SAM is associated with the circular polarization of the beam, whereas the OAM is associated with the geometry of the beam, such that the trapped particle experiences an additional tangential force. Particles trapped on the axis of a beam can be set to rotate by either the SAM and OAM of the light, in the case of birefringent [5,6] and absorbing particles [7,8]. On the other hand, nonabsorbing (transparent) and isotropic particles, such as liquid droplets, cannot be rotated by SAM, such as a circularly polarized beam. Nevertheless, it is possible to optically rotate such particles using the OAM of light [9,2,10,11], as was first demonstrated by Volke-Sepulveda et al. using transparent silica beads in a liquid [9] and by McGloin et al. using water aerosol droplets in air [2]. However, in those cases, the beads and droplets exhibit only orbital motion, making circular trajectories around the center of a beam due to the doughnut shape of the laser beam. The spinning type of motion for such particles—such as when a particle remains in place and spins around its axis—has not yet been demonstrated.

In this paper, we demonstrate a method to optically spin a nonbirefringent and nonabsorbing (transparent) microparticle—a glycerol droplet—around its axis when it is optically trapped in air by an optical vortex beam. The results presented here expand on and explain the preliminary observations presented by Hanstorp et al. in 2017 [12]. In this experiment, a droplet is initially trapped in the ring of a Laguerre–Gaussian light beam. The droplet is unconstrained azimuthally and demonstrates an orbital motion around the axis of the beam caused by the angular momentum of the light. By reducing the laser power, the droplet moves towards the waist of the laser beam. At some point, the size of the droplet becomes of the order of the size of the laser beam. The trapped droplet is then azimuthally constrained. The angular momentum of the light then causes the particle to spin around its own axis. The rate at which a trapped droplet rotates is continuously controlled from zero to maximum using spin–orbit angular momentum coupling performed by rotating a quarter-wave plate, as described in [8,11]. The motion of the trapped droplet is observed using a high-speed camera, and the frequency of rotation is measured using a photodiode.

* Corresponding author.
E-mail address: maks.ivannov@gmail.com (M. Ivanov).

https://doi.org/10.1016/j.optcom.2018.06.021
Received 26 April 2018; Received in revised form 8 June 2018; Accepted 9 June 2018

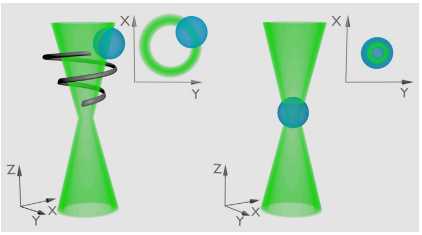

Fig. 1. Schematic of a droplet in an optical vortex trapping beam. Left: The droplet is trapped above the waist of the beam. Inset: The droplet is orbiting around the axis of the beam. As the power of the beam is reduced, the droplet moves to the axial position, as indicated by the black spiraling trajectory. Right: The droplet is trapped at the waist of the beam. Inset: The droplet positioned at the axis of the laser beam is spinning.

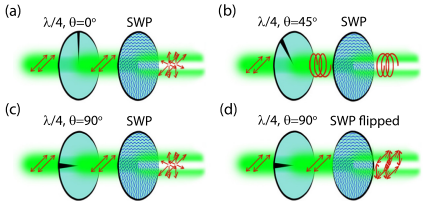

Fig. 2. Schematic showing the preparation of the trapping beam. θ indicates the orientation of the quarter-wave plate, $\lambda/4$, with respect to the direction of the incident polarization. SWP denotes an S-waveplate. SWP flipped denotes an S-waveplate that is physically flipped around the Z-axis. The red arrows schematically indicate the polarization state. The resulting polarizations are (a) radial, (b) circular, (c) radial, (d) azimuthal.

2. Beam preparation

A single optical vortex beam was used to optically levitate and rotate liquid droplets in air. The complex amplitude of an optical vortex beam can be written in the form

$$u(r, \phi, z) = A(r, z)e^{il\phi}, \quad (1)$$

where r, ϕ and z are the cylindrical coordinates, A is the amplitude of the beam (e.g., a nonzero-order Laguerre–Gaussian or Bessel–Gaussian beam), and $e^{il\phi}$ describes the azimuthally varying phase of a beam, with l being the strength or the topological charge of the optical vortex. The intensity profile of such a beam is ring-shaped or doughnut-shaped in the transverse plane. The droplet is trapped in the ring of maximum beam intensity, as schematically shown in the left part of Fig. 1. The phase front of the optical vortex beam varies helically around the axis of the beam upon propagation. Due to this helical variation, its Poynting vector is tilted with respect to the axis of the beam with a local angle given by $\theta_{screw} = l/kr$, where k is the wavenumber [13]. This tilt gives rise to the OAM of the beam, which imparts a tangential force on the trapped droplet. This is not restricted azimuthally due to the cylindrical symmetry of the intensity distribution, making the droplet orbit around the axis of the beam. The direction of rotation is determined by the handedness of the helical phase front—i.e., by the sign of the topological charge $\pm l$. The geometry of the trapping beam makes it possible to optically rotate particles of any composition, including nonbirefringent and nonabsorbing droplets.

The optical vortex beam can be generated by various methods. This experiment employed an S-waveplate, which is a nanograting-based q-plate, in order to make use of the spin–orbit coupling of angular momentum in the beam to control the spinning frequency of a trapped droplet. A Gaussian beam propagating through an S-waveplate transforms to an optical vortex beam with a Laguerre–Gaussian beam profile ($l \neq 0$) (Fig. 2). The conversion is accomplished using the following transformation of the polarization state: the initial left (right) circular polarization (with $l = 0$) transforms to right (left) circular polarization (with $|l| = 1$), (Figs. 2b and 3b); the initial linear polarization (with $|l| = 0$) becomes radial (with $|l| = 1$) if the S-waveplate is aligned parallel to the orientation of the incident linear polarization (Figs. 2a,c and 3a,c) and azimuthal (with $|l| = 1$) if aligned perpendicularly (Figs. 2d and 3d). In general, the generated radially and azimuthally polarized beams should be vortex free. However, in the region(s) where the retardation of the S-waveplate slightly deviates from the half-wave value, these beams become elliptically polarized with vortex phase $|l| = 1$ (Fig. 3). The stiffness of the optical trapping due to the different polarization patterns does not vary significantly [14] and does not affect the presented results. Detailed information on the beam conversion with aid of the S-waveplate/q-plate can be found in [15,16,11] and references within. The transmittance, T, of the S-waveplate depends on the incident wavelength, which for 532 nm is $T \geq 50\%$ [17]. The damage threshold of the S-waveplate LIDT≈ 5 J/cm^2 for $\lambda = 532$ nm and LIDT> 20 J/cm^2 for $\lambda = 1064$ nm [17].

The experimentally obtained polarization maps shown in Fig. 3 confirm the polarization states of the generated beams. The interferograms in the same figure confirm the presence of azimuthally varying phase. The interferograms show the positions of points of bifurcation of the interference lines (the "characteristic fork"), which indicate the point around which the phase circulates. For a circularly polarized beam, the point of bifurcation coincides with the center of the beam (Fig. 3b). The location of the bifurcation point is (x; y) = (0.02; 0), mm, with (0; 0) being the center of the beam. The radius of the ring of maximum intensity is 0.42 mm. However, for radially/azimuthally polarized beams, the center of the phase circulation shifts from the center of the beam to (−0.21; −0.01), (−0.27; −0.03) and (−0.29; 0.03) mm, respectively (Fig. 3a,c,d). The fact that the position of the phase circulation does not coincide with the center of a beam results in an asymmetric distribution of OAM over the beam. The effect of this asymmetry on the motion of droplets will be discussed later.

2.1. Rotational frequency control

The total angular momentum per photon is given by AM $= (l - \sigma)\hbar$, with the orbital part represented by OAM $= l\hbar$ and the spin part by $SAM = -\sigma\hbar$, and $\sigma = \pm 1$, for left/right circularly polarized beam, respectively. Note that here AM $= (l - \sigma)\hbar$ and $\sigma = \pm 1$ has been used instead of the conventional way of writing AM $= (l + \sigma)\hbar$ with $\sigma = \mp 1$ [4]. With the beam prepared as described above, the total AM experienced by the droplet per photon is given by AM $= (l - \sigma)\hbar = (-1 - 0)\hbar = -1\hbar$ for the radially polarized beam (the trapped droplet demonstrates right-hand rotation), AM $= (l - \sigma)\hbar = (+1 - 0)\hbar = +1\hbar$ for the azimuthally polarized beam (the trapped droplet demonstrates left-hand rotation) and AM $= (l - \sigma)\hbar = (-1 + 1)\hbar = 0$ for the right-hand circularly polarized beam (no rotation). The maximum frequency of rotation can thus be obtained with a linearly (radially/azimuthally) polarized beam and with zero rotational frequency using a circularly polarized beam. The transient polarization states give intermediate values of the AM. By changing the orientation of the quarter-wave plate (Fig. 2) to alter in turn the polarization state of the trapping beam, the rotational frequency of the droplet can thus be controlled. This effect of the spin–orbit coupling of the angular momentum in the beam is used to gradually control the frequency of the rotation of the

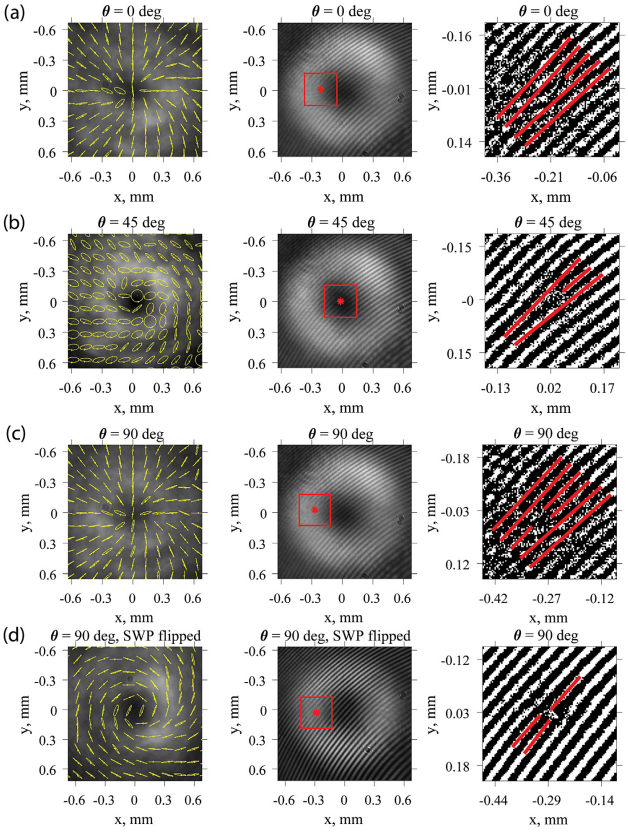

Fig. 3. Experimentally obtained polarization maps and interferograms of a beam prepared as shown in Fig. 2. θ denotes the orientation of a quarter-wave plate with respect to the direction of the incident polarization. First column: the polarization distribution is superimposed on the intensity distribution. Second column: the position of the characteristic "fork" is marked by a red star. Polarization of reference beam used to generate interference is vertical. Third column: magnified area marked by the red square in the second column. The position and direction of the bifurcation lines are highlighted by red lines. Topological charges are as follows: (a) $l = -1$, (b) $l = -1$, (c) $l = -1$, (d) $l = +1$. (For interpretation of the references to color in this figure legend, the reader is referred to the web version of this article.)

droplet, as demonstrated by [8] for absorbing particles and by [11] for nonabsorbing and nonbirefringent solid particles. In this work, the maximum OAM value is restricted to $|l| = 1$. In general, however, it is not limited to this value. The maximum value is determined by the charge, q, of the plate, which is controlled in the production of the plate.

2.2. Transition from orbiting to spinning

The switch from orbiting to spinning character of motion is governed by the geometry of the beam; this can be illustrated with an analogy with the motion of an object being pulled down a water vortex in a sink or bath: such an object experiences a reduction in the radius of its orbit and a corresponding increase in the angular velocity. The vertical position of a droplet depends on the power of the trapping beam. By lowering the power, the droplet gradually falls down from its stable trapping position above the focal region to the second stable position in the focal region (Fig. 1). The radius of the circle described by the orbiting droplet is approximately equal to the waist of the beam at the vertical position of the droplet. When the droplet is within (or close to) the focal area, the beam waist is smaller than the droplet diameter (right part of Fig. 1). The droplet still experiences AM and the orbiting motion is hence transferred to the spinning motion when the droplet is locally confined. The transition from orbiting to spinning motion is accompanied by an increase in rotational frequency.

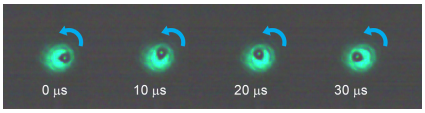

Fig. 4. Snapshots of a rotating transparent glycerol droplet (n = 1.47) levitated in air with a radially polarized optical vortex beam of strength $l = -1$. The bright spot in the center of the dark droplet is the Fresnel spot. Trapping power is 196 mW. Focal length of the trapping lens is $f = 8$ mm. Droplet diameter is 24.2 μm.

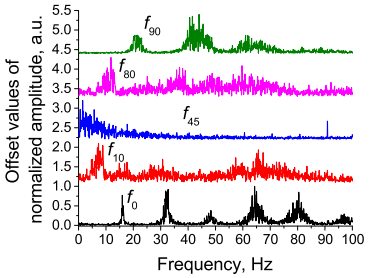

Fig. 5. Angular frequencies f_θ obtained from the Fourier-transformed photodiode signals acquired at different angles θ of the quarter-wave plate orientation (see text for details). The greatest rotation rates, seen as the fundamental Fourier component $f_0 = 16$ Hz and $f_{90} = 20$ Hz, correspond to the quarter-wave plate orientations at $\theta = 0°$ and 90°, respectively. An orientation of the quarter-wave plate at 45° leads to no rotation—that is, $f_{45} = 0$ Hz; 10° and 80° orientations lead to intermediate values of rotational frequency of $f_{10} = 9$ Hz and $f_{80} = 11.5$ Hz, respectively. Trapping power is 230 mW, droplet diameter 19.5 μm, beam diameter measured as the diameter of the ring of maximum intensity 39.2 μm.

3. Results and discussion

A diode pumped solid-state (DPSS) continuous-wave (cw) laser (Laser quantum gem532, 532 nm, 2 W maximum power) was used for this experiment. An S-waveplate (Altechna R&D) and a quarter-wave plate were used to modulate the phase, spatial distribution, and polarization of the trapping beam (Figs. 2 and 3). The motion of a trapped glycerol droplet (n = 1.47), shown in Fig. 4, was captured with a Phantom Miro eX4 high-speed camera equipped with a Canon MP-E 65 mm lens and a Canon EF 2X III Extender lens. To quantify the rotational frequency, the light scattered from the trapped droplet was collected using a photodiode. The time series obtained with the photodiode was Fourier-transformed to obtain the rotational frequency of the droplet.

3.1. Rotational frequency control

Fig. 5 shows the Fourier-transformed photodiode signal obtained from a 19.5 μm droplet orbiting in a ring of light, as shown in Fig. 4. The maximum rotational frequency, marked by f_0 and f_{90}, is achieved with a linear polarization state incident on the S-waveplate, which corresponds to the orientation of the quarter-wave plate at 0° and 90° with respect to the orientation of the polarization of the incident beam. Deviation from these orientations dramatically decreases the orbiting frequency: 10° deviation (i.e., the orientation of the quarter-wave plate at 10° or 80°) results in the frequency being approximately halved (shown as the curves f_{10} and f_{80} in Fig. 5); 45° orientation, which corresponds to circular polarization, completely eliminates the AM experienced by the droplet and the droplet stops rotating (curve f_{45} in Fig. 5). The direction of rotation remains the same, independent of the orientation of the quarter-wave plate. Reversal of the rotational motion is achieved by physically flipping the S-waveplate around the Z (gravity) axis (that is, by aiming the light through the front face of the plate instead of the back face), which reverses the handedness of the helicity of the generated optical vortex. The "fork" in Fig. 3d then points in the opposite direction to that observed in Fig. 3a–c.

The shift of the "characteristic fork" from the center of a beam (as shown in Fig. 3) leads to an aperiodic motion of the trapped droplet and hence a widening of the peaks in the frequency spectrum recorded with the photodiode. The difference between the rotational frequencies f_0 and f_{90} is caused either by disturbances due to the open trapping chamber or a slight misalignment of the optical components. The appearance of strong higher harmonics has two origins, being due either to the photodiode being positioned at neither 0° or 90° with respect to the droplet position and beam axis, or due to the aperiodic motion mentioned above.

3.2. Transition from orbiting to spinning

By reducing the laser power of the trapping beam, the droplet approaches both the focal plane of the laser beam and the beam axis. As a result, due to a decrease in the radius of the orbit, the droplet rotates faster. Fig. 6 shows the droplet rotational frequency as a function of the beam power for different trapping lens focal lengths and different droplet sizes. The size distribution of droplets, typical power levels and other practical information can be found in Appendix. The behavior is similar for all focal lengths investigated. Larger beam divergence causes more rapid transformation of the droplet from orbiting to spinning.

In the limit where the droplet diameter is equal to or greater than the beam diameter, the nature of the rotation changes from orbiting to spinning. The insets on the right side of Fig. 6 show an orbiting droplet trapped at 197 mW and a spinning droplet trapped at 98 mW. From the high-speed camera recording, it can be observed that the droplet conserves its axial position. However, the axial constraint makes it difficult to spot the spin in the video recording (see image insets in Fig. 7). The spinning of the particles is instead verified by the time series of the signal from the photodiode, which indeed shows a spinning particle. To verify this, two cases were compared. In the first case, the quarter-wave plate was oriented at 45°, such that the polarization before the S-waveplate is circular and the total AM experienced by the droplet is this zero. In the second case, the quarter-wave plate was oriented at 90°, such that the polarization before the S-waveplate is linear and AM $= -1\hbar$ (see Fig. 5 and Section 2.1). As shown in Fig. 7, there is a clear difference between the two signals, despite the similar image sequences observed with the high-speed camera. The analysis indicates that the droplet spins with a frequency of $f_{90} = 65.6$ Hz when AM is maximum, and stops spinning when AM is minimum, giving a frequency of $f_{45} = 0$ Hz.

In the case of axial localization of the isotropic spinning droplet, there are two reasons a nonzero photodiode signal is seen. Over a short time scale, an inhomogeneity or impurity in droplet composition could give rise to a periodic signal. However, since the droplet is in the liquid phase, it should smear out over a long time scale, unless the impurity inside the droplet is trapped by the beam and constituted the main contribution to the signal. Over a long time scale, variability in the position of the droplet gives rise to the observed frequency. An asymmetric distribution of OAM or a slight inclination of the plane of rotation of the droplet with respect to the normal to the direction of gravity would result in nanometer-scale variations in the position, which is the main cause of the observed periodic signal.

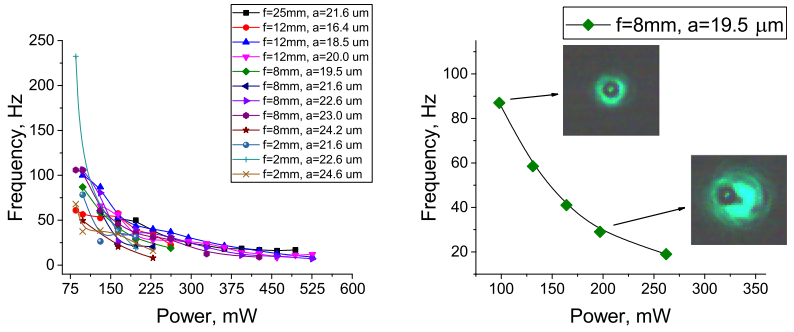

Fig. 6. Angular frequency of the droplet rotation as a function of the trapping power. The left side shows the dependency under various specified experimental conditions, while the right side is an example of a particular case. f is the focal distance of the trapping lens in mm, and a is the droplet diameter in μm. Image insets on the right side: glycerol droplet trapped on the axis (top) and within the ring of light (bottom) of Laguerre–Gaussian beam. Trapping power is 98 mW and 197 mW, respectively. Droplet diameter is 19.5 μm.

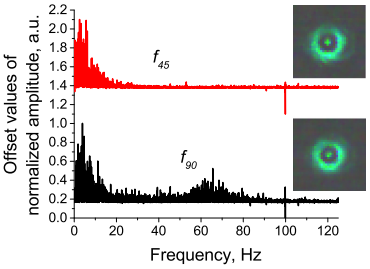

Fig. 7. Comparison of two Fourier-transformed photodiode signals obtained at two different orientations of the quarter-wave plate. The quarter-wave plate oriented at 45° (circular polarization, AM is minimum) leads to zero spin, $f_{45} = 0$ Hz, while the 90° orientation (linear polarization, AM is maximum) leads to spin at a frequency of $f_{90} = 65.6$ Hz. Insets: snapshots from the high-speed camera recordings showing a glycerol droplet trapped on the axis of the Laguerre–Gaussian beam; the bright spot in the center of each droplets is the Fresnel spot. Trapping power is 98 mW, and droplet diameter 19 μm.

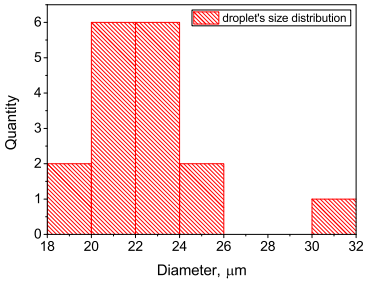

Fig. A.8. Size distribution of droplets used in the experiment.

4. Conclusion

We have demonstrated a single-beam technique for optical levitation and rotation of nonabsorbing (transparent) and nonbirefringent liquid droplets in air. The trapped droplet can be made to either orbit or spin around the axis of the trapping beam. The type of rotational motion depends on the size of the local waist of the trapping beam at the point of trapping. The vertical trapping position is controlled by the power level of the trapping laser beam. The frequency of the rotation of the droplet depends on the polarization of the beam (even though the droplet is not birefringent) due to the spin–orbit coupling of the angular momentum in the beam. The polarization is continuously controlled by the orientation of the quarter-wave plate. This single-beam method may be preferential to multiple-beam technique on account of interference between two beams of slightly different frequencies, and for extending the abilities of conventional optical tweezers and complex setups in the analysis and probing of microparticles, as discussed in [12]. Although the experiment was performed in air with liquid droplets the described method can be successfully used in conventional optical tweezers with samples in any phase (gas/liquid/solid) as long as the standard condition $n_p > n_s$ for refractive indices of surrounding, n_s, and particle/sample, n_p, is met. Additionally, this method can find applications outside optics, such as in fluid dynamics, where rotating droplets could be achieved in the study of collisional dynamics of liquid droplets in studies of raindrop formation [18].

Appendix

For the experiment glycerol droplets (n = 1.47) were used. Size distribution of droplets is shown in Fig. A.8 The droplets were prepared using a commercial printer cartridge (Hewlett–Packard C6614). The cartridge works as a drop-on-demand system, where a droplet is ejected each time a TTL pulse is sent to the cartridge from a pulse generator (see Ref. [18] and references within for the droplet generation technique). Glycerol has no absorption in the visible range of wavelength [19]. Negligible level of absorption could originate from contamination of the glycerol solution. Purity of used glycerol (produced by Fisher Scientific) was 99.6%.

Other experimental parameters are specified in Table A.1.

Table A.1
Experimental parameters.

Focal length, f, mm	Corresponding beam spot diameter at the waist[a], D, μm	Beam diameter[b] at 196 mW power level, D_P, μm, (see Figs. 4 and 6)	Typical power required to levitate the droplet[c], P_1, mW	Typical power prior the droplet is lost from the trap[c], P_2, mW
25	8.5	53 ± 5	500	165
12	4.1	47 ± 5	440	100
8	2.7	40 ± 5	365	115
2	0.7	31 ± 5	260	125

[a] Calculated as $D = 1.27\lambda f / D_0$. D_0 = 2 mm — spot size of the beam on the lens, f — focal length of the length, λ = 532 nm — light's wavelength.
[b] Beam diameter is measured as the diameter of the ring of maximum intensity.
[c] Measured after the trapping lens. Trapping laser: CW, λ = 532 nm.

References

[1] D.G. Grier, A revolution in optical manipulation, Nature 424 (6950) (2003) 810–816. http://dx.doi.org/10.1038/nature01935.
[2] D. McGloin, D.R. Burnham, M.D. Summers, D. Rudd, N. Dewara, S. Anandc, Optical manipulation of airborne particles: techniques and applications, Faraday Discuss. 137 (2008) 335–350. http://dx.doi.org/10.1039/b702153d.
[3] M.P. MacDonald, L. Paterson, K. Volke-Sepulveda, J. Arlt, W. Sibbett, K. Dholakia, Creation and manipulation of three-dimensional optically trapped structures, Science 296 (5570) (2002) 1101–1103. http://dx.doi.org/10.1126/science.1069571.
[4] S.M. Barnett, L. Allen, R.P. Cameron, C.R. Gilson, M.J. Padgett, F.C. Speirits, A.M. Yao, On the natures of the spin and orbital parts of optical angular momentum, J. Opt. 18 (2016) 064004. http://dx.doi.org/10.1088/2040-8978/18/6/064004.
[5] M.E.J. Friese, T.A. Nieminen, N.R. Heckenberg, H. Rubinsztein-Dunlop, Optical alignment and spinning of laser-trapped microscopic particles, Nature 394 (1998) 348–350. http://dx.doi.org/10.1038/28566.
[6] A.T. ONeil, I. MacVicar, L. Allen, M.J. Padgett, Intrinsic and extrinsic nature of the orbital angular momentum of a light beam, Phys. Rev. Lett. 88 (5) (2016) 053601. http://dx.doi.org/10.1103/PhysRevLett.88.053601.
[7] H. He, M.E.J. Friese, N.R. Heckenberg, H. Rubinsztein-Dunlop, Direct observation of transfer of angular momentum to absorptive particles from a laser beam with a phase singularity, Phys. Rev. Lett. 75 (5) (1995) 826–829. http://dx.doi.org/10.1103/PhysRevLett.75.826.
[8] N.B. Simpson, K. Dholakia, L. Allen, M.J. Padgett, Mechanical equivalence of spin and orbital angular momentum of light: an optical spanner, Opt. Lett. 22 (1) (1997) 52–54. http://dx.doi.org/10.1364/OL.22.000052.
[9] K. Volke-Sepulveda, V. Garces-Chavez, S. Chavez-Cerda, J. Arlt, K. Dholakia, Orbital angular momentum of a high-order bessel light beam, J. Opt. B: Quantum Semiclass. Opt 4 (2002) S82. http://dx.doi.org/10.1088/1464-4266/4/2/373.
[10] O. Brzobohaty, M. Siler, J. Jezek, P. Jakl, P. Zemanek, Optical manipulation of aerosol droplets using a holographic dual and single beam trap, Opt. Lett. 38 (22) (2013) 4601–4604. http://dx.doi.org/10.1364/OL.38.004601.
[11] M. Gecevicius, R. Drevinskas, M. Beresna, P.G. Kazansky, Single beam optical vortex tweezers with tunable orbital angular momentum, Appl. Phys. Lett. 104 (2014) 231110. http://dx.doi.org/10.1063/1.4882418.
[12] D. Hanstorp, M. Ivanov, A.F.A. Hernandez, J. Enger, A.M. Gallego, O. Isaksson, C.-J. Karlsson, R.M. Villa, A. Varghese, K. Chang, A versatile system for optical manipulation experiments, Proc. SPIE 10347 (2017) 10347. http://dx.doi.org/10.1117/12.2272983.
[13] J. Leach, S. Keen, M.J. Padgett, C. Saunter, G.D. Love, Direct measurement of the skew angle of the poynting vector in a helically phased beam, Opt. Express 14 (25) (2006) 11919–11924. http://dx.doi.org/10.1364/OE.14.011919.
[14] T.A. Nieminen, N.R. Heckenberg, H. Rubinsztein-Dunlop, Forces in optical tweezers with radially and azimuthally polarized trapping beams, Opt. Lett. 33 (2) (2008) 122–124. http://dx.doi.org/10.1364/OL.33.000122.
[15] A. Matijosius, P. Stanislovaitis, T. Gertus, V. Smilgevicius, Formation of optical vortices with topological charge $|l| = 1$ and $|l| = 1/2$ by use of the s-waveplate, Opt. Commun. 324 (2014) 1–9. http://dx.doi.org/10.1016/j.optcom.2014.03.023.
[16] A. D'Errico, M. Maffei, B. Piccirillo, C. de Lisio, F. Cardano, L. Marrucci, Topological features of vector vortex beams perturbed with uniformly polarized light, Sci. Rep. 7 (40195) (2017). http://dx.doi.org/10.1038/srep40195.
[17] Workshop of photonics. URL https://www.wophotonics.com/product/radial-polarization-converter-s-waveplate/.
[18] M. Ivanov, K. Chang, I. Galinskiy, B. Mehlig, D. Hanstorp, Optical manipulation for studies of collisional dynamics of micron-sized droplets under gravity, Opt. Express 25 (2) (2017) 1391–1404. http://dx.doi.org/10.1364/OE.25.001391.
[19] R.D. Birkhoff, L.R. Painter, J.M. Heller, Optical and dielectric functions of liquid glycerol from gas photoionization measurements, J. Chem. Phys. 69 (9) (1978) 4185–4188. http://dx.doi.org/10.1063/1.437098.

A4

TOWARDS THE GENERATION OF BROADBAND OPTICAL VORTICES: EXTENDING THE SPECTRAL RANGE OF A GEOMETRIC PHASE RETARDER BY POLARIZATION-SELECTIVE FILTERING

M. Gecevicius, **M. Ivanov**, M. Beresna, A. Matijosius,
V. Tamuliene, T. Gertus, A. Cerkauskaite, K. Redeckas,
M. Vengris, V. Smilgevicius, and P. G. Kazansky

J. Opt. Soc. Am. B **35**, 190 (2018)

Towards the generation of broadband optical vortices: extending the spectral range of a q-plate by polarization-selective filtering

MINDAUGAS GECEVICIUS[1,3], MAKSYM IVANOV[2], MARTYNAS BERESNA[1], AIDAS MATIJOSIUS[2*], VIKTORIJA TAMULIENE[2], TITAS GERTUS[4], AUSRA CERKAUSKAITE[1], KIPRAS REDECKAS[2], MIKAS VENGRIS[2], VALERIJUS SMILGEVICIUS[2], AND PETER G. KAZANSKY[1]

[1] Optoelectronics Research Centre, University of Southampton, SO17 1BJ, Southampton, United Kingdom
[2] Vilnius University Laser Research Center, 10 Sauletekio avenue, LT- 10223, Vilnius, Lithuania
[3] State Key Laboratory of Luminescent Materials and Devices, South China, University of Technology, Guangzhou 510640, China
[4] Altechna R&D Ltd., Mokslininku st. 6A, LT-08412, Vilnius, Lithuania
[*] Corresponding author: aidas.matijosius@ff.vu.lt

Compiled July 19, 2019

Optical vortex beams in the visible and nIR spectrum over a wide spectral region are generated by a single S-Waveplate polarization converter using polarization-selective filtering. A spectral coverage of 600 nm is demonstrated, with maximum efficiency at a wavelength of 530 nm. The broadband coverage is obtained using polarization filtering, which is applicable for any component based on geometric phase retardation. The efficiency of the filtering varies from 50% to 95% depending on the wavelength. This technique has a potential application in stimulated emission depletion (STED) microscopy and lithography.

OCIS codes: (050.4865) Optical vortices; (230.5440) Polarization-selective devices.

http://dx.doi.org/10.1364/ao.XX.XXXXXX

1. INTRODUCTION

Optical orbital angular momentum (OAM) of $l\hbar$ per photon ($\hbar$ is the reduced Planck constant) [1] rises in the light fields with screw wavefront dislocations [2]. Phase of these beams varies azimuthally and their complex amplitude is proportional to $e^{il\phi}$, where l is referred to as topological charge, r and ϕ are the radius and azimuthal angle, respectively. Such OAM beams are frequently referred to as Optical Vortices (OVs) [3]. Due to the presence of OAM and doughnut shaped intensity distribution OVs have found applications in various areas [4–9]. In most of those applications broadband or at least widely tunable OVs are desired; however, their generation is technically challenging due to inherent dependence on wavelength λ. Indeed, the wavefront of OVs which give rise of OAM has the tilt of $l\lambda/2\pi r$ [10].

An exotic method of broadband OV generation exploits nonlinear processes [11]. However, the simpler (hence more practical) techniques rely on amplitude, phase and/or polarization modulation of a Gaussian beam in a dedicated optical component. The most common component is a forked hologram recorded on photographic film [12] or displayed with spatial light modulator [13] that modulates amplitude or phase of an initial beam. Due to the diffractive nature of such modulation, this technique suffers from chromatic angular dispersion [14] and requires compensation schemes. The widest OV bandwidth demonstrated to date used a forked grating inscribed in a phase hologram and covered 250 nm range with the central wavelength of $\lambda_0 = 800$ nm [15].

Phase plates with varying azimuthal thickness can generate OVs over 140 nm range in the visible [16]. Their bandwidth depends on the phase plate material.

Polarization-based methods include axially-symmetric polarizer [17], quarter [18] and half [19] waveplates, and a glass cone [20]. These methods can theoretically produce OVs in the entire visible spectrum, however, they lack sufficient spatial resolution in the axial part of the component, which is essential in applications such as stellar coronagraphy [21]. Additionally, the methods described in [19, 20] are limited to $|l|$=2. Due to dispersive nature of glass, OV generated with the glass cone [20] exhibits spatial and chromatic dispersions. Separately, polarization grating [22] should be mentioned. It provides extremely high efficiency over wide spectral region, however, suffers chromatic dispersion and has a relatively low damage threshold of liquid crystals.

Recognition of eigenmodes of light in the form of Laguerre-Gaussian (LG) modes in a homogeneous anisotropic medium

(e.g. uniaxial crystals) [23], created a wave of subsequent studies of broadband OVs generation from spin-orbit coupling of angular momentum (AM) of light in uniaxial and biaxial crystals. Biaxial crystals demonstrated bandwidth of 250 nm after additional compensation of chromatic dispersion [24]. Uniaxial crystals demonstrated 360 nm bandwidth (but are not limited to this value) [25–27]. To generate OV, Gaussian beam should be focused onto the crystal. The radial index of the generated LG mode depends on the angle of divergence of the initial beam and crystal length. Q-plate is another class of components that uses spin-to-orbit coupling of AM. Q-plate is a spatially variant half-wave plate, which by changing polarization of the incident beam changes its geometric (Pancharatnam-Berry) phase [28]. When slow (fast) optical axis spatially varies in the form of $\psi = q\phi$ (with q half-integer) and birefringent phase retardation is π (half-wave) then the AM of light is not transferred to the material but directly converts from spin to orbital. Three most common techniques of inducing π phase retardation are based on liquid crystals (LC), photonic crystals (PC) and nano-gratings (sub-wavelength gratings). LC based q-plates allow tuning of a plate to a certain wavelength by changing the applied voltage [29, 30], but do not allow simultaneous coverage of a broad spectrum range. PC based q-plates demonstrate 300 nm bandwidth (from 500 to 800 nm) [31]. Nano-grating (sub-wavelength grating) based q-plates are also referred to as super-structured wave plates (S-waveplates). The period of spatial structures in such plates is shorter than the wavelength of light in the visible spectrum [32–34]. These components exhibit high spatial resolution of patterning in the axial area and are resistant to optical damage [35]. However, their specified bandwidth is 20 nm around the central wavelength.

Recently, it was suggested that additional polarization sensitive [36] or spatial filtering [37] can significantly broaden the spectral performance of Pancharatnam-Berry phase elements. However, the experimental efforts were confined to far-infrared spectral range and did not demonstrate the polarization sensitive beam cleaning as spatial filtering was performed instead [37]. Similar polarization filtering was performed to reduce dispersion of topological charge of high order OVs [38] (without theoretical description of the process). Yet, enhancement of spectral performance was not demonstrated.

In this article, using proposed polarization-sensitive filtering, we demonstrate generation of an optical vortex beam over the entire visible and near infrared range, from temporarily coherent and incoherent light sources. This technique allows converting any wavelength dependent (chromatic) Pancharatnam-Berry phase element to an achromatic one. We have employed a high damage threshold S-waveplate with an initial bandwidth of 20 nm (around the central wavelength of 532 nm) and demonstrated that it can be used to generate high contrast OV beams at any given wavelength in the range between 400 nm and 1040 nm. The efficiency of the filtering and possible applications of this technique are discussed.

2. OPTICAL VORTICES OVER OCTAVE-SPANNING SPECTRAL RANGE

A. Theory

Although topological charge l of the S-waveplate could reach higher values [39], in the following we restrict our considerations to $l = 1$. The S-Waveplate acts as a half-wave plate phase retarder and it's operation can be described by the Jones matrix formalism. The matrix for the S waveplate is as follows:

$$M_s = \begin{bmatrix} \cos(2\theta) & \sin(2\theta) \\ \sin(2\theta) & -\cos(2\theta) \end{bmatrix}; \quad (1)$$

where θ is an azimuthal angle of the optical axis of a half-wave plate. The resulting light field E_{out} can be presented as an action of a half-wave plate converter M_S on the initial field E_{in}: $E_{out} = M_s E_{in}$. If a right-handed circularly polarized light is transmitted through the S-Waveplate, a left-handed circularly polarized OV (with the topological charge equal to 1) is generated:

$$E_{out} = \frac{1}{\sqrt{2}} M_s \begin{bmatrix} 1 \\ i \end{bmatrix} E_{in} = \frac{1}{\sqrt{2}} e^{i2\theta} \begin{bmatrix} 1 \\ -i \end{bmatrix} E_{in}, \quad (2)$$

where $E_{in} = e^{-r^2/w^2} e^{-i(2\pi/\lambda_0)r^2/(2R')}$ is Gaussian envelope, $R' = z(1 + (z'/z)^2)$, $z' = \pi w_0^2/\lambda$, $r^2 = x^2 + y^2$, x, y and z are Cartesian coordinates, w is waist of the beam and λ is the wavelength of light. So, left (right) handed circularly polarized light passed S-waveplate acquires vortex phase and orthogonal right(left) handed circular polarization. However, if the wavelength of incident light, λ, differs from the wavelength the S-waveplate was designed for, λ_0, the value of phase retardation would be different for different wavelengths: $\Delta = \pi\lambda_0/\lambda$. It means that only light at the wavelength λ_0 would remain circularly polarized. Arbitrary wavelength λ would acquire elliptical polarization and phase retardation Δ. By multiplying Jones vector for left circular polarization with Jones matrix for the retarder (S-waveplate) with phase retardation Δ and azimuth θ (orientation of optical axis), we can calculate how circular polarization of the input light will be transformed:

$$E_{el} = \frac{1}{\sqrt{2}} \begin{bmatrix} cos^2(\theta) + e^{i\Delta} sin^2(\theta) & (1 - e^{i\Delta}) sin(\theta) cos(\theta) \\ (1 - e^{i\Delta}) sin(\theta) cos(\theta) & sin^2(\theta) + e^{i\Delta} cos^2(\theta) \end{bmatrix} \begin{bmatrix} 1 \\ i \end{bmatrix} E_{in} = \frac{1}{\sqrt{2}} \begin{bmatrix} cos^2(\theta) + e^{i\Delta} sin^2(\theta) + i(1 - e^{i\Delta}) sin(\theta) cos(\theta) \\ (1 - e^{i\Delta}) sin(\theta) cos(\theta) + i(sin^2(\theta) + e^{i\Delta} cos^2(\theta)) \end{bmatrix} E_{in} \quad (3)$$

Eq. 3 does not give much information on phase or polarization dependence of the beam on phase retardation Δ or azimuthal angle θ. Now let us assume that the light with such polarization E_{el} (Eq. 3) passes the left L or right R circular polarizer (quarter wave plate and linear polarizer). Then, the electric fields (E_R and E_L) will be following:

$$E_{right} = RE_{el} = \frac{1}{2\sqrt{2}}(1 - e^{i\Delta}) e^{i2\theta} \begin{bmatrix} 1 \\ -i \end{bmatrix} E_{in}; \quad E_{left} = LE_{el} = \frac{1}{2\sqrt{2}}(1 + e^{i\Delta}) \begin{bmatrix} 1 \\ i \end{bmatrix} E_{in}, \quad (4)$$

where R and L are the Jones matrices for right and left circular polarizers, respectively:

$$R = \frac{1}{2} \begin{bmatrix} 1 & i \\ -i & 1 \end{bmatrix}; L = \frac{1}{2} \begin{bmatrix} 1 & -i \\ i & 1 \end{bmatrix}; \quad (5)$$

After the left-handed circularly polarized light of $\lambda \neq \lambda_0$ passes through the S-waveplate and a right-handed circular polarizer, the electric field E_R (Eq. 4) becomes similar to what

we would expect after passing through the S-waveplate when $\lambda = \lambda_0$ (Eq. 2). It contains the same factor $e^{i2\theta}$ which indicates the azimuthal phase variation of the field, i.e. presence of an OV. However, after the left-handed circular polarizer, the electric field E_L (Eq. 4) does not have this azimuthally dependent term. Therefore, after the S-waveplate, the circularly polarized light of wavelength $\lambda \neq \lambda_0$ can be separated into two parts according to the handedness of polarization. Only one of the polarizations will exhibit the azimuthally varying phase dependence, i.e. become an OV.

The ratio of the two resultant fields depends only on the phase retardation of the retarder:

$$I_R = E_{Rx}E^*_{Rx} + E_{Ry}E^*_{Ry} = \frac{1}{2}(1 - \cos \pi\lambda_0/\lambda) \quad (6)$$

$$I_L = E_{Lx}E^*_{Lx} + E_{Ly}E^*_{Ly} = \frac{1}{2}(1 + \cos \pi\lambda_0/\lambda) \quad (7)$$

In summary, even if any S-Waveplate or, in general, any other optical element based on the phase control of circularly polarized light by half-wave plates (e.g. [40]) is designed for a specific wavelength, a desired transformed part of the beam can be easily separated out using a circular polarizer.

As an illustration, using previous equations 4 and a Fourier propagation method, a situation was simulated, where a circularly polarized beam passes through the S-Waveplate, quarter-wave plate and a linear polarizer (Fig. 1). The modelled S-Waveplate is set for $\lambda_0 = 530$ nm wavelength, whereas the spectrum of the incident light ranges from 400 nm to 1000 nm. The results indicate that the contrast of the vortex beam generated with the S-Waveplate strongly depends on the wavelength (Fig. 1 (ii)). However, after passing the circular polarizer, at all wavelengths a high contrast OV is obtained (Fig. 1 (iii)), with zero intensity at the center. Due to the wavelength mismatch all the "background", i.e. not phase modulated part of the beam is separated to the orthogonally polarized field (Fig. 1 (iv)).

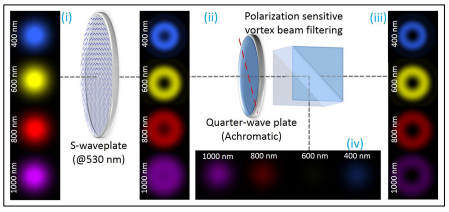

Fig. 1. The simplified schematic and numerical model for OVs generation and polarization-sensitive beam cleaning. Gaussian beams (i) pass through the S-Waveplate, resulting in OVs with different contrast, depending on the wavelength (ii). The quarter-wave plate and linear polarizer work as a polarization-sensitive vortex beam filter that separates the vortex beam (iii) and the background with no phase modulation (iv).

B. Experiment

We used an S-Waveplate designed for 530 nm (fabricated by Altechna R&D, developed at the University of Southampton [32, 33]). The S-Waveplate was illuminated with femtosecond light pulses tuned in the range of 400 − 1040 nm from an optical parametric amplifier "Topas" (Light Conversion Ltd.). The experimental setup was similar to the one illustrated in the Fig. 1. However, to achieve a perfect achromatic behaviour in a wide spectral range, achromatic quarter-wave plates (for circular polarization generation and for circular analyser) were replaced with two Fresnel rhombs and a calcite crystal was used to separate two orthogonal polarizations. The beam profiles were measured using a CCD camera (Chameleon CMLN-13S2M-CS).

C. Results and discussion

The contrast (intensity in the center of the beam divided by the maximum intensity of the beam: I_{min}/I_{max}) of the OVs generated by the S-Waveplate strongly depended on the wavelength (Fig. 2 (ii)). At wavelengths close to the design wavelength of 530 nm, the generated beams exhibited a well-defined doughnut shape, while at nearly twice longer wavelength ($\sim$ 1000 nm) the generated beam had a flat top profile with no sign of singularity at the center. However, after the polarization-sensitive beam cleaning part of the setup (second Fresnel rhomb and calcite crystal), vortex and Gaussian parts of the beams were separated into two beams (Fig. 2 (iii,iv)).

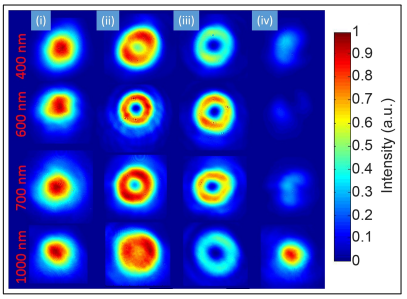

Fig. 2. Experimental intensity distributions of: (i) Initial Gaussian beam before S-Waveplate; (ii) – beam after S-Waveplate; (iii) filtered vortex part of the beam (after a quarter-wave plate and a linear polarizer); (iv) Gaussian (background) part of the beam (after quarter-wave plate and linear polarizer).

The further analysis of beams presented in Fig. 2 (ii,iii) and (iii,iv) is shown in Fig. 3 and 4, respectively. The performance of the polarization-sensitive beam cleaning was evaluated by comparing the contrast of the generated OVs before and after beam cleaning (Fig. 3 (a)). Before beam cleaning, the contrast exhibit a strong dependence on wavelength, whilst after the cleaning, contrast of OV is similar at all wavelengths. Small variations in the contrast after cleaning is caused by the variations in the quality of the input Gaussian beam (Fig. 2 (i)) rather than the chromaticity of the setup.

In order to confirm the presence of phase helicity in the vortex part of the beam and its absence in the orthogonally polarized part, both parts of the beams were injected into a Michelson interferometer and interference patterns were measured (Fig. 3 (b)). As predicted, the interference pattern of the vortex beam exhibited a forked structure (which is a clear indication of the phase helicity) whereas the orthogonally polarized Gaussian (background) part of the beam produced regular fringes.

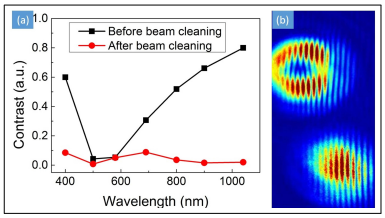

Fig. 3. (a) The contrast of generated vortex beams at different wavelength before and after the polarization sensitive beam cleaning. (b) Interference of vortex- and Gaussian part (background) of the beam (at 1000 nm).

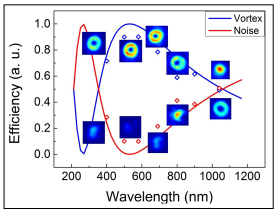

Fig. 4. Polarization sensitive beam cleaning efficiency dependence on the wavelength. Experimental points are compared with the theoretical curve. Insets demonstrate measured beam profiles of generated OVs and beams profiles of filtered out background at different wavelengths.

The reason for one polarization component to acquire vortex structure and for other not to is following. The beam is being transformed to OV by acquiring phase retardation $\lambda_0/2$ and changing its polarization state to orthogonally polarized. When the incident wavelength $\lambda \neq \lambda_0$, the phase delay and polarization state depend on λ; the beam become elliptically polarized. Dividing the beam into two orthogonally polarized parts and selecting the polarization orthogonal to initial, we automatically select the light which acquired $\lambda_0/2$ phase delay. Therefore, one polarization component carry an OV and other does not.

Fig. 2 (iii,iv) shows that unlike the contrast, the power ratio between the cleaned vortex part of the beam and not phase modulated background (Gaussian "noise") part strongly depends on wavelength. The efficiency of the vortex/Gaussian conversion at different wavelengths (Fig. 4) can be evaluated using Eq. 7. Maximum efficiency is achieved at the design wavelength of the S-Waveplate; the efficiency remains above 50% at the wavelength nearly two times larger than the design wavelength, demonstrating successful OV generation in the 600 nm wavelength range (in this range, the efficiency is more than 50%). Obviously the bandwidth scales with the central wavelength: an S-Waveplate designed for the 1 μm wavelength would cover the bandwidth of 1.2 μm.

Besides OVs generation in a broad wavelength range, the presented scheme can also work as a polarization selective vortex converter. The handedness of circular polarization determines whether the Gaussian beam passing through the setup stays Gaussian or is converted to an OV. Therefore, for example, if we have two beams with different wavelengths and orthogonal circular polarizations, only one of them will be converted to a vortex beam and the other would remain unaffected (Fig. 5 (a)). This could be useful for stimulated emission depletion (STED) applications as both beams could travel in the same optical path and just before the objective, one of them would be converted to a vortex beam. The advantage of such geometry has already been demonstrated in [6, 41], where an OV was generated using a highly chromatic optical component, which imposed a limit on how close the two wavelengths could be. Since our method is based on polarization selection, there is no such wavelength limitation for the two beams; only the "correctly" polarized beam will be converted to a vortex. In order to demonstrate how this works in practice, we performed an experiment using the setup illustrated in Fig. 5 (a). We used three lasers with different wavelengths: red – HeNe laser (633 nm), green – second harmonics of Nd:YAG laser (532 nm), blue – OPA output at 400 nm wavelength. Orthogonally polarized beams of two of the lasers (red and green or blue and green) were launched collinearly through the polarization sensitive OV generator. As shown in Fig. 5 (b), in each case, only one beam (green in the presented case) was transformed into a vortex whereas the other remained Gaussian. With currently available laser sources intensity efficiency of the methods does not impose limitation for the application. The proposed scheme with single optical path for both excitation and depletion beams could significantly facilitate extremely complicated process of alignment of STED systems.

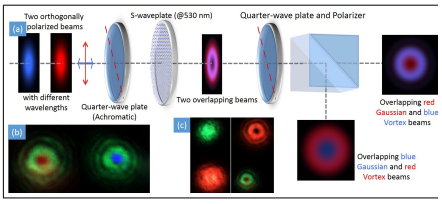

Fig. 5. Polarization selective vortex beam generation: (a) experimental set-up and modeled results; (b) experimentally measured profiles of green (532 nm) vortex beam after polarization transformation superimposed with orthogonally polarized red (633 nm) and blue (400 nm) Gaussian beams in the middle; (c) experimental beam profiles (532 nm and 633 nm) before (on the left) and after (on the right) polarization sensitive transformation.

3. OPTICAL VORTEX GENERATED FROM AN INCOHERENT WHITE LIGHT SOURCE

A. Theory

In this section, we expand our previous considerations to generate "white" light OV. Hereafter, white light means a broadband incoherent light emitted by an incandescent halogen lamp. Temporally incoherent incident light field $A(t)$ is given by the Gaussian-Gaussian noise model [42]:

$$A(t) = \frac{1}{\sqrt{N}} \sum_{j=1}^{N} e^{(it\Omega_j + i\xi_j)}, \quad (8)$$

where $\Omega_j = \omega_j - \omega_0$, ω_0 and ω_j are the central and normally distributed random frequencies, respectfully; dispersion σ^2 ($\sigma = (\omega_1 - \omega_2)/2\sqrt{2}$, $\omega_{1,2} = 2\pi c/\lambda_{1,2}$, c – speed of light). ξ_j are uniformly distributed random phases. N has to be significantly large in the simulation (here $N = 471$). The wavelengths $\lambda_1 = 360$ nm and $\lambda_2 = 830$ nm, $\lambda_0 = 530$ nm. Intensity distributions after each component in the experimental setup are obtained by the multiplication of the Fourier transformed complex amplitude $A(t)$ by the Jones matrix of the corresponding optical element. For example, the vortex E_V and not phase modulated E_G parts of the beam after the polarization filtering are given by:

$$E_{V(G)} = E_{right(left)} S(\omega), \tag{9}$$

where $S(\omega)$ is the Fourier transform of the $A(t)$, $E_{right(left)}$ is given by Eq. 4. Such field has Gaussian shaped spectrum and obeys Gaussian statistics [42]. Modeled intensity distributions are shown in the top row of the Fig. 7.

B. Experiment

For the white-light experiment the light source in the experimental setup described in the section 3B was substituted by a 55 W tungsten halogen bulb and used as the source of an incoherent broadband white light. The light from the halogen bulb was collected (without focusing system) by a multimode gradient optical fiber (86 cm long, cladding diameter 850 μm, core diameter 130 μm) placed close to the lamp. Only the light propagating through the core of the fiber was then selected by the first aperture (diameter 0.95 mm) placed 21 mm after the tip of the fiber. The spatial coherence of the light was controlled by the size of this aperture. It should be small enough to provide sufficient degree of spatial coherence for the generated optical vortex to be visible, i.e. to posses deep axial minimum of intensity ([26, 43] and references within). "White"-light beam with a high degree of spatial coherence was then collimated with the aid of a pair of lenses in the telescope configuration and spatially filtered by the second aperture (diameter 110 μm) placed in the common focus between these lenses. The role of the second aperture was to endow the beam with nearly Gaussian intensity profile and to control its waist size. The polarization tailoring of the beam were achieved by Fresnel rhombs and a Glan polarizer. An angle cut calcite crystal was used to separate two polarization states. Colored images of the beam were obtained by Canon 600d camera with the default settings for the white balance, saturation, contrast and color tone.

C. Results and discussion

Bandwidth of the incident white light spans from 325 nm to 1030 nm and is shown in the Fig. 6a (solid black curve marked as "Initial experimental"). However, for modeled intensity distributions spectrum in the limits of human eye perception was used: from 360-830 nm (hollow brown circles in the Fig. 6a). The "white" light beam acquired its vortex structure upon propagation through the S-waveplate designed for conversion of light in the 20 nm bandwidth (as stated by the manufacturer) around its central wavelength of 532 nm. Due to the far exceeding bandwidth of the incident "white" light, the visibility of the vortex core (zero intensity at the axis) is "masked" in the beam right after the S-waveplate (Fig. 7). As described in the previous sections, the maximum conversion efficiency is around design wavelength of the S-waveplate. Hence, the central part of the beam right after the S-waveplate is filled by the pink-violet shades, which are result of the substruction of green shades from

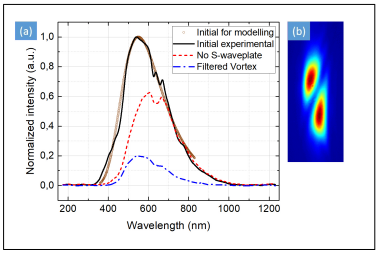

Fig. 6. (a) Spectra of the "white" light beam in different states. *Experimental*: Black (solid): initial unpolarized white light; Red (dashed): spectrum of the polarized collimated beam after passing all the polarization optics but the S-waveplate; Blue (dashed-doted): vortex part of the beam after the polarization filtering (i.e. beam passed all the polarization optics and the S-waveplate). *Modeled*: Brown (hollow circles): initial spectrum used for modeling; cut at the limits of visible light. (b) Generated "white" light OV focused by a cylindrical lens. See text for details.

the white color. After the polarization selective filtering vertically polarized part of the beam with "clean" vortex structure (zero axial intensity) is spatially separated from the horizontally polarized background part of the beam having no phase singularity. Intensity normalized experimental images are shown in the Fig. 7 bottom row and demonstrate good agreement with the model. Outer red shades and inner blue shades of the circle of light of OV could be explained by the scattering of white light on objects smaller then the wavelength of light, which are the nano "cracks" the grating of the S-waveplate is made of.

The spectrum of the filtered optical vortex is shown in the Fig. 6a marked as "Filtered vortex" (dashed-dotted blue curve). Red dashed curve in the Fig. 6a marked as "No S-waveplate" shows spectrum of the beam after it passed through all the polarizing optics in the setup (under condition that the S-waveplate is removed from the setup). Because some of the polarizing elements were made from calcite, the spectrum of the beam was cut at the blue side, so it differs from initial and spans from 400 to 1000 nm. The spectrum of the filtered vortex has its maximum at 545 nm and spans from 410 to 900 nm. Conversion efficiency at different wavelengths differs as described in the previous sections.

Different frequency components acquire different phase delay, resulting in a topological charge dispersion [44]. Based on this effect vortex with half integer topological charge $|l| = 1/2$ can be generated when the S-waveplate is illuminated by twice the wavelength it is designed for [34]. Above described polarization filtering compensate topological charge dispersion resulting in equal TC for all spectral components [38]. To demonstrate unit topological charge of the generated "white" light OV $|l| = 1$ the beam after the polarization filtering was focused by a cylindrical lens (focal distance f = 125 mm) as described in [45]. At the focal area the light possessed one dark stripe across the intensity distribution (Fig. 6b) indicating that the value of topological charge is $|l| = 1$. OV generation occurs through the phase and polarization modulation. Thus, optical vortices at different frequency components demonstrate coaxiality, hence, avoid anomalous spectral behavior near the vortex core [46].

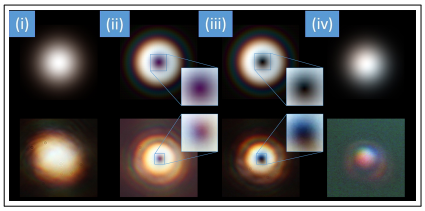

Fig. 7. Intensity normalized numerical plots (top row) and experimental images (bottom row) of the beam from incoherent light source in the states (i), (ii), (iii) and (iv) as described in the Figs. 1 and 2.

4. CONCLUSIONS

We have demonstrated generation of optical vortices over the visible and nIR wavelength range by using a single three-component scheme based on polarization-sensitive filtering. The filtering scheme consists of widely available components, is simple to implement and can be extended to any optical element based on the phase control of circularly polarized light, e.g. q-plates, not only as optical vortex converter but also as, e.g., Airy beam converter [40]. The demonstrated wavelength range spans over 600 nm over the VIS and nIR range with the efficiency of filtering higher than 50%. Due to the polarization modulation the presented scheme ensures coaxiality, no spatial dispersion of optical vortices generated at different wavelengths, which could be useful for generation of ultrashort OV shaped pulses in quantum communication systems and data transformation through photonic fibers. We have also demonstrated the polarization-selective vortex generation, where only one of two orthogonally polarized beams with different wavelengths is transformed to optical vortex (doughnut mode) with no limit on how close the two wavelengths could be. Proposed scheme with single optical path for both excitation and depletion beams could significantly facilitate extremely complicated process of alignment of STED systems.

M. Ivanov acknowledges financial support from the Erasmus Mundus Action 2 MID project.

REFERENCES

1. M. Padgett, J. Courtial, and L. Allen, "Light's orbital angular momentum," Phys. Today **57**, 35 (2004).
2. J. F. Nye and M. V. Berry, "Dislocations in wave trains," Proc. R. Soc. London A Math. Phys. Eng. Sci. **336**, 165–190 (1974).
3. P. Coullet, L. Gil, and F. Rocca, "Optical vortices," Opt. Commun. **73**, 403–408 (1989).
4. H. Huang, G. Xie, Y. Yan, N. Ahmed, Y. Ren, Y. Yue, D. Rogawski, M. J. Willner, B. I. Erkmen, K. M. Birnbaum, S. J. Dolinar, M. P. J. Lavery, M. J. Padgett, M. Tur, and A. E. Willner, "100 tbit/s free-space data link enabled by three-dimensional multiplexing of orbital angular momentum, polarization, and wavelength," Opt. Lett. **39**, 197–200 (2014).
5. M. P. J. Lavery, F. C. Speirits, S. M. Barnett, and M. J. Padgett, "Detection of a spinning object using light's orbital angular momentum," Science **341**, 537–540 (2013).
6. L. Yan, P. Gregg, E. Karimi, A. Rubano, L. Marrucci, R. Boyd, and S. Ramachandran, "Q-plate enabled spectrally diverse orbital-angular-momentum conversion for stimulated emission depletion microscopy," Optica **2**, 900–903 (2015).
7. J. Fischer and M. Wegener, "Three-dimensional optical laser lithography beyond the diffraction limit," Laser Photonics Rev. **7**, 22–44 (2012).
8. G. Foo, D. M. Palacios, , and J. G. A. Swartzlander, "Optical vortex coronagraph," Opt. Lett. **30**, 3308—-3310 (2005).
9. M. Geceviius, R. Drevinskas, M. Beresna, and P. G. Kazansky, "Single beam optical vortex tweezers with tunable orbital angular momentum," Appl. Phys. Lett. **104**, 231110 (2014).
10. J. Leach, S. Keen, M. J. Padgett, C. Saunter, and G. D. Love, "Direct measurement of the skew angle of the poynting vector in a helically phased beam," Opt. Express **14**, 11919–11924 (2006).
11. S. Ramachandran, C. Smith, P. Kristensen, and P. Balling, "Nonlinear generation of broadband polarisation vortices," Opt. Express **18**, 23212–23217 (2010).
12. V. Y. Bazhenov, M. V. Vasnetsov, and M. S. Soskin, "Laser beams with screw dislocations in their wavefronts," Pis. Zh. Eksp. Teor. Fiz. (JETP Lett.) **52**, 1037—-1039(429—-432) (1990).
13. H. I. Sztul, V. Kartazayev, and R. R. Alfano, "Laguerre-gaussian supercontinuum," Opt. Lett. **31**, 2725–2727 (2006).
14. M. S. Soskin, P. V. Polyanskii, and O. O. Arkhelyuk, "Computer-synthesized hologram-based rainbow optical vortices," New J. Phys. **6**, 196 (2004).
15. J. Atencia, M.-V. Collados, M. Quintanilla, J. Marin-Saez, and I. J. Sola, "Holographic optical element to generate achromatic vortices," Opt. Express **21**, 21056–21061 (2013).
16. J. Grover A. Swartzlander, "Achromatic optical vortex lens," Opt. Lett. **31**, 2042–2044 (2006).
17. Y. Tokizane, K. Oka, and R. Morita, "Supercontinuum optical vortex pulse generation without spatial or topological-charge dispersion," Opt. Express **17**, 14519–14525 (2009).
18. T. Wakayama, K. Komaki, Y. Otani, and T. Yoshizawa, "Achromatic axially symmetric wave plate," Opt. Express **20**, 29260–29265 (2012).
19. F. Bouchard, H. Mand, and M. Mirhosseini, "Achromatic orbital angular momentum generator," New J. Phys. **16**, 123006 (2014).
20. N. Radwell, R. D. Hawley, J. B. Gotte, and S. Franke-Arnold, "Achromatic vector vortex beams from a glass cone," Nat. Commun. **7**, 10564 (2016).
21. S. R. Nersisyan, N. V. Tabiryan, D. Mawet, and E. Serabyn, "Improving vector vortex waveplates for high-contrast coronagraphy," Opt. Express **21**, 8205–8213 (2013).
22. C. Oh and M. J. Escuti, "Achromatic diffraction from polarization gratings with high efficiency," Opt. Lett. **33**, 2287–2289 (2008).
23. A. V. Volyar and T. A.Fadeeva, "Generation of singular beams in uniaxial crystals," Opt. Spectrosc. **94**, 235—244 (2003).
24. C. Fallet and G. Sirat, "Achromatization of conical diffraction: application to the generation of a polychromatic optical vortex," Opt. Lett. **41**, 769–772 (2016).
25. Y. A. Egorov, T. A. Fadeyeva, and A. V. Volyar, "The fine structure of singular beams in crystals: colours and polarization," J. Opt. A: Pure Appl. Opt. **6**, S217 – S228 (2004).
26. V. Shvedov, W. Krolikowski, A. Volyar, D. N. Neshev, A. S. Desyatnikov, and Y. S. Kivshar, "Focusing and correlation properties of white-light optical vortices," Opt. Express **13**, 7393 – 7398 (2005).
27. E. Brasselet, Y. Izdebskaya, V. Shvedov, A. S. Desyatnikov, W. Krolikowski, and Y. S. Kivshar, "Dynamics of optical spin-orbit coupling in uniaxial crystals," Opt. Lett. **34**, 1021 – 1023 (2009).
28. L. Marrucci, C. Manzo, and D. Paparo, "Optical spin-to-orbital angular momentum conversion in inhomogeneous anisotropic media," Phys. Rev. Lett. **96**, 163905 (2006).
29. S. Slussarenko, A. Murauski, T. Du, V. Chigrinov, L. Marrucci, and E. Santamato, "Tunable liquid crystal q-plates with arbitrary topological charge," Opt. Express **19**, 4085–4090 (2011).
30. Y. S. Rumala, G. Milione, T. A. Nguyen, S. Pratavieira, Z. Hossain, D. Nolan, S. Slussarenko, E. Karimi, L. Marrucci, , and R. R. Alfano, "Tunable supercontinuum light vector vortex beam generator using a q-plate," Opt. Lett. **38**, 5083–5086 (2013).
31. K. Yamane, Y. Toda, and R. Morita, "Ultrashort optical-vortex pulse

generation in few-cycle regime," Opt. Express **20**, 18986–18993 (2012).
32. M. Beresna, M. Gecevicius, and P. G. Kazansky, "Polarization sensitive elements fabricated by femtosecond laser nanostructuring of glass," Opt. Mater. Express. **1**, 783–795 (2011).
33. M. Beresna, M. Geceviius, P. G. Kazansky, and T. Gertus, "Radially polarized optical vortex converter created by femtosecond laser nanostructuring of glass," Appl. Phys. Lett. **98**, 201101 (2011).
34. A. Matijosius, P. Stanislovaitis, T. Gertus, and V. Smilgevicius, "Formation of optical vortices with topological charge $|l| = 1$ and $|l| = 1/2$ by use of the s-waveplate," Opt. Commun. **324**, 1–9 (2014).
35. Altechna R&D, "Damage threshold," http://www.altechna.com/download/wop/Operation-Manual-_130701.pdf.
36. L. R. Watkins and M. Derbois, "White-light ellipsometer with geometric phase shifter," Appl. Opt. **51**, 5060–5065 (2012).
37. A. Niv, G. Biener, V. Kleiner, and E. Hasman, "Polychromatic vectorial vortex formed by geometric phase elements," Opt. Lett. **32**, 847–849 (2007).
38. M. Sakamoto, R. Fukumoto, N. Murakami, R. Morita, and K. Oka, "Dispersion reduction in generation of high-order optical vortex using axially symmetric half-wave plates," Opt. Rev. **22**, 174–178 (2015).
39. R. Drevinskas and P. G. Kazansky, "High-performance geometric phase elements in silica glass," APL Photonics **2**, 066104 (2017).
40. M. Gecevicius, M. Beresna, R. Drevinskas, and P. G. Kazansky, "Airy beams generated by ultrafast laser-imprinted space-variant nanostructures in glass," Opt. Lett. **39**, 6791–6794 (2014).
41. M. Reuss, J. Engelhardt, and S. W. Hell, "Birefringent device converts a standard scanning microscope into a sted microscope that also maps molecular orientation," Opt. Express **18**, 1049–1058 (2010).
42. R. Loudon, *The Quantum Theory of Light* (Oxford Science Publications, 2000), 3rd ed.
43. D. M. Palacios, I. D. Maleev, A. S. Marathay, and J. G. A. Swartzlander, Phys. Rev. Lett. **92**, 143905 (2004).
44. G. A. Swartzlander and J. Schmit, Phys. Rev. Lett. **93**, 093901 (2004).
45. V. Denisenko, V. Shvedov, A. S. Desyatnikov, D. N. Neshev, W. Krolikowski, A. Volyar, M. Soskin, and Y. S. Kivshar, Opt. Express **17**, 23374 – 23379 (2009).
46. M. V. Berry, New J. Phys. **4**, 66.1 – 66.14 (2002).

A5

GENERATION OF RADIALLY POLARIZED BEAMS AND HIGHER ORDER POLARIZATION SINGULARITIES BY OPTICAL PARAMETRIC AMPLIFICATION OF OPTICAL VORTICES

P. Stanislovaitis, **M. Ivanov**, A. Matijosius, V. Smilgevicius, and T. Gertus

Opt. Eng. **56**, 095101 (2017)

Optical Engineering 56(9), 095101 (September 2017)

Generation of radially polarized beams and higher order polarization singularities by optical parametric amplification of optical vortices

Paulius Stanislovaitis,[a,*] Maksym Ivanov,[a] Aidas Matijošius,[a] Valerijus Smilgevičius,[a] and Titas Gertus[b]
[a]Vilnius University, Laser Research Center, Vilnius, Lithuania
[b]Workshop of Photonics, Vilnius, Lithuania

Abstract. We show a method to form radially and azimuthally polarized beams as well as higher order polarization singularities by superposition of optical vortices with opposite topological charges obtained by optical parametric amplification. The proposed method could find applications in optical trapping of particles, nonlinear optics experiments, and laser material processing. [DOI: 10.1117/1.OE.56.9.095101]

Keywords: optical vortices; radial polarization; polarization singularities; optical parametric amplification.

Paper 170877 received Jun. 22, 2017; accepted for publication Aug. 16, 2017; published online Sep. 9, 2017.

1 Introduction

Radially polarized beams were first generated in 1972.[1] Later on, their unique properties were discovered. It was found that a smaller focal spot can be achieved with a radially polarized beam than using a conventional linearly or circularly polarized light.[2–4] In addition, a strong longitudinal electric field component has been shown to exist in the vicinity of the focus of the radially polarized beam.[4] These properties have led to a number of new applications, among which are laser material processing,[5–8] optical trapping and manipulation of microscopic particles,[9,10] and acceleration of electrons by the longitudinal electric field component.[11–13]

Several methods have been proposed to generate radially polarized beams inside a laser resonator [1,14–18] as well as outside the resonator. Outside of a laser resonator, the radial polarization of a beam can be achieved by converting circularly polarized light by a radial analyzer (a polarizer which only transmits a radial polarization),[19,20] the radial polarization converter (the S-waveplate),[21] superimposing two orthogonally polarized Hermite–Gaussian modes,[22] using a spatial light modulator[23–25] or propagating a circularly polarized optical vortex through a uniaxial birefringent crystal and splitting it by focusing into a radially and azimuthally polarized components.[26]

Radially and azimuthally polarized beams are two examples of a wide family of beams with polarization singularities. Yang et al.[27] has demonstrated an experimental generation of such beams by superposition of Laguerre–Gaussian modes. They used a spatial light modulator to generate two optical vortices of different topological charges and superimposed them.

In this paper, we propose a technique to generate beams with polarization singularities and demonstrate it experimentally. The proposed method can be used to create powerful beams, limited only by the damage threshold of the nonlinear crystal (NLC). In the theoretical part of this paper, we discuss the underlying physical principles of the technique and in the experimental part the concept of the technique is introduced. The experimental results and possible extensions of the method are presented and discussed in the last two sections of the experimental part.

2 Theoretical

To generate beams with polarization singularities, we use a superposition of two optical vortices obtained by optical parametric amplification. The signal and idler waves after the optical parametric amplification are combined using a quarter-waveplate to create the output beam with the desired polarization.

2.1 *Polarization Singularities as a Superposition of Optical Vortices*

The polarization vector of a radially polarized beam can be written as follows:

$$\vec{v}_r = A(r)\begin{bmatrix}\cos\phi\\ \sin\phi\end{bmatrix}, \tag{1}$$

where r and ϕ are radial and azimuthal coordinates in the cylindrical coordinate system and $A(r)$ is the beam's envelope, which depends only on r. Using the well-known trigonometric identities, the polarization vector in Eq. (1) can be rewritten as a sum of two circularly polarized optical vortices with opposite topological charges

$$\vec{v}_r = \frac{1}{2}A(r)\left\{\exp(i\phi)\begin{bmatrix}1\\ -i\end{bmatrix} + \exp(-i\phi)\begin{bmatrix}1\\ i\end{bmatrix}\right\}. \tag{2}$$

Note that in Eq. (2) the polarization handedness of the optical vortices is opposite as well as the sign of their topological charges.

A similar equation can be written for the azimuthal polarization vector

*Address all correspondence to: Paulius Stanislovaitis, E-mail: paulius.stanislovaitis@ff.stud.vu.lt

$$\vec{v}_a = A(r)\begin{bmatrix} -\sin\phi \\ \cos\phi \end{bmatrix} = \frac{i}{2}A(r)\left\{\exp(i\phi)\begin{bmatrix} 1 \\ -i \end{bmatrix} - \exp(-i\phi)\begin{bmatrix} 1 \\ i \end{bmatrix}\right\}. \quad (3)$$

Also, higher order polarization singularities can be expressed as a superposition of optical vortices with higher topological charge

$$\vec{v}_l^{(1)} = A(r)\begin{bmatrix} \cos l\phi \\ \sin l\phi \end{bmatrix} = \frac{1}{2}A(r)\left\{\exp(il\phi)\begin{bmatrix} 1 \\ -i \end{bmatrix} + \exp(-il\phi)\begin{bmatrix} 1 \\ i \end{bmatrix}\right\}, \quad (4)$$

or

$$\vec{v}_l^{(2)} = A(r)\begin{bmatrix} -\sin l\phi \\ \cos l\phi \end{bmatrix} = \frac{i}{2}A(r)\left\{\exp(il\phi)\begin{bmatrix} 1 \\ -i \end{bmatrix} - \exp(-il\phi)\begin{bmatrix} 1 \\ i \end{bmatrix}\right\}, \quad (5)$$

for two types of beams with polarization singularities. When $l = 1$, Eq. (4) reduces to a simple radial polarization beam [as in Eq. (1)] and Eq. (5) reduces to an azimuthal polarization beam, just like in Eq. (3). Therefore, throughout this text, when we talk about the general class of beams with phase singularity, we will call these beams radial-type (RT) and azimuth-type (AT), respectively. This is just a limited classification for the purposes of this work. For more extensive analysis of polarization singularities, see the papers by Vyas et al.[28] and Brown.[29]

2.2 *Phase Relations in the Optical Parametric Amplification*

Optical parametric amplification is used in this work to obtain two optical vortices of opposite topological charges. Therefore, we analyze phase relations among the interacting waves. A certain phase difference between the optical vortices is important in order to obtain the desired output beam.

Assuming the full phase matching, a nearly lossless medium and the slowly varying amplitude approximation the well-known coupled wave equations can be rewritten in the following form:[30]

$$\frac{du_1}{d\zeta} = -u_3u_2\sin\Theta, \quad (6)$$

$$\frac{du_2}{d\zeta} = -u_3u_1\sin\Theta, \quad (7)$$

$$\frac{du_3}{d\zeta} = u_1u_2\sin\Theta, \quad (8)$$

$$\frac{d\Theta}{d\zeta} = -K\cot\Theta\frac{d}{d\zeta}\ln(u_1u_2u_3), \quad (9)$$

where ζ is the normalized propagation distance, u_1, u_2, and u_3 are the absolute amplitudes of the signal, idler, and pump waves, respectively, and Θ is the net phase, which can be expressed as

$$\Theta = \psi_3(\zeta) - \psi_2(\zeta) - \psi_1(\zeta), \quad (10)$$

where $\psi_3(\zeta)$, $\psi_2(\zeta)$, and $\psi_1(\zeta)$ are the phases of the signal, idler, and pump waves, respectively. Equation (9) can be integrated[30] to show that

$$u_1u_2u_3\cos\Theta = \Gamma, \quad (11)$$

where Γ is a constant. The relation in Eq. (11) holds true during the parametric interaction for all values of ζ.

In the optical parametric amplification process, only the signal and pump waves are injected, while the idler wave is generated inside the crystal. Therefore, the initial condition for the idler wave is $u_2(0) = 0$. Inserting this into Eq. (11), we can see that $\Gamma = 0$. Afterwards, the amplification takes place and the idler wave appears, therefore, $u_2(\zeta) > 0$ for values $\zeta > 0$. Then, for Eq. (11) to hold true, it is required that $\cos\Theta = 0$. From this, it follows that

$$\Theta = \pm\frac{\pi}{2}. \quad (12)$$

The $\pm$ sign in Eq. (12) determines the energy transfer direction between the waves. In the optical parametric amplification, the energy transfer takes place from the pump to the signal and idler waves; therefore, the solution $\Theta = -\pi/2$ is appropriate for this case. From this solution and Eq. (10), the phase of the idler wave can be expressed

$$\psi_2(\zeta) = [\psi_3(\zeta) - \psi_1(\zeta)] + \frac{\pi}{2}. \quad (13)$$

The square brackets in Eq. (13) emphasize that the idler's phase depends on the phase difference between the pump and the signal waves. Therefore, if a phase shift is introduced into either the signal or the pump wave, the idler's phase will change accordingly.

Let us discuss a particular case. The pump is a plane wave. Assuming a negligible pump depletion, we can consider that $\psi_3(\zeta) = \psi_{30} = \text{const}$. The signal beam is an optical vortex with a topological charge l. If a constant phase shift $\Delta\psi_1$ is introduced to the signal wave, the phase of the signal wave will then be $\psi_1(z,\phi) = l\phi + \Delta\psi_1$. Inserting the pump's and signal's phases into Eq. (13), the idler's phase can be obtained

$$\psi_2(\zeta,\phi) = \psi_{30} - l\phi - \Delta\psi_1 + \frac{\pi}{2}. \quad (14)$$

The idler wave has the azimuthal phase modulation and its sign is opposite to that of the signal. In addition, as the signal's phase changes by a constant $\Delta\psi_1$, the idler's phase changes by $-\Delta\psi_1$. Therefore, the phase difference between the signal and idler waves can be controlled by changing the signal's phase. Alternatively, the phase shift could be introduced to the pump wave, whereas the signal's phase remained unchanged. As will be described in the experimental section, this phenomena will be used to obtain the desired phase difference between the signal and the idler waves at the output of the NLC.

2.3 *Transformation of the Amplified Beam by a Quarter-Waveplate*

After the optical parametric amplification, we use a quarter-waveplate to combine the amplified signal and idler optical vortices into the output beam with the desired polarization singularity.

First of all, the coordinate system has to be defined. We choose the left-handed coordinate system and measure all the polarization and optical vortex wavefront handedness with respect to the source. In that case, a polarization vector $\begin{bmatrix}1\\ i\end{bmatrix}$ will be left-handed and $\begin{bmatrix}1\\ -i\end{bmatrix}$ right-handed. Also, the wavefront of an optical vortex with topological charge $l>0$ will be left-handed and with $l<0$ will be right-handed. Thus, we can see from Eqs. (2)–(5) that the wavefront of each optical vortex has a different handedness than its polarization vector.

With the coordinate system defined, we can now define the rotation transform. The matrix of the counter-clockwise rotation transform by angle α around the z-axis will be

$$\hat{T}=\begin{bmatrix}\cos\alpha & -\sin\alpha\\ \sin\alpha & \cos\alpha\end{bmatrix}. \tag{15}$$

This transform rotates a vector by angle α counter-clockwise. The inverse of this transform would naturally be the counter-clockwise rotation by $-\alpha$ (or, in other words, the clockwise rotation by α). Its matrix would be

$$\hat{T}^{-1}=\begin{bmatrix}\cos\alpha & \sin\alpha\\ -\sin\alpha & \cos\alpha\end{bmatrix}. \tag{16}$$

The Jones matrix of a simple quarter-waveplate[31] would be

$$\hat{A}=\begin{bmatrix}1 & 0\\ 0 & i\end{bmatrix}. \tag{17}$$

If the quarter-waveplate is rotated counter-clockwise by angle α, its matrix would be

$$\hat{Q}=\hat{T}\hat{A}\hat{T}^{-1}=\begin{bmatrix}\cos^2\alpha+i\sin^2\alpha & \cos\alpha\sin\alpha(1-i)\\ \cos\alpha\sin\alpha(1-i) & i\sin^2\alpha+\cos^2\alpha\end{bmatrix}. \tag{18}$$

In the experiment, a NLC wit type-II phase matching is used for the optical parametric amplification. It produces two orthogonally polarized signal and idler optical vortices. The two optical vortices are then transformed by the quarter-waveplate into the output beam with the desired polarization structure. We will now discuss two cases with different phase shifts between the signal and idler waves.

1. The phase shift between the signal and idler waves is $\pi/2$. In this case, assuming sufficiently large gain (so that the signal and idler waves will have approximately the same intensity), we can write the polarization vector of the outgoing beam

$$\vec{v}=\begin{bmatrix}\exp(il\phi)\\ i\exp(-il\phi)\end{bmatrix}. \tag{19}$$

If a quarter-waveplate, rotated by angle $\alpha=45$ deg counter-clockwise is placed in the path of the beam, then $\cos\alpha=\sin\alpha=1/\sqrt{2}$. Inserting this into Eq. (18), the Jones matrix of such a waveplate would be

$$\hat{A}=\begin{bmatrix}1 & -i\\ -i & 1\end{bmatrix}. \tag{20}$$

The normalization and phase factors have been dropped in Eq. (20). Multiplying the vector in Eq. (19) by the Jones matrix in Eq. (20) and refactoring the expression, we can obtain the output polarization vector after the quarter-waveplate

$$\vec{w}=\begin{bmatrix}1 & -i\\ -i & 1\end{bmatrix}\begin{bmatrix}\exp(il\phi)\\ i\exp(-il\phi)\end{bmatrix}=2\begin{bmatrix}\cos(l\phi)\\ \sin(l\phi)\end{bmatrix}. \tag{21}$$

We can see that at the output of the quarter-waveplate, an RT beam will be present. In the simplest case, when $l=1$ it will be a radially polarized beam.

Therefore, if there is a $\pi/2$ phase shift between the signal and idler waves, a quarter-waveplate, rotated by 45 deg counter-clockwise, can transform the two orthogonally polarized optical vortices with opposite topological charges into a radially polarized beam (or any other RT beam, depending on the choice of the topological charge of the vortex). In the case when the signal is a unit-charged vortex ($l=1$), the resulting beam is radially polarized as shown in Fig. 1(a).

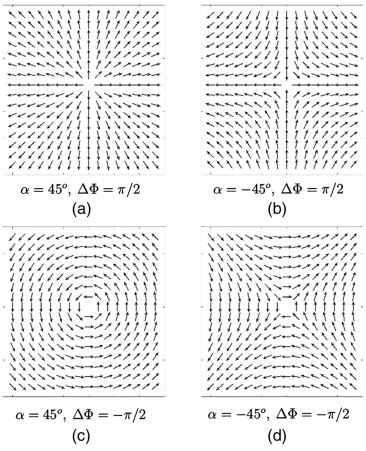

Fig. 1 Possible polarizations of output beams width different orientations of the quarter-waveplate (α) and phase shifts between the signal and the idler waves ($\Delta\Phi$) when $l=1$. On the left, the polarization of a radially (a) and azimuthally (c) polarized beam is shown. (b) and (d) Polarization patterns shown are obtained when the quarter-waveplate is rotated to the opposite direction.

2. Consider the same situation as in case 1, except with the $-\pi/2$ phase shift between the signal and idler waves. Now, the polarization vector of the combined signal-idler beam can be written

$$\vec{v} = \begin{bmatrix} i\exp(il\phi) \\ \exp(-il\phi) \end{bmatrix}. \tag{22}$$

The quarter-waveplate is also rotated by 45 deg counterclockwise. Following the same calculations, the result is obtained

$$\vec{w} = \begin{bmatrix} 1 & -i \\ -i & 1 \end{bmatrix} \begin{bmatrix} i\exp(il\phi) \\ \exp(-il\phi) \end{bmatrix} = 2\begin{bmatrix} -\sin(l\phi) \\ \cos(l\phi) \end{bmatrix}. \tag{23}$$

In this case, a beam of AT family is generated, which in the simplest case $l = 1$, reduces to an azimuthally polarized beam [Fig. 1(c)].

If quarter-waveplate is rotated clockwise instead of counter-clockwise, then $\alpha = -45$ deg. In this case, the result would be another type of polarization singularity that does not belong neither to RT nor to AT family [Fig. 1(b) and 1(d)].

In an experiment, if a polarizer is put in the way of the output beam, a Hermite–Gaussian mode with two maxima will be observed. It will happen in both cases whether the quarter-waveplate is rotated clockwise or counter-clockwise. The result of such an experiment might be ambiguous. To determine whether the quarter-waveplate is oriented correctly, we have to rotate the polarizer. If the Hermite–Gaussian modes rotate in the same direction as the polarizer does, then a radially or azimuthally polarized beam is present at the output [Fig. 1(a) and 1(c)]. If the Hermite–Gaussian mode rotates in the opposite direction, it indicates the presence of a phase singularity of another type [Fig. 1(b) and 1(d)].

3 Experimental

3.1 *Experimental Background*

The basic idea of the proposed method is to obtain two optical vortices with opposite topological charges by means of the optical parametric amplification and to superimpose them by using a quarter-waveplate. The pump beam carries no topological charge while the signal beam is an optical vortex. According to the law of the topological charge conservation,[32] the idler wave will be formed with a topological charge opposite to that of the signal. Afterward, with a properly oriented quarter-waveplate, the combined signal-idler beam is converted to a radially or azimuthally polarized beam (in case of $l = 1$) or another beam of RT/AT type.

The conceptual design of the experiment is shown in Fig. 2. The signal and pump waves are combined in a collinear fashion using the wavelength-selective mirror M. The signal wave is amplified in the NLC (Fig. 2). The optical parametric amplification has to take place in a type II NLC so that the polarizations of the signal and idler beams are perpendicular. In addition, the wavelengths of the signal and idler beams have to coincide (the parametric interaction is degenerate with respect to the wavelength). The initial phase of the signal beam (or alternatively the pump beam) is controlled by a phase retarder (PR), which in the simplest case can be a glass plate that can be rotated to change the optical path of the passing beam or, alternatively, could be a mirror mounted on a piezoelectric translation stage. A $\pi/2$ phase difference between the signal and idler waves has to be achieved at the output of the crystal by controlling the angle of the phase retarder. After the crystal, the wavelength-selective filter F absorbs all the remaining pump beam. Then, a properly oriented quarter-waveplate turns this composite signal-idler beam into a beam with a polarization singularity.

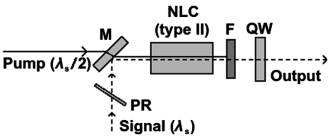

Fig. 2 The conceptual experimental setup: M, a wavelength-selective mirror; PR, phase retarder (for example a thin glass plate which can be rotated to adjust the initial phase of the signal beam), NLC, nonlinear crystal (type II); F, filter, which filters out the pump beam; and QW, the quarter-waveplate. The pump beam is purely Gaussian and the signal beam is an optical vortex. The output is a beam with a polarization singularity.

3.2 *Key Points in the Experimental Design*

- The phase difference between the signal and idler beams at the output of the crystal has to be $\pi/2$ for RT beams or $-\pi/2$ for AT beams.
- The beams have to be properly collimated. In the optical parametric amplification process, the phase conjugation takes place, therefore, the wavefront has to be as flat as possible. Otherwise, if the signal beam's wavefront is concave, the idler's wavefront will be convex and vice versa. This can cause distortions of the output beam.
- The influence of the walk-off has to be diminished. For that purpose, an NLC with critical phase matching can be chosen and the beam diameter has to be chosen sufficiently large.
- Gain should be sufficiently high. The energies of the output signal and idler beams will be different by the amount of the initial signal's energy. Therefore, if the gain is sufficiently high, this difference will be diminished.

3.3 *Experimental Setup*

Figure 3 shows the realization of the proposed experimental design. The detailed information about the light source and the optical elements used in the experiment is given in Table 1.

The input beam was generated by a YAG:Nd laser with the pulse duration of 50 ps at 1-kHz repetition rate. The input beam was collimated, linearly polarized, and had a diameter of 2.175 mm at $1/e$ level. Then, the beam was split into two branches by the beam splitter BS1: one to generate the pump beam (the pump branch) and one to generate the signal beam (signal branch).

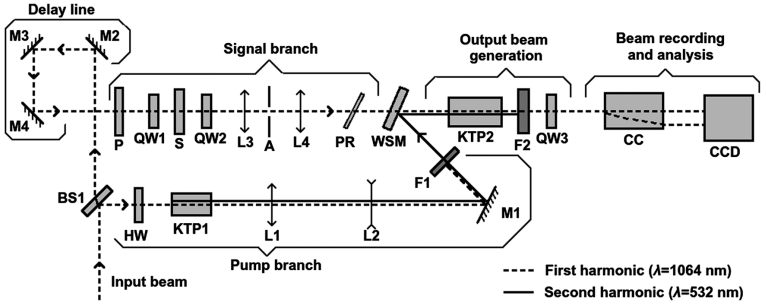

Fig. 3 The experimental setup. BS1, a beam splitter; P, a polarizer; M1 to M4, mirrors; HW, a half-wave-plate; QW1 to QW3, quarter-waveplates; L1 to L4, lenses; S, an S-waveplate; PR, the phase retarder; KTP1 and KTP2, nonlinear crystals; A, an aperture; WSM, a wavelength-selective mirror; F1, F2, filters; CC, a birefringent calcite crystal; and CCD, a CCD camera.

Table 1 Information about the optical elements in the experimental setup.

Item(s)	Description	Additional information (if available)
BS1	Beam splitter	
M1 to M4	Mirrors	
P	Polarizer	
HW	$\lambda/2$ waveplate	$\lambda = 1064$ nm
KTP1, KTP2	NLCs (KTP)	Length: 8 mm, aperture: 4.5×4.5 mm, type-II phase matching (e-oe)
L1	Lens	Focal length: 38.4 cm
L2	Lens	Focal length: −23.8 cm, distance from L1: 19.5 cm
QW1, QW2, and QW3	$\lambda/4$ waveplate	$\lambda = 1064$ nm
S	S-waveplate	$\lambda = 1064$ nm
L3	Lens	Focal length: 28.6 cm
L4	Lens	Focal length: 19.2 cm, distance from L3: 56.25 cm
A	Aperture	Diameter: 300 μm, distance from L3: 35 cm
PR	Phase retarder	A thin glass plate (thickness: 2.9 mm, refractive index: 1.525)
WSM	Wavelength-selective mirror	Reflects the pump beam ($\lambda = 532$ nm), transmits the signal beam ($\lambda = 1064$ nm)
F1	Filter	СЗФ – 23 (Russian), absorption at $\lambda = 1064$ nm
F2	Filter	KC-10 (Russian), absorption at $\lambda = 532$ nm
CC	Calcite crystal	An angle-cut birefringent crystal for the analysis of the beam's polarization structure
CCD	CCD camera	Model: Spiricon SP620U

In the pump branch, the $\lambda/2$ waveplate HW was used to correct the polarization direction, and the second harmonic was generated in the NLC KTP1. Lenses L1 and L2 were then used to collimate the beam. The filter F1 filtered out the remains of the first harmonic beam. The second harmonic beam was used as the pump beam in the output beam generation stage.

The purpose of the signal branch is to convert the first harmonic beam to an optical vortex, which was used as the signal part in the output beam generation stage. Mirrors M2, M3, and M4 constitute a delay line to compensate the optical path differences between the signal and the pump beams. The polarizer P was used to correct any depolarization, resulting from reflections in the delay line. The system QW1-S-QW2, consisting of two $\lambda/4$ waveplates QW1 and QW2 and an S-waveplate, was used to convert the signal beam to a vortex of unit topological charge. The $\lambda/4$ waveplate QW1 was used to produce a circularly polarized beam, whereas the S-waveplate converted it to an optical vortex.[33] Afterward, QW2 converted the optical vortex back into the linear polarization. The beam vortex was then collimated using the lenses L3 and L4 and an aperture A was placed between them in order to filter out unwanted beam distortions. The phase retarder PR was then used to correct the phase of the signal beam.

Both pump and signal beams were combined by the wavelength-selective mirror WSM. The parametric amplification took place in the NLC KTP2, producing the two oppositely charged signal and idler vortex beams. The filter F2 then filtered off the remains of the pump beam, and the signal and idler beams were converted to the output beam with a polarization singularity by the $\lambda/4$ waveplate QW3, as discussed in previous sections.

The output beam's profile was recorded with the CCD camera. The polarization structure was analyzed using a birefringent calcite crystal (CC in the schematic), which separates the two orthogonal polarizations of the beam. The polarization structure of the beam was determined from the spatial distribution of the polarization components.

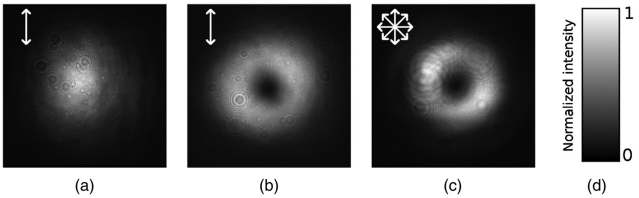

Fig. 4 (a) The intensity patterns of the initial pump beam, (b) signal beam, (c) the output beam, and (d) the color map of the normalized intensity. The polarization states of the beams are indicated by the arrows. The pump beam is a Gaussian beam, whereas the initial signal beam carries a topological charge of $l = 1$. The output beam is radially polarized. The powers of the pump, signal, and the output beams are 0.9 W, 0.55 mW, and 290 mW, respectively, with the pulse duration of 50 ps.

3.4 *Experimental Results*

The recorded intensity profiles of the beams are shown in Fig. 4. Their polarization states are given by the small arrows in the top-left corner of the images. Figure 4(a) shows the intensity profile of the Gaussian pump beam. The signal beam, shown in Fig. 4(b), is an optical vortex with a unit topological charge. It was formed using an S-waveplate from a circularly polarized Gaussian beam.[33] The resulting radially polarized beam is shown in Fig. 4(c). The powers of the pump, signal, and the radially polarized output beam were 0.9 W, 0.55 mW, and 290 mW, respectively, with the pulse duration of 50 ps.

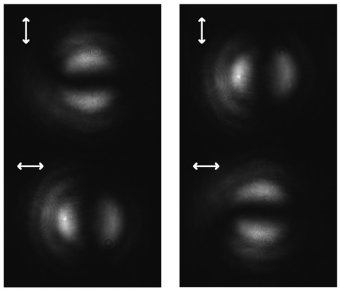

Fig. 5 (Top) the vertical and (bottom) the horizontal polarization components of a (a) radially and (b) azimuthally polarized beams after the CC. The polarization states are indicated by the arrows. The color map is the same as in Fig. 4(d).

Analysis of the output beam was carried out using the CC. The intensity profiles of the separated polarization components are depicted in Fig. 5 with the small arrows indicating the polarization direction. Figure 5(a) shows the observed polarization components of the radially polarized beam. The vertical polarization component [Fig. 5(a) upper image] has two maxima, situated vertically with respect to each other, whereas the horizontal polarization component [Fig. 5(a) lower image] has two horizontally situated maxima. The radial polarization was verified by rotating the CC (Fig. 6).

In addition, an azimuthally polarized beam was obtained by changing the phase between the signal and idler beams using the PR. Its analyzed mode structure is depicted in Fig. 5(b). The vertical polarization component [Fig. 5(b) upper image] now has two horizontally situated maxima, whereas the horizontal polarization component has [Fig. 5(b) lower image] the vertically situated maxima.

Another important point in this experiment is the amplification gain. The previously shown results were obtained at the gain of about 500 times. At the gain value of about 30, the periphery of the beam does not get correct polarization and side lobes were observed (Fig. 7).

3.5 *Possible Extensions of the Method*

So far, we have shown that by using this method, cylindrical vector beams that are a superposition of optical vortices with opposite topological charges can be produced. However, if the topological charge of the pump beam was chosen not equal to zero, then the idler wave would be formed in accordance to the topological charge conservation law[32]

$$l_p = l_s + l_i, \tag{24}$$

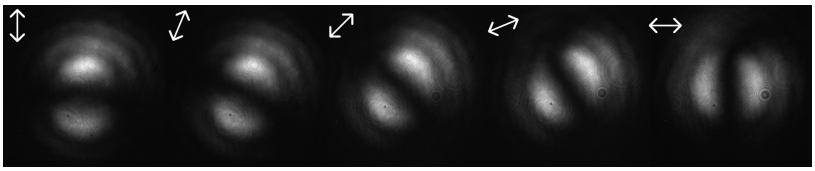

Fig. 6 Observed patterns of one of the polarization components of the radially polarized beam as the CC was rotated. The polarization state is indicated by the white arrows. The color map is the same as in Fig. 4(d).

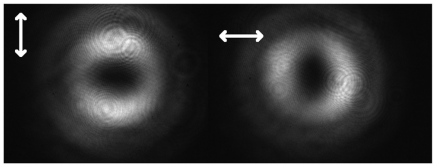

Fig. 7 (a) The vertical and (b) horizontal polarization components of the output beam at low gain of about 30 times. The arrows indicate the polarization states of the beams. The proper Hermite–Gaussian modes were not obtained. The side lobes are visible at the periphery of the beam. The color map is the same as in Fig. 4(d).

where l_p, l_s, l_i are the topological charges of the pump, signal, and idler waves, respectively.

Manipulation of topological charges of pump and signal waves allows the creation of other types of beams with polarization singularities, which will not be discussed in this paper. Such beams have also been obtained using a spatial light modulator by Yang et al.[27]

The proposed method could be easily automated. For example, instead of a thin glass plate, a mirror mounted on a piezoelectric translation stage can be used to control the phase of the signal or pump beam allowing easy switching between the radially and azimuthally polarized beams. In addition, a spatial light modulator could be used to modulate the initial signal beam and provide an easy way to obtain beams with polarization singularities of higher orders. While it is possible to obtain beams with polarization singularities by a spatial light modulator directly, the proposed method utilizes the optical parametric amplification, thus allowing the creation of higher power beams than could be obtained using a spatial light modulator directly. In combination with automation possibilities, this method could find applications in optical trapping of particles.

4 Conclusions and Discussion

We have shown a technique to generate optical beams with polarization singularities by optical parametric amplification of an optical vortex and subsequent beam conversion by a quarter-waveplate. Since this technique employs the optical parametric amplification, it does not require a powerful initial signal beam. It can produce a powerful output beam while using simple methods to obtain the initial signal beam such as a printed vortex hologram or a spatial light modulator, which would normally be limited by the optical damage threshold if used to obtain the desired output beams directly.

In addition to this, the proposed method can be easily automated. If a spatial light modulator is used to modulate the initial signal beam, it can provide an easy computer-controlled way of switching between the modes of the beam. In combination with increased power output, this method could find applications in optical trapping of particles and other applications such as nonlinear optics research and laser material processing.

However, in this paper, we have demonstrated only the basic idea and discussed the underlying physical principles of the method. More research is needed to determine the influence of dispersion and group velocity mismatch for ultrashort pulses and how it affects the quality of the resulting beam. In our case, we used 50 ps pulses in the KTP crystal. The dispersion length was of the order of several kilometers, therefore, the second and higher order dispersion effects were negligible. In addition, some phenomena that are characteristic of ultrashort pulse amplification might be utilized in this method, such as the spatial capture (also called "trapping") of the amplified waves under the pump wave packet[34–36] or the giant subharmonic pulse generation.[37]

Acknowledgments

The authors thank Dr. Vygandas Jarutis and Dr. Viktorija Tamulienė for fruitful discussions, which helped to improve the quality of the manuscript.

References

1. D. Pohl, "Operation of a ruby laser in the purely transverse electric mode te01," *Appl. Phys. Lett.* **20**(7), 266–267 (1972).
2. S. Quabis et al., "Focusing light to a tighter spot," *Opt. Commun.* **179**, 1–7 (2000).
3. T. Grosjean and D. Courjon, "Smallest focal spots," *Opt. Commun.* **272**(2), 314–319 (2007).
4. R. Dorn, S. Quabis, and G. Leuchs, "Sharper focus for a radially polarized light beam," *Phys. Rev. Lett.* **91**, 233901 (2003).
5. R. Weber et al., "Effects of radial and tangential polarization in laser material processing," *Phys. Procedia* **12**, 21–30 (2011).
6. V. G. Niziev and A. V. Nesterov, "Influence of beam polarization on laser cutting efficiency," *J. Phys. D: Appl. Phys.* **32**(13), 1455–1461 (1999).
7. O. J. Allegre et al., "Laser microprocessing of steel with radially and azimuthally polarized femtosecond vortex pulses," *J. Opt.* **14**(8), 085601 (2012).
8. M. Kraus et al., "Microdrilling in steel using ultrashort pulsed laser beams with radial and azimuthal polarization," *Opt. Express* **18**, 22305–22313 (2010).
9. Q. Zhan, "Trapping metallic Rayleigh particles with radial polarization," *Opt. Express* **12**, 3377–3382 (2004).
10. W. Cui et al., "Trapping metallic particles under resonant wavelength with 4π tight focusing of radially polarized beam," *Opt. Express* **24**, 20062–20068 (2016).
11. A. Sell and F. X. Kärtner, "Attosecond electron bunches accelerated and compressed by radially polarized laser pulses and soft-x-ray pulses from optical undulators," *J. Phys. B: At. Mol. Opt. Phys.* **47**(1), 015601 (2014).
12. D. N. Gupta et al., "Electron acceleration to gev energy by a radially polarized laser," *Phys. Lett. A* **368**(5), 402–407 (2007).
13. V. Marceau, A. April, and M. Piché, "Electron acceleration driven by ultrashort and nonparaxial radially polarized laser pulses," *Opt. Lett.* **37**, 2442–2444 (2012).
14. K. Yonezawa, Y. Kozawa, and S. Sato, "Generation of a radially polarized laser beam by use of the birefringence of a c-cut Nd:YVO4 crystal," *Opt. Lett.* **31**, 2151–2153 (2006).
15. M.-D. Wei, Y.-S. Lai, and K.-C. Chang, "Generation of a radially polarized laser beam in a single microchip Nd:YVO4 laser," *Opt. Lett.* **38**, 2443–2445 (2013).
16. J. L. Li et al., "Converging-axicon-based radially polarized ytterbium fiber laser and evidence on the mode profile inside the gain fiber," *Opt. Lett.* **32**, 1360–1362 (2007).
17. J.-F. Bisson et al., "Radially polarized ring and arc beams of a neodymium laser with an intra-cavity axicon," *Opt. Express* **14**, 3304–3311 (2006).
18. M. A. Ahmed et al., "Multilayer polarizing grating mirror used for the generation of radial polarization in Yb:YAG thin-disk lasers," *Opt. Lett.* **32**, 3272–3274 (2007).
19. Q. Zhan and J. R. Leger, "Microellipsometer with radial symmetry," *Appl. Opt.* **41**, 4630–4637 (2002).
20. Q. Zhan and J. R. Leger, "Interferometric measurement of the geometric phase in space-variant polarization manipulations," *Opt. Commun.* **213**(46), 241–245 (2002).
21. M. Beresna et al., "Radially polarized optical vortex converter created by femtosecond laser nanostructuring of glass," *Appl. Phys. Lett.* **98**(20), 201101 (2011).
22. N. Passilly et al., "Simple interferometric technique for generation of a radially polarized light beam," *J. Opt. Soc. Am. A* **22**, 984–991 (2005).
23. M. Bashkansky, D. Park, and F. K. Fatemi, "Azimuthally and radially polarized light with a nematic SLM," *Opt. Express* **18**, 212–217 (2010).

24. S. Zhou et al., "Creation of radially polarized optical fields with multiple controllable parameters using a vectorial optical field generator," *Photonics Res.* **4**, B35–B39 (2016).
25. X. Dong et al., "Generation of radially polarized beams using spatial light modulator," *Optik—Int. J. Light Electron Opt.* **123**(5), 391–394 (2012).
26. T. Fadeyeva et al., "Natural shaping of the cylindrically polarized beams," *Opt. Lett.* **35**(22), 3787–3789 (2010).
27. C.-H. Yang et al., "Independent manipulation of topological charges and polarization patterns of optical vortices," *Sci. Rep.* **6**, 31546 (2016).
28. S. Vyas, Y. Kozawa, and S. Sato, "Polarization singularities in superposition of vector beams," *Opt. Express* **21**(7), 8972–8986 (2013).
29. T. G. Brown, "Unconventional polarization states," *Prog. Opt.* **56**, 81–129 (2011).
30. Y. R. Shen, *The Principles of Nonlinear Optics*, John Wiley & Sons, New York (1984).
31. B. E. A. Saleh and M. C. Teich, *Fundamentals of Photonics*, John Wiley & Sons, New York (1991).
32. M. S. Soskin and M. V. Vasnetsov, "Nonlinear singular optics," *Pure Appl. Opt.* **7**(2), 301–311 (1998).
33. Workshop of Photonics, "Operation manual of the s-waveplate," https://photonicsolutioncenter.com/sites/default/files/Operation-Manual-130701.pdf (9 August 2017).
34. M. M. Sushckik et al., "Parametric amplification and generation of light," *Radiophys. Quantum Electron.* **13**(5), 489–521 (1970).
35. M. M. Sushckik et al., "Trapping of parametrically coupled waves by pulses and beams of pump radiation," *Radiophys. Quantum Electron.* **12**(2), 235–238 (1969).
36. M. M. Sushckik et al., "Excitation of parametrically amplified waves during spatial capture by pumping-radiation wave packets," *Radiophys. Quantum Electron.* **13**(2), 192–196 (1970).
37. S. A. Akhmanov, V. A. Vysloukh, and A. S. Chirkin, *Optics of Femtosecond Laser Pulses*, American Institute of Physics, New York (1992).

Biographies for the authors are not available.

A6

OPTICAL MANIPULATION FOR STUDIES OF COLLISIONAL DYNAMICS OF MICRON-SIZED DROPLETS UNDER GRAVITY

M. Ivanov, K. Chang, I. Galinskiy, B. Mehlig, and D. Hanstorp

Opt. Express **25**, 1391 (2017)

Research Article | Vol. 25, No. 2 | 23 Jan 2017 | OPTICS EXPRESS 1391

Optics EXPRESS

Optical manipulation for studies of collisional dynamics of micron-sized droplets under gravity

MAKSYM IVANOV,[1] KELKEN CHANG,[2] IVAN GALINSKIY,[3] BERNHARD MEHLIG,[2] AND DAG HANSTORP[2,*]

[1]*Vilnius University Laser Research Center, LT-10223 Vilnius, Lithuania*
[2]*Department of Physics, University of Gothenburg, SE-412 96 Gothenburg, Sweden*
[3]*Facultad de Ciencias, Departamento de Fisica, Universidad Nacional Autonoma de Mexico, Ciudad Universitaria, CdMx 04510, Mexico*
[*]*dag.hanstorp@physics.gu.se*

Abstract: A new experimental technique for creating and imaging collisions of micron-sized droplets settling under gravity is presented. A pair of glycerol droplets is suspended in air by means of two optical traps. The droplet relative velocities are determined by the droplet sizes. The impact parameter is precisely controlled by positioning the droplets using the two optical traps. The droplets are released by turning off the trapping light using electro-optical modulators. The motion of the sedimenting droplets is then captured by two synchronized high-speed cameras, at a frame rate of up to 63 kHz. The method allows the direct imaging of the collision of droplets without the influence of the optical confinement imposed by the trapping force. The method will facilitate efficient studies of the microphysics of neutral, as well as charged, liquid droplets and their interactions with light, electric field and thermodynamic environment, such as temperature or vapor concentration.

OCIS codes: (040.1490) Cameras; (100.2000) Digital image processing; (350.4855) Optical tweezers or optical manipulation.

References and links

1. H. R. Pruppacher and J. D. Klett, *Microphysics of clouds and precipitation* (Springer, 2010).
2. R. A. Shaw, "Particle-turbulence interactions in atmospheric clouds," Annu. Rev. Fluid Mech. **35**, 183–227 (2003).
3. W. W. Grabowski and L. P. Wang, "Growth of cloud droplets in a turbulent environment," Annu. Rev. Fluid Mech. **45**, 293–324 (2013).
4. T. B. Low and R. List, "Collision, coalescence and breakup of raindrops. Part I: Experimentally established coalescence efficiencies and fragment size distributions in breakup," J. Atmos. Sci. **39** (7), 1591–1606 (1982).
5. K. V. Beard and H. T. Ochs III, "Collisions between small precipitation drops. Part II: Formulas for coalescence, temporary coalescence, and satellites," J. Atmos. Sci. **52**, 3977–3996 (1995).
6. R. Bordás, Ch. Roloff, D. Thévenin and R. A. Shaw, "Experimental determination of droplet collision rates in turbulence," New J. Phys. **15**, 045010 (2013).
7. M. Szakáll, S. Kessler, K. Diehl, S. K. Mitra and S. Borrmann, "A wind tunnel study of the effects of collision processes on the shape and oscillation for moderate-size raindrops," Atmos. Res. **142**, 67–78 (2014).
8. B. Nagare, C. Marcolli, O. Stetzer and U. Lohmann, "Comparison of measured and calculated collision efficiencies at low temperatures," Atmos. Chem. Phys. **15**, 13759–13776 (2015).
9. B. J. Devenish, P. Bartello, J-L Brenguier, L. R. Collins, W. W. Grabowski, R. H. A. IJzermans, S. P. Malinowski, M. W. Reeks, J. C. Vassilicos, L. P. Wang and Z. Warhaft, "Droplet growth in warm turbulent clouds," Q. J. R. Meteorol. Soc. **138**, 1401–1429 (2012).
10. A. Ashkin and J. M. Dziedzic, "Optical levitation of liquid drops by radiation pressure," Science **187**, 1073–1075 (1975).
11. R. J. Hopkins, L. Mitchem, A. D. Ward and J. P. Reid, "Control and characterisation of a single aerosol droplet in a single-beam gradient-force optical trap," Phys. Chem. Chem. Phys. **6**, 4924–4927 (2004).
12. R. Power, J. P. Reid, S. Anand, D. McGloin, A. Almohamedi, N. S. Mistry and A. J. Hudson, "Observation of the binary coalescence and equilibration of micrometer-sized droplets of aqueous aerosol in a single-beam gradient-force optical trap," J. Phys. Chem. A **116**, 8873–8884 (2012).
13. M. Horstmann, K. Probst and C. Fallnich, "Towards an integrated optical single aerosol particle lab," Lab Chip **12**, 295–301 (2012).
14. Y. Jiang, A. Umemura and C. K. Law, "An experimental investigation on the collision behaviour of hydrocarbon droplets," J. Fluid Mech. **234** 171–190 (1992).

http://dx.doi.org/10.1364/OE.25.001391
Received 1 Dec 2016; revised 5 Jan 2017; accepted 6 Jan 2017; published 18 Jan 2017

Optics EXPRESS

15. K. Gustavsson and B. Mehlig, "Statistical models for spatial patterns of heavy particles in turbulence," Adv. Phys. **65**, 1–57 (2016).
16. C. Tang, P. Zhang and C. K. Law, "Bouncing, coalescence, and separation in head-on collision of unequal-size droplets," Phys. Fluids **24**, 022101 (2012).
17. A. V. Sergeyev and R. A. Shaw, "An inexpensive uniform-size aerosol generator," Meas. Sci. Technol. **17**, N41–N44 (2006).
18. I. Galinsky, O. Isaaksson, I. R. Salgado, M. Hautefeuille, B. Mehlig and D. Hanstorp, "Measurement of particle motion in optical tweezers embedded in a Sagnac interferometer," Opt. Express **23**, 27071–27084 (2015).
19. K. Nishino, H. Kato and K. Torii, "Stereo imaging for simultaneous measurement of size and velocity of particles in dispersed two-phase flow," Meas. Sci. Technol. **11**, 633–645 (2000).
20. X. G. Zhang and R. H. Davis, "The rate of collisions due to Brownian or gravitational motion of small drops," J. Fluid Mech. **230**, 479–504 (1991).
21. X. G. Zhang, R. H. Davis and M. F. Ruth, "Experimental study of two interacting drops in an immiscible fluid," J. Fluid Mech. **249**, 227–239 (1993).
22. A. Frohn and N. Roth, *Dynamics of droplets* (Springer-Verlag, 2000).
23. Physical properties of glycerine and its solutions (Glycerine Producers' Association,1963).
24. J. Lu, H. Nordsiek and R. A. Shaw, "Clustering of settling charged particles in turbulence: theory and experiments," New J. Phys. **12**, 123030 (2010).
25. D. R. MacGorman and W. D. Rust, *The Electrical Nature of Storms* (Oxford University Press, 1998).
26. J. N. Cuzzi, R. C. Hogan, J. M. Paque and A. R. Dobrovolskis, "Size-selective concentration of chondrules and other small particles in protoplanetary nebula turbulence," Astrophys. J. **546**, 496–508 (2001).
27. O. Isaksson, M. Karlsteen, M. Rostedt and D. Hanstorp, "Manipulation of optically levitated particles," Proc. SPIE **8810**, 88100O (2013).
28. M. Ivanov, M. Viderström, K. Chang, C. Ramirez Contreras, B. Mehlig and D. Hanstorp, "Spectroscopy and optical imaging of coalescing droplets," Proc. SPIE **9922**, Optical Trapping and Optical Micromanipulation XIII, 99220I (2016).
29. E. Bodenschatz, S. P. Malinowski, R. A. Shaw and F. Stratmann, "Can we understand clouds without turbulence?" Science **327**, 970–971 (2010).

1. Introduction

In their textbook on the microphysics of clouds, Pruppacher and Klett [1] devote an entire chapter to collisions of droplets settling under gravity. The primary concern in this problem is the determination of the collision efficiency. The collision efficiency, defined as the ratio of the collision cross-section to the geometric cross-section, is a dimensionless measure of the probability of collision. In addition to determining the droplet growth rates (see e.g. [1]), the collision efficiency is a key ingredient in the collision theory of cloud droplets widely used in many weather and climate models [2, 3]. The collision efficiency is the most uncertain aspect of collision rate theories [3]. Experimental determination of the collision efficiency remains elusive [1, 4–8], although recent studies have yielded some empirical conclusions [9].

In recent years, advances in optical manipulation and high-speed imaging techniques have provided the opportunity of controlling and measuring the size and trajectories of individual droplets in air. In a pioneering study, Ashkin and Dziedzic [10] observed the collision and coalescence between an optically levitated droplet and a gravitationally settling droplet. This study was followed by a large number of investigations. For example, Hopkins *et al.* [11] used optical tweezers to observe the coagulation of aerosol droplets, and they determined the droplet growth rates using cavity-enhanced Raman spectroscopy (CERS) with nanometer precision. Power *et al.* [12] used a single-beam gradient-force optical trap to coalesce droplets of 2 μm to 12 μm in diameter and observed the elastically scattered light from the trapped particles to investigate the time-resolved dynamics of mixing. Horstmann *et al.* [13] constructed a single-aerosol particle trap and coupled it to a conventional optical tweezer to guide and coalesce droplets of 500 nm to 19 μm in diameter. In all of the above studies, optical tweezers provide a fully controllable and convenient way to investigate droplet collisions. However, the light field interacts with the trapped droplets and modifies their dynamics. The work presented here demonstrates a new method of optical manipulation technique that circumvents this problem. The method allows us to precisely image droplet collisions in free fall.

Optics EXPRESS

2. Experimental background

We trap two glycerol droplets of different sizes in air by means of two pairs of focused counter-propagating beams (Fig. 1). Two microscope objectives MO1 and MO2 focus light from two counter-propagating beams to a common focal point, forming the lower trap for the small glycerol droplet. Similarly, the microscope objectives MO3 and MO4 focus light from two laser beams to a second point, forming the upper trap for the large glycerol droplet. The two traps are vertically separated. By switching off the laser beams with the appropriate timing, the droplets fall under the influence of gravity and may collide at a predictable distance below the lower trap. The droplet motion is captured by two high-speed digital video cameras arranged in a horizontal plane. Their lines of sight intersect at an angle of 90°.

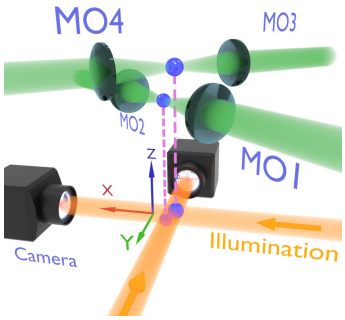

Fig. 1. The principle scheme for studies of droplet interactions. MO1, MO2 and MO3, MO4 are microscope objectives that focus the laser light and form the "lower" and "upper" optical trap, respectively. The droplets are illuminated with LEDs, and their motion recorded by a pair of cameras with their lines of sight arranged at a 90° angle.

The geometry of the collision process is described in Fig. 2. A droplet with radius a_1 is positioned above a second droplet with radius a_2, where $a_1 > a_2$. The impact parameter, χ, is the projection of the distance between the centers of the two droplets perpendicular to their initial relative velocity, $V_1 - V_2$. The projections of the impact parameter onto the x-z and y-z planes yield χ_x and χ_y, respectively, and they are related by the equation

$$\chi = \sqrt{\chi_x^2 + \chi_y^2}\,. \tag{1}$$

In the experiment, we control the droplet impact parameter χ by adjusting the relative horizontal position between the two traps. At a critical impact parameter, χ_c, a grazing trajectory results, as depicted in Fig. 2(b). The collision efficiency is defined as $E = \chi_c^2/(a_1 + a_2)^2$. The geometrical arrangement of the droplets is described by the dimensionless impact number, defined as [14]

$$\mathrm{B} = \frac{\chi}{a_2\,(1+\Gamma)}\,, \tag{2}$$

where χ is the impact parameter defined in equation (1), a_2 is the radius of the small droplet and $\Gamma = a_1/a_2$ is the size ratio. Thus, values of 0 or 1 for the impact number designate head-on or grazing collisions, respectively.

A droplet falling under the influence of gravity and Stokes drag in still air acquires a terminal velocity (Eq. (10-138) of [1])

$$V = \frac{2}{9}\left(\frac{\rho_d}{\rho_a} - 1\right)\frac{g\,a^2}{\nu}\,, \tag{3}$$

Optics EXPRESS

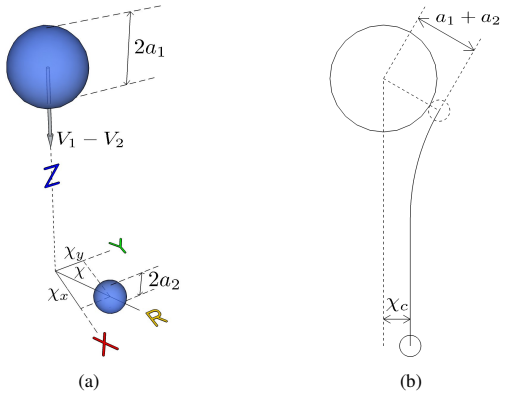

Fig. 2. Panel (a) shows the geometry for the determination of the impact parameter, χ, of the collision process from its two orthogonal projections on x and y-axes. Two droplets with radii a_1 (top) and a_2 (bottom) fall in gravitational field, along the z-axis. The parameters χ_x and χ_y are the projections of the impact parameter χ onto the x and y-axes, respectively. Panel (b) shows the trajectory of the interacting droplets under gravity, as observed from the reference frame of the larger droplet. χ_c is the critical impact parameter for a grazing trajectory of the smaller droplet.

where $g = 9.81\ \mathrm{ms}^{-2}$ is the acceleration of gravity, a is the droplet radius, $\nu = 1.6 \times 10^{-5}\mathrm{m}^2\mathrm{s}^{-1}$ is the kinematic viscosity of air, and $\rho_d = 1.26 \times 10^3\ \mathrm{kg\ m}^{-3}$ and $\rho_a = 1.23\ \mathrm{kg\ m}^{-3}$ are the densities of the droplet and air, respectively. In our study, the droplets are composed of glycerol, but other types of chemical composition can also be used. The Reynolds number

$$\mathrm{Re} = \frac{V\,a}{\nu}\,, \tag{4}$$

measures the effect of convective forces relative to the fluid viscous forces [15]. A value of Re $\ll 1$ allows a Stokesian description of the motion of the droplet. In this process, there are two relevant time scales. First, the droplet relaxes to its terminal velocity in time $\tau_d = V/g$. Second, the representative convective time scale in quiescent air is $\tau_a = a/V$. The ratio of these time scales defines the dimensionless Stokes number

$$\mathrm{St} = \frac{\tau_d}{\tau_a} = \frac{2}{9}\left(\frac{\rho_d}{\rho_a} - 1\right)\mathrm{Re}\,. \tag{5}$$

The Stokes number measures the importance of particle inertia.

Whether or not the droplet kinetic energy can overcome the interfacial energy barrier and coalesce is measured by the Weber number, defined in terms of the radius of the small droplet [16]

$$\mathrm{We} = \frac{2\,a_2\,\rho_d\,(V_1 - V_2)^2}{\sigma}\,, \tag{6}$$

where $\sigma = 6.34 \times 10^{-2}\ \mathrm{Nm}^{-1}$ is the surface tension of glycerol. The droplet physical and kinematic parameters investigated in this work are summarized in Table 1.

Optics EXPRESS

Table 1. Droplet Physical Characteristics and the Collision Parameters in the Experiments

Experimental section	4.1		4.2		4.3	
Diameter, $2a$ (μm)	31.9	40.0	29.9	37.9	29.9	33.9
Terminal velocity, V (cms^{-1})	3.55	5.58	3.12	5.01	3.12	4.01
Reynolds number, Re	0.04	0.07	0.03	0.06	0.03	0.04
Stokes number, St	8.0	15.9	6.6	13.5	6.6	9.7
Diameter ratio, Γ	1.25		1.27		1.13	
Impact number, B	0.51		0.50		0.14	
Weber number, We	2.6×10^{-4}		2.1×10^{-4}		4.7×10^{-5}	

3. Experiment

3.1. Optics and imaging system

A sketch of the experimental setup is shown in Fig. 3. A laser beam generated by a solid state laser (Laser quantum "gem532", 532 nm, 2 W maximum power) passes through a beam splitter (BS) to form two optical traps at different heights, which we named the "upper" and "lower" trap. The transmitted beam that is collinear to the incident beam is used to form the "lower" trap. This beam is split a second time by a polarizing beam splitter PBS1. A micro-lens (MO) with focal length 5 mm focuses each beam such that the foci of the two counter-propagating beams overlap. The combined trapping power from the two beams is approximately 350 mW. In a similar manner, the reflected beam from BS is used to create the "upper" trap, which is positioned approximately 2 mm above the lower trap. Two half wave plates (HW1 and HW2) and the polarizing beam splitters ensure that the counter propagating beams have orthogonal polarization states, thus eliminating undesirable interference at the focal points. Two electro-optical amplitude modulators (EOM1 and EOM2) and two polarizers (P1 and P2) allow us to control the timing of the release of the droplets. The region where the droplets interact is illuminated by two collimated cold white light LED (Thorlabs MCWHL5) operated at 10% of the maximum power. Shadow images are observed by two perpendicularly mounted high speed cameras (Phantom Miro LAB310). In order to minimize heating by the LED the illumination is pulsed synchronously with the droplet collisions. The cameras are equipped with Infinity Model K2 DistaMax Long-Distance Microscope System set to 5×-30× magnification with a mean working distance of 13 cm. Laser light from the trapped droplets is blocked by a notch filter (Thorlabs NF533-17), so that the cameras see only shadow images of the droplets with a bright Poisson spot in the center.

3.2. Droplet generation and size control

We generate droplets in the size range from 4 to 60 μm in diameter using a commercial printer cartridge (Hewlett-Packard C6614). The cartridge works as a drop-on-demand system, where a droplet is ejected each time a TTL pulse is sent to the cartridge from a pulse generator (see [17] and [18] and references within for the droplet generation technique). The cartridge, washed and filled with a solution mixed with 90% (by volume) of distilled water and 10% of glycerol (produced by Fisher Scientific with a purity of 99.6%), produces droplets with a uniform diameter

Optics EXPRESS

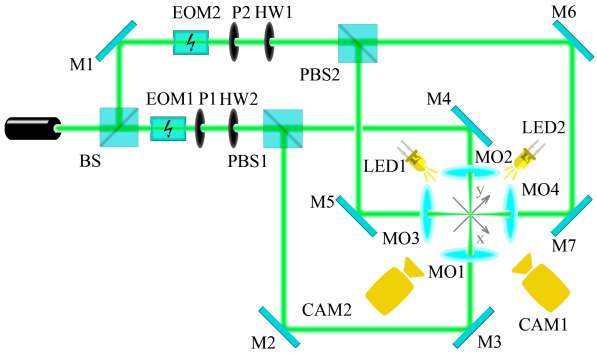

Fig. 3. Sketch of the experimental setup. BS - beam splitter, EOM - electro-optical modulators, M - mirrors, P - polarizers, HW - half-wave plates, PBS - polarizing beam splitters, MO - micro-lenses, LED - illumination, CAM - high speed digital movie camera. The x-y coordinate system represents the laboratory frame. The z-axis points out of the page, whereas gravity points into the page.

of approximately 22 μm. The water evaporates rapidly as the droplet descends down towards the trap. Hence, the size of the trapped droplet can be controlled by changing the mixing ratio of glycerol solution. As an example, a solution containing 5% of glycerol in water yields droplets of approximately 11 μm in diameter after the water has completely evaporated away. Alternatively, the droplet can be made larger by allowing two drops to coalesce in the trap. The size of the largest droplet that can be levitated is determined by the laser beam waist and the available laser power. For the results presented in this work, the droplet size distribution is in the range from 29.9 to 40.0 μm in diameter.

3.3. Droplet chamber

An important part of the setup is the chamber for delivery, trapping and interaction of droplets. Air current within the chamber easily affects the droplet motion. In order to shield the droplets from air turbulence, the cartridge and micro-lenses are mounted in an enclosed chamber. The chamber is made out of metal and cover glass plates connected by flexible construction sealant (Sikaflex 291i). The flexible connection allows the movement of the micro-lenses to be decoupled from the metal plates of the chamber. Hence, the position of the optical traps can be independently adjusted without breaking the seal. Droplets descend from the cartridge through a flexible polymer tubing and enter the chamber through a glass cylindrical tube (2.5 cm in diameter) placed above the chamber. Droplets ejected from the cartridge travel a few centimeters before reaching their terminal velocity and descend vertically down the tube to the trapping points. The chamber has four windows on the sides for illumination and optical access and one on top for visual control and physical access. The volume of the chamber is approximately 0.24 liters.

3.4. Initial control

In order to produce a collision, the two droplets are released from the same horizontal position but at different vertical positions. As a coarse adjustment the separation of the traps is adjusted by moving the lenses for the optical traps (MO1/MO2 or MO3/MO4) in pair. Fine adjustment in the separation of the traps is accomplished by distributing the input power in one of the counter-propagating beams for the optical trap asymmetrically. This is done with a slight rotation of the half wave plate HW1 or HW2 that is placed before the beam enters the polarizing beam

splitters PBS1 or PBS2 (Fig. 3). The vertical separation of the two optical traps is 1.7 mm, which is sufficiently large for the upper droplet to reach its terminal velocity before approaching the lower droplet.

3.5. Release mechanism

The droplets are released from the optical traps by switching off the laser beams using electro-optical amplitude modulators (EOM1 and EOM2) (Thorlabs EO-AM-NR-C4) in combination with linear polarizers (P1 and P2) (Fig. 3). The polarizers P1 and P2 are aligned along the initial polarization vector of the laser beam. By applying the half wave voltage V_π to the EOMs (in our case V_π = 186 V), the EOMs rotate the polarization by 90°, so it is being blocked by the polarizers P1 and P2. Hence, the optical traps are turned off and the droplets are released.

3.6. Acquisition system and timing mechanism

The imaging system consists of two high-speed digital movie cameras (Phantom Miro LAB310 from Vision Research) arranged in a horizontal plane with an angular separation of approximately 90°. Shadow images of the droplets are obtained by projecting incoherent collimated light from two LEDs (Thorlabs MCWHL5) onto the sensors of the cameras (see e.g. [19]). This arrangement not only offers a simple approach in the alignment of the two droplets, but also allows a precise determination of the droplet positions and impact parameters. Movies of the droplet motion are recorded synchronously by the cameras at a resolution of 64 × 768 pixels (width × height). The field of view is sufficiently large to observe both the trapped droplets and the interaction region. In order to resolve the droplet motion at high spatial resolution, each camera is equipped with a K2 DistaMax long-distance microscope from Infinity Photo-Optical Company. Each camera pixel observes an area of 3.98 μm × 3.98 μm in space, so that the total field of view is 0.26 mm by 3.06 mm (width × height). The maximum frame rate at this resolution is 63000 Hz. After loading the droplets into both traps, the LED illumination projects shadows of the droplets onto the camera sensors for the fine positioning (see section 3.4). Both cameras and voltage supply for the EOMs are synchronised and controlled by an external pulse generator (BNC model 565). At time t_0, the pulse generator delivers a trigger signal to the voltage supply of the EOM2 to release the upper droplet, and to initiate the recording of the movies on both cameras. At time $t_{2/3}$ when the upper droplet has traveled 2/3-rd of its way to the lower droplet, a second signal synchronized with the first one triggers the voltage supply to the EOM1 to release the lower droplet. The cameras continue imaging the motion of both droplets until they are out of view. For the initial separation of 1.7 mm, 2/3-rd of it is 1.134 mm and $t_{2/3}$ is approximately 100 ± 50 ms, depending on the droplet size. For a glycerol droplet of 31.9 μm in diameter, $t_{2/3}$ is 100.012 ms.

3.7. Spatial resolution

To map out the laboratory coordinates in real space, a Thorlabs calibration mask (model R2L2S3P1) containing uniform dots of 62.5 μm in diameter arranged in a square lattice with a separation of ℓ =125 μm between adjacent dots is placed in the mutual focal plane of the cameras. An automated particle center finding routine, written in the Matlab programming language, was used to extract the two-dimensional coordinates of the center of the dots, from which the mean separation between adjacent dots L (in pixels) was derived. The spatial resolution of each pixel, R, was obtained from $R = \ell/L$. In our experiments, the spatial resolution was approximately 4.0±0.4 μm per pixel. Because the light sources were collimated, the error in determining the diameters of the droplets is expected to be fairly small, which is shown as follows. The areas of the dot shadows were measured to size the dots. The areas were equal to the number of pixels below a certain threshold. By this method, the shadow diameters of the dots were consistently about 1.06 times larger than the actual diameter of the dots. After correction for the bias, the

uncertainty in determining the mean diameters was about 2 μm, which is representative of the error in the sizing of the droplets.

4. Results

We have recorded 127 movies of collisions of droplets with different impact parameters and sizes. In the following sections, we present three main cases: the coalescence of a gravitationally settling droplet with an optically trapped droplet (section 4.1), the collision between two gravitationally settling droplets in the absence of trapping laser light resulting in non-coalescence 4.2), and coalescence (section 4.3). In all three cases we show the trajectories of droplets as they fall, collide and possibly coalesce.

4.1. Coalescence of droplets in an optical trap

Figure 4 shows the coalescence process between a gravitationally settling droplet and an optically trapped droplet, imaged at a frame rate of 32 kHz, similar to the experiments in [10–13]. The settling droplet is 31.9±2.0 μm in diameter, whereas the optically trapped droplet is 40.0±2.0 μm in diameter, and the resultant droplet is 43.8±2.0 μm in diameter. The high value of impact number B = 0.51, calculated from the projections of droplet separations χ_x and χ_y, indicates no coalescence in the case of absence of laser field. In this experiment, the laser light in the lower trap holds the larger droplet stationary in space and guides the settling droplet towards the trap, as can be seen in the trajectories in Fig. 4. As the two droplets reach a critical separation, they merge to form a larger drop. The resulting droplet stays in the trap and executes a damped oscillatory motion (see Visualization 1). For clarity, this video has been slowed down by a factor of 320 to 100 fps.

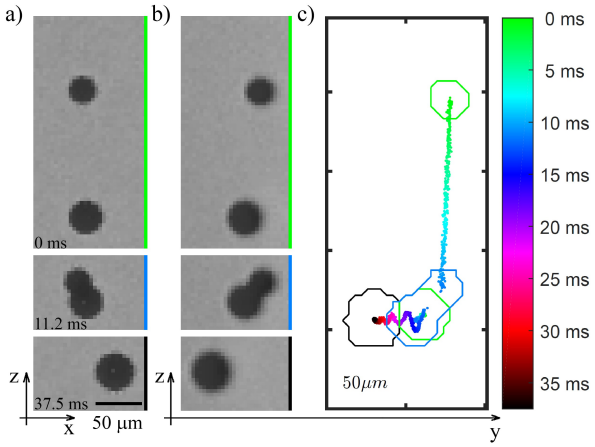

Fig. 4. Coalescence of two droplets while the bottom droplet is trapped by laser light as viewed in (a) the x-z plane and (b) the y-z plane. Panel (c) shows the droplet trajectories as well as their surfaces extracted from the movie recorded in panel (b). Adjacent tick marks on both axes indicate spatial separation of 50 μm. The color bar indicates the progression in time in milliseconds.

Figure 5 shows the coalescence process that is shown in Fig. 4 in a more detailed frame-by-frame sequence of images at a temporal resolution of 31.25 μs per frame. In both sequences, the coalescence process is completed within a time scale of approximately 180 μs. In comparison

Optics EXPRESS

with earlier works [11–13], in which the droplets were guided by the trapping laser light, in our case droplet coalescence is still the favored outcome.

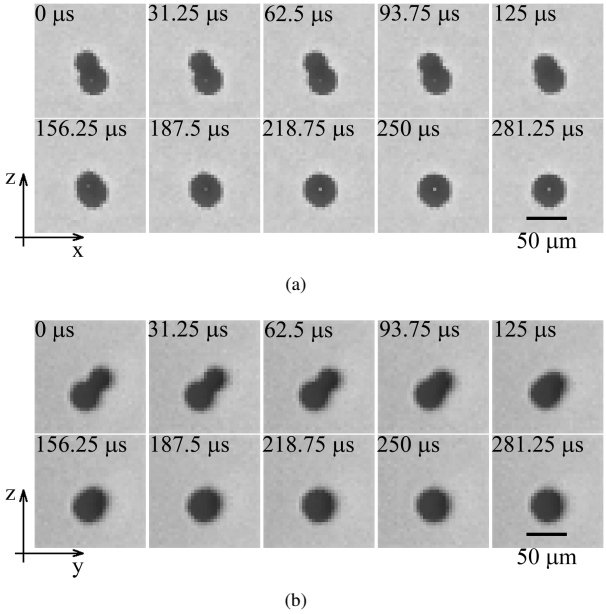

Fig. 5. Projection on x and y directions of time resolved coalescence of two droplets when the bottom droplet is trapped by laser light.

4.2. *Gravitational settling with kiss-and-tumbling motion*

Figure 6 shows the motion of two droplets of different sizes settling under gravity, imaged at a frame rate of 63 kHz. The diameter of the larger droplet is 37.9±2.0 µm and the diameter of the smaller droplet is 29.9±2.0 µm. The impact number, calculated from the projection of droplet separations χ_x and χ_y, is B = 0.5. Before the larger droplet affects the smaller one (0 ms in Fig. 6) the separation between them is $\chi_x = 14\pm2$ µm along the x-axis. Consideration based on the initial geometry of the droplet trajectories predicts that they will collide. However, as the large droplet approaches the small one, it deflects the small droplet to the side without touching, so much so that when the large droplet finally catches up with the small one the separation χ_x reaches a maximum of 35±2.0 µm (at t = 16.5 ms on Fig. 6). As the large droplet continues to fall, the small droplet moves around the large one and gradually recovers its initial vertical motion (t = 25.3 ms in Fig. 6) due to Stokesian microscopic reversibility. This microscopic kiss-and-tumbling motion, whereby the small droplet bends its trajectory around the big droplet without touching, has been theoretically described by Zhang and Davis [20] and observed in experiment for sub-millimeter-size droplets [21]. The total interaction time, which is approximately the duration of time the centers of the droplets stay within a separation of $a_1 + a_2$ from each other, is approximately 4.2 ± 0.1 ms. The movie describing this process is available as supplementary material (see Visualization 2). The temporal resolution in this movie is 15.86 µs. For clarity, this movie has been slowed down to 100 fps.

Optics EXPRESS

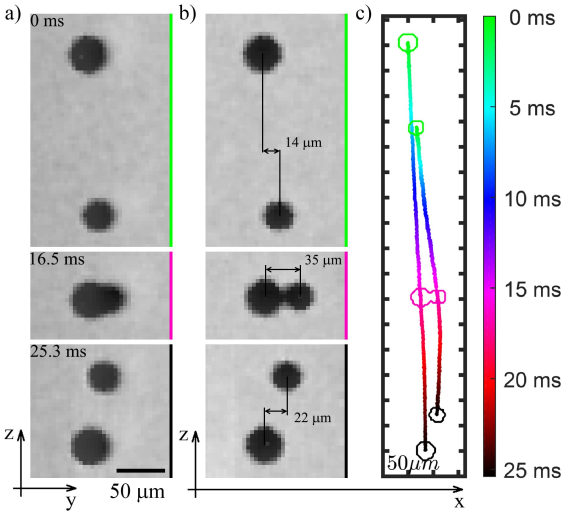

Fig. 6. The motion of two droplets settling in quiescent air under gravity as viewed on (a) the y-z plane and (b) the x-z plane that results in kiss-and-tumbling motion. Panel (c) shows the trajectories of the two droplets as seen in panel (b). Adjacent tick marks on both axes indicate spatial separation of 50 µm. Color bar indicates temporal progression in milliseconds.

4.3. *Gravitational settling with permanent coalescence*

In Fig. 7 and 8, the sequences of images show the coalescence process of droplets settling under gravity and interacting without the geometrical confinement of the laser light (see Visualization 3), imaged at 63 kHz. The diameters of droplets before interaction are 29.9±2.0 and 33.9±2.0 µm, and the diameter of the resultant droplet is 37.9±2.0 µm. The impact parameter, calculated from the projection of droplet separations χ_x and χ_y, is B = 0.14, indicating a near head-on collision. The separation between the centers of the droplets along the x axis is χ_x = 5.98 µm (0 ms in Fig. 7). During the next 11.7 ms, as both droplets approach each other, the larger droplet displaces the smaller droplet, thereby increasing χ_x to as much as 12 µm prior to coalescence. The droplets spent as much as 5.8 ± 0.2 ms together during which time their center-to-center separation stays less than or equal to the sum of their radii $a_1 + a_2$. During coalescence the droplets are being pulled towards each other by capillary forces. The center of mass of the newly formed droplet is in between those of the individual droplets. The duration of the coalescence process is approximately 150 µs. In the accompanying movie (see Visualization 3), the temporal resolution of the image acquisition system is 15.86 µs from frame to frame, but for clarity the movie has been slowed down to 100 fps.

Similar to previous section, the horizontal separation between droplets increases as the droplets approach each other (Fig. 7). But on the contrary, the droplet interaction here results in coalescence. The main difference, between this and the previous section, is the value of the impact parameter: B = 0.14 in the case of coalescence and B = 0.5 in the case of non-coalescence. A smaller impact parameter allows the droplets to come into physical contact. Our estimation of the collision kinetic energy (CKE) and the surface energy (SE) of colliding droplets (as discussed in [4] and [7]) showed that the CKE is insufficient to overcome the SE of the droplets (the CKE is 4 orders of magnitude less than the SE). This implies that the role of the CKE is to bring the two droplets close to each other, so that other intermolecular forces could activate the coalescence

Optics EXPRESS

process.

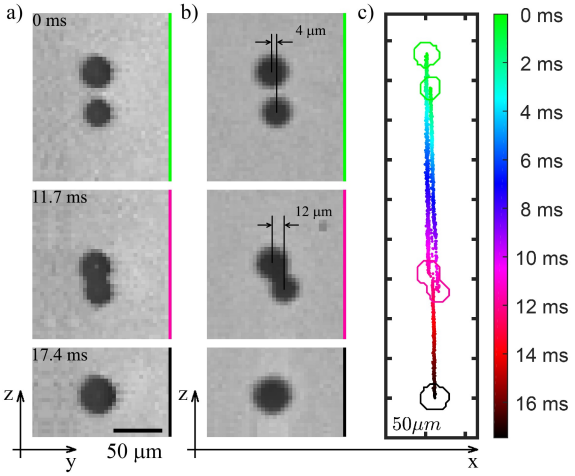

Fig. 7. Snapshots of two droplets that interact without the influence of laser light resulting in coalescence as seen on (a) the y-z plane and (b) the x-z plane. Panel (c) shows the trajectories of the droplets rendered from the images featured in panel (b). Adjacent tick marks on both axes indicate spatial separation of 50 µm. Color bar indicates temporal progression in milliseconds.

5. Discussion

In the present study we have implemented an optical trapping technique to measure the collision trajectories of free-falling droplets. We discuss in the following a number of points that require further considerations.

5.1. Thermal effects

In addition to thermal fluctuations in the surrounding air, two major sources of heat are present in the experiment. First, thermal inkjet technology uses heat, as opposed to mechanical pressure, to force the liquid out of the print head nozzle. Second, although the absorption coefficient of glycerol is small, the focusing effect due to the spherical shape of the droplet invariably heats up the droplets and the air around it. This may have three implications. First, the droplets evaporate and decrease in size. We have measured the evaporation rate of trapped droplet. After the droplet has reached an equilibrium in the trap, the droplet size would have to reduce by as much as 0.5 µm in diameter in order to produce a detectable change in the image. This process happens across a time scale of approximately 10 minutes. We found that the droplet evaporates according to the d^2-law [22], that is the radius decreases in time following the relation $r^2(t) = r^2(0) - \beta t$, where $r(t)$ is the droplet radius at a given time t, $r(0)$ is the initial droplet radius and β is the evaporation coefficient. On the other hand, the time scale during which the droplets interact is of the order of 10 ms, which is approximately 10000 times smaller than the time scale of evaporation. We therefore conclude that the effect of evaporation is negligible in the collision process.

Second, the temperature gradient between the droplet and the surrounding air may give rise to convective air flow and so it raised the question “How much do the droplet trajectories deviate from those derived purely based on isothermal hydrodynamic considerations?”. We did notice

Optics EXPRESS

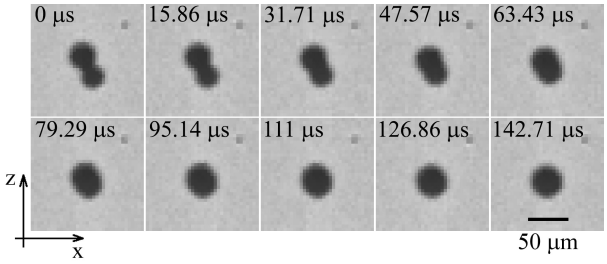

(a)

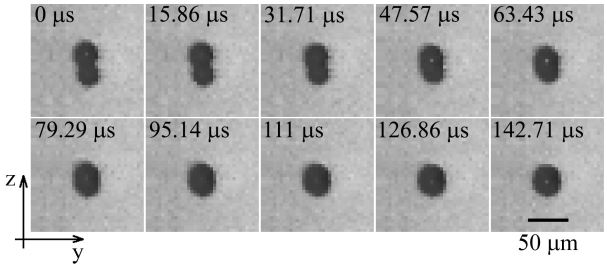

(b)

Fig. 8. Frame-by-frame sequence of images showing the coalescence of two droplets sedimenting in quiescent air as seen on the (a) x-z plane and (b) the y-z plane.

that small droplets ($a \leqslant 2\,\mu$m) occasionally move upwards when released from the trap whereas large droplets ($a > 2\,\mu$m) consistently fall in the same direction as gravity without any apparent convective motion. The droplets reported in this work are typically in the size range of $a \geqslant 15\,\mu$m, so we believe convective motion should be negligible.

Third, the glycerol droplet surface tension diminishes linearly with increasing temperature, albeit very weakly [23]. The surface tension decreases by 7.6% from a value of 6.34×10^{-4} Nm^{-1} at 20 °C to 5.86×10^{-4} Nm^{-1} at 90 °C. Since the optical quality of the upper and lower traps are nearly identical, the droplets should be in nearly the same thermodynamic state upon contact, so that the coalescence mechanism is purely governed by hydrodynamical processes, and that there is no formation of thermal shock waves. The thermal conditions of the droplet environment is certainly one aspect we can control and improve in subsequent experiments.

5.2. Chemical and aerosol contamination

We precisely control the volumetric mixing ratio of the water and glycerol solution in each experiment. However, the chemical and aerosol content of the room air is not monitored. For the individual experiments presented here, we have taken precautionary steps to reduce the probability of contamination by shielding the levitation chamber from its external environment, as described in section 3.3, and isolating the chamber from the room air for up to a day so that undesirable contaminants may settle out of the observation volume. Our current effort is to eliminate this uncertainty by filtering the air in a recirculation loop.

5.3. Electrical charge

Perhaps the largest uncertainty in connection with the hydrodynamics of the collision process is the state of the electrostatic charge on the droplets in our experiments. Earlier experiments utilizing nozzle-based droplet generation technique have noted accumulation of charges on the droplets upon ejection from the nozzle orifice [24]. While the presence of electrical charge may be an undesirable aspect in a hydrodynamic experiment, the dynamics of charged droplets is of particular relevance to the atmosphere [25] and protoplanetary nebula [26]. In the context of our experiment, which concerns the collision process of binary droplets in a gravitational field, the presence of charge may add complexity but is not at all unfavorable. Possible diagnostic measures to determine the amount of electrical charge on individual droplets include applying a DC or AC electric field across the droplet and measuring the displacement from its equilibrium position [27].

5.4. Mixing time scale

Upon initiation of the coalescence process, mixing occurs internally inside the newly formed droplet. The characteristic time scale of the mixing process can be estimated using dimensional analysis [16]. Due to size dissimilarity, the capillary pressure within the small droplet exceeds that within the large droplet by an order of magnitude of $2\,\sigma\,(1/a_2 - 1/a_1)$. This small pressure difference drives the small droplet into the large droplet and disperses the liquid inside the newly formed droplet. This is a fair assumption because large scale motion is most effective at transporting momentum. The characteristic velocity of the large scale motion, u, can be obtained from the dimensional relation $\rho_d\,u^2/2 = 2\,\sigma\,(1/a_2 - 1/a_1)$. This motion occurs at a time scale given by $T = D/u$, where D is the diameter of the newly formed droplet. For a 37.9 μm droplet as discussed in section 4.3, the corresponding time scale is approximately 30 μs. Such a motion is within the resolution limit of our imaging system and is an interesting topic for further research.

6. Conclusion

We have developed a new technique to image the trajectories of a pair of micron-sized droplets settling and colliding under gravity. Unlike previous studies with optical tweezers, in our experiment the droplets interact without the confinement of the optical trap. We have full control over the initial conditions of the collision process, namely the impact parameter, the size ratio, and the chemical compositions of the droplets.

For large impact parameter (B = 0.5), we have observed that the approaching droplets repel each other from their settling trajectories. For small impact parameter (B = 0.14), the collision results in permanent coalescence. To the best of our knowledge this is the first attempt to probe interactions of micron-sized droplets under gravity with fully controllable initial conditions. The experiment described here indicates the potential of the technique for studying the important problem of droplet growth by gravitational collision of cloud droplets. In more sophisticated experiments, the technique could be used to obtain fluorescence spectra of colliding droplets [28], and to probe collision between electrically charged droplets, post-collision dissipative phenomena and rotational dynamics of spinning droplets. Progress in these areas of study will advance our understanding of the strong interactions between turbulence and the microphysical processes in clouds [29].

Funding

Knut and Alice Wallenberg Foundation (Dnr. KAW 2014.0048) “Bottlenecks for particle growth in turbulent aerosols”. The Swedish Institute scholarship through the Visby Programme.

Acknowledgments

The authors thank J. Wettlaufer for valuable discussions.

NOTES

Vilnius University Press
Saulėtekio al. 9, LT-10222 Vilnius
e-mail: info@leidykla.vu.lt,
www.leidykla.vu.lt
Print run copies 17